Multimodal Imaging Utilizing MALDI IMS, IF, Autofluorescence, and Histological Staining for the Investigation of Lipids Integral to the Adaptive Immune Response

By

Marissa Arlene Jones

Dissertation

Submitted to the Faculty of the

Graduate School of Vanderbilt University

in partial fulfillment of the requirements

for the degree of

DOCTOR OF PHILOSOPHY

in

Chemistry

May 14, 2021

Nashville, Tennessee

Approved:

Richard M. Caprioli, Ph.D.

Jeffrey M. Spraggins, Ph.D.

Mark R. Boothby, M.D., Ph.D.

David E. Cliffel, Ph.D.

John A. McLean, Ph.D.

This work is dedicated to the immune compromised and to those with illnesses that remain unnamed or unbelieved.

ACKNOWLEDGEMENTS

I am lucky to have many people to thank for the support and encouragement I have received while pursing my PhD. First, I would like to thank my advisors Dr. Richard Caprioli and Dr. Jeff Spraggins for the opportunities and lessons I have learned during my time in the Caprioli Lab. Next, I would like to thank my committee, Dr. Mark Boothby, Dr. John McLean, and Dr. David Cliffel. Thank you for challenging me, taking the time to teach me, and encouraging me. Your excitement for discovery and encouragement is infectious. Thank you for taking the time to help me learn to write and encouraging my many, many questions. I would like to thank the Boothby lab. Thank you for treating me like one of your own and letting your lab be my second home. A special thanks to Dr. Sung Hoon Cho for being a great collaborator. Much of his work brought about the discoveries highlighted in Chapter III and IV.

I also want to thank the current and past members of the MSRC who helped me along the way. Thank you for listening to my ideas, taking my informational interviews, providing feedback, and lending your expertise. A special thank you to Jamie, your kindness did not go unnoticed and I still have the headband you gave to me when I was having a hard day. Audra, thank you for teaching me what it means to train someone well. I have enjoyed our learning as well as our banter. Lisa and Maureen, you included me, you took the time to explain, and you were always kind. Junhai, your jokes and smile helped me laugh, even on the hard days. Thank you for helping me sort through my projects, organize my thoughts, and chase down answers with me. To all the other graduate students and post-docs, thank you for your camaraderie. Thank you for listening to all my talks and providing great feedback, for taking this journey with me, taking the time to teach me, and for listening as I sat on the filing cabinet. Especially, thanks Josiah. It really helps to have someone who is in your cohort that you truly enjoy and is rooting for you. I'm rooting for you as well. A shout out to Jeff, who believed in me before anyone else did. Thanks for taking a chance on me. Thanks for teaching me about FT-ICR MS, reading and editing my work, and helping me along the way. Thanks to Elizabeth for your mentorship and friendship. It means more than I can say.

Beyond the science community, thank you to my church community, especially my small group. Meeting with you every Monday has vastly improved my life. Thank you for your support and keeping me grounded. I thank God for you. Thank you to my family. Dad, thanks for answering all my phone calls. Mom, thank you for showing me what it means to be a strong woman. Thanks for loving on me extra and helping me organize. You both helped form me into who I am today, and I am so happy I have you as parents. To Jake. What can I even say? You love me, you support me, and I am honored you chose me. I am incredibly proud of the man you are and the way you put others first. I am thankful that I got to spend these times with you.

TABLE OF CONTENTS

LIST OF TABLES

LIST OF FIGURES

ABBREVIATIONS

Immunofluorescence (IF)

Germinal center (GC)

White Pulp (WP)

Red Pulp (RP)

Mass Spectrometry (MS)

Matrix-assisted laser desorption/ionization (MALDI)

Fourier transform ion cyclotron resonance (FT-ICR)

Continuous accumulation of selected ions (CASI)

Imaging mass spectrometry (IMS)

Hematoxylin and eosin (H&E)

Activation-induced cytidine deaminase green fluorescent protein (AID-GFP)

Formalin fixed paraffin embedded (FFPE)

Fresh frozen (FF)

Optimal cutting temperature (OCT)

Carboxymethyl cellulose (CMC)

1,5-diaminonaphthalene (DAN)

Phosphate Buffered Saline (PBS)

Indium tin oxide (ITO)

Receiver operator curve (ROC)

Phosphatidylethanolamine (PE)

Phosphatidic acid (PA)

Glycerophosphoserine (PS)

Glycerophosphoinositol (PI)

Ceramide (Cer)

Sphingomyelin (SM)

Phosphatidylglycerol (PG)

Lyso (L)

Sheep red blood cell (SRBC)

Region of interest (ROI)

Antibody (Ab)

Dice-Sorensen coefficient (DSC)

Fluorescence emission (F_{em})

Conditional knockout (cKO)

Root mean squared (RMS)

Ialpha (IgA)

Igamma 2c (IgG2c)

CHAPTER 1

INTRODUCTION

Overview

The immune system is integral to survival. Immunity, like many biological processes, is a balance. An underactive immune system, referred to as immunodeficiency disorders, can leave the body without the necessary tools to fight off infection. Examples of an underactive immune system include severe combined immunodeficiencies ('boy in a bubble'),[1] common variable immunodeficiency,[2] and X-Linked Agammaglobulinemia.[3] While the more common case on the opposite end of the spectrum, an overactive immune system can cause a wide range of adverse health effects. Examples of diseases in which the immune system is overactive include asthma,[4] eczema,[5] and allergic rhinitis.[6] In addition, a wide variety of diseases and disorders are not only overactive but result in a self-attacking adaptive immune system in which the immune system attacks normal and healthy tissues and often causes destruction. Diseases in which the adaptive immune system misperforms this way are called autoimmune diseases which affect up to 23.5 million Americans. Although current research separates these diseases into more specific categories, in 2005, autoimmune diseases affected eight percent of the total population making it a world-wide problem.[7,8] In addition, autoimmune diseases were the top cause of morbidity in women in the United States and are the second highest cause of chronic illness in women.[9] Some common examples of the over 80+ autoimmune diseases include type 1 diabetes,[10] rheumatoid arthritis,[11,12] and systemic lupus erythematosus.[13]

Although autoimmune diseases and immunity disorders are currently typically studied in a disease-specific manner, the lack of standardized diagnostics and care, chronic nature, and financial burden to patients indicate the pressing need to better understand healthy adaptive immunity to aid in investigating the alterations to ideal immune function.[14] While the basic mechanisms of antibody response have been highly investigated, much remains unknown about the cellular and molecular basis for immune.[15–17]

ADAPTIVE IMMUNITY

The immune system consists of two main subgroups. One subgroup is innate immunity, which fights against foreign bodies, injuries and pathogens and is considered the general immune system. Innate immunity focuses on protection and bacteria-killing substances. It is the first line of defense against a foreign body or pathogen with scavenger cells. The second subgroup, adaptive immunity, is different in that its efforts are more targeted against specific pathogens or mutated cells. Its defense consists primarily of B and T lymphocytes and antibodies (Table 1.1).[18]

Innate Immunity	Adaptive Immunity
Less specific natural immunity[19]	Specific and targeted immunity[20]
Immediate response, first line of defense[21]	Delayed response[22]
Granulocytes, natural killer cells, monocytes, macrophages, dendritic cells[19]	Primarily T and B lymphocytes[22]
No memory or affinity maturation[19]	Memory and affinity maturation[20]
Recognizes self and foreign pathogens[21,22]	Recognizes pathogens via antigens[22]

Table 1.1 A comparison of adaptive immunity vs. innate immunity.

The lymphatic system is the organ system the body uses to carry out an immune response and consists of the lymph nodes, thymus, tonsils, spleen, and Peyer's patches. Humoral immunity is the antibody mediated response used during an adaptive immune response and takes place within the lymphatic system. [23] Humoral immunity encompasses the extracellular fluids such as secreted antibodies.[23] This humoral immunity response involves the interplay between memory B cells, plasma cells and long-lived plasma cells. Within humoral immunity, memory b cells can diversify into plasma cells and become long-lived plasma cells that make antibodies to improve immune memory. However, memory B cells can also differentiate and diversify in germinal centers to improve the specificity of that germinal center response.[24]

Although these immune responses can take place in many lymphatic organs, the spleen is the largest secondary immune organ containing approximately one fourth of the body's lymphocytes, with functions that include antigen presentation, initiation of immune response, and production of antibodies against antigens in blood.[25,26] These functions occur in the two main substructures of the spleen: red pulp and white pulp. The red pulp is the area of the spleen that includes red blood cells and acts as a blood filter to remove foreign or damaged material. The white pulp is the area of the spleen that includes white blood cells and contains germinal centers (roles in improving antibody specification), follicles (non-GC white pulp regions), and periarteriolar lymphoid sheaths (surrounds central arteries), and the marginal zone (the zone between white pulp and red pulp).[25] General morphology is annotated in Figure 1.1.

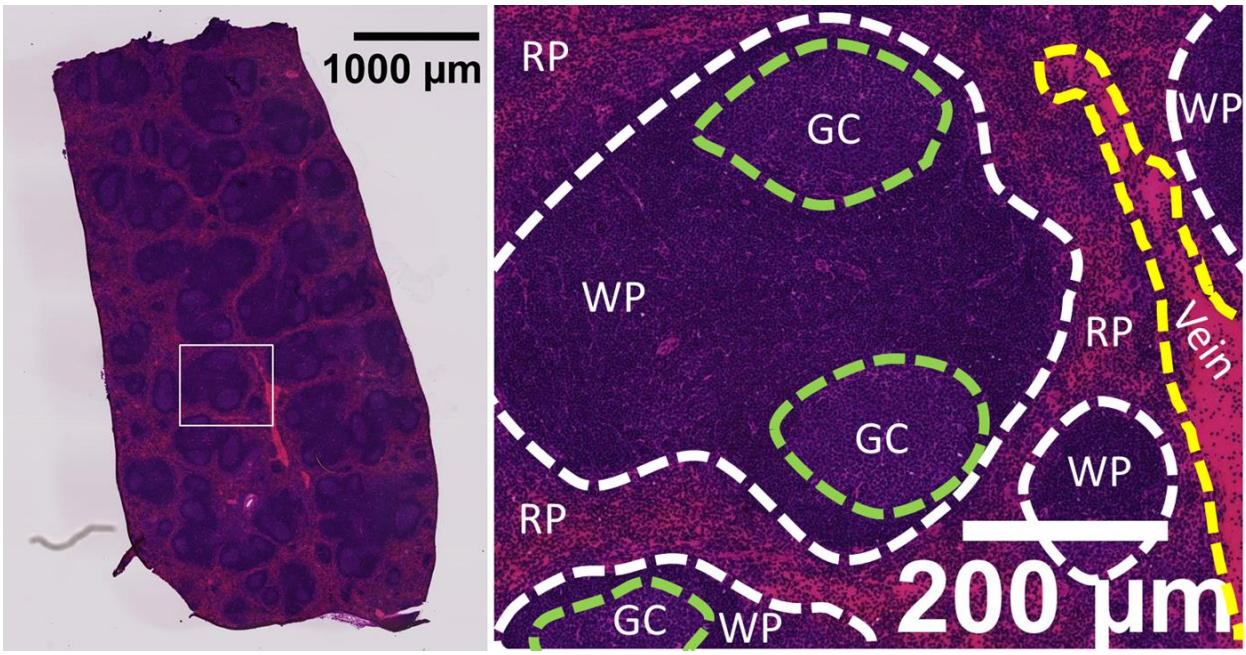

Figure 1.1. General Spleen Structure. *A half spleen is depicted on the left with a 1000 µm in the upper right. The white box is the zoom-in region annotated on the right with a 200 µm scale bar. The marginal zone can be found at the interface between the white pulp (WP), and red pulp (RP) at higher magnification. The germinal center (GC) outlined in green is found within the WP. A vein is also outlined in yellow.*

GERMINAL CENTERS

Germinal centers are a specific subregion in the splenic white pulp involved in the adaptive immune response. Herein we will focus primarily on the spleen due to its large size and active role in germinal center production. More specifically, this work focuses on germinal centers due to their dynamic role in the adaptive immune response beyond physical structure and involvement in a variety of adaptive immunity diseases and disorders. Germinal centers (GCs) are sites of B cell proliferation and antibody differentiation. GCs consist of two main zones, a dark zone in which B cell proliferation takes place, and a light zone in which B cell diversification through antibody class switching and affinity selection occurs.[27] (Figure 1.2) Although B cells originate in the bone marrow, they can be trafficked to the spleen to undergo a germinal center interaction to improve antibody affinity to a pathogen. It was discovered in 2016 that, in mice, GC light zones are hypoxic, reducing B cell proliferation and impairing B cell memory by decreasing antibody class switching.[27] However, the function of this hypoxic niche is not yet known.

The goal of this research is to develop multimodal imaging methods to study splenic germinal center dynamics. All multimodal methods include sample preparation strategies for improving lipid analysis and specific modalities for tying germinal center substructure to lipid expression. The methods will then be applied to germinal center lipid expression and the effect of disrupting this lipid expression on germinal center dynamics. Determining lipids involved in germinal center dynamics can lead to an improved understanding of the adaptive immune response to provide insight into the body's response to disease as well as provide the background work needed for applications in adaptive immunity diseases and disorders.

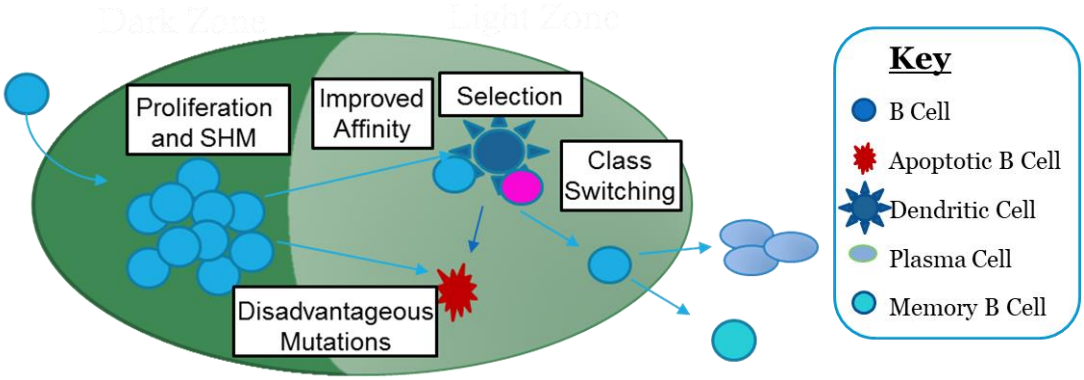

Figure 1.2. Germinal center substructures. *Germinal centers are made up of light and dark zones in which proliferation and somatic hypermutation takes place in the dark zone and affinity maturation (right) and selection take place in the light zone (left). B cells are tested against dendritic cells to check for improved affinity. If cells show appropriate affinity, they can go on to become memory B cells or plasma cells, but if they do not have affected affinity, they can either be destroyed or reintroduced into the dark zone.*

CURRENT GERMINAL CENTER RESEARCH

Mouse Models to Study the Immune System

A variety of mouse models have been used to investigate immune function. Although there are many models to investigate immune efficacy, in general, mice can be genetically modified to test the function of biochemicals by investigating the response to their absence. For example, B and T cell deficient mice have been used to investigate the roles of these cells in specific immune responses. Lipids are especially important in the mediation of a variety of immune responses, but the creation of lipid-deficient mice is not trivial because one must first identify the lipid to target and then investigate the means of mediating the target precursors to lipid production to create a knockout.[28] In addition, because of the integral function of lipids required for mice health and function, inducible lipid knockout mechanisms that produce a partial reduction in specific lipids are needed many lipids are required to study lipids with this method.[29,30]

Analytical Methods to Study the Immune System

The two most widely applied methods of germinal center analysis, flow cytometry and immunohistology, do not provide the chemical and spatial specificity needed for a discovery-based investigation of lipids integral to germinal centers.[31] In flow cytometry, stained cells in suspension are emitted with a laser light source and the forward and side scatter are measured to quantitate the number of cells expressing that fluorophore (Figure 1.3).

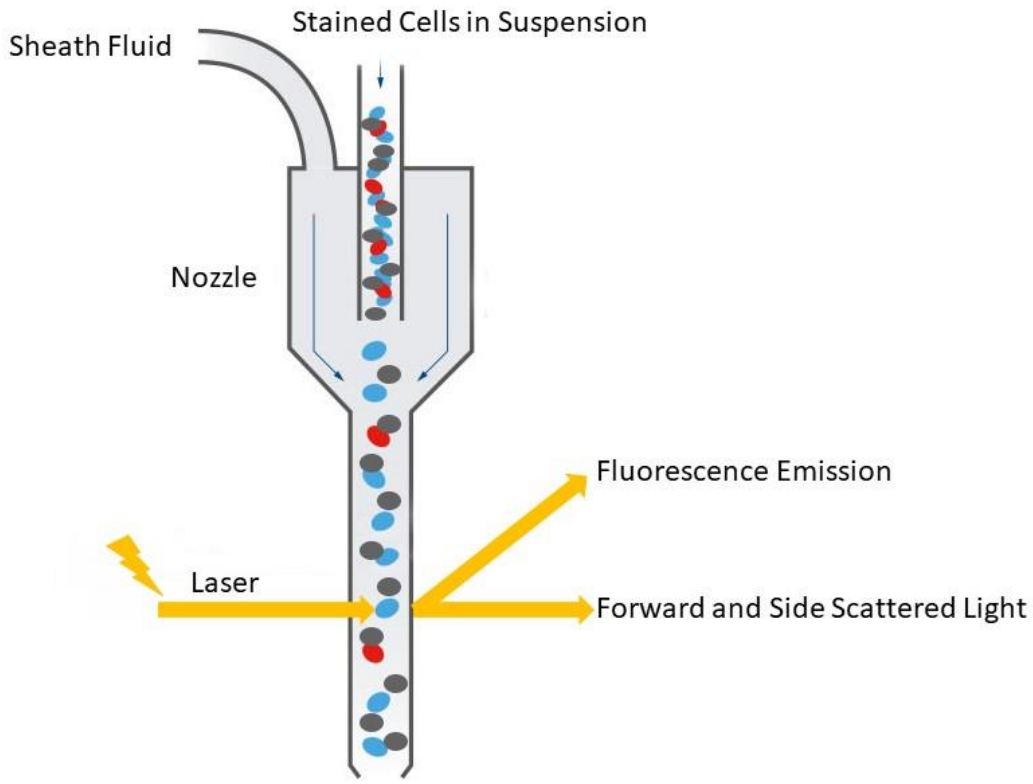

Figure 3. Flow Cytometry. *Cells can be used to determine physical and chemical characteristics of cells. In our experiments, cells are primarily identified as different immune cells and different stages of maturity. First, a sample containing suspended stained cells is injected into the flow cytometer and moved forward to by a sheath fluid to ideally separate cells to flow one at a time. A laser is focused on a cell and the fluorescence emission is used to provide an identity marker to the cell.*

There are many fluorophores used to investigate adaptive immunity, primarily in B and T cells. Flow cytometry has the advantageous ability to identify very specific cell types with multiple markers. In addition, flow cytometry is easily quantifiable and highly reproducible.[31] However, flow cytometry does not enable the analysis of GC responses spatially. Histological analysis of GC allows for the spatial investigation of tissues, but only limited numbers of antibodies can be used on a single tissue section. Although laser capture microdissection followed by flow cytometry has been used, the throughput of these analyses is not feasible for large datasets.[32]

MASS SPECTROMETRY

While other analytical methods for investigating the role of lipids in germinal centers and adaptive immunity in general provide integral results, these technologies do not provide the breadth of coverage and spatial information needed to perform and untargeted investigation. Mass spectrometry (MS) enables the detection of biomolecules from complex matrixes without the need for labeling or fluorescent tagging. The output of this analytical technique is a mass spectrum in which the *m/z* is plotted on the x axis vs. the intensity of each peak on the y axis. Although there are many types of mass spectrometers, every mass spectrometer includes an ionization source, mass analyzer, and a detector.

A variety of ionization techniques are used to generate ions to be analyzed and detected in the gas phase, but each ionization source is uniquely suited for generating ions from different molecular classes from metabolites to proteins. Two of the most common methods of gas phase ionization include MALDI and ESI (Matrix-assisted laser desorption/ionization, electrospray ionization). ESI was invented by John B. Fenn around 1989.[33] MALDI, a soft ionization technique, was invented simultaneously in 1988 by Tanaka and the lab of Karas and

Hillencamp.[34] One large difference between these two ionization sources is the way the sample is introduced. ESI allows for the detection of multiple charged species but uses a sample in solution. MALDI allows primarily for singly charged species, but the sample is introduced in a solid state. A typical MALDI MS experiment collects a group of spectra or a single spectrum from a spotted standard or a single space.

TOF and FTICR mass analyzers

The second part of every mass spectrometer is the mass analyzer. The most widely available mass analyzer for MALDI MS instruments is a time-of-flight analyzer. A TOF mass analyzer determines the m/z value based on the time it takes an ion to travel through a field-free region of a defined length after being accelerated by an electric field of a designated strength. This measurement relies on the definition of kinetic energy. A second type of mass analyzer, Fourier transform ion cyclotron resonance (FT-ICR) mass analyzers, are less common but enable higher mass resolution due to the mechanism by which ions are analyzed and detected. FT-ICR MS was invented by Alan Marshal and Melvin Comisarow in 1974.[35] In general, the FT-ICR analyzer is different from a TOF analyzer in that it relies on cyclotron frequency rather than velocity and size of molecules to determine the *m/z* ratio. Another important difference is that the FT-ICR has a decoupled source enabling methods of improving ion sensitivity such as continuous accumulation of selected ions (CASI). The mass analyzer is made up of six plates- two trapping plates, two excitation plates, and two detection plates. An RF is applied to the excitation plates, propelling ions into a cyclotron orbit. Ions with a greater m/z ratio respond first to this RF pulse and ions coalesce into packets. As this ion packet passes close to the detector plate, the detector plate emits a stream of negatively charged electrons that are read and converted through a Fourier transform that is explained in detail in many other sources. [36] For

this work, we will primarily use FT-ICR MS coupled with MALDI IMS (imaging mass spectrometry).

A typical MALDI IMS experiment consists of tissue preparation and cryosectioning, matrix application, MALDI IMS data acquisition, spectra collection at each pixel, and an ion image for each m/z being generated. (Figure 1.4) In chapter II, we will discuss tissue preparation in depth, but in general tissues are often fresh frozen and sectioned at 10-20 μm and thaw mounted on indium tin oxide coated glass. Matrix is then applied by a robotic sprayer or by sublimation. Sublimation often creates smaller crystal sizes and is optimal for high spatial resolution, but it lacks the reproducibility of robotic spraying. MALDI IMS data acquisition usually occurs in a region of interest, but it is important to maintain the tissue context and image outside the tissue to check for delocalization.

IMS enables the unlabeled mapping of molecules directly from tissue sections in a raster pattern, which enables the visualization of *m/z* in a regio-centeric manner. Although throughout this work we will use MALDI IMS, a variety of IMS technologies exist (desorption electrospray ionization, secondary ion mass spectrometry, etc.).[37–39] MALDI IMS enables the detection of a wide range of molecules from metabolites to proteins. MALDI is specifically suited for lipid analysis from tissue sections due to the nature of lipids in tissue. Lipids are found in high abundance and have easily ionizable head groups and molecular weight generally below *m/z* 1000.[40] High abundance is important for analyzing small portions of tissue. Phospholipids, the most ionized form of lipid by MALDI, are equipped with head groups that produce phosphate anions or nitrogen-centered cations that enhance ease of ionization.[40] A molecular weight below *m/z* 1,000 is the most sensitive operation range for most commercial mass spectrometers and allows for the diffusion of lipids into the matrix layer during desorption.

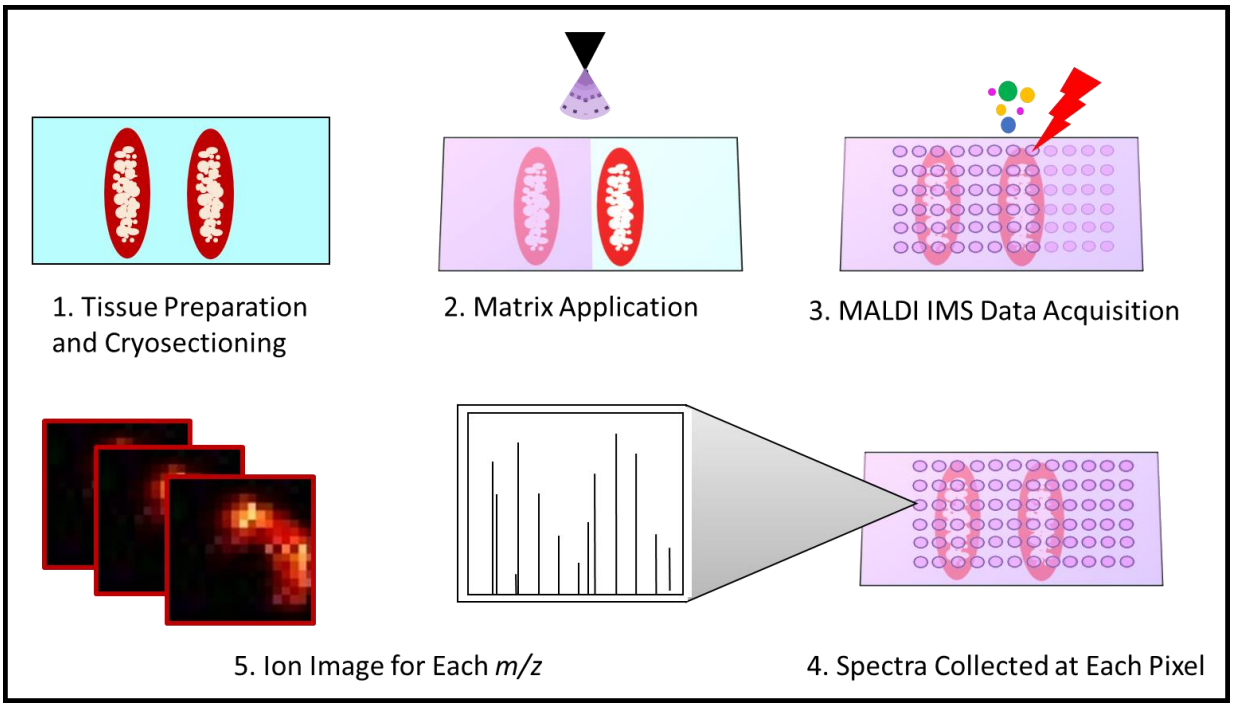

Figure 1.4. MALDI IMS workflow. *Tissues are first prepared and cryosectioned followed by matrix application and MALDI IMS data acquisition. A spectrum is created at each laser ablation. A single m/z value can be selected and formulated into an ion image in a pixel-wise fashion.*

In recent years, MALDI IMS has seen a vast improvement in spatial resolution, especially with instrument modifications. Ideally, MALDI IMS would be able to interrogate tissues on a single cell basis, but with increased spatial resolution comes quadrupled time of acquisition, decreased sensitivity, and increased file size (Figure1.5).

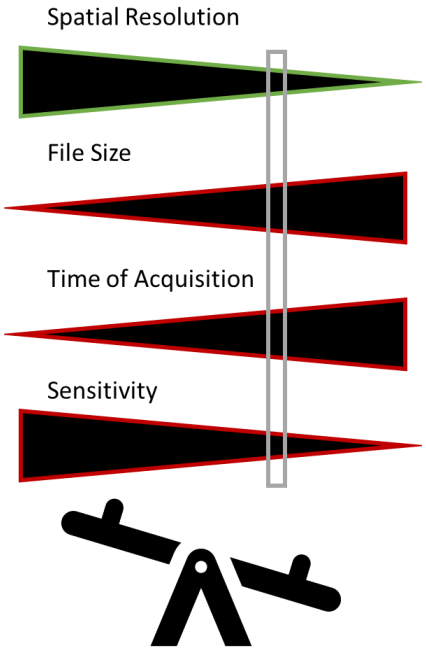

Figure 1.5. Balancing MALDI IMS experimental parameters. *As spatial resolution increases, file size, time of acquisition and sensitivity are all negatively affected. A balance between increased spatial resolution, file size, time of acquisition, and sensitivity is required for a successful MALDI IMS experiment.*

Currently commercial platforms are limited to 20-30 µm, [41,42] but with instrument modifications, we have seen spatial resolutions down to a single micron.[41,42] With this increase in spatial resolution, the ability to tie this data to specific biological contexts has become crucial. To do this, a variety of analysis tools exist for integrating MALDI IMS data in a multimodal workflow,[43–45] but these tools lack to ability to handle large image sizes of a variety of file types. To address the need to analyze such large diverse images, in this work, primarily R cardinal, home-built R scripts, FlexImaging (Bruker Daltonics) and SCiLS are used.[46–48] This need for home-built data analysis tools is due to the high spatial resolution, image size, registration accuracy, and image types.

Multimodal Imaging for Molecular Characterization of the Immune System

Multimodal imaging allows for correlation of the chemical and spatial specificity of MALDI IMS with other modalities. A variety of modalities have been coupled with MALDI IMS. MALDI IMS provides high molecular specificity with the ability to multiplex with no tags; however, it has not yet been able to reach the spatial resolutions of microscopy. Autofluorescence and fluorescence emission (F_{em}) provides generally low chemical specificity, but it has high spatial resolutions and enables high accuracy alignment because it is a non-destructive technique. Immunofluorescence (IF) allows for high chemical specificity, and although one method allows for IF staining prior to MALDI IMS, it is generally non-compatible. However, IF has high spatial resolution and allows for the differentiation of light and dark zones in germinal centers. Historically, MALDI IMS is commonly correlated with histology to identify biologically relevant regions and even guide imaging experiments.[47,49] However, hematoxylin and eosin staining (H&E) does not provide the chemical specificity of other staining methods

and only allows for general structure identification no cell function, thus, other modalities are required (Figure 1.6).

Transgenic fluorophores allow for the chemical specificity of immunofluorescence without the negative sample preparation effects of IF staining. Transgenic fluorophores are genetically encoded reporter fluorophore that directly follow a specific protein or gene. Activation-induced cytidine deaminase green fluorescent protein (AID-GFP) is a transgenic fluorophore we use to identify germinal centers in splenic tissue, due to the higher activity within germinal centers.[50] AID is essential for isotype switching and affinity maturation during adaptive immunity.[50] By combining the previously mentioned technologies, we can garnish information not previously known about germinal centers in a molecular specific spatial manner.

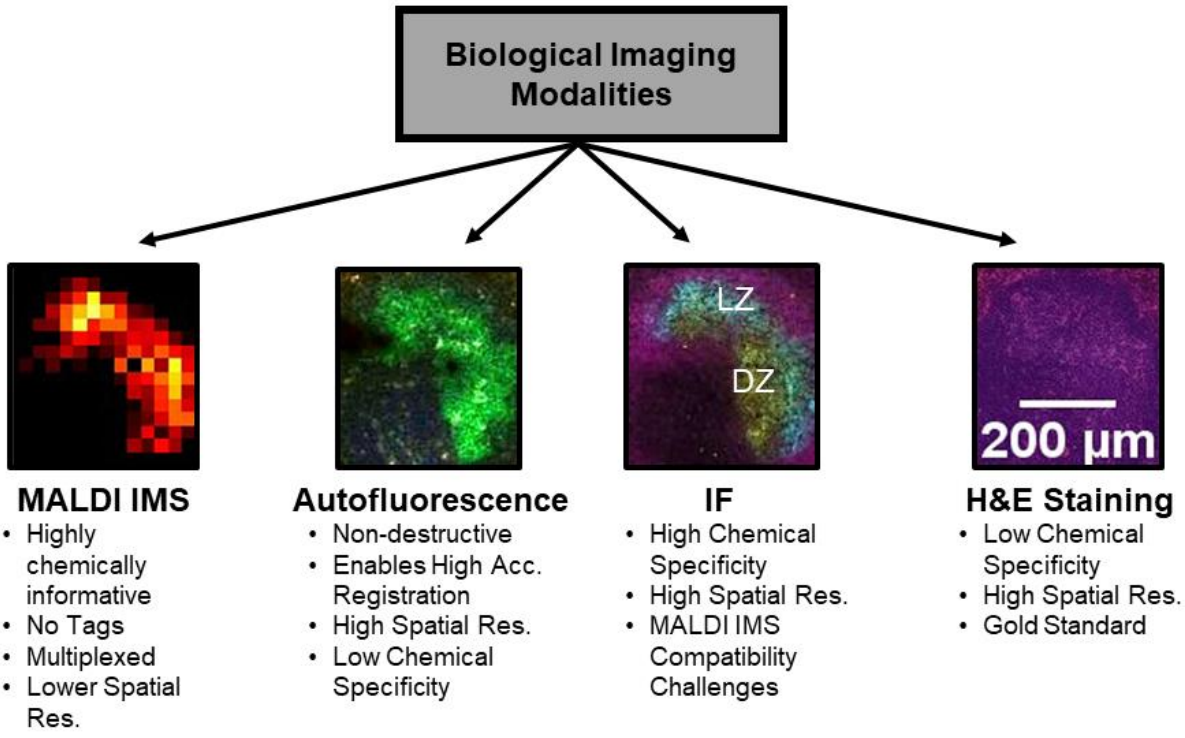

Figure 1.6. Multimodal Imaging Considerations. *In this work, we pair MALDI IMS, autofluorescence/ fluorescence emission, IF, and H&E to study splenic germinal centers. The modality and key characteristics of each are listed.*

SUMMARY AND RESEARCH OBJECTIVES

Adaptive immunity is integral to a broad range of diseases, but much still remains unknown about the spatial effects of micronutrients and the lipids involved in germinal center dynamics. This project seeks to discover the lipidomic changes that take place during GC formation and explore the mechanisms by which these lipids are involved in GC dynamics using multimodal imaging integrating MALDI IMS, H&E, and IF. The first goal of this project was to assess the effects of tissue preparation on lipids detected by MALDI IMS to determine an optimal tissue preparation strategy for spleen tissue. Tissue morphology is greatly impacted by tissue preparation and is integral for high spatial resolution imaging and multimodal imaging.

These methods were then applied to develop a multimodal imaging technique which integrated a genetically encoded fluorophore. The fluorescence emission data were combined with IMS data through multi-modal image processing with advanced registration techniques, and data-driven image fusion fluorophore directed data mining was applied. In an unbiased analysis of spleens, this integrated technology enabled identification of ether lipid species preferentially enriched in germinal centers. This finding led to a third goal of determining the effect of ether lipid knockdown on germinal center expression and germinal center lipid localization. A tamoxifen-induced genetic knockout of PexRAP, a peroxisomal enzyme that executes a late step in ether lipid synthesis, was used to study the role of ether lipids in germinal centers. Developing this multimodal method provided a method for high resolution multimodal imaging and data analysis that could be applied to many biological projects. In addition, determining the lipids localized to the germinal center may provide insight into treatment targets for autoimmune disorders or targets for further study and lipidomic modulation of adaptive immunity.

In this work we seek to address the following goals:

Objective 1: Access methods for tissue preservation to optimize lipid expression and tissue morphology.

Objective 2: Develop a multimodal workflow that employs fluorophore-directed data mining, using image fusion analysis.

Objective 3: Access the lipidomic effect of ether lipid depletion through PexRAP cKO in mice splenic germinal centers.

CHAPTER II

ANALYISIS OF THE EFFECT TISSUE PREPARATION STRATEGIES HAVE ON LIPIDS IN SPLEEN AS DETERMINED USING MALDI FT-ICR IMS

Acknowledgements

The authors gratefully acknowledge Dr. Sung Hoon Cho and Prof. Mark R. Boothby for providing the spleen tissues for this research and Dr. Nathan Heath Patterson for useful discussions. The authors acknowledge the following funding sources for support: Institute of Diabetes and Digestive and Kidney Diseases (U54DK120058 awarded to J.M.S. and R.M.C.), NIH National Institute of Allergy and Infectious Disease (R01 AI138581 awarded to J.M.S.), the NIH National Institute of General Medical Sciences (2P41GM103391 awarded to R.M.C.), the National Institute of Environmental Health Sciences training grant (T32ES007028, E.K.N), and NSF DGE-1445197 (awarded to M.A.J.).

Overview

MALDI IMS enables untargeted molecular mapping directly from tissue sections and is ideal for studying the spatial distributions of the lipidome. There are a wide variety of sample preparation techniques currently in use for MALDI IMS. Different tissue sample preparation approaches prior to MALDI IMS can alter both the localization of endogenous lipids and sensitivity with which they are detected, biasing resulting analyses. Here, we present a systematic study of various sample preparation methods, including fixation, freezing, and washing, to determine the effects on the spectral quality and tissue morphology. We use MALDI IMS and histological staining

(hematoxylin and eosin) to explore the effects of sample preparation on robustness, tissue structure, and approach sensitivity. Using murine splenic tissue, we determined that varying freezing method had no effect on molecular coverage and sensitivity of resultant lipid spectra. However, formalin fixation prior to freezing and ammonium formate washing after tissue processing had variable effects, such as increased sensitivity for specific lipids and classes. Overall, this study will serve as a guide for appropriate sample preparation, optimization, and data analysis for a variety of biological applications.

INTRODUCTION

MALDI IMS enables label-free visualization of molecules directly from tissue sections.[51] This technology is ideal for untargeted discovery of the tissue molecular landscape that can be spatially correlated to histological data. The localization of discrete molecules can help us understand the function or disfunction of cells within the tissue. For example, MALDI IMS has been used to investigate a variety of infections, diseases and cancers.[52–61] MALDI IMS is adept for interrogating lipids, metabolites, peptides and protein distributions in biological tissues. Although MALDI IMS detects a broad range of molecules, lipids are particularly assessable because they have high ionization efficiencies and are highly abundant. Lipids play an important role in biological functions, such as cell signaling, energy storage and forming cellular membranes.[40] As such, lipids are central to the investigation of metabolism and metabolic products, allowing for greater molecular insights into healthy and disease phenotypes. However, to obtain the most amount of information from samples, we must compare and optimize the available sample preparation and data analysis approaches to ensure high reproducibility, sensitivity, and analytical significance. Current work comparing sample preparation strategies primarily focuses on improving the number of detectable features [62] rather than investigating

spectral differences between the different preparations. Herein, we investigate not only the number of detectable features, but trends based on accurate mass identification.

A variety of sample preparation methods are currently used to prepare a tissue for lipid detection with MALDI IMS. Although there are many sample preparation strategies we could test, herein we focus on the effects of fixation, common freezing practices, and ammonium formate washing. To begin, fixation methods preserve tissue and reduce biological hazards by killing many pathogens.[63–65] There are many types of fixing methods including ethanol, methanol, formalin, and others.[63,66] Formalin fixation is the most common fixative and can be applied before or after tissue sectioning and can be reduced into three different methods: formalin fixed and embedded in paraffin (FFPE), formalin fixed then fresh frozen or fresh frozen then fixed. Proteins and lipids are cross linked during formalin fixation, forming a more stable tissue matrix and both the method and time of fixation affect the chemical landscape.[63] For example, after 24 years of fixation there is an increase in lyso compounds, fatty acids, and phosphatidic acid.[67] Although it is common practice to submerge tissue in formalin for a minimum of 24 hours,[68] the exact fixation times varies with fixative and sample type (e.g. density of the tissue, size, and thickness).[69] Recent studies have shown that fixation affects lipid detection within tissues after as little as 15 min of fixation, where small metabolites and lipids showed a ~90% decrease in ion intensity.[70]

Fixed tissues are often embedded in paraffin for stabilization during storage and improved sectioning.[62] FFPE samples are readily available because they can be stored for years at room temperature, resulting in vast collections of annotated specimens stored in tissue banks and the abundance of samples are often available for wide-scale analyses.[71] Unfortunately, lipid detection is decreased in FFPE tissues compared to fresh frozen (FF) alternatives. While FFPE is commonly and successfully used for peptide IMS analysis, this requires harsh solvents that dissolve lipids and

results in poor detection. Because of this difficulty, formalin fixed tissue without paraffin embedding is more commonly used for imaging peptides and lipids.[62] However when tissues are fixed and immediately frozen, ice crystals form and puncture cellular membranes, producing holes within the tissue that introduce artifacts in the tissue structure.[72] Sucrose solution is used as an MS-compatible cryo-protectant that can prevent ice crystal formation and other freezing artifacts by adjusting solution tonicity within the tissues.[73,74]

Because of the challenges associated with MALDI IMS analysis of fixed tissue (complex reaction products, solubility, etc.), FF tissue is often used to simplify tissue preparation and maintain molecular distributions. Although molecular information is conserved, tissue morphology is negatively impacted from freezing artifacts[69] when compared to FFPE samples.[19] A variety of procedures exist to reduce freezing artifacts and three of the most common include using dry ice, liquid nitrogen, or isopentane. The samples can be frozen directly on crushed dry ice pellets or blocks[75], floating or submerging in liquid nitrogen,[76] or floating on an isopentane bath. Tissues are prone to cracking after snap freezing with liquid nitrogen.[77] Because liquid nitrogen freezes more quickly than dry ice, it results in fewer freezing artifacts in highly lipidic samples. However, dry ice is more easily accessible. Incorporating an isopentane bath slows tissue freezing and result in reduced tissue cracking and artifacts.

Balancing the tissue structure and ease of molecular ionization is key to any sample preparation. Embedding materials preserve tissue morphology and is often necessary when small, fragile, or heterogeneous tissues or tissues require cryosectioning.[73] Commonly, optimal cutting temperature (OCT) embedding material is used for histological assessment, but reduces ionization efficiency of analytes during MS analysis. While OCT can be removed[78] for MALDI IMS analysis of proteins[79], it introduces numerous background peaks and reduces sensitivity of lipids and small

metabolites. Carboxymethyl cellulose (CMC) is an alternative embedding material results in fewer spectral interferences in the lipid mass range.[80] Moreover, each fixation or embedding method introduces some chemical background. To combat this, a variety of washes can be incorporated after sectioning to improve MALDI IMS signal by removing salts and other chemical artifacts from sample preparation. Ammonium formate or ammonium acetate washes remove salt, improving analyte ionization.[81] These solutions are also not vacuum stable, so they are easily removed upon introduction into the high vacuum of the MS source, and thus do not create contaminates in the resulting mass spectra.

To investigate the spectral and tissue structural effects of these common tissue preservation and preparation methods, we evaluated the resulting lipids detected after various sample preparation methods using MALDI IMS and evaluated tissue structure using histological staining. Tissue structural integrity is especially important for multimodal experiments as serial sections are often used to connect the disparate datasets, and the spatial alignment of these sections is paramount to driving biological conclusions. To address this gap in knowledge, we have explored the effects of tissue preparation strategies on specific lipid groups. Moreover, we have demonstrated the effects tissue preparation strategies have on tissue structure and how this relates to multimodal experiments.

MATERIALS AND METHODS

Materials

1,5-diaminonaphthalene (DAN), CMC sodium salt, neutrally buffered formalin, and sucrose were all purchased from Sigma-Aldrich Chemical Co. (St. Louis, MO). Phosphate buffered saline (PBS), isopentane, and ammonium formate were purchased from Fisher Scientific (Pittsburg, PA).

Sample Preparation

Animal experiments were approved by the Vanderbilt Institutional Animal Care and Use Committee. Mouse spleens were excised from non-perfused mice in a mixture of male and female (M=3, F=2) C57BL/6 control mice aged 6 to 8 weeks. Each spleen was sectioned into four equal parts ~4 mm in width. Each fourth was prepared according to a different sample preparation methods: frozen on crushed dry ice pellets, frozen over liquid nitrogen, [30] frozen over isopentane or formalin fixed and frozen over isopentane.[82] After freezing spleens were embedded in 2.6% CMC (Figure 2.1a).

Samples were submerged in 50 mL of 10% neutrally buffered formalin (NBF) [83] for 24 hours at ~20 °C. Where specified, samples were submerged in different amounts of sucrose solutions (15%, 20%, 30% w/v, PBS) for 30 min, followed by an additional 30 min in a new sucrose solution, and an overnight incubations.[72] All tissues were stored under nitrogen at -80 °C prior to sectioning. Frozen tissue was cryosectioned at -20 °C into 12 µm tissue sections at a depth of 360 µm using a cryostat 3050S (Leica Microsystems GmbH, Wetzlar, Germany) to ensure consistency and comparability of tissue sections and resultant data across all experimental conditions. All structures of the spleen (i.e., red pulp, white pulp, and germinal centers) can be investigated at this depth. The sections were thaw mounted onto indium tin oxide coated (ITO) glass slides (Delta Technologies, Loveland, CO, USA) for IMS experiments or Superfrost Plus Gold glass microscope slides (Erie Scientific, Ramsey, MN, USA) for microscopy experiments. Two serial sections were collected for H&E staining and MALDI IMS. Slides were washed with 50 mM ammonium formate (pH 6.4, 4 °C) for 20 sec, twice. [81] Samples were then dried under a stream of nitrogen before DAN matrix was applied.

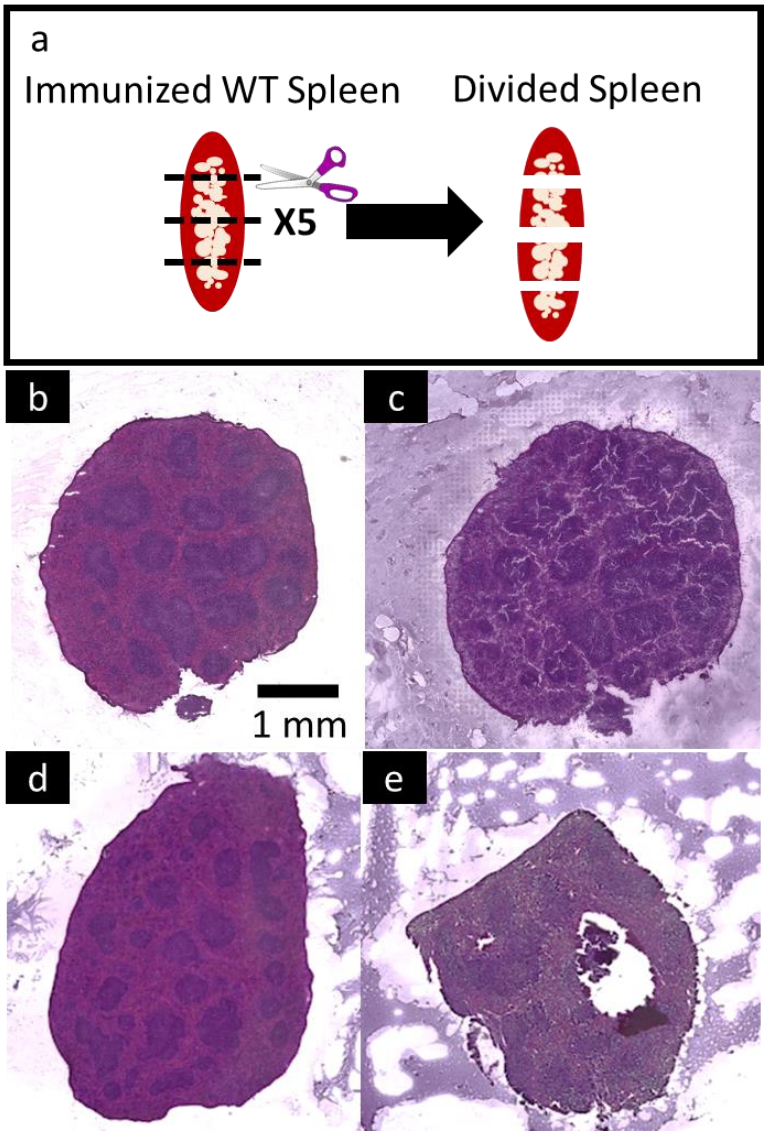

Figure 2.1.Experimental design and histological stains. *a) Mice were sacrificed one week after immunization with sheep red blood cells, excised, and divided into four parts. Each part was processed according to a different tissue preparation as follows: formalin fixed for 24 hours sucrose sunk fresh frozen on isopentane tissue, fresh frozen on dry ice, fresh frozen over liquid nitrogen, and fresh frozen over isopentane. b) H&E stains depicting spleen stained after MALDI IMS from fresh frozen tissue and c) fresh frozen ammonium formate washed tissue. Serial section H&E showing d) fresh frozen and e) formalin fixed sucrose sunk fresh frozen tissue. A scale bar depicts 1 mm in the bottom right of panel b.*

Histological and IMS Analysis

H&E staining was performed on the same sample after MALDI IMS and a serial section as previously described [84] and scanned with a Leica SCN 400 optical slide scanner at 10x (Leica Microsystems GmbH, Wetzlar, Germany). DAN matrix (10 mg/mL in 90% acetonitrile) was deposited using an automated nebulizer (TM Sprayer, HTX Technologies, Carrboro, NC, USA).[85] The TM-Sprayer settings were as follows: solvent flow rate of 0.15 mL/min, nozzle speed of 1200 mm/min, nozzle temperature of 85°C, track spacing of 1.5 mm, 8 passes with 90-degree rotation on every other pass, resulting in a matrix density of 0.002182 mg/mm^2. Nitrogen was used as a nebulizing gas and was set to 10 psi. Although many matrices are used to study lipids using MALDI IMS, we chose to limit the factors affecting our experiment by using a commonly used matrix, DAN. This matrix is often used because of its high sensitivity and ability to be used in both positive and negative ion modes. The effects of different matrices on lipid detection has been previously studied showing the potential of each matrix.[86] However, DAN is widely used for lipidomic analyses, due to its sensitivity and ability to detect lipids in both positive and negative ion modes.[84,87]

High mass resolution data was acquired with a 15T Bruker MALDI FT-ICR solariX mass spectrometer (Bruker Daltonics, Billerica, MA). The instrument is equipped with a Smartbeam II 2kHz Nd: YAG (355nm) laser and a dynamically harmonized ParaCell ion cyclotron resonance detector. Data were collected in negative ion mode from *m/z* 200-2000 with a raster step of 75 µm on one half of the sample and in positive mode from *m/z* 400-2000 with a raster step of 75 µm on the other half. The data size was 1 MB per spectrum. Each pixel consisted of 500 laser shots with the small setting of the laser (~50 µm footprint) at a frequency of 2000 Hz. The laser power was adjusted between 50 and 70% to maintain a base peak intensity of 1x10 ^{7} a.u. ion intensity or

higher. For positive mode experiments, a resolving power of 261,000 was achieved at *m/z* 400, and for negative mode experiments, a resolving power of 138,000 at *m/z* 400 was achieved. Internal calibration was performed using red phosphorus in both positive and negative ion mode resulting in <5 ppm mass error. Ion images were normalized using root mean squared normalization. Imaging experiments were performed as technical replicates on five different biological samples.

Data Processing

Data was analyzed using SCiLS (2017a, version 5.00.9510, Bruker Daltonics, Billerica, MA). Receiver operator curve (ROC) analysis was used to filter for changing species using ROC values of greater than 0.6 and less than 0.4. These peaks were identified by accurate mass using LIPID MAPS[88–91]. This subset was further tested for statistical significance using a two-tailed paired t-test. Fold change values were calculated by estimating a noise floor for each experiment (3,000-5,000 a.u.). Data was visualized utilizing the web tool ClustVis to create heatmaps.[92]

RESULTS AND DISCUSSION

Histological Staining

To investigate tissue preservation and lipidomic profiles of lipids from mouse spleen using various tissue preparation strategies (Table 2.1), we performed H&E staining and IMS. Qualitatively, the structure of FF tissues visualized using H&E staining showed no difference using the tested freezing strategies (Figure 2.2). However, ammonium formate washing causes increased hematoxylin staining of CMC and increased tissue structural artifacts after MALDI IMS (Figure 2.1b-c). Due to the lack of tissue disruption in a serial section H&E, we believe that without fixation prior to ammonium formate washing, the matrix removal process in conjunction with the

ammonium formate wash dries the tissue, resulting in cracking. In addition, sectioning and mounting formalin fixed tissues sections results in folding and bubbles (Figure 2.1d-e) compared to FF tissues. Although freezing on dry ice is suitable for tissues not fixed in formalin, our results indicate that tissues fixed in formalin would benefit from a freezing method like floating the tissues on isopentane for freezing, which reduces freezing artifacts and cracking and balances speed and temperature (Figure 2.2).

FIXATION	CRYOPROTECTION	FREEZING	EMBEDDING	WASH
Fixed 24 hours	Sucrose	Isopentane	CMC	ammonium formate
Fixed 24 hours	Sucrose	Isopentane	CMC	None
None		Dry Ice	CMC	ammonium formate
None		Dry Ice	CMC	None
None		Nitrogen	CMC	ammonium formate
None		Nitrogen	CMC	None
None		Isopentane	CMC	ammonium formate
None		Isopentane	CMC	None

Table 2.1. Tested sample preparations. Eight sample preparations were tested. Sample preparations were either formalin fixed for 24 hours and submerged in gradient solutions of sucrose followed by fresh freezing or unfixed and fresh frozen. Three materials were used for freezing: isopentane, dry ice, and liquid nitrogen. All samples were embedded in CMC and either washed or unwashed.

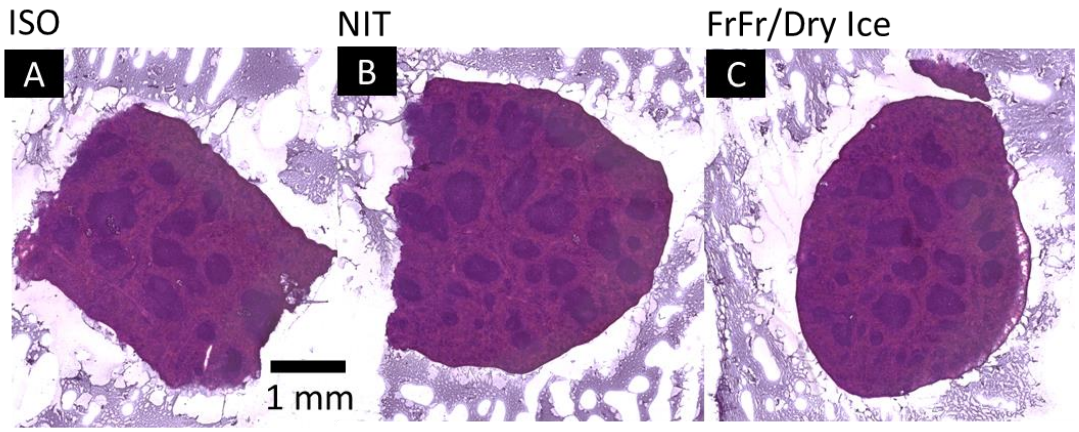

Figure 2.2. Freezing strategies histological stains. *H&E stains of spleens that have undergone different freezing strategies: a) isopentane frozen mouse spleen with a 1mm scale bar, b) nitrogen frozen spleen, and c) dry ice frozen tissue*.

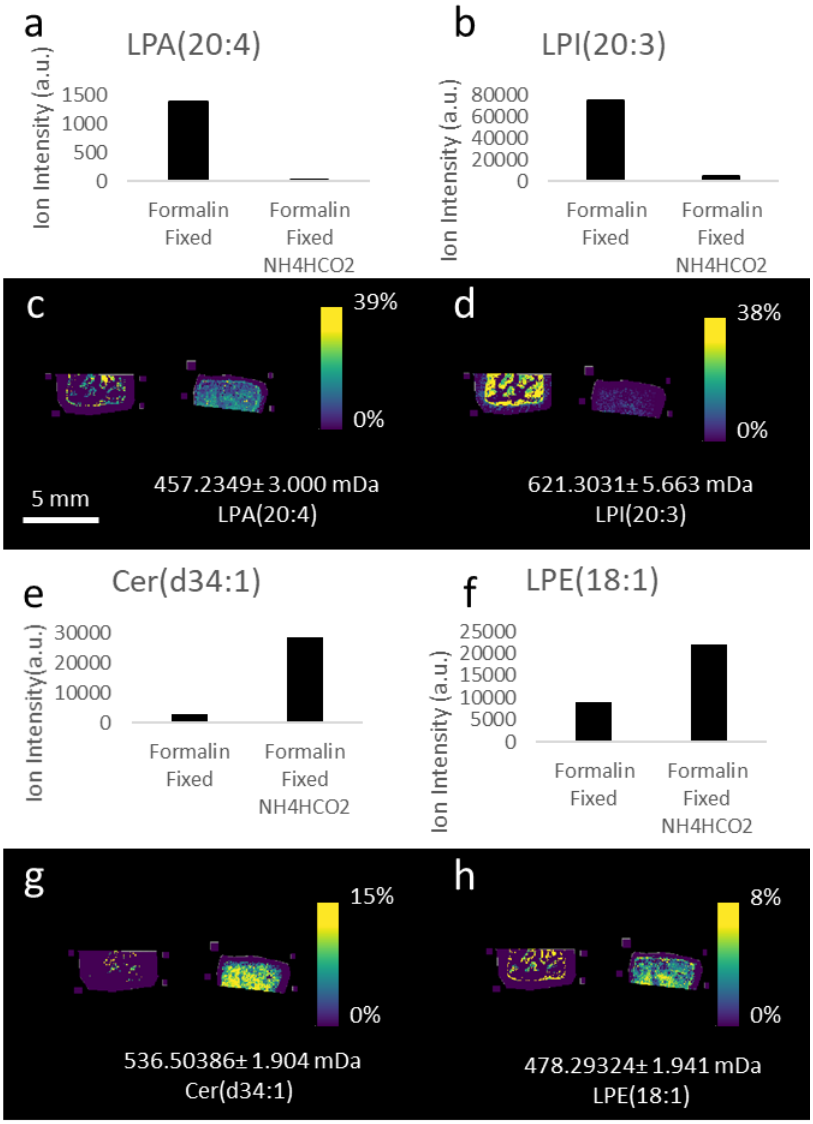

Figure 2.3. Formalin fixed vs. formalin fixed ammonium formate washed tissues. *Bar graphs (a, b, e, f) and ion images (c, d, g, f) depicting the ion intensity (a.u.) difference between formalin fixed and formalin fixed ammonium formate washed tissues for the lipids LPA(20:4), LPI(20:3), Cer(d34:1), and LPE(18:1) (p= 0.07, 0.07, 0.02, and 0.07, respectively) as identified by accurate mass in negative ion mode with formalin fixed on left and formalin fixed ammonium formate washed on right.*

MALDI IMS

Negative Ion Mode

Typically, sample preparation strategies are compared based on the number of spectral features detected. In general, different freezing strategies did not significantly affect spectral features (i.e., ROC 0.4-0.6); however, formalin fixed tissue sections produce the most features (2285±307) in negative ion mode, followed by FF tissue sections (1759±522 features) (Appendix A Table 1-2). When comparing FF to formalin fixed tissues, there is a significant difference in the number of detectable features ($p=0.0002$) (Appendix A Table 2). Ammonium formate washing also significantly decreased the number of features for both formalin fixed and FF tissues ($p=0.009$ and $p=0.01$, respectively; Appendix A Table 1,3). However, simply measuring the number of features does not differentiate whether these observations are a result of changes to lipidomic profiles or chemical noise. For example, although formalin fixed samples produce the most features, there are no lipid classes in positive or negative ion mode that show enhanced detection with fixation compared to FF tissues. In addition, FF and formalin fixed ammonium formate samples exhibited no significant difference in the number of features but showed significant changes in individual lipid intensities, indicating that formalin fixation introduces more chemical noise (Appendix A Table 2.1-12, Appendix A Table 2.35-42, Figure 2.4-9).

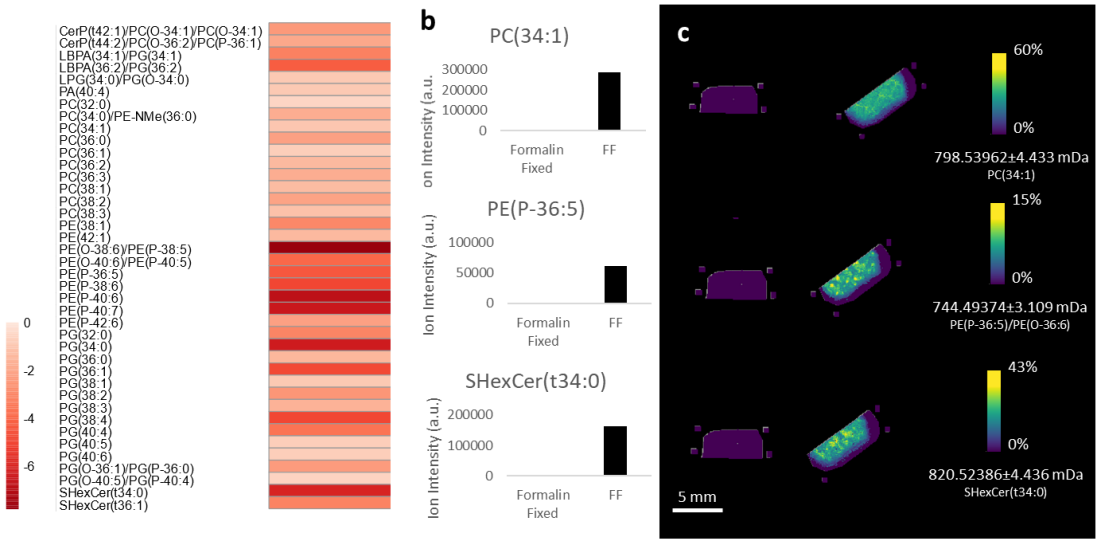

Figure 2.4. Formalin fixed vs. FF sodiated. *a) A heatmap depicting the average log2 fold change of $[M+Na]^+$ ions with decreased intensity in formalin fixed fresh frozen (formalin fixed) samples compared to fresh frozen (FF) samples. (ROC values >0.4 and <0.6) b) A bar graph c) and ion images showing the representative ion intensity and spatial distribution of PC(34:1) (p=0.8), PE(P-36:5) (p=0.000002), and SHexCer(t34:0) (p=0.01) as identified by accurate mass with formalin fixed on left and FF on right.*

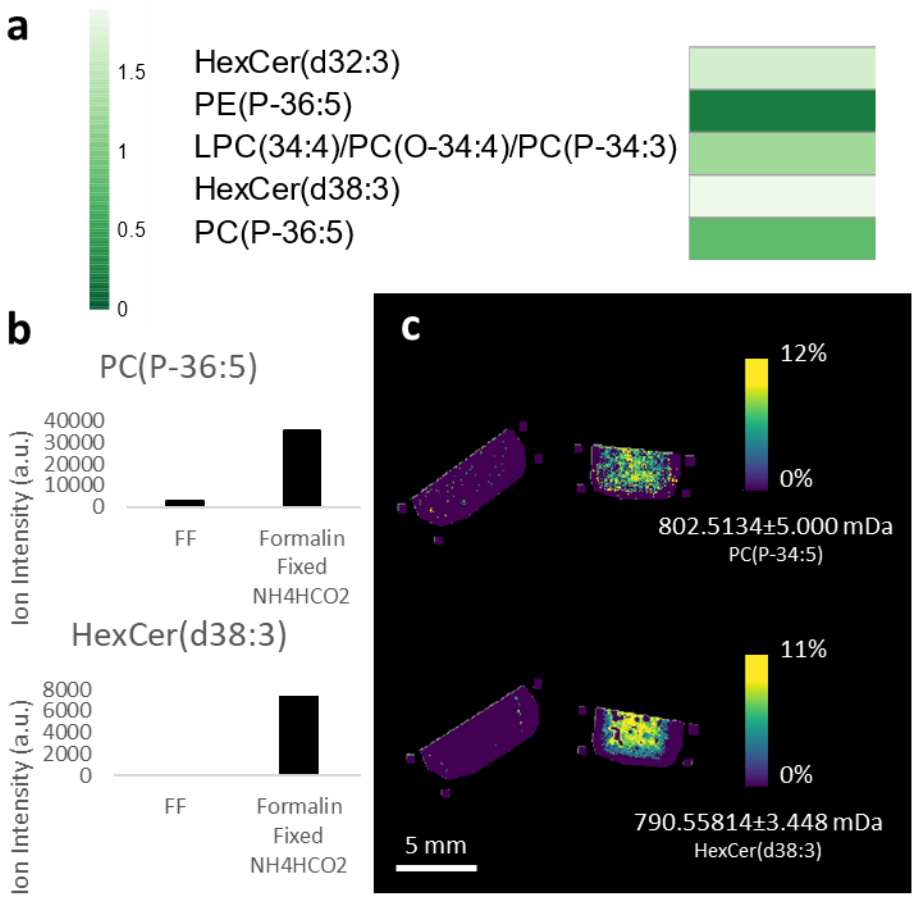

Figure 2.5. FF vs. formalin fixed ammonium formate washed tissues potassiated. *A heatmap depicting the average log2 fold change of $[M+K]^+$ ions with decreased intensity in fresh frozen (FF) samples compared to formalin fixed fresh frozen ammonium formate washed (formalin fixed NH_4HCO_2) samples. (ROC values >0.4 and <0.6) b) A bar graph c) and ion images showing the representative ion intensity and spatial distribution of HexCer(d38:3) (p=0.03) as identified by accurate mass with FF on left and formalin fixed NH_4HCO_2 on right.*

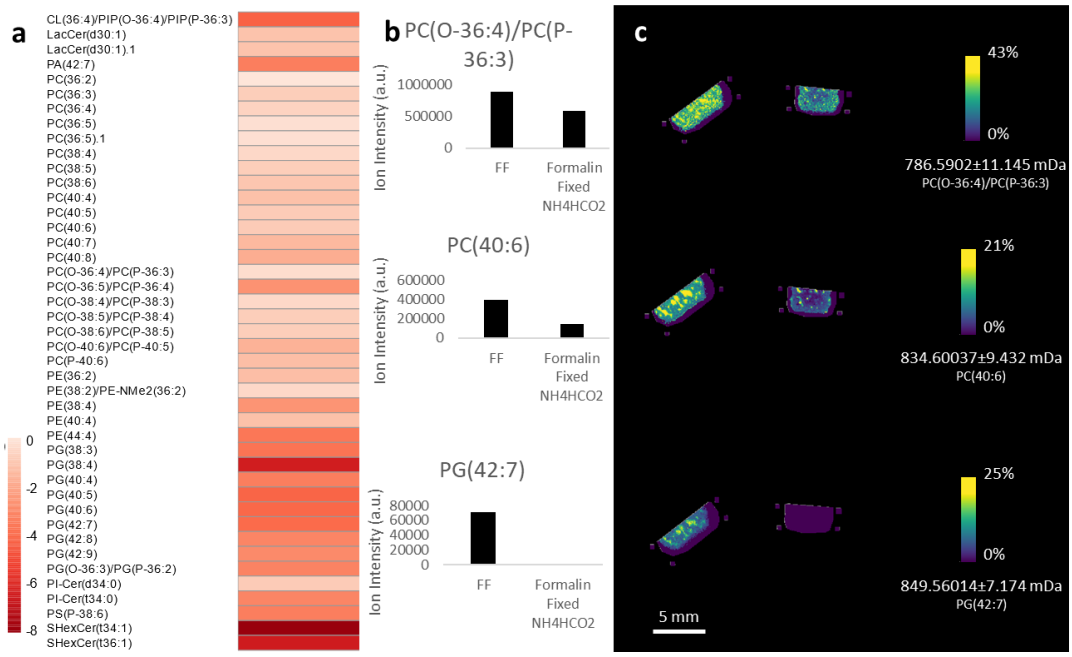

Figure 2.6. FF vs. formalin fixed ammonium formate washed tissues protonated. *a) A heatmap depicting the average log2 fold change of $[M+H]^+$ ions with increased intensity in fresh frozen (FF) samples compared to formalin fixed fresh frozen ammonium formate washed (formalin fixed NH_4HCO_2) samples. (ROC values >0.4 and <0.6) b) A bar graph c) and ion images showing the representative ion intensity and spatial distribution of PC(O-36:4)/PC(P-36:3) (p=0.02), PC(40:6) (p=0.09), and PG(42:7) (p=0.07) as identified by accurate mass with FF on left and formalin fixed NH_4HCO_2 on right.*

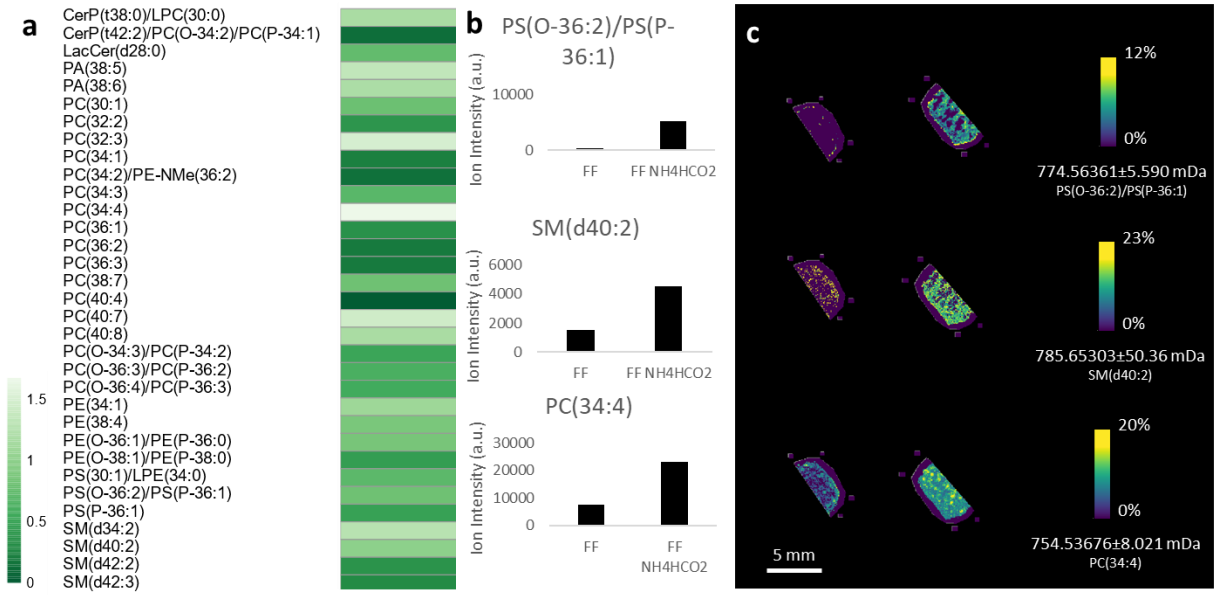

Figure 2.7. FF vs. FF ammonium formate washed tissues protonated*. a) A heatmap depicting the average log2 fold change of* $[M+H]^+$ *ions with decreased intensity in fresh frozen (FF) samples compared to fresh frozen ammonium formate washed (FF* NH_4HCO_2*) samples. (ROC values >0.4 and <0.6) b) A bar graph c) and ion images showing the representative ion intensity and spatial distribution of PS(O-36:2)/PS(P-36:1) (p=0.02), SM(d40:2) (p=0.01), and PC(34:4) (p=0.02) as identified by accurate mass with FF on left and FF ammonium formate washed on right.*

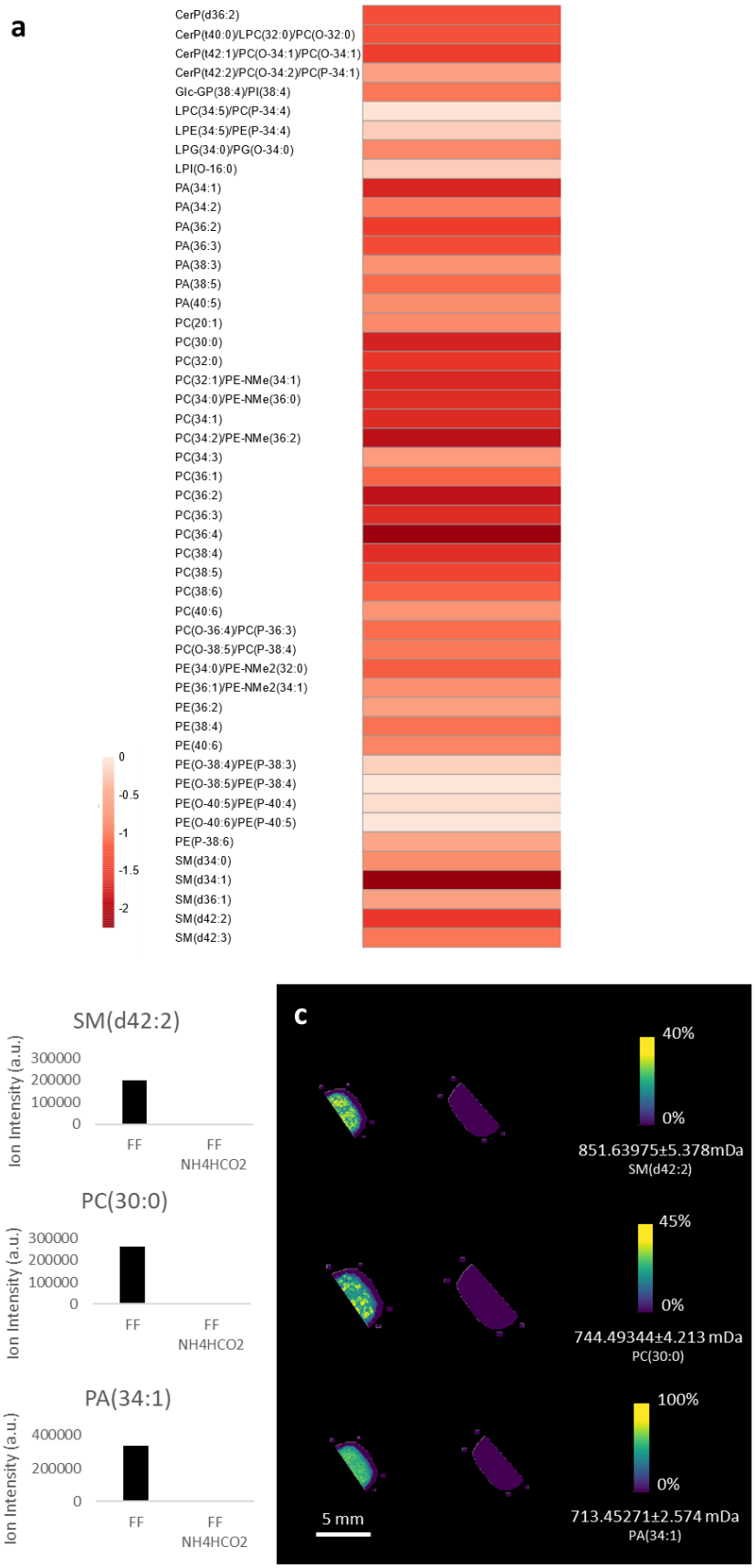
a
CerP(d36:2)
CerP(t40:0)/LPC(32:0)/PC(O-32:0)
CerP(t42:1)/PC(O-34:1)/PC(O-34:1)
CerP(t42:2)/PC(O-34:2)/PC(P-34:1)
Glc-GP(38:4)/PI(38:4)
LPC(34:5)/PC(P-34:4)
LPE(34:5)/PE(P-34:4)
LPG(34:0)/PG(O-34:0)
LPI(O-16:0)
PA(34:1)
PA(34:2)
PA(36:2)
PA(36:3)
PA(38:3)
PA(38:5)
PA(40:5)
PC(20:1)
PC(30:0)
PC(32:0)
PC(32:1)/PE-NMe(34:1)
PC(34:0)/PE-NMe(36:0)
PC(34:1)
PC(34:2)/PE-NMe(36:2)
PC(34:3)
PC(36:1)
PC(36:2)
PC(36:3)
PC(36:4)
PC(38:4)
PC(38:5)
PC(38:6)
PC(40:6)
PC(O-36:4)/PC(P-36:3)
PC(O-38:5)/PC(P-38:4)
PE(34:0)/PE-NMe2(32:0)
PE(36:1)/PE-NMe2(34:1)
PE(36:2)
PE(38:4)
PE(40:6)
PE(O-38:4)/PE(P-38:3)
PE(O-38:5)/PE(P-38:4)
PE(O-40:5)/PE(P-40:4)
PE(O-40:6)/PE(P-40:5)
PE(P-38:6)
SM(d34:0)
SM(d34:1)
SM(d36:1)
SM(d42:2)
SM(d42:3)
0
-0.5
-1
-1.5
-2
SM(d42:2)
Ion Intensity (a.u.)
300000
200000
100000
0
FF
FF NH4HCO2
PC(30:0)
Ion Intensity (a.u.)
300000
200000
100000
0
FF
FF NH4HCO2
PA(34:1)
Ion Intensity (a.u.)
400000
200000
0
FF
FF NH4HCO2
c
40%
0%
851.63975±5.378mDa
SM(d42:2)
45%
0%
744.49344±4.213 mDa
PC(30:0)
100%
0%
713.45271±2.574 mDa
PA(34:1)
5 mm

Figure 2.8. FF vs. FF ammonium formate washed potassiated. *a) A heatmap depicting the average log2 fold change of $[M+K]^+$ ions with increased intensity in fresh frozen (FF) samples compared to fresh frozen ammonium formate washed (FF NH_4HCO_2) samples. (ROC values >0.4 and <0.6) b) A bar graph c) and ion images showing the representative ion intensity and spatial distribution of SM(d42:2) (p-0.04), PC(30:0) (p=0.01), and PA(34:1) (p=0.04) as identified by accurate mass with FF on left and FF NH_4HCO_2 on right.*

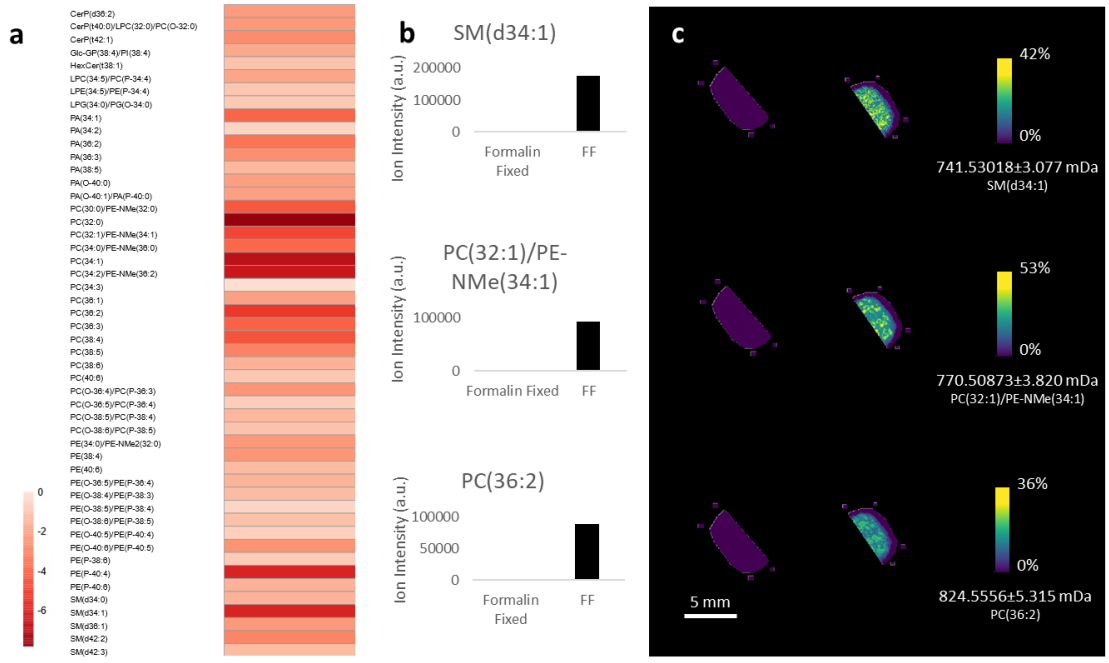

Figure 2.9. Formalin fixed vs. FF potassiated. *a) A heatmap depicting the average log2 fold change of $[M+K]^+$ ions with decreased intensity in formalin fixed fresh frozen (formalin fixed) samples compared to fresh frozen (FF) samples. (ROC values >0.4 and <0.6) b) A bar graph c) and ion images showing the representative ion intensity and spatial distribution of SM(d34:1) (p=0.04), PC(32:1)/PE-NMe(34:1) (p=0.02), and PC(36:2) (p=0.03) as identified by accurate mass with formalin fixed on left and FF on right.*

We find a variety of trends in lipid classes affected by each tissue preparation. Largely, ammonium formate washing and fixation are more detrimental to the detection of many lipids in negative ion mode. Formalin fixation removed 68 PE lipids and only improved detection of two lipids compared to other procedures (Appendix A Table 13). For example, many PE and PE ether lipids were easier to detect in FF tissues, such as PE(42:4) and PE(P-38:4)/PE(O-38:5), which showed 4±2-fold changes for both lipids ($p<0.5$, Figure 2.10). However, in formalin fixed tissues, ammonium formate improved the detection of 52 PE lipids (Appendix A Table 14). For example, a 1.2±0.84 fold increase was observed for PE(36:2) (Figure 2.11). The combination of formalin fixation and ammonium formate washing washed away 38 PE lipids, but improved the detection of 2 PE lipids (Appendix A Table 15). For example, an 330±250 ($p=0.02$) and 270±200 ($p=0.01$) fold decrease was observed after formalin fixation and ammonium formate washing in PE(P-38:6) and PE(O-36:5)/PE(P-36:4) (Figure 2.12). However, in FF tissues results were more varied in that 22 PE and PE ether lipids (e.g., PE(40:8) and PE(38:1)) showed improved detection after ammonium formate washing, but 23 PE and PE ether lipids showed hindered detection in FF tissues (Figure 2.13-2.16, Appendix A Table 2.16). These changes are not simply a result of solubility as PE lipids are enhanced by ammonium formate washing. Although the recommendation changes for specific lipids, overall FF ammonium formate washed samples provide the broadest coverage and greatest increase in detection for PE and PE ether lipids, but specific lipids may have reduced detection.

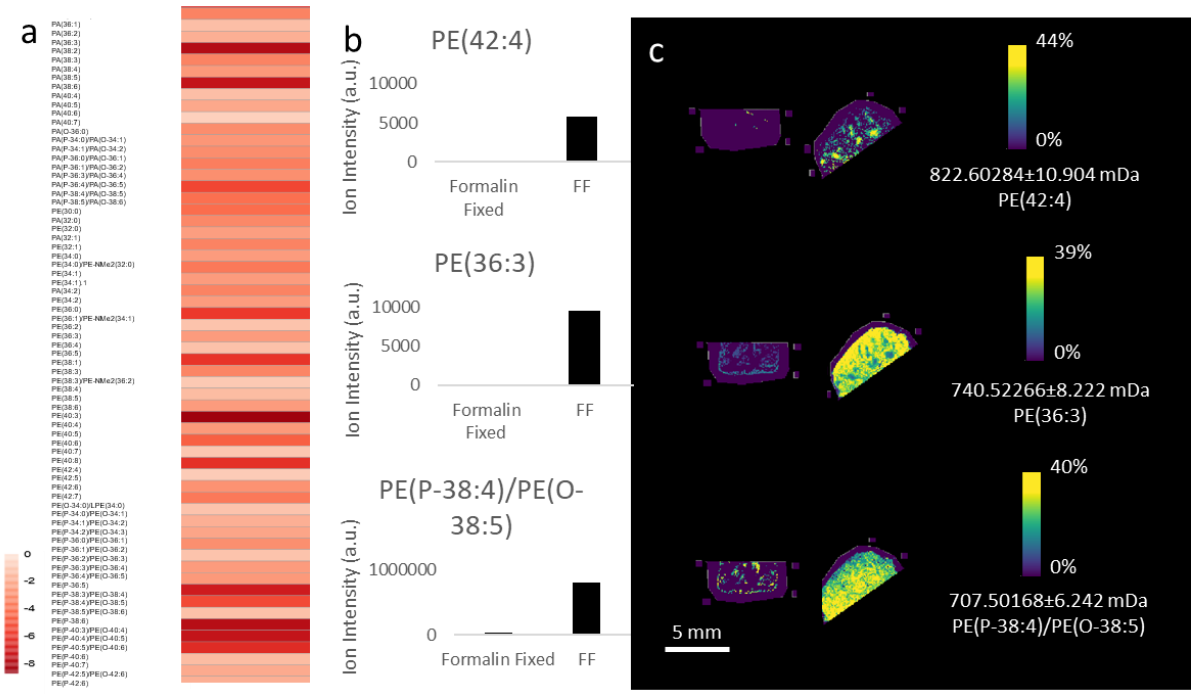

Figure 2.10. Formalin fixed vs. FF deprotonated. *a) A heatmap depicting the average log2 fold change of [M-H]- ions with increased intensity in formalin fixed fresh frozen samples compared to fresh frozen (FF) samples. (ROC values >0.4 and <0.6) b) A bar graph c) and ion images showing the representative ion intensity and spatial distribution PE(42:4) (p=0.2), PE(36:3) (p=0.004), and PE(P-38:4)/PE(O-38:5) (p=0.01) as identified by accurate mass with formalin fixed on left and FF on right.*


Cer(d34:1)
Cer(d42:1)
Cer(d42:2)
CerP(d34:0)
CerP(d34:1)
CerP(d36:1)
CerP(d36:2)
CerP(d38:1)
CerP(d40:1)
CerP(d42:1)
CerP(d42:2)
CerP(d44:3)
HexCer(d34:1)
HexCer(d40:1)
HexCer(d42:1)
HexCer(d42:2)
HexCer(t30:0)
LBPA(34:1)
LBPA(36:2)
LPA(18:0)
LPA(18:1)
LPA(20:1)
LPA(20:4)
LPA(22:4)
LPA(22:6)
LPA(32:0)
LPC(14:1)
LPC(16:0)
LPC(16:1)
LPC(18:4)
LPC(20:5)
LPC(30:6)
LPE(16:0)
LPE(18:0)
LPE(18:1)
LPE(20:0)
LPE(20:1)
LPE(20:2)
LPE(20:4)
LPE(22:4)
LPE(22:5)
LPE(22:6)
LPE(34:0)
LPG(18:1)
LPG(18:2)
LPG(20:4)
LPG(22:6)
LPI(16:0)
LPI(18:0)
LPI(18:1)
LPI(20:4)
LPI(32:0)/PI(O-32:0)
LPS(18:0)
LPS(P-16:0)
LPS(P-18:0)
PA(26:1)
PA(30:0)
PA(32:0)
PA(32:2)
PA(34:0)
PA(34:1)
PA(34:2)
PA(34:3)
PA(36:1)
PA(36:2)
PA(36:3)
PA(36:4)
PA(38:2)
PA(38:3)
PA(38:4)
PA(38:5)
PA(38:6)
PA(40:4)
PA(40:5)
PA(40:6)
PA(40:7)
4
3
2
1
0
PA(40:5)
PA(40:6)
PA(40:7)
PA(O-32:1)/LPA(32:1)/PA(P-32:0)
PA(O-34:2)/PA(P-34:2)
PA(O-36:0)
PA(P-34:0)/PA(O-34:1)
PA(P-36:1)/PA(O-36:2)
PA(P-36:3)/PA(O-36:4)
PA(P-38:3)/PA(O-38:4)
PA(P-38:4)/PA(O-38:5)
PE(32:0)
PE(32:1)
PE(34:0)
PE(34:1)
PE(34:2)
PE(36:0)
PE(36:1)
PE(36:2)
PE(36:3)
PE(36:4)
PE(38:1)
PE(38:2)
PE(38:3)
PE(38:4(OH))
PE(38:4)
PE(38:5)
PE(38:6)
PE(40:3)
PE(40:4)
PE(40:5)
PE(40:6)
PE(40:7)
PE(42:6)
PE(O-18:0)/LPE(O-18:0)
PE(P-20:0)/LPE(P-20:0)
PE(P-34:0)/PE(O-34:1)
PE(P-36:0)/PE(O-36:1)
PE(P-36:1)/PE(O-36:2)
PE(P-38:3)/PE(O-38:4)
PE(P-38:5)/PE(O-38:6)
PE(P-40:3)/PE(O-40:4)
PE(P-40:4)/PE(O-40:5)
PE(P-40:6)
PE-Cer(d36:1)
PE-Cer(d42:1)
PE-Cer(t32:1)
PE-Cer(t36:3)
PE-NMe(28:0)
PE-NMe(32:0)
PE-NMe(34:1)
PE-NMe(36:2)
PG(32:0)
PG(36:3)
PI(32:0)
PI(32:1)
PI(34:0)
PI(34:1)
PI(34:2)
PI(36:1)
PI(36:2)
PI(36:3)
PI(36:4)
PI(38:2)
PI(38:4)
PI(38:5)
PI(38:6)
PI(40:5)
PI(40:6)
PI(P-38:3)/PI(O-38:4)
PI(P-38:4)/PI(O-38:5)
PI-Cer(d38:2)
PS(24:0)
PS(32:0)
PS(34:0)
PS(34:1)
PS(34:2)
PS(36:1)
PS(36:2)
PS(36:4)
PS(38:3)
PS(38:4)
PS(38:5)
PS(38:6)
PS(40:4)
PS(40:5)
PS(40:6)
PS(42:5)
PS(42:7)
PS(P-38:4)/PS(O-38:5)

Figure 2.11. Formalin fixed vs. formalin fixed ammonium formate washed deprotonated. *A heatmap depicting the average log2 fold change of [M-H]- ions with decreased intensity in formalin fixed fresh frozen samples compared to formalin fixed fresh frozen ammonium formate washed (NH_4HCO_2) samples. (ROC values >0.4 and <0.6).*

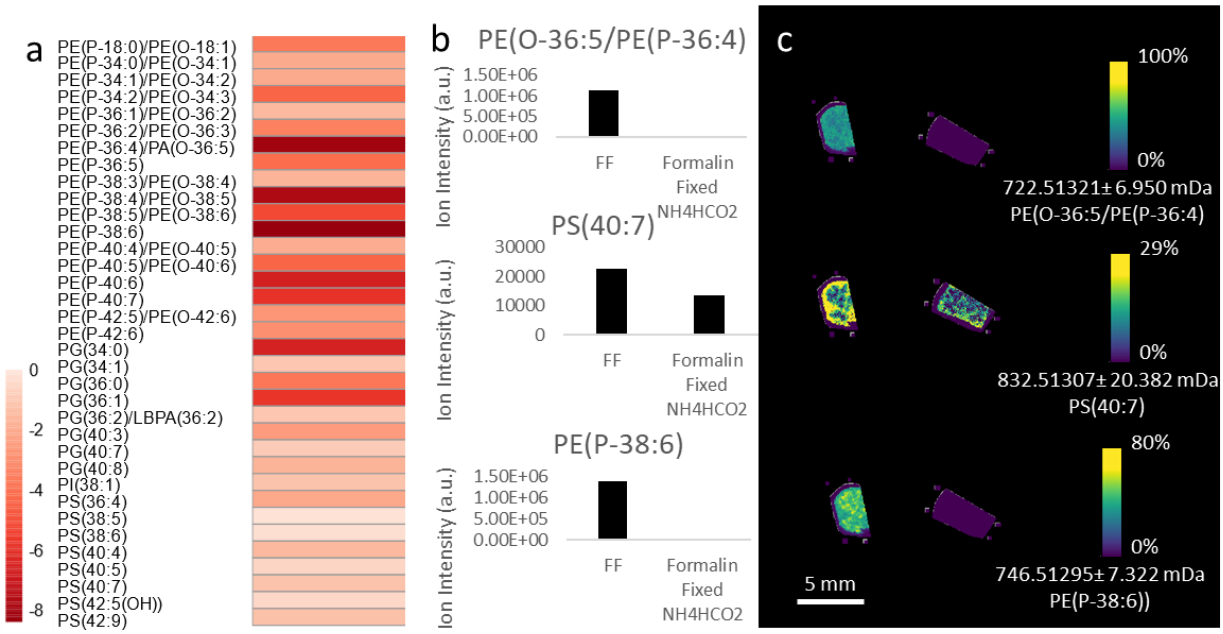

Figure 2.12. FF vs. formalin fixed ammonium formate washed deprotonated*. a) A heatmap depicting the average log2 fold change of [M-H]$^-$ ions with increased intensity in fresh frozen (FF) samples compared to formalin fixed fresh frozen ammonium formate washed (formalin fixed NH_4HCO_2) samples. (ROC values >0.4 and <0.6) b) A bar graph c) and ion images showing the representative ion intensity and spatial distribution PE(P-36:5)/PE(O-36:4) (p=0.04), PS(40:7) (p=0.04), and PE(P-38:6) (p=0.02) as identified by accurate mass with FF on left and formalin fixed NH_4HCO_2 on right.*

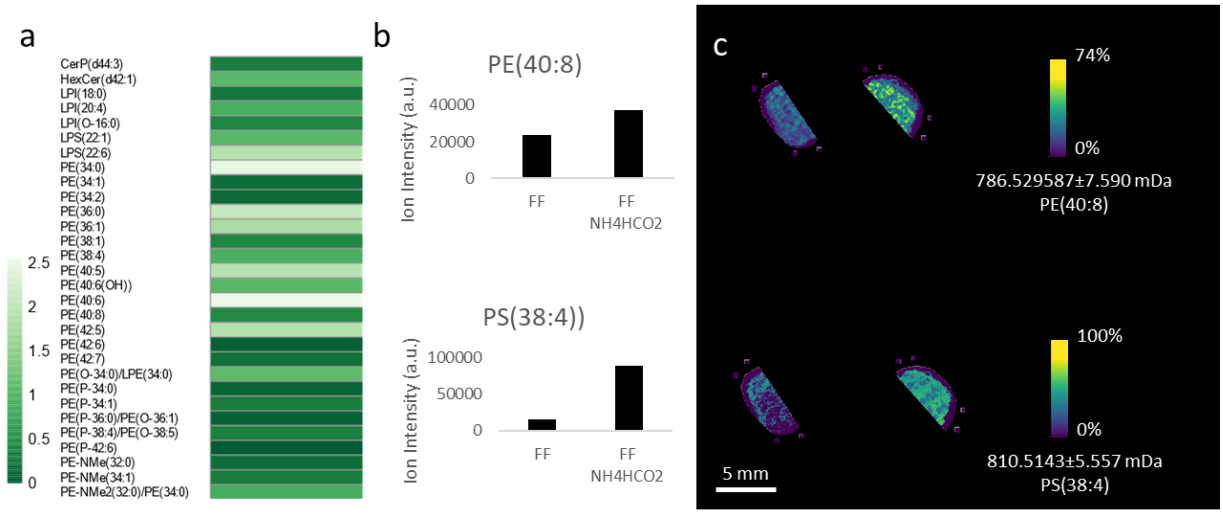

Figure 2.13. FF vs. FF ammonium formate washed deprotonated. *a) A heatmap depicting the average log2 fold change of [M-H]$^-$ ions with decreased intensity in fresh frozen (FF) samples compared to fresh frozen ammonium formate washed (FF NH_4HCO_2) samples. (ROC values >0.4 and <0.6) b) A bar graph c) and ion images showing the representative ion intensity and spatial distribution PE(40:8) (p=0.16) and PS(38:4) (p=0.01) as identified by accurate mass with FF on left and FF ammonium formate washed on right.*

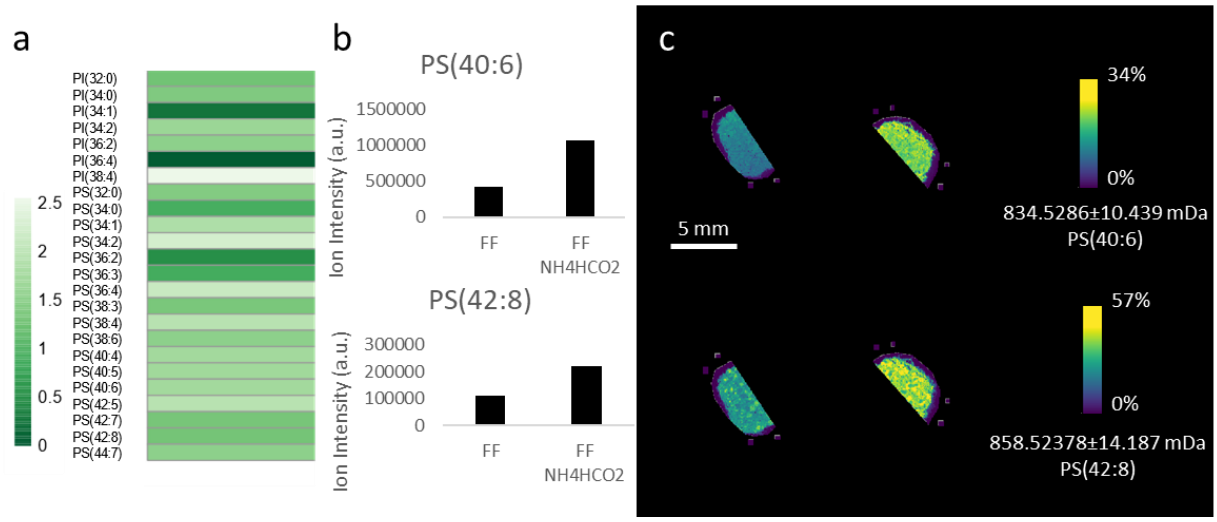

Figure 2.14. FF vs. FF ammonium formate washed deprotonated. *a) A heatmap depicting the average log2 fold change of [M-H]- ions with decreased intensity in fresh frozen (FF) samples compared to fresh frozen ammonium formate washed (FF NH_4HCO_2) samples. (ROC values >0.4 and <0.6) b) A bar graph c) and ion images showing the representative ion intensity and spatial distribution of PS(40:6) (p=0.004) and PS(42:8) (p=0.01) as identified by accurate mass with FF on left and FF NH_4HCO_2 on right.*

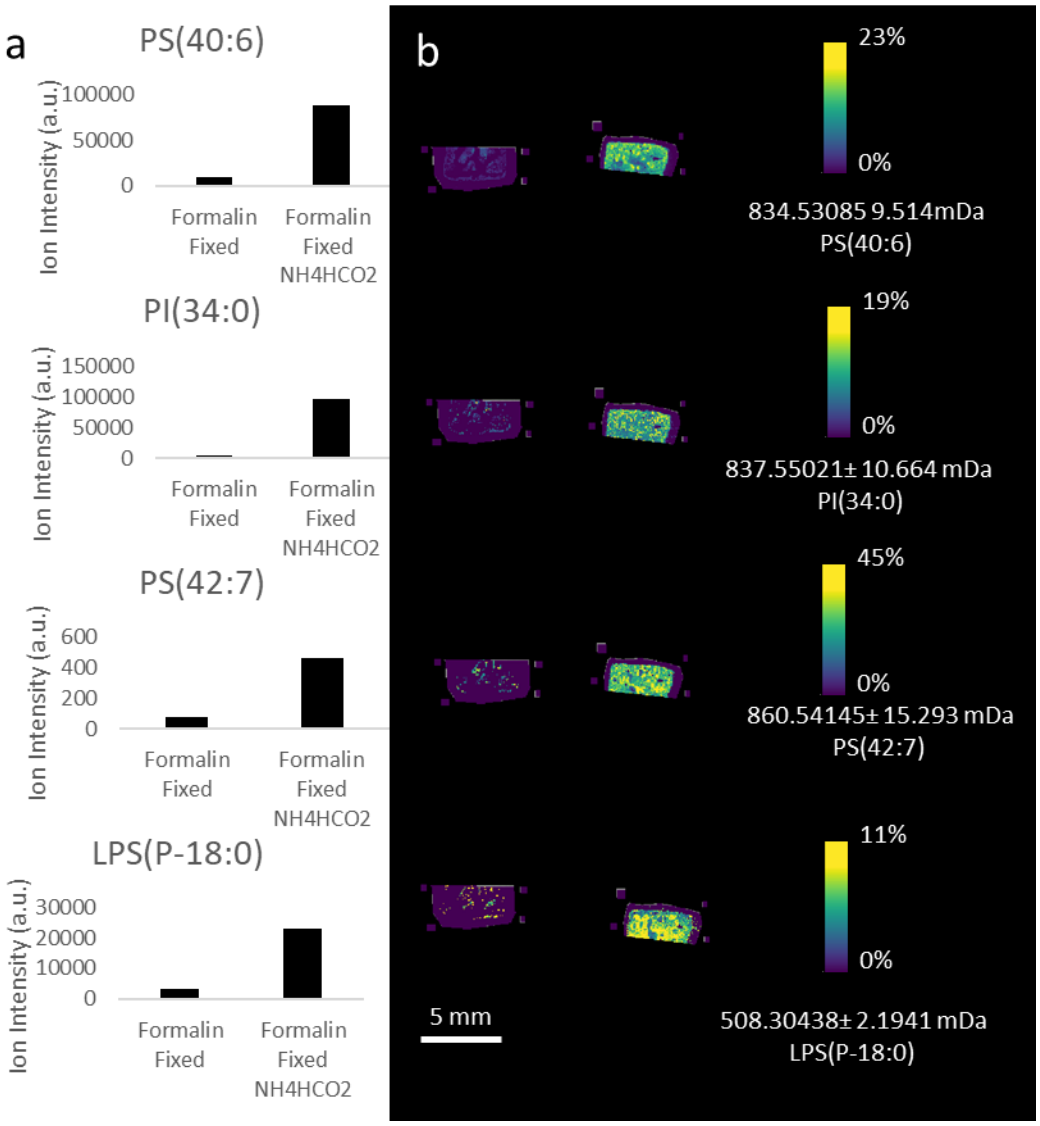

Figure 2.15. Formalin fixed vs. formalin fixed ammonium formate washed deprotonated. *a) A bar graph of select [M-H]$^-$ ions with decreased intensity in formalin fixed fresh frozen samples compared to formalin fixed fresh frozen ammonium formate washed samples. (ROC values >0.4 and <0.6) b) and ion images showing the representative ion intensity and spatial distribution PS(40:6) (p=0.03), PI(34:0) (p=0.04) PS(42:7) (p=0.04), and LPS(P-18:0) (p=0.01) as identified by accurate mass with formalin fixed on left and formalin fixed fresh frozen ammonium formate washed samples on right.*

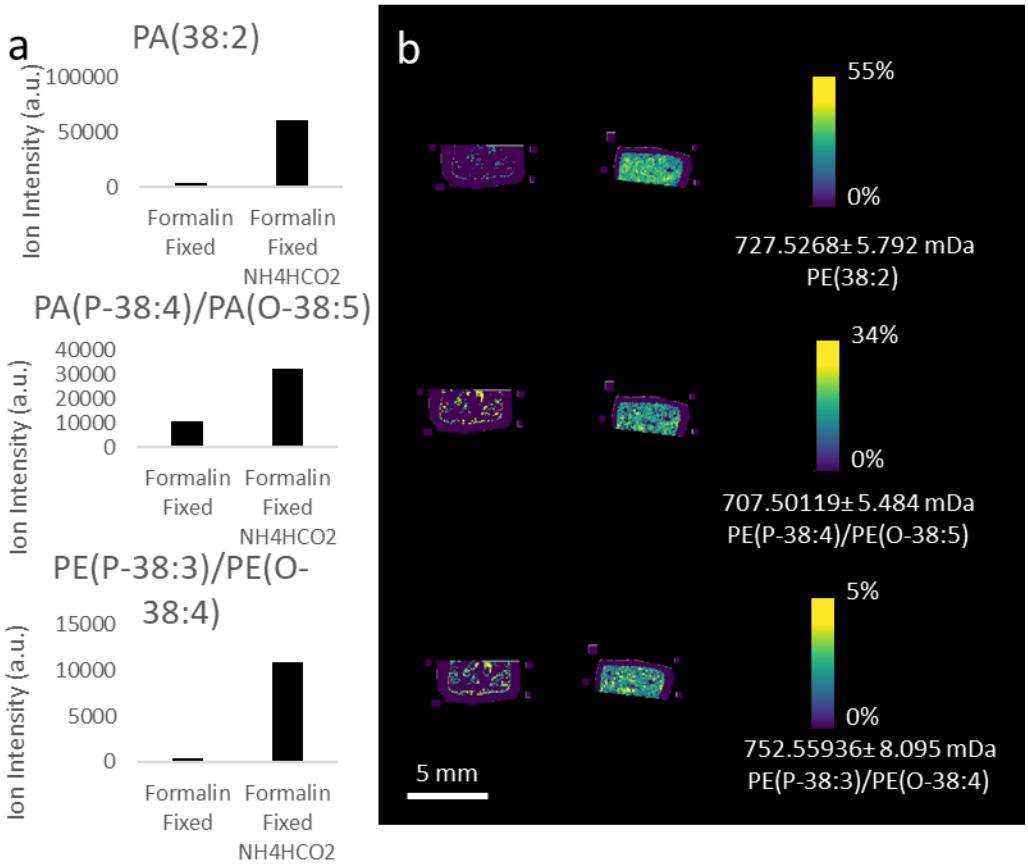

Figure 2.16. Formalin fixed vs. formalin fixed ammonium formate washed deprotonated. *a) A bar graph of select [M-H]$^-$ ions with decreased intensity in formalin fixed fresh frozen samples compared to formalin fixed fresh frozen ammonium formate washed samples. (ROC values >0.4 and <0.6) c) and ion images showing the representative ion intensity and spatial distribution PA(38:2) (p=0.05), PA(P-38:4)/PA(O-38:5) (p=0.01), and PE(P-38:3)/PE(O-38:4) (p=0.02) as identified by accurate mass with formalin fixed on left and formalin fixed ammonium formate washed samples on right.*

Contrarily, ceramides (Cer) are clearly washed away during fixation, but trends are less clear in FF tissues with ammonium formate washing. Formalin fixation decreased the detection of 12 ceramides. A 3±2-fold ($p=0.0001$) decrease in ion intensity was detected for HexCer(d42:1) after fixation (Figure 2.17). However, three ceramide lipids were increased in formalin fixed tissues. For example, a 2.8±0.58 and a 3±2-fold increase ($p=0.009$, $p=0.008$) was observed for CerP(d36:2) and PE-Cer(d42:1) respectively (Figure 2.18, Appendix A Table 2.17). Washing fixed tissue with ammonium formate enhanced the detection of 21 ceramides. For example, a 9±3-fold increase was observed for Cer(d34:1) after ammonium formate washing in formalin fixed tissues (Figure 2.3). When combining formalin fixation and ammonium formate washing four lipids show increased ion intensity(Figure 2.18). In FF tissues, seven ceramide lipids are washed away by ammonium formate washing and only two ceramide lipids (e.g., CerP(d44:3) and HexCer(d42:1)) are enhanced by ammonium formate washing (Figure 2.18, Appendix A Table 2.18). Further, formalin fixation without washing resulted in poor detection of 13 ceramides (Appendix A Table 2.17). On the other hand, ammonium formate washing of formalin fixed tissues resulted in no hindered detection of ceramides and much improvement in the detection of ceramides, possibly due to the improved tissue structure in formalin fixed ammonium formate washed tissues (Appendix A Table 2.19-20). In FF tissues, ceramides are most readily detected in unwashed tissues, due to the negative effects of ammonium formate washing and formalin fixation on ceramide lipid detection and should be the standard if interested in ceramide detection. If formalin fixed tissues must be used, we recommend ammonium formate washing for improved detection and tissue structure (Figure 2.19).

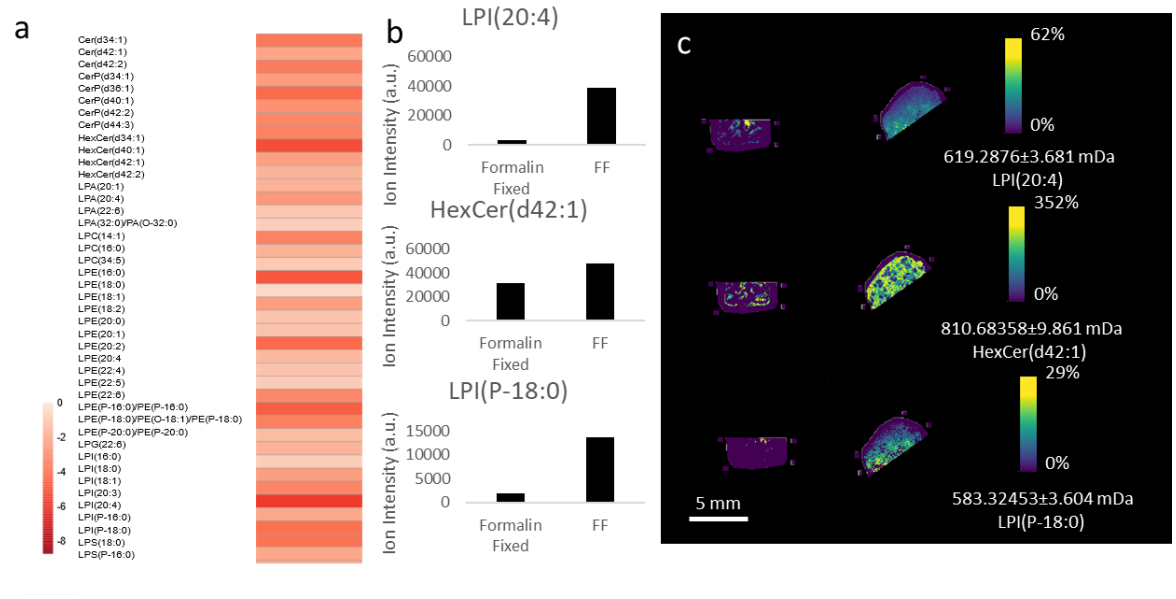

Figure 2.17. Formalin fixed vs. FF deprotonated. *a) A heatmap depicting the average log2 fold change of [M-H]$^-$ ions with increased intensity in formalin fixed fresh frozen samples compared to fresh frozen (FF) samples. (ROC values >0.4 and <0.6) b) A bar graph c) and ion images showing the representative ion intensity and spatial distribution LPI(P-16:0) (p=0.1), HexCer(d42:1) (p=0.06), and LPI(P-18:0) (p=0.001) as identified by accurate mass with formalin fixed samples on left and FF on right.*

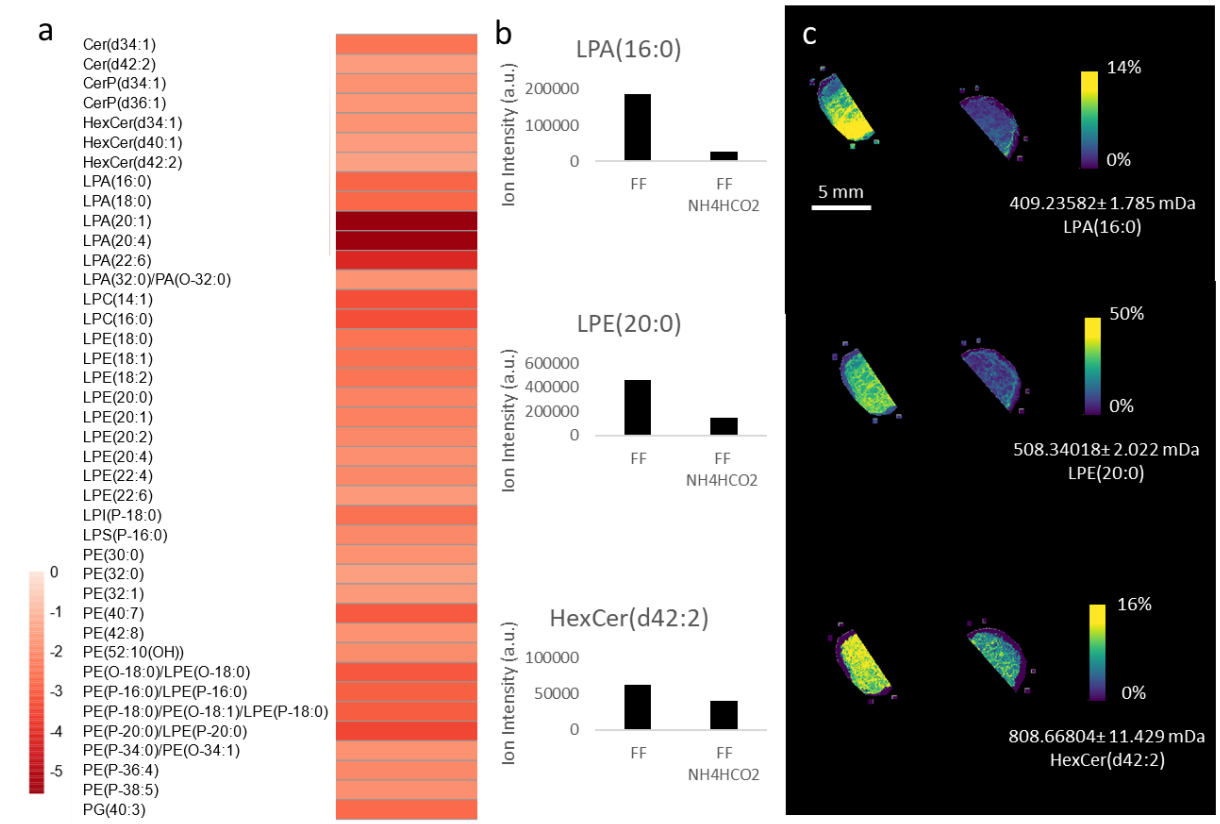

Figure 2.18. FF vs. FF ammonium formate washed deprotonated. *a) A heatmap depicting the average log2 fold change of [M-H]- ions with increased intensity in fresh frozen (FF) samples compared to fresh frozen ammonium formate washed (FF NH_4HCO_2) samples. (ROC values >0.4 and <0.6) b) A bar graph c) and ion images showing the representative ion intensity and spatial distribution LPA(16:0), LPE(20:0), HexCer(d42:2) as identified by accurate mass with FF on left and FF NH_4HCO_2 on right.*

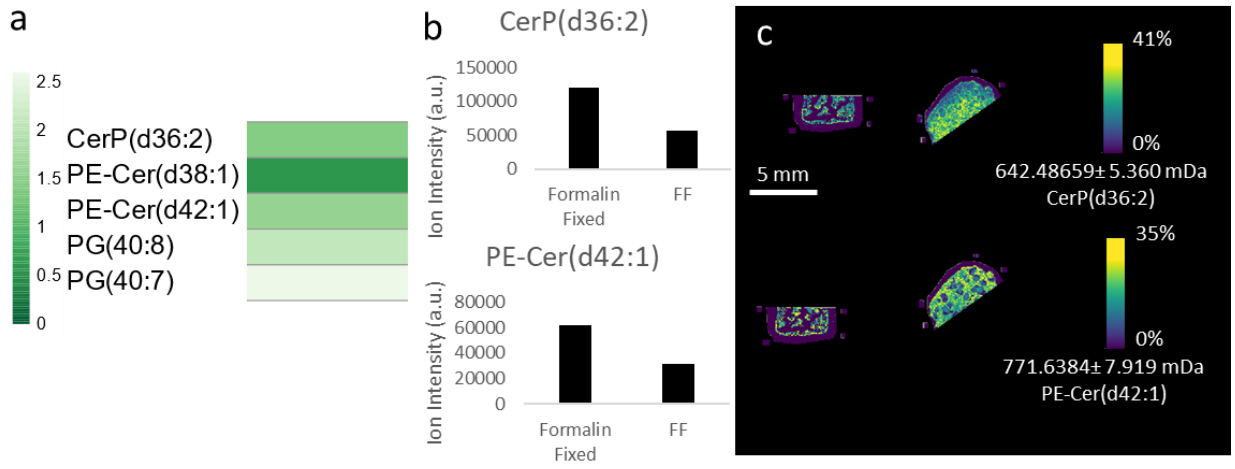

Figure 2.19. Formalin fixed vs. FF deprotonated. *a) A heatmap depicting the average log2 fold change of [M-H]$^-$ ions with increased intensity in formalin fixed fresh frozen samples compared to fresh frozen (FF) samples. (ROC values >0.4 and <0.6) b) A bar graph c) and ion images showing the representative ion intensity and spatial distribution CerP(d36:2)(p=0.009) and PE-Cer(d42:1) (p=0.008) as identified by accurate mass with formalin fixed samples on left and FF on right.*

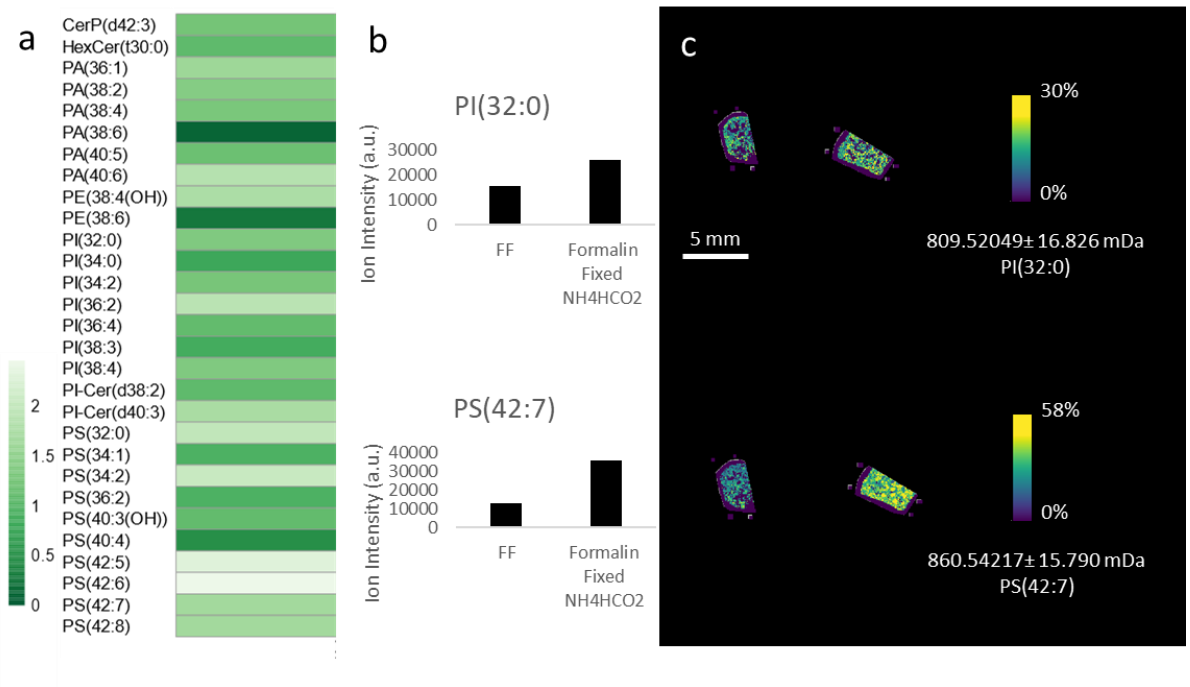

Figure 2.20. FF vs. Formalin fixed ammonium formate washed deprotonated. *a) A heatmap depicting the average log2 fold change of [M-H]- ions with decreased intensity in fresh frozen (FF) samples compared to formalin fixed fresh frozen ammonium formate washed (formalin fixed NH_4HCO_2) samples. (ROC values >0.4 and <0.6) b) A bar graph c) and ion images showing the representative ion intensity and spatial distribution PI(32:0) (p=0.1) and PS(42:7) (p=0.05) as identified by accurate mass with FF on left and formalin fixed ammonium formate washed on right.*

Overall, FF ammonium formate washed tissues are recommended for the study of PI lipids. If formalin fixed tissues must be used, ammonium formate washing increases the depth of coverage while hindering few PI lipids. Contrary to ceramides, the detrimental effects of formalin fixation can be outweighed, in many cases, by the improvements in ion intensity after ammonium formate washing (Appendix A Table 2.21-24). PI lipids were more easily detected in FF tissues than in formalin fixed tissues, such as LPI(P-18:0) (4.8±0.20-fold increase, p=0.001, Figure 2.17). However, after ammonium formate washing of formalin fixed tissues, 23 PI lipids exhibited higher ion intensity than formalin fixation alone. (*e.g.*, PI (34:0), Figure 2.3, Figure 2.11). However, LPI(20:3) was detected in higher ion intensity without ammonium formate washing by 10±9-fold (p=0.06) in formalin fixed tissues (Figure 2.2a, Figure 2.11). When combining formalin fixation and ammonium formate washing and comparing the levels of detection to FF tissues, 10 PI lipids show improved detection, while three are washed away (Appendix A Table 2.24). For instance, a 3±1 (p=0.1) fold increase was noted for PI(32:0) (Figure 2.20). This trend continues in FF tissues in that 10 PI lipids are enhanced by ammonium formate washing and only one is washed away.

Like ceramides and PI lipids, PS lipids were overall negatively affected by formalin fixation. Eighteen PS lipids were more easily detected in FF tissues than in formalin fixed tissues (e.g., PS(40:4) and PS(40:6), Figure 22, Appendix A Table 2.25). However, if fixation is needed, ammonium formate washing recuperated some of these losses. In formalin fixed tissues, ammonium formate washing improved the detection of 21 PS lipids (Appendix A Table 2.26). For example, a 7±3 and 13±7-fold increase ($p<0.05$) was observed for PS(42:7) and PS(40:6), respectively, after ammonium formate washing (Figure 2.15) compared to unwashed fixed samples. Regardless of fixation, ammonium formate washing enhanced the detection PS lipids. In FF tissues, 24 PS lipids in were detected in higher ion intensities after ammonium formate washing

(*e.g.*, PS(44:7) and PS(42:8), Figure 2.14, Appendix A Table 2.27). When FF tissues were compared to formalin fixed ammonium formate washed samples results were mixed. The detection of 11 PS lipids were improved (Figure 2.3), but 11 PS lipids were also washed away (Figure 2.20). Fixation also resulted in ten PG lipids being removed (Figure 2.21). Overall, PS lipids are most broadly detected in higher ion intensities in FF tissues and often enhanced by ammonium formate washing and PG lipids are more easily detected in unwashed FF tissues.

FF spleen tissue without ammonium formate is recommended for lyso lipid detection due to broad lyso lipid molecular coverage and tissue adhesion. We hypothesize that this trend is primarily due to solubility of lyso lipids. Overall, 20 and 38 lyso lipids are washed away by ammonium formate washing FF and formalin fixed tissues, respectively. Many lyso lipids such as LPA(16:0) and LPE(20:0) are more readily detected in FF tissues without ammonium formate, where LPA(16:0) and LPE(20:0) exhibited a 3.7±2.4 ($p=0.1$) and 2.4±0.80 ($p=0.06$) fold improvement, respectively (Figure 2.18). Moreover, formalin fixation washes away 32 lyso lipids. (Appendix A Table 29-30). For example, LPI(P-18:0) had a 4.8±0.20 ($p=0.001$) fold decrease in fixed tissues compared to FF tissues (Figure 2.17). Formalin fixation combined with ammonium formate washing washes away 11 lyso lipids (Appendix A Table 2.31-32) such as, LPI(20:3) exhibited a 10±9 ($p=0.07$) fold decrease after ammonium formate washing in fixed tissue (Figure 2.3). Overall, very few lyso lipids are enhanced in fixed or washed tissues (Appendix A Table 2.29-32). For example, LPE(18:1) ($p=0.07$) which showed a 5±2-fold increase in formalin fixed tissues after ammonium formate washing (Figure 2.3).

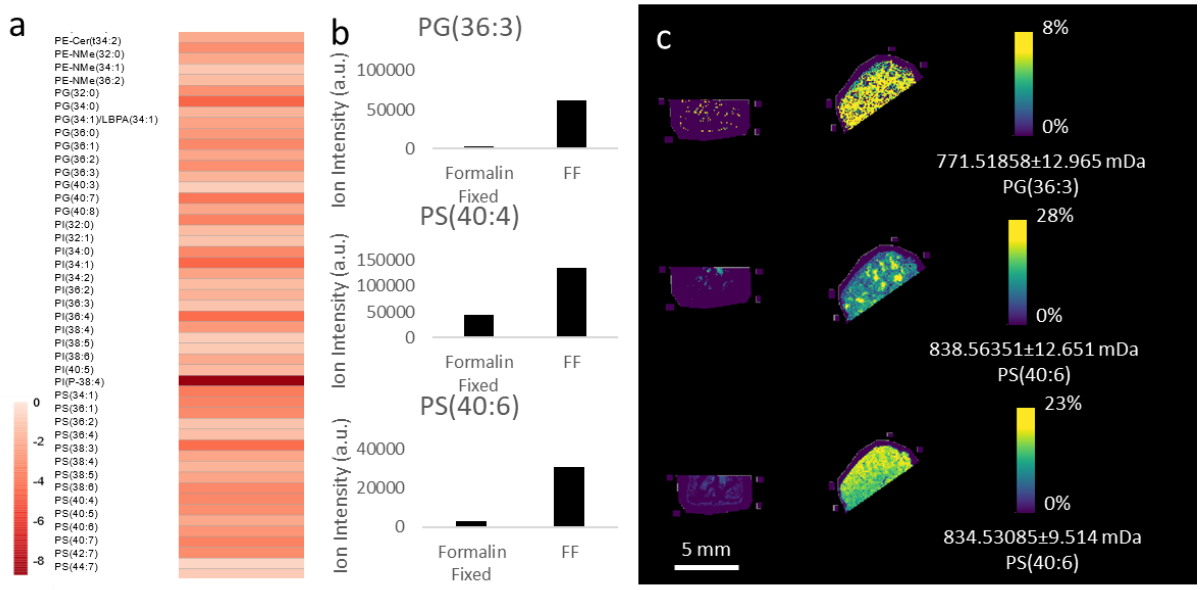

Figure 2.21. Formalin fixed vs. FF deprotonated. *a) A heatmap depicting the average log2 fold change of [M-H]$^-$ ions with increased intensity in formalin fixed fresh frozen samples compared to fresh frozen (FF) samples. (ROC values >0.4 and <0.6) b) A bar graph c) and ion images showing the representative ion intensity and spatial distribution PG(36:3) (p=0.06), PS(40:4) (p=0.02), and PS(40:6) (p=0.03) as identified by accurate mass with formalin fixed samples on left and fresh frozen on right.*

Positive ion Mode

Similarly, to negative ion mode, the number of features is not reliable for investigating the chemical effects of sample preparation methodologies in positive ion mode. After IMS analysis, we found that formalin fixed tissue sections produced the most features (2,684±1028) followed by FF tissues (2,016±848) (Appendix A Table 2.32-34). We saw a significant difference in ammonium formate washed tissues regardless of tissue preparation ($p<0.05$) (Appendix A Table 2.32-34). However, we did not see a significant difference between the number of features detected in FF and formalin fixed tissues ($p=0.09$), FF and formalin fixed ammonium formate washed tissues ($p=0.8$), or among freezing strategies ($p=0.9$) (Appendix A Table 2.32-34). Beyond investigating the number of features, we also investigated the specific ions affected by each sample preparation (Appendix A Table 2.43-84).

In positive ion mode, we find a variety of trends, but recommendations are more complex than in negative ion mode. When looking at PC lipids, trends are adduct-dependent. In FF tissues, ammonium formate washing enhances 17 protonated and 14 sodiated lipids (lower intensity), such as $[PC(34:4)+H]^+$ (Figure 2.7, 2.22) but shows decreased ion intensity in 21 potassiated PC lipids (Appendix A Table 2.60). It was originally thought that ammonium formate washes away all salt adduct lipids thus increasing the ionization efficiency of the protonated lipids. However, we find that not only are protonated lipids enhanced by ammonium formate washing, but so are sodiated lipids (Figure 2.7,2.22). For example, [PC(34:1)+Na]+ shows a 1.0±0.28-fold increase ($1.09x10^6$ to $1.13x10^6$ average ion intensity in a.u.) and [PC(34:1)+H]+ shows a 1.2 ±0.14-fold increase ($1.62x10^6$ to $1.89x10^6$ average ion intensity in a.u.). This trend indicates that ammonium formate washing removes potassium more efficiently than sodium. In addition, formalin fixation worsens the detection of 20 protonated, 12 sodiated, and 19 potassiated PC lipids but can be partially

recovered with ammonium formate washing (Figure 2.23-24, Appendix A Table 2.59-60). For example, 16±5 ($p=0.04$) fold decrease was detected for $[PC(40:6)+H]^+$ (Figure 26). Ammonium formate washing continues to improve the detection of sodiated PC lipids for both FF and formalin fixed tissue (Appendix A Table 2.59-60), but decreases the number of PC lipids detected in the potassiated adduct. Formalin fixation does not enhance the detection of PC lipids, except for one potassiated PC lipid (e.g. $[LPC(34:3)/PC(O-34:4)/PC(P-34:3)+K]^+$, Appendix A Table 2.61, Figure 2.26). However, when combing the two, formalin fixation and ammonium formate washing, it does not enhance the detection of many PC lipids (only five), but rather wash away 56 PC lipids and is therefore not recommended (Appendix A Table 2.61).

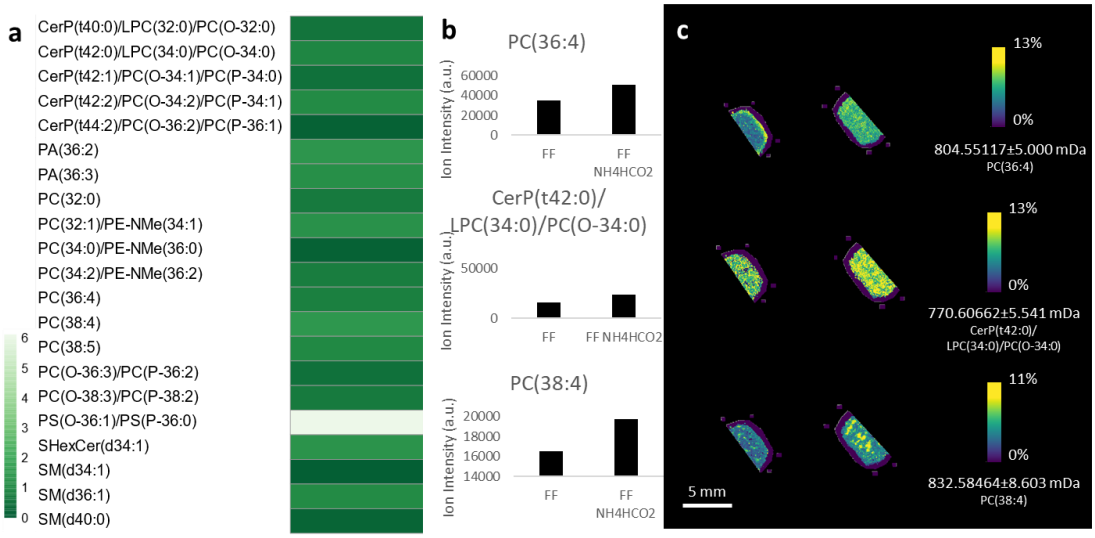

Figure 2.22. FF vs. FF ammonium formate washed sodiated. *a) A heatmap depicting the average log2 fold change of* $[M+Na]^+$ *ions with decreased intensity in fresh frozen (FF) samples compared to fresh frozen ammonium formate washed (FF* NH_4HCO_2*) samples. (ROC values >0.4 and <0.6) b) A bar graph c) and ion images showing the representative ion intensity and spatial distribution of PC(36:4) (p=0.005), CerP(t42:0)/LPC(34:0)/PC(O-34:0) (p=0.01), and PC(38:4) (p=0.01) as identified by accurate mass with FF on left and FFF* NH_4HCO_2 *on right.*

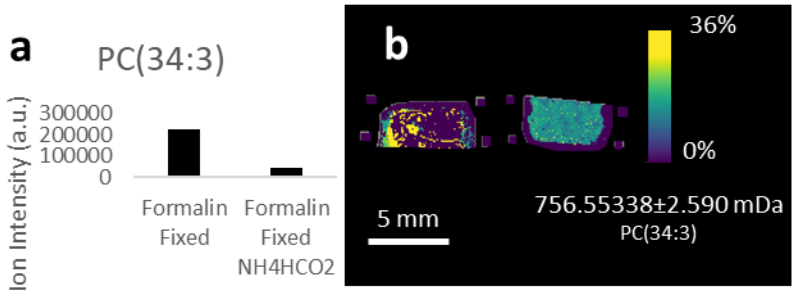

Figure 2.23. Formalin fixed vs. formalin fixed ammonium formate washed protonated. *a) A bar graph depicting the only ion, PC(34:3) to have a log2 fold change of $[M+H]^+$ ions with increased intensity in formalin fixed fresh frozen (formalin fixed) samples compared to formalin fixed fresh frozen ammonium formate washed (formalin fixed NH_4HCO_2) samples. (ROC values >0.4 and <0.6) b) An ion image showing the representative ion intensity and spatial distribution of PC(34:3) (p=0.3) as identified by accurate mass with formalin fixed on left and formalin fixed NH_4HCO_2 on right.*

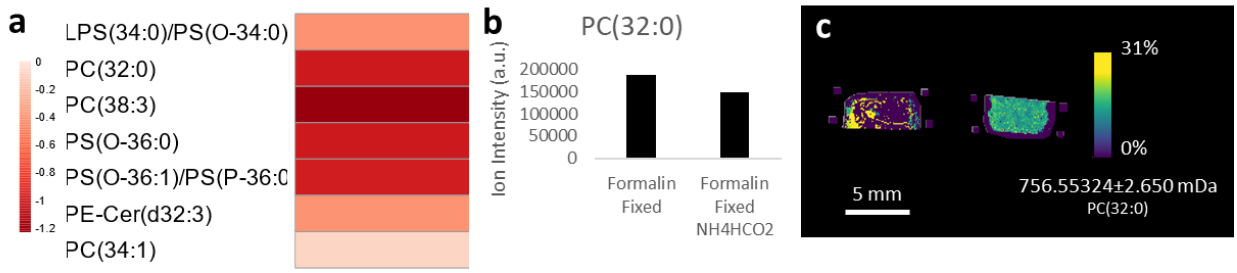

Figure 2.24. Formalin fixed vs. formalin fixed ammonium formate washed sodiated. *a) A heatmap depicting the average log2 fold change of* $[M+Na]^+$ *ions with decreased intensity in formalin fixed sucrose sunk fresh frozen (formalin fixed) samples compared to formalin fixed sucrose sunk fresh frozen ammonium formate washed (formalin fixed* NH_4HCO_2*) samples. (ROC values >0.4 and <0.6) b) A bar graph c) and ion images showing the representative ion intensity and spatial distribution of PC(32:0) (p=0.002) as identified by accurate mass with formalin fixed on left and formalin fixed* NH_4HCO_2 *on right.*

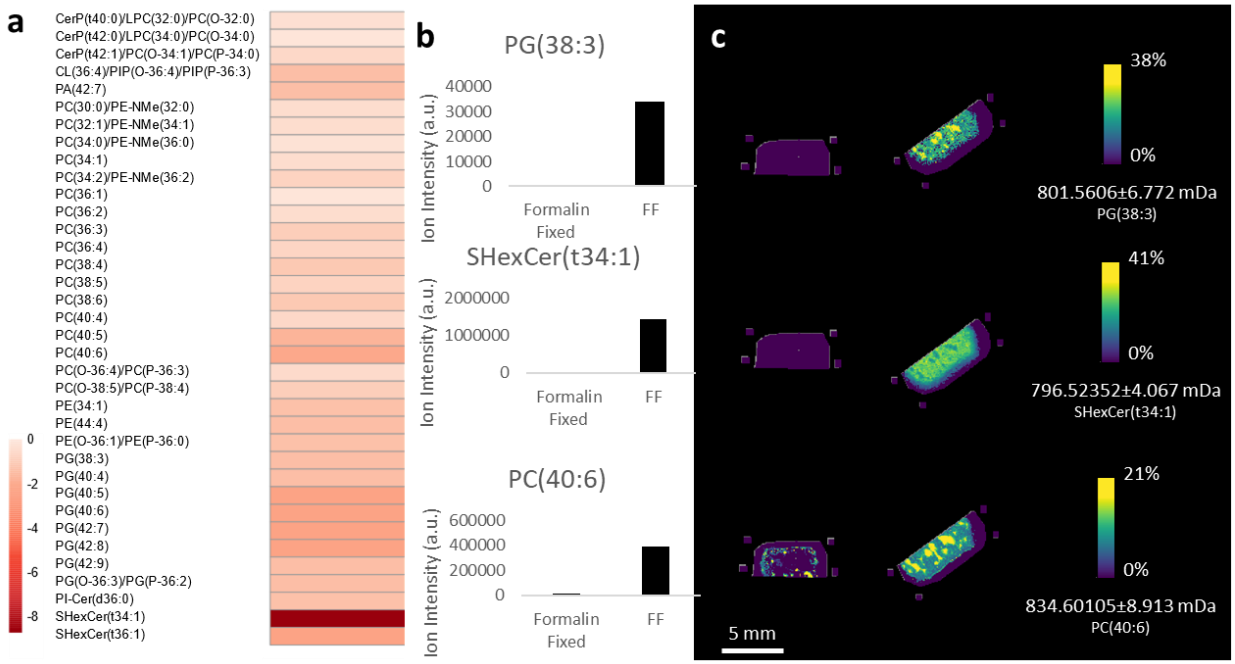

Figure 2.25. Formalin fixed vs. FF protonated. *a) A heatmap depicting the average log2 fold change of $[M+H]^+$ ions with decreased intensity in formalin fixed fresh frozen (formalin fixed) samples compared to fresh frozen (FF) samples. (ROC values >0.4 and <0.6) b) A bar graph c) and ion images showing the representative ion intensity and spatial distribution of PG(38:3) (p=0.07), SHexCer(t34:1) (0.06), and PC(40:6) (p=0.07) as identified by accurate mass with formalin fixed on left and FF on right.*

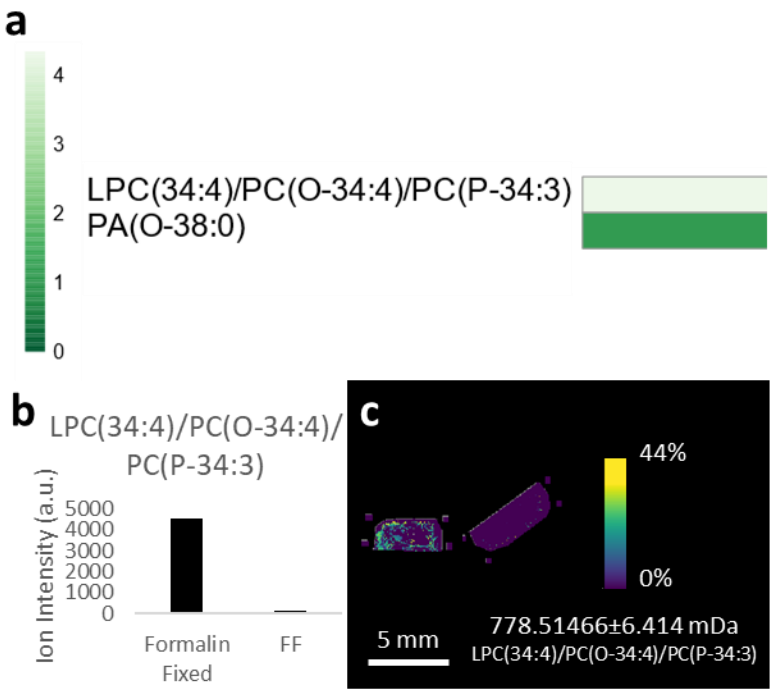

Figure 2.26. Formalin fixed vs. FF potassiated. *a) A heatmap depicting the average log2 fold change of $[M+K]^+$ ions with increased intensity in formalin fixed sucrose sunk fresh frozen (formalin fixed) samples compared to fresh frozen (FF) samples. b) A bar graph c) and ion images showing the representative ion intensity and spatial distribution of LPC(34:4)/PC(O-34:4)/PC(P-34:3) as identified by accurate mass with formalin fixed on left and FF on right. c) A heatmap depicting the average log2 fold change of $[M+K]^+$ ions with increased intensity in formalin fixed fresh frozen (formalin fixed) samples compared to FF samples. (ROC values >0.4 and <0.6)*

Similarly, PE lipids also show adduct-dependent trends. In FF tissues, protonated lipids show more improvement after ammonium formate washing and more sodium and potassium are removed, reducing salt adducted species (Appendix A Table 2.62). For example, a 15±3 (p=0.000002) fold decrease was detected for $[PE(P\text{-}36:5)/PE(O\text{-}36:6)+Na]^+$ after ammonium formate washing (Figure 2.27). However, this trend is reversed in formalin fixed tissues, perhaps due to the increased salt content after fixation (Appendix A Table 2.63, Figure 2.7, 2.22). However, formalin fixation is largely detrimental across all adducts with seven, 11, and 17 PE lipids being detected in lower ion intensities in protonated, sodiated, and potassiated forms (Figure 2.25, 2.9, 2.23, Appendix A Table 2.64). For example, 19±10 (p=0.01) and 4± 2 (p=0.05) fold decreases were observed for $[PE(P\text{-}36:5+Na]^+$ and $[PE(O\text{-}38:5)/PE(P\text{-}38:4)+K]^+$, respectively (Figure 2.25, 2.4, Appendix A Table 2.65). *b) A bar graph c) and ion images showing the representative ion intensity and spatial distribution of PE(P-36:5)(p=0.00002), LBPA(34:1)/PG(34:1) (p=0.008), and PG(36:1) (p=0.002) as identified by accurate mass with FF on left and FF* NH_4HCO_2 *on right.*

This is also similar for ceramides, where salt adduct detection is improved with ammonium formate washing in formalin fixed tissues, but mainly improved in the sodiated form in FF tissues (Appendix A Table 2.66-67). For example, in formalin fixed tissues a 3±2 (p=0.2) fold increase was detected for $[CerP(t42:1)+Na]^+$ after ammonium formate washing (Figure 2.28, Appendix A Table 2.67), while in FF tissues a 2±1 (p=0.01) fold increase was detected for $[CerP(t42:0)+Na]^+$ (Appendix A Table 2.31, 2.44). In addition, formalin fixation washes away many ceramide species across all adducts (e.g. $[SHexCer(t34:1)+H]^+$ and $[SHexCer(t36:1)+Na]^+$, Figure 2.25, Figure 2.4, Appendix A Table 2.69). When combining fixation and ammonium formate washing, six ceramide lipids have improved detection (e.g. $[PE\text{-}Cer(t36:2)+H]^+$ and $[HexCer(d38:3)+K]^+$) (Appendix A Table 2.70, Figure 2.30, 2.5) and 29 Ceramide lipids are washed away (e.g. $[SHexCer(t34:1)+H]^+$

[SHexCer(t36:1)+Na]$^{+}$, and [CerP(t40:0)+K]$^{+}$(Figure 2.24, 2.21, 2.30, 2.3, Appendix A Table 2.70). This indicates that while some ceramides are improved by ammonium formate washing, some are soluble and washed away during fixation and ammonium formate washing. In general, if targeting ceramides, ammonium formate washing is very lipid dependent but fixation is not recommended.

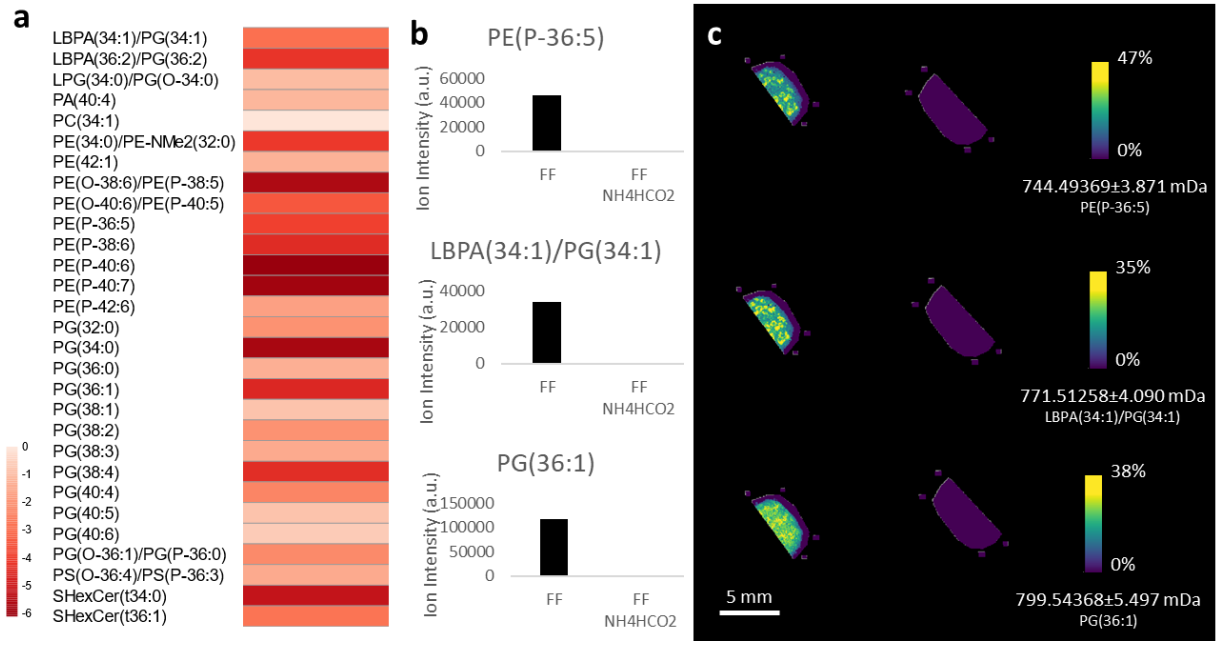

Figure 2.27. FF vs. FF ammonium formate washed sodiated. *a) A heatmap depicting the average log2 fold change of $[M+Na]^+$ ions with increased intensity in fresh frozen (FF) samples compared to fresh frozen ammonium formate washed (FF NH_4HCO_2) samples. (ROC values >0.4 and <0.6)*

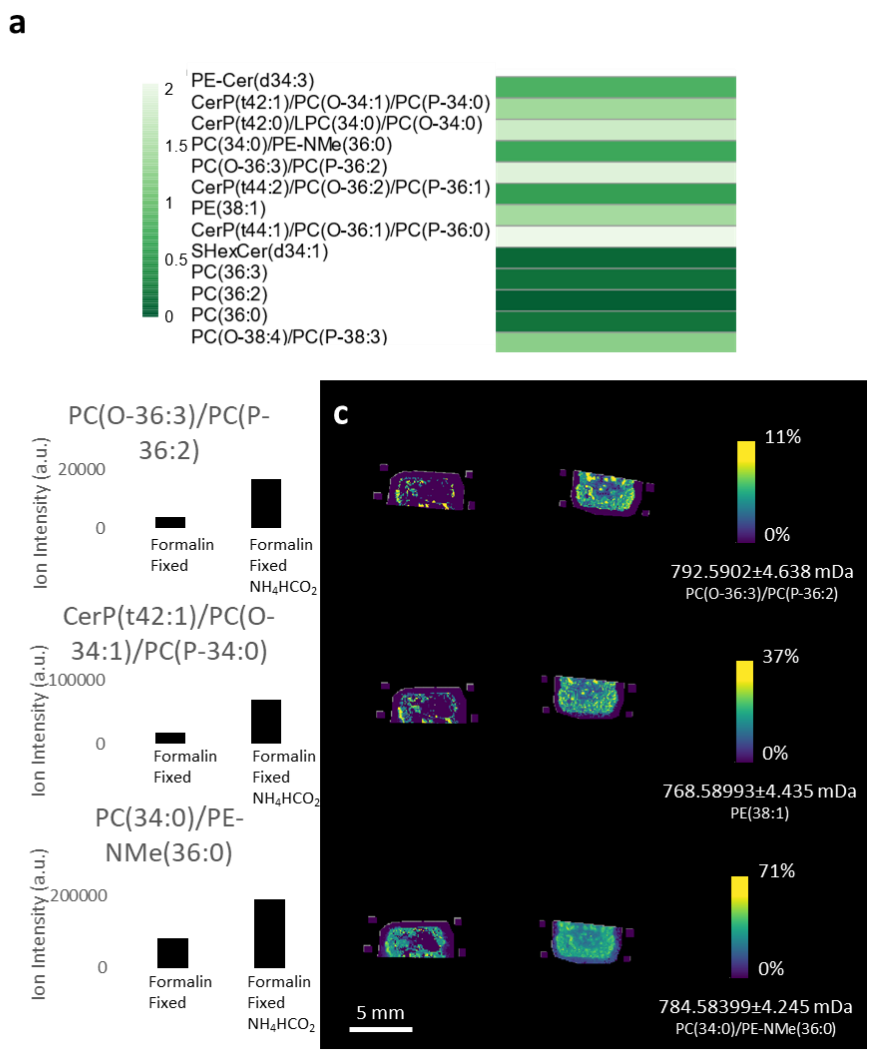

Figure 2.28. Formalin fixed vs. formalin fixed ammonium formate washed sodiated. *a) A heatmap depicting the average log2 fold change of* $[M+Na]^+$ *ions with decreased intensity in formalin fixed sucrose sunk fresh frozen samples compared to formalin fixed sucrose fresh frozen ammonium formate washed samples. (ROC values >0.4 and <0.6) b) A bar graph c) and ion images showing the representative ion intensity and spatial distribution of PC(O-36:3)/PC(P-36:2)), CerP(t42:1)/PC(O-34:1)/PC(O-34:0)), and PC(34:0)/PE-NMe(36:0) as identified by accurate mass with formalin fixed samples on the left and formalin fixed ammonium formate washed on right.*

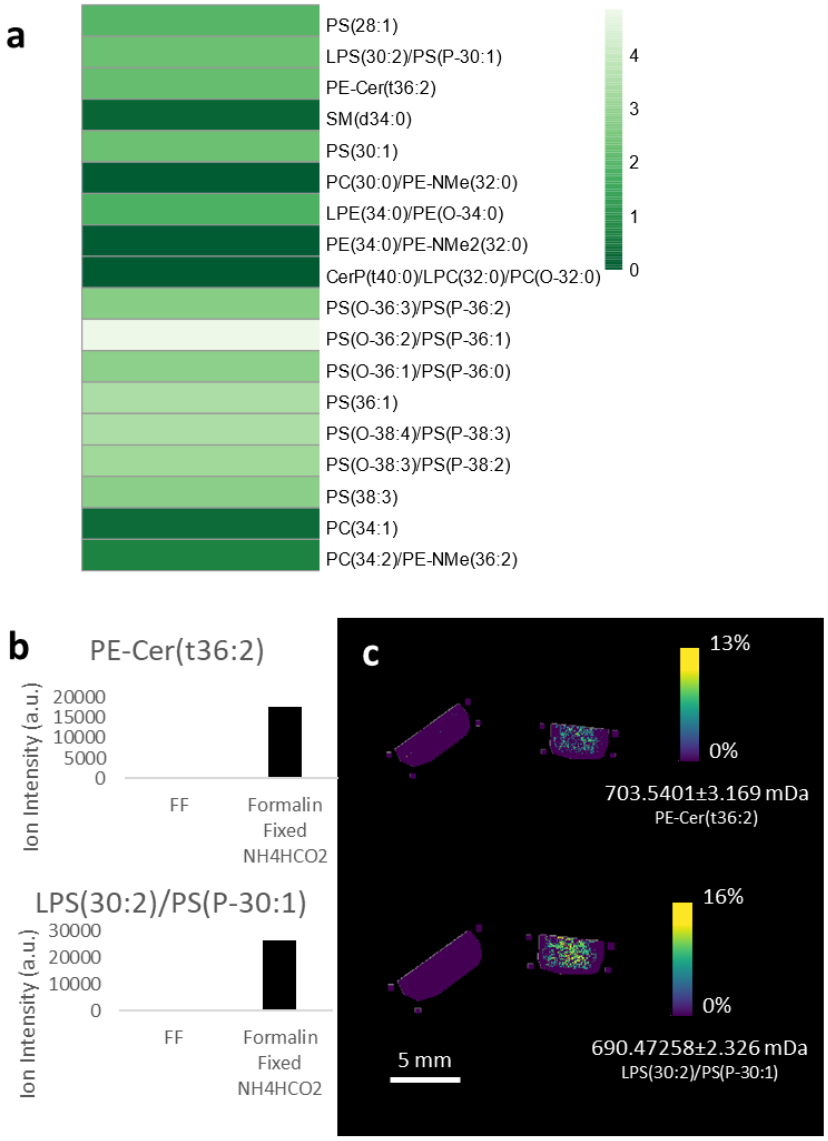

Figure 2.29. FF vs. formalin fixed ammonium formate washed protonated. *a) A heatmap depicting the average log2 fold change of $[M+H]^+$ ions with decreased intensity in fresh frozen (FF) samples compared to formalin fixed fresh frozen ammonium formate washed (formalin fixed NH_4HCO_2) samples. (ROC values >0.4 and <0.6) b) A bar graph c) and ion images showing the representative ion intensity and spatial distribution of PE-Cer(t36:2) (p=0.2) and LPS(30:2)/PS(P-30:1) (p=0.08) as identified by accurate mass with FF on left and formalin fixed NH_4HCO_2 on right.*

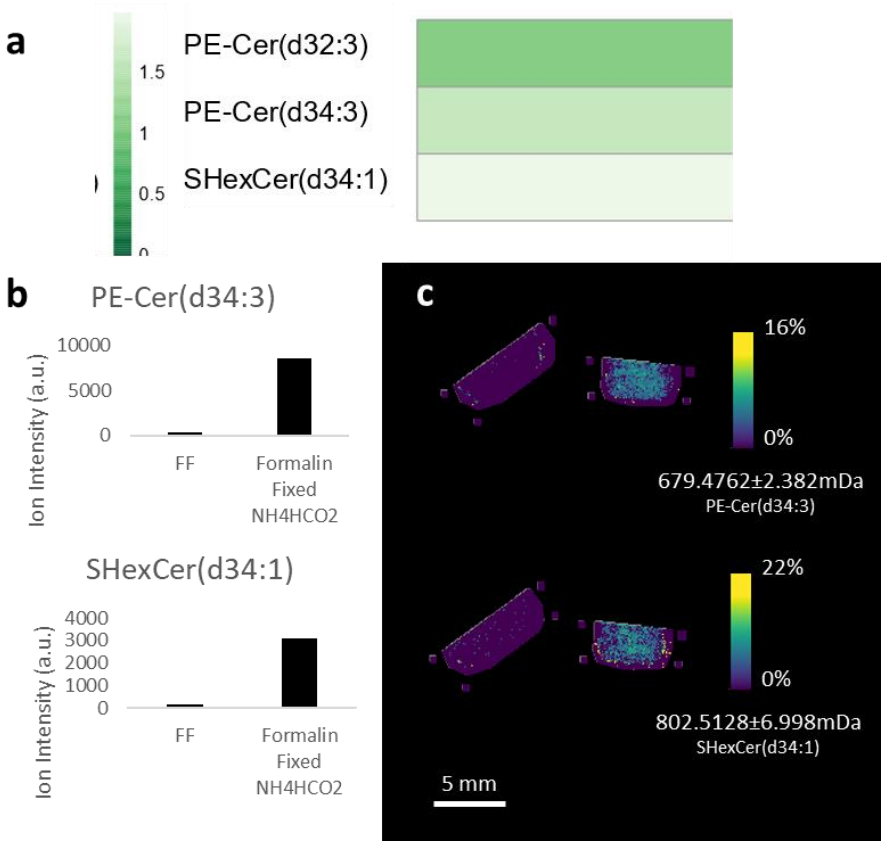

Figure 2.30. FF vs. formalin fixed ammonium formate washed sodiated. *a) A heatmap depicting the average log2 fold change of $[M+Na]^+$ ions with decreased intensity in fresh frozen (FF) samples compared to formalin fixed fresh frozen ammonium formate washed (formalin fixed NH_4HCO_2) samples. (ROC values >0.4 and <0.6) b) A bar graph c) and ion images showing the representative ion intensity and spatial distribution of PE-Cer(d34:3)(p=0.0.01) and SHexCer(d34:1) (p=0.2) as identified by accurate mass with FF on left and formalin fixed NH_4HCO_2 on right.*

Similarly, for PA lipids, the choice of whether to ammonium formate wash is also lipid dependent. In FF tissues, six PA lipids were more easily detected after ammonium formate washing (Appendix A Table 2.70). For example, a 3.7±1.8 (p=0.03) fold increase was detected for [PA(O-38:0)+K]$^+$, (Figure 2.33). Contrarily, 14 PA lipids of detected across all adducts were washed away during ammonium formate washing (Appendix A Table 2.71). For example, [PA(34:1)+K]$^+$ showed a 54±40 (p=0.04) fold decrease after ammonium formate washing (Figure 2.8). Compared to using FF tissues, formalin fixation is largely detrimental (Appendix A Table 2.72). Furthermore, when combing fixation and ammonium formate washing, PA lipids were removed, and none showed improved detection. A total of 10 PA lipids are washed away after combing formalin fixation and ammonium formate washing (Appendix A Table 2.72-74). For instance, a 13±7-fold decrease in ion intensity was detected for [PA(34:1)+K]$^+$ (p=0.07, Figure 2.34).

Largely, SM lipids were the least affected by fixation, but highly affected by ammonium formate washing (Appendix A Table 2.75-78). Only five potassiated SM lipids were detected in lower ion intensities after fixation. For example, SM(d34:1) had a 65±26 (p=0.04) fold decrease after formalin fixation (Figure 2.9). However, like other lipid classes, SM lipids showed improved detection primarily in protonated and sodiated adducts after ammonium formate washing (four and three SM lipids, respectively), but five potassiated SM lipids were detected in lower ion intensities after ammonium formate washing. For example, [SM(d40:2)+H]$^+$ showed a 2.0±0.35 (p=0.01) fold increase with ammonium formate washing while, [SM(d42:2)+K]$^+$ showed a 35±26 (p=0.04) fold decrease with ammonium formate washing (Figure 2.7-8). When combining formalin fixation and ammonium formate washing, little change was detected for SM lipids with one protonated adduct improved and one potassiated adduct was detected in lower ion intensity (i.e. [SM(d42:3)+K]$^+$, Figure 2.32).

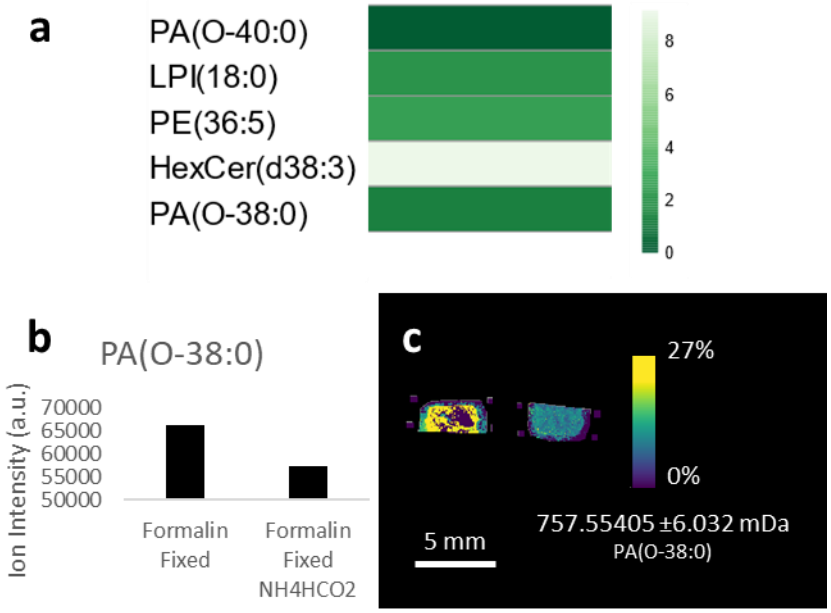

Figure 2.31. FF vs. FF ammonium formate washed potassiated. *a) A heatmap depicting the average log2 fold change of* $[M+K]^+$ *ions with decreased intensity in fresh frozen (FF) samples compared to fresh frozen ammonium formate washed (FF* NH_4HCO_2*) samples. (ROC values >0.4 and <0.6) b) A bar graph c) and ion images showing the representative ion intensity and spatial distribution of PA(O-38:0) (p=0.03) as identified by accurate mass with FF on left and FF* NH_4HCO_2 *on right.*

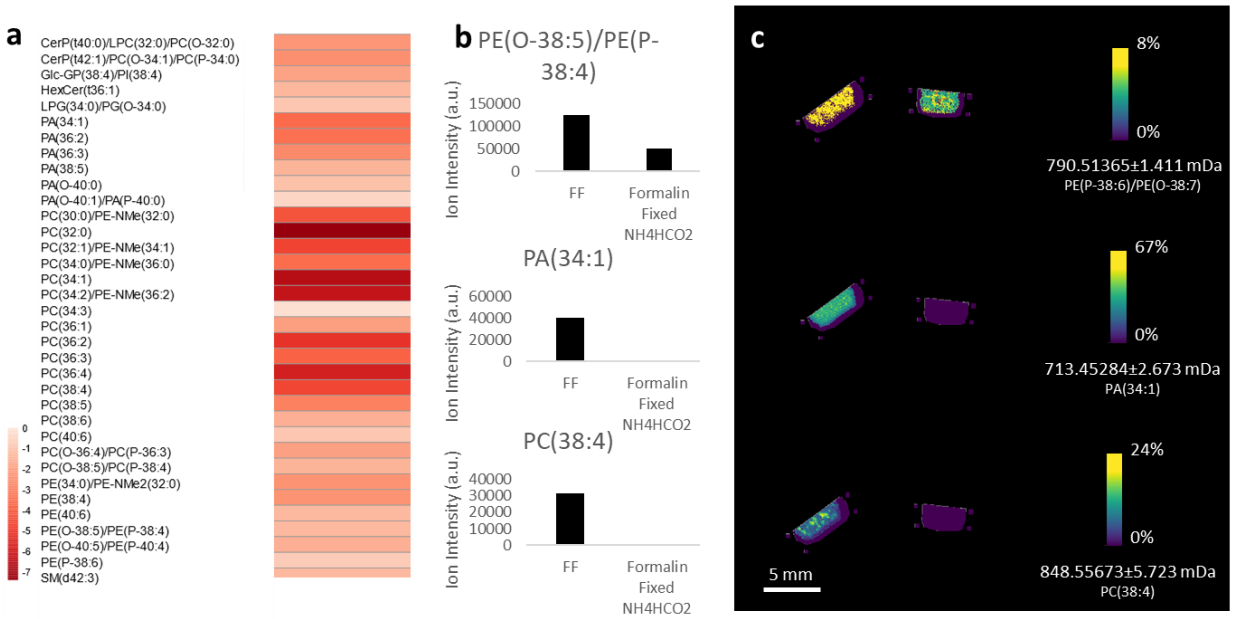

Figure 2.32. FF vs. formalin fixed ammonium formate washed potassiated. *a) A heatmap depicting the average log2 fold change of* $[M+K]^+$ *ions with increased intensity in fresh frozen (FF) samples compared to formalin fixed fresh frozen ammonium formate washed (formalin fixed* NH_4HCO_2*) samples. (ROC values >0.4 and <0.6) b) A bar graph c) and ion images showing the representative ion intensity and spatial distribution of PE(O-38:5)/PE(P-38:4) (p=0.003), PA(34:1) (p=0.07), and PC(38:4) (p=0.05) as identified by accurate mass with FF on left and formalin fixed* NH_4HCO_2 *on right.*

Similarly, PS lipids are unchanged by fixation, but effected by ammonium formate washing. In FF tissues, three protonated and one sodiated PS lipid signal were enhanced after ammonium formate washing (Appendix A table 2.78). For example, in FF tissues, ammonium formate washing resulted in a 1.8±0.48-fold increase for PS(O-36:2)/PS(P-36:1) (p=0.02) (Figure 2.7). However, in formalin fixed tissues, no PS lipids show improved detection with ammonium formate washing, but three sodiated lipids show hindered detection (i.e., LPS(34:0), PS(O-36:0), and PS(O-36:1)/PS(P-36:0), Figure 2.24, Appendix A Table 2.79-82). When combining formalin fixation and ammonium formate washing, nine PS lipids are washed away, but three protonated lipids show enhanced signal. (Appendix A Table 2.82).

Unlike SM and PS lipids, PG lipids are more difficult to detect in tissues that are formalin fixed and/or ammonium formate washed. Formalin fixation does not improve PG lipid detection and removes 24 PG lipids (Appendix A Table 2.83). For example, a 17±12 (p=0.04) fold decrease was detected for $[PG(34:3)+H]^+$ after fixation (Figure 2.25). Similarly, ammonium formate washing of FF tissues removes 26 PG lipids (Appendix A Table 2.84), such as a 17±12(p=0.04), 24±9 (p=0.002) fold decrease was observed for $[PG(34:3)+H]^+$ and $[PG(36:1)+Na]^+$ (Figure 2.27, 2.33).) Furthermore, combining formalin fixation and ammonium formate washing removes 25 PG lipids and no PG lipids show improved detection (Appendix A Table 2.85). These results indicate that unwashed FF tissue should be used when targeting PG lipids, perhaps due to the soluble nature of PG lipids.

Even though previous results indicate formalin fixed ammonium formate washed tissues are suitable for the detection of many lipids,[62] this process alters the detection of various classes of lipids as exemplified in PG lipids. When choosing the optimum sample preparation method, the interrogated lipid class would need to be weighed against the improvement in ion intensity and

tissue structure. In summary, an untargeted experiment should use FF tissues when possible as it results in an overall higher signal intensity than formalin fixed tissue. However, if formalin fixed tissues must be used, ammonium formate washing improves tissue integrity. Furthermore, we demonstrate that formalin fixation is detrimental for lipid classes, while ammonium formate largely improves detection of protonated and sodiated lipids, except for PG lipids.

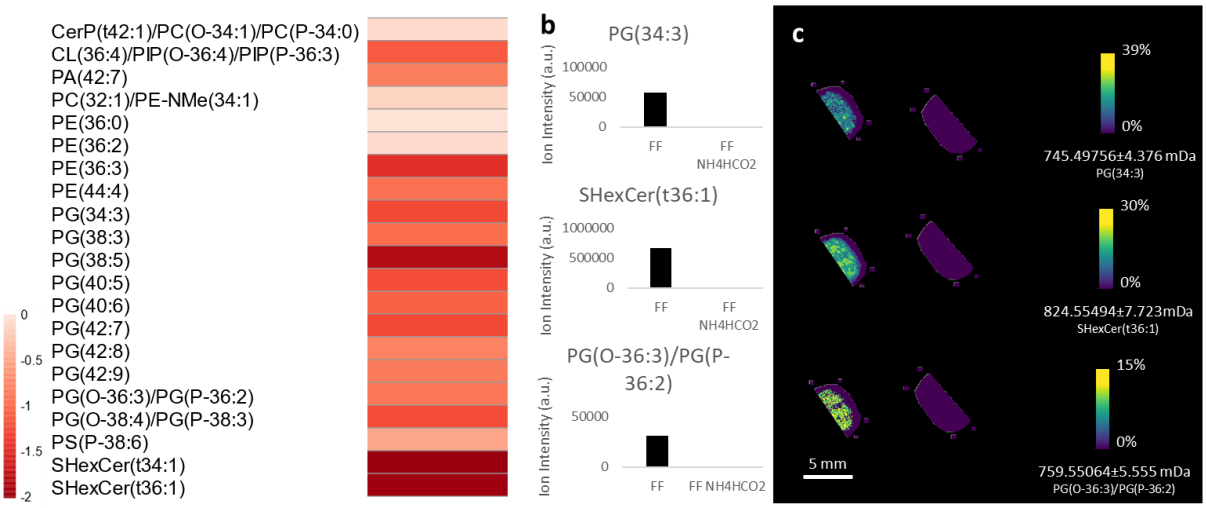

Figure 2.33. FF vs. FF ammonium formate washed protonated. *a) A heatmap depicting the average log2 fold change of $[M+H]^+$ ions with increased intensity in fresh frozen (FF) samples compared to fresh frozen ammonium formate washed (FF NH_4HCO_2) samples. (ROC values >0.4 and <0.6) b) A bar graph c) and ion images showing the representative ion intensity and spatial distribution of PG(34:3) (p=0.04), SHexCer(t36:1) (p=0.08) , and PG(O-36:3)/PG(P-36:2) (p=0.06)as identified by accurate mass with FF on left and FF NH_4HCO_2 on right.*

CONCLUSION

Our investigation of the spectral and tissue structural effects of eight common tissue preparations for MALDI IMS and tissue structure provides important insight into the lipid classes affected by tissue preparations (Table 2.1). Furthermore, we have demonstrated how each sample preparation strategy affects individual lipids and tissue morphology. The spectral and spatial effects of tissue preparation are central to understanding biological findings. Not only does sample preparation affect tissue morphology and the spectral outcomes of these experiments, but it is irreversible and affects the conclusions that can be drawn. The ability to separate biological differences from methodological effects is paramount for discerning the biological conclusions of an experiment. While further investigation into the mechanisms behind these trends and exact role fixation plays in lipid structure is warranted, our research lays a foundation for identifying the spectral and structural changes resulting from various types of tissue preparation, a foundation which can be built upon when employing a multimodal approach to investigate specific lipid classes in tissue.

CHAPTER III

DISCOVERING NEW LIPIDOMIC FEATURES USING CELL TYPE SPECIFIC FLUOROPHORE EXPRESSION TO PROVIDE SPATIAL AND BIOLOGICAL SPECIFICITY IN A MULTIMODAL WORKFLOW WITH MALDI IMAGING MASS SPECTROMETRY

Acknowledgements

This chapter has been adapted from research originally published in the Journal of Analytical Chemistry. Jones, M. A., Cho, S. H., Patterson, N. H., Van De Plas, R., Spraggins, J. M., Boothby, M. R., Caprioli, R. M. Discovering new lipidomic features using cell type specific fluorophore expression to provide spatial and biological specificity in a multimodal workflow with MALDI Imaging Mass Spectrometry. *Anal. Chem.* (2020). doi:10.1021/acs.analchem.0c00446. This work was supported by NSF DGE-1445197 (M.A.J. and R.M.C.), NIH grants P41 GM103391 (R.M.C.), U45-DK120058 (R.M.C.), R01 AI113292 and R01 HL106812 (M.R.B.). The Vanderbilt Mass Spectrometry Research Center and Core are gratefully acknowledged, particularly M. Wade Calcutt and Emilio Rivera for expert assistance with LC-MS/MS method development. Whole slide imaging was performed in the Digital Histology Shared Resource at Vanderbilt University Medical Center (www.mc.vanderbilt.edu/dhsr).

Overview

Identifying the spatial distributions of biomolecules in tissue is crucial for understanding integrated function. Imaging mass spectrometry (IMS) allows simultaneous mapping of thousands of biosynthetic products such as lipids but has needed a means of identifying specific cell-types or functional states to correlate with molecular localization. We report, here, advances starting from identity marking with a genetically encoded fluorophore. The fluorescence emission data were integrated with IMS data through multimodal image processing with advanced registration techniques and data-driven image fusion. In an unbiased analysis of spleens, this integrated technology enabled identification of ether lipid species preferentially enriched in germinal centers. We propose that this use of genetic marking for microanatomical regions of interest can be paired with molecular information from IMS for any tissue, cell-type, or activity state for which fluorescence is driven by a gene-tracking allele and ultimately with outputs of other means of spatial mapping.

INTRODUCTION

Simultaneously mapping the spatial localizations of biomolecules enables the formulation of new hypotheses and can test models related to physiology, disease pathogenesis and clinical applications. Although a variety of technologies exist for spatial localization of metabolites, these technologies face barriers in providing full biological context to findings because biosynthesis and steady-state levels of molecular determinants of cell metabolism and function may be regulated post-translationally. Thus, complementary imaging modalities are required for correlation of molecular images with biologically relevant substructures. MALDI IMS enables the mapping of thousands of unlabeled molecules, including lipids and other metabolic products, directly from tissue sections at high spatial resolution.[51] The challenge of correlating ion

localization to unambiguous identification of microanatomical regions of interest (ROIs) is a computational and experimental challenge.

Microscopy images collected from stained tissue (e.g. staining of tissues by hematoxylin and eosin (H&E) or Immunofluorescence (IF)) [49,93,94] are generally used to provide biological context to IMS data. It has been reported that with low laser fluence, immunofluorescence can be performed on the same tissue section;[57] however, this does not enable the detection of low abundance lipids. In addition, imaging of lipid and protein distributions on the same tissue section has also been reported[95], but the abundance of proteins that identify cell types often require a more sensitive technique than MALDI IMS. The use of serial sections, the standard method of providing this biological context, limits the discriminant power of scoring cell identity or functional status (e.g., activity of a particular gene) for small regions of interest. Moreover, differences in spatial resolution can make correlating IMS and microscopy images challenging. Routine spatial resolution of most IMS experiments is 10-30 μm but can attain 5 μm resolution using specialized instruments less than the thickness of sections used.[96,97] These considerations highlight the need for a multimodal workflow in which biological features can be identified at a microanatomic scale in IMS analyses.[98] The spatial colocalization of a transgenic fluorophore with IMS data provides enhanced biological specificity and advanced data-mining strategies to uncover molecular correlations with ROIs.

Every multimodal analysis has three central processes: registration (alignment of images in 2-D space),[99] data mining (parsing through data for relevant m/z values),[44] and molecular identification (elucidation through MS/MS).[97] Traditionally, multimodal imaging has relied on manual interpretation of co-registered ion images,[100] which is prone to human bias. Other supervised and unsupervised approaches have been used to improve data analysis.[101–107] Each of

these approaches still requires an independent benchmark to define cells or structures. Herein we provide evidence of a new approach that enabled the identification of ROIs on the same tissue section using a cell-type specific transgenic fluorophore to provide biological specificity and the basis for fluorophore-directed data mining.

To develop this technology, we analyzed the spleens of unimmunized and immunized mice using a well-characterized tracking allele that encodes green fluorescent protein (GFP) to enable high accuracy image registration and provide biological context[48]. Data mining strategies such as manual interpretation[44,100], standard segmentation[108], and data-driven image fusion[109] were subsequently applied to determine whether lipids could be mapped to a feature of normal microanatomy in immune responses. The analyses show that data-driven image fusion allowed for the most robust mining of multimodal data by leveraging the correlation of F_{em} and IMS to identify previously unknown spatial molecular relationships.

MATERIALS AND METHODS

Materials

MALDI matrix DAN was purchased from Sigma-Aldrich Chemical Co. (St. Louis, MO, USA). Sheep red blood cells (SRBC), ammonium formate, carboxymethyl cellulose sodium salt, isopropyl alcohol, mass spectrometry grade water, chloroform, and acetonitrile were purchased from Fisher Scientific (Pittsburg, PA, USA); streptavidin-Alexa647 antibody (Ab) and chemically conjugated monoclonal Ab (GL7-FITC, αIgD-PE and αCD35-biotin) were purchased from BD Biosciences (San Jose, CA). C57BL/6-J mice and breeding stock transgenic for a bacterial artificial chromosome that integrates a translational fusion of GFP with AID into the Aicda locus (AID-GFP mice; stock# 018421) were obtained from Jackson Laboratory and bred with C57BL/6-J. All mice were housed in ventilated micro-isolators under Specified-Pathogen-

Free conditions in a Vanderbilt mouse facility and used in accordance with protocols approved by the Institutional Animal Care & Use Committee.

Tissue Preparation

AID-GFP (n=3) and C57BL/6-J (n=3) mice age six to seven weeks were immunized with sheep red blood cells (2x108 intraperitoneally) to compare with non-immunized controls (C57BL6-J, n=3) and euthanized eight days post-immunization. Spleens were extracted, snap-frozen on dry ice in tissue molds, and stored at -80 ˚C prior to sectioning. Samples were post-embedded in degassed 2.6% (w/v) carboxymethyl cellulose over dry ice. Tissues were sectioned at 12 µm using a cryostat (Leica 3050S) at -17 ˚C and thaw-mounted onto ITO (Delta Technologies) or Super Frost Gold Plus microscope slides (Fisher Scientific). Three serial sections with one section of each sample type were placed on triads of slides with the central slide (ITO) destined for IMS and the peripheral slides (Super Frost Gold Plus) used for H&E and IF (Figure 3.1). After sectioning, slides were placed in a desiccator for 15 minutes prior to any secondary imaging modality. Fem was performed on all sections and slides. All fluorescence microscopy data were collected using a Nikon 90i (Nikon, Melville, NY, USA) and then used for alignment and identification of GCs via detection of Fem of transgenic fluorophore. FITC, TRITC, and DAPI filters were used, all with 150 ms exposures at 10x magnification and autofocusing in the GFP channel. After Fem scanning, ammonium formate washing was performed to remove excess salts and enhance IMS signal. Samples on ITO slides for IMS were washed four times (each for 15 s without agitation) in 50 mM ammonium formate (pH of 6.4 at 4˚C) and then placed in a desiccator (15 min) to ensure drying before matrix application.[81]

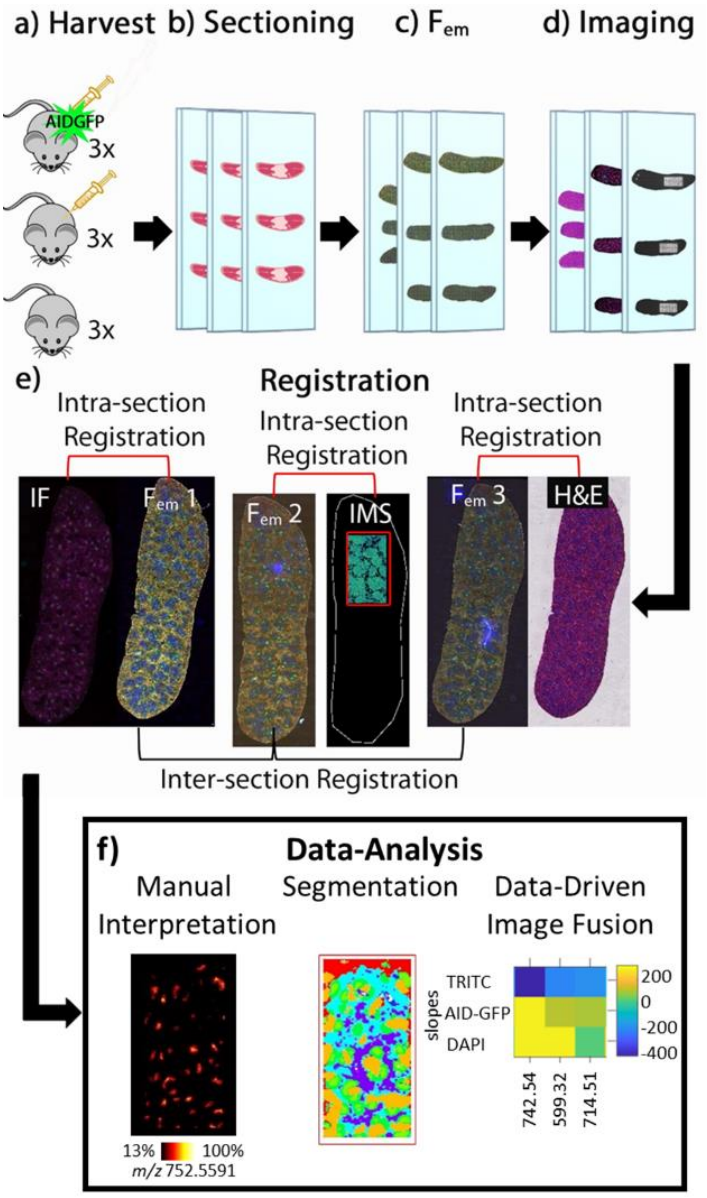

Figure 3.1. A workflow for multimodal analysis and data extraction. *Shown are a schematic (a) and representative data (b-f) to illustrate the initial IMS analyses. a) Mice of the indicated genotypes (bearing or lacking an Aicda BAC transgene engineered to express AID-GFP translational fusion protein) and immunization status were used starting at 6-7 weeks of age. b-d) Spleens harvested 8 d post-immunization were used to generate triads of serial tissue sections (12 µm thickness) (b), followed by fluorescence emission (F_{em}) and other imaging modalities (c). After*

processing, immunofluorescence (IF), IMS, and hematoxylin and eosin staining (H&E) were each performed with one of the three sections (d). (e) F_{em} data from sections 1-3, as indicated, are shown adjacent to the IF, a single m/z from negative ion mode IMS, and H&E images from the same section as the F_{em}. Intra- and intersection registrations were then performed using a published method in which IMS data are aligned with the post IMS laser ablation marks, and all other modalities were aligned to IMS data through F_{em} on each section. (f) Manual interpretation, segmentation, and data-driven image fusion were performed with publicly available software to map ions of interest, as detailed in the methods.

Concurrently, IF was performed on one serial section, and H&E staining was performed on a second serial section. For IF, frozen tissue sections were air dried (1 min) and rehydrated (two times, each for 1 min) in ice cold (4°C) phosphate-buffered saline (PBS). Slides were then fixed with fresh 1% paraformaldehyde for 10 minutes and washed (three times, each for 2 min) with PBS and then treated with M.O.M. blocking buffer (1 hour at 20 °C) (Vector Lab; Burlingame, CA). Sections were then incubated (3 hours at 4˚ C) with 25-30 µL of primary antibody [α-GL7-FITC (1:50), α-IgD-PE (1:200), and α-CD35-biotin (1:200)], washed 3 times with PBS, followed by incubation with streptavidin-Alexa 647 (1:200) in blocking buffer for 1-2 hours at 4 ˚C and again washing 3x with PBS and mounting with Prolong Diamond anti-fade reagent (Thermo Fisher, Waltham, MA). Immunohistochemistry scans were collected using an Aperio Versa 200 using DAPI, FITC, Cy3, and Cy5 at 10x with exposure time optimized for each sample.

For H&E, sections were fixed in 95% EtOH followed by 70% EtOH (30 sec each) and rinsed in Milli-Q water until clear. Sections were first stained in hematoxylin (2.5 min), rinsed in water, dipped in 0.5% ammonium hydroxide and rinsed in water, and then dipped 20 times in

70% EtOH followed by 95% ethanol 20 times. After staining with eosin for 1 minute, slides were further prepared through 20 dips in 95% ethanol and a second fresh wash in 95% ethanol for 10 seconds. Slides were then moved to a 100% ethanol solution for 20 dips twice and then placed in xylenes for two minutes prior to cover slipping.

For the IMS modality, matrix was applied to ammonium formate-washed samples with a robotic sprayer (TM Sprayer, HTX, Chapel Hill, NC, USA) operated at a speed of 1200 mm/min with a track spacing of 1.5 mm, using nitrogen as a flow gas at 10 PSI. Recrystallized 1,5-DAN was dissolved in a 9:1 (v/v) solution of acetonitrile/deionized water at a concentration of 10 mg/mL and sonicated 15 min. The sprayer nozzle was held at 85˚ C to deposit matrix in eight "criss-cross" passes at a flow rate of 0.15 mL/min with a pushing solvent of 90/10 (v/v) acetonitrile/ H2O for an average density of 6.667 µg/mm^2.

Mass Spectrometry Imaging

Negative ion mode IMS data were acquired with a 9.4T Bruker FT-ICR SolariX mass spectrometer (Bruker Daltonics, Billerica, MA, USA) equipped with a 2 kHz Nd: YAG (wavelength: 355nm) laser and an Infinity ion cyclotron resonance (ICR) cell. Laser power was optimized for each sample by adjusting in the range of 18-20%. Data were collected in negative ion mode from m/z 200-2,000 with a raster step of 30 µm and a data size of 1 MB per spectrum with a free induction decay (FID) length of 0.8389 s. Each pixel consisted of 500 laser shots with the minimum laser energy focus setting (~10 µm) at a frequency of 2000 Hz, and a smart walk of 25 µm was enabled to increase sensitivity. The mass-selecting quadrupole was set to m/z 350 and TOF of 0.8 ms. The resolving power of all imaging experiments was ~80,000 at m/z 766.54. External calibration was performed prior to analysis, and internal lock-mass calibration was performed using m/z 885.5494 ([PI(18:0_20:4)-H]$^-$) during image acquisition. For image fusion

analysis, a higher spatial resolution image was generated using the same 9.4T FT-ICR with similar settings except that the raster step was 15 µm without Smartwalk enabled, and 750 laser shots per pixel were generated at a laser power of 13%. All datasets are available at https://figshare.com/s/ab2f73880453100e0c2c.

Image Registration.

Image registration techniques were performed according to previously published methods;[48] however, rather than using AF images for registration, we used F_{em} / AF images. For registration, source images were transformed to match the corresponding target images - in this work, the IMS coordinate system with the source image being the other modalities connected through F_{em} (Figure 3.1e, Table 3.1). This transformation involved some deformation of images determined through an iterative function designed to improve alignment. Due to the need to integrate multi-modal data, we used the affine registration model with a mean distance error at ~1 µm for same-section registration and ~10 µm for registration of two adjacent sections, with the minimum image resolution as the limiting factor in each case.[47]

SOFTWARE	PURPOSE	LOCATION
FIJI	Figure formation, Image Registration	https://fiji.sc/
FLEXIMAGING	Image Visualization, Spotlist Generation	https://www.bruker.com/products/mass-spectrometry-and-separations/ms-software/fleximaging/overview.html
QUPATH	Multimodal Image Data Extraction	https://qupath.github.io/
RSTUDIO	Segmentation/IMS Data Analysis, imzml Reconfiguring, Data Extraction	https://cran.r-project.org/mirrors.html
SCILS	Exportation to imzml	https://www.bruker.com/products/mass-spectrometry-and-separations/ms-software/scils/overview.html
IMAGE FUSION	Data Mining	https://fusion.vueinnovations.com/
MSRC REGISTRATION TOOLBOX	Image Registration	https://github.com/nhpatterson/regtoolboxmsrc
PRISM	Statistical Analysis	https://www.graphpad.com/scientific-software/prism/
XCALIBUR	LC-MS/MS Data Analysis	https://www.thermofisher.com/order/catalog/product/OPTON-30487
LIPIDMAPS	Lipid Accurate Mass and MS/MS Prediction	http://www.lipidmaps.org/tools/ms/

Table 3.1. Software and data analysis tools for performing this method. *The software tool, purpose, and location for download or purchase are listed from left to right.*

Registration Experimental Considerations

All modalities were aligned to IMS data on a per pixel basis by linking of the theoretical pixel location in each image to the laser ablation marks made by the IMS laser in a raster across the tissue. Both single-section multi-image and multi-section multi-image workflows were used in registration16. Images were exported as high-resolution jpeg, tiff, mha, or png files. All images were registered to a pixel map, or theoretical grid, generated from a coordinate extraction from flex imaging, using a padding of 10 to add area to the images around the edges (Figure 3.2, Table 3.1). We used external fiducial marks (rectangular regions external to the tissue) to reduce inaccuracy that could be introduced in determination of the exact center of the ablation mark for alignment to the theoretical pixel map of tissue at high spatial resolutions (Table 3.1). These fiducial benchmarks were acquired at half the spatial resolution and were used to enable high accuracy alignment with the center of the theoretical pixel map obtained from the spot list map. Laser ablation sites post-acquisition as well as external fiducial marks were recorded in the FITC channel. Masks in FIJI were used to increase accuracy of registration 43, and image figures were created using FIJI, utilizing its pre-programmed macros.

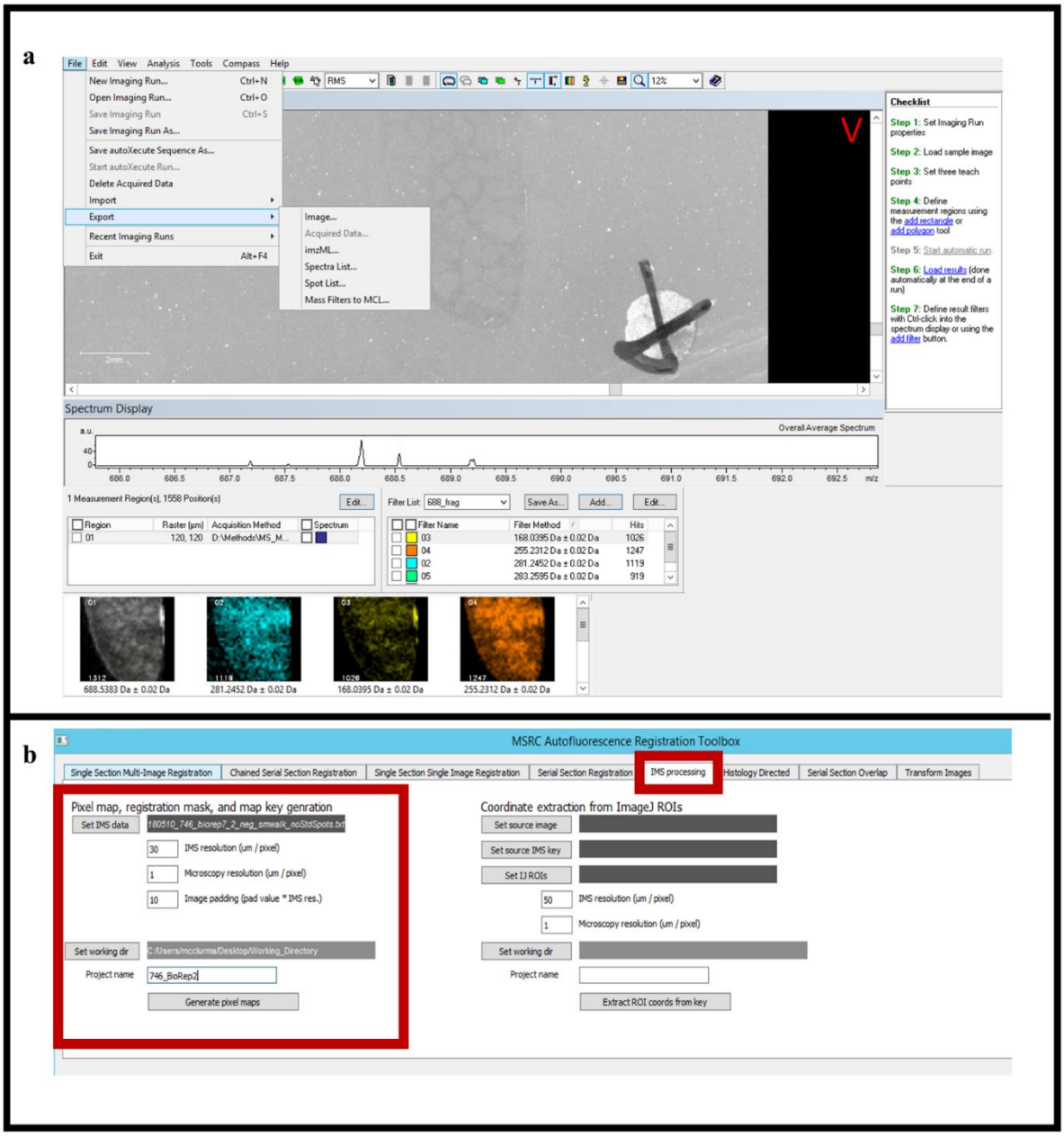

Figure 3.2. Screenshots illustrate how to extract the spot list and make a pixel map. *a) Within FlexImaging, a Bruker IMS data analysis tool is used to extract the spot list. Go to file -> export -> SpotList. b) That spot list is then converted into a pixel map within the MSRC Autofluorescence Registration Toolbox. A screenshot showing the parameters used in this experiment are shown.*

IMS Data Analysis.

All data was RMS normalized and further analyses were performed: Manual interpretation analyses were performed in SCiLS, and spatially shrunken centroid segmentation analysis was performed in R with the package Cardinal. Image fusion analyses were performed according to previously published methods[109], utilizing the partial least-squares regression correlation to link image pairs of IMS images' fluorescence emission data. Localization to germinal centers was determined using QuPath software for annotation and an R script for data extraction. Weighted averages were tested for significance with ratio T tests (Figure 3.3).

To quantify overlap (congruence) in two adjacent sections across entire data sets, samples from immunized AID-GFP transgenic mice were annotated for GC localization in FIJI using regions of interest and imported into R.[43,108] A custom script was used to determine the Sorenson dice coefficient between each serial section, and the coefficients determined for each section pair were then averaged (Figure 3.4 and Table 3.2). IMS data were initially preprocessed by importation into SCiLS and root mean square normalized. These normalized data were then converted to imzml format and imported in the R environment via Cardinal package. Images were generated in R and overlaid with all other modalities. Data were further analyzed through manual interpretation, spatially shrunken centroid segmentation with the Cardinal package, and via image fusion to enable correlation of IMS m/z channels to RGB channels in a partial least squares model. For manual interpretation, each ion image was screened visually for its relationship to the GC images in side-by-side comparisons, and only those ions that appeared to localize specifically were selected.

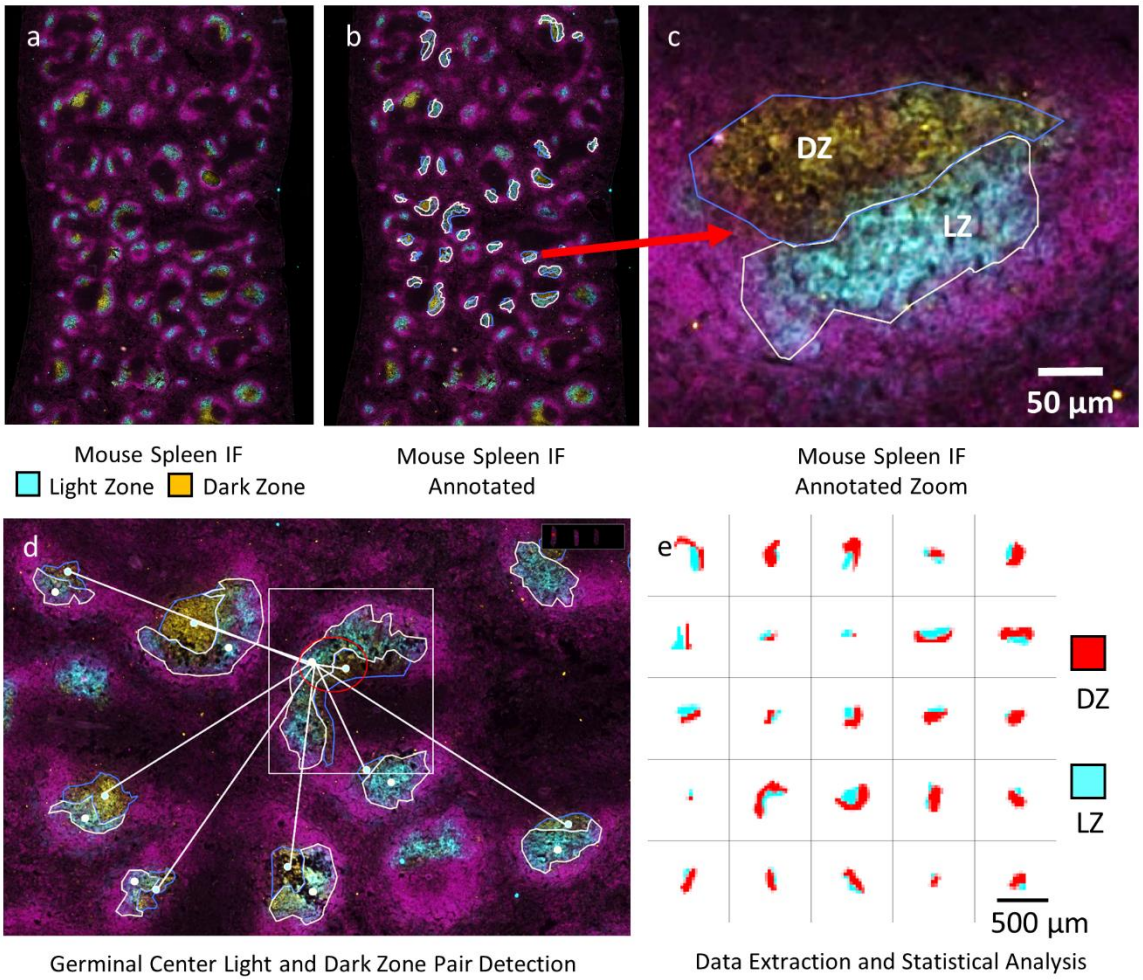

Figure 3.3. A workflow for annotation and data extraction in QuPath. *a) IF samples were loaded into QuPath and the light zone, indicated in blue, and the DZ, indicated in yellow, are shown. b) The mouse spleen was annotated manually. c) A zoom in of a single annotation with both DZ and LZ sub regions is shown. d) GC pairs were detected by Euclidian distance. e) Data was extracted from GC pairs with LZs and DZs larger than 5 contiguous pixels and statistical analyses were performed.*

SAMPLE	**DICE COEFFIECENT**
SERIAL HE, 725	0.83
SERIAL IHC, 725	0.85
SERIAL IHC, 745	0.80
SERIAL HE, 737	0.79
SERIAL IHC, 737	0.78
MEAN DICE	**0.81**
ST. DEV. DICE	**0.029**

Table 3.2. Serial section comparison. *For each serial section, a Dice Coefficient was determined and the mean and standard deviation are shown.*

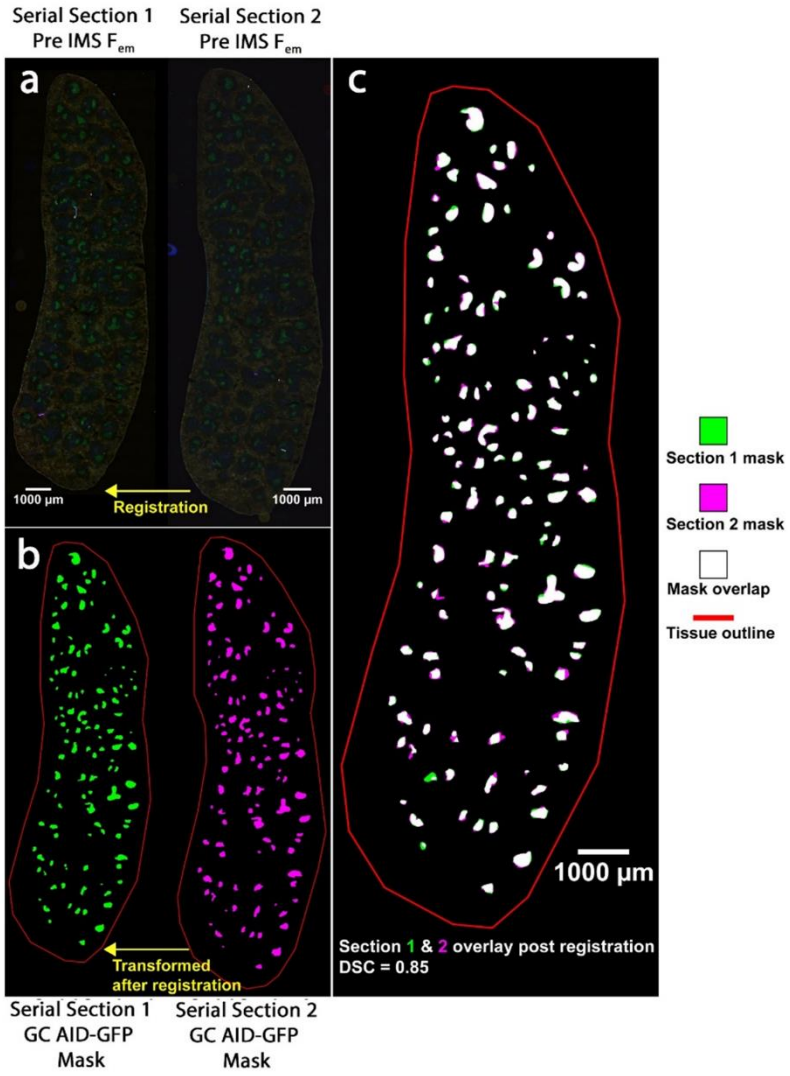

Figure 3.4. Serial section accuracy: a visual representation. *The F_{em} images from two registered serial sections of mouse spleen after SRBC immunization depicted in a) were used to annotate AID-GFP GC. b) Masks of these annotations were generated, and c) the overlap between these annotations is visually shown in white with a Dice-Sorenson coefficient (DSC) of 0.85. To the right, a color legend is shown to indicate the section mask, overlap, and tissue outline. A scale bar can be found in white indicating 1000 µm. See Table 3.2 for more information.*

For spatially shrunken centroid data analysis, data were exported into R by importing data into SCiLS and enacting extraction of peak lists via the file tab “export SCiLS report table” (Figure 3.5). This was accomplished by importing the data into R in the correct format to be read into Cardinal using a home-built R script. Data were then segmented until k means clustering produced a GC-like segment. Each ion image was analyzed separately, and the top m/z ions for each segment with their weights were exported into Excel for further analysis. The ions with a T statistic above 15 were selected due to previous manual interpretation results showing that both m/z 776.5596 and m/z 752.5591 were GC-specific ions. Ions were only tested statistically to determine whether they were present in all three biological replicates in this refined list (Table 3.3).

	BIOLOGICAL REP 1		BIOLOGICAL REP 2		BIOLOGICAL REP 3	
	m/z	T statistics	*m/z*	T statistics	*m/z*	T statistics
	871.5659	34.48	883.5369	42.26	871.5659	68.09
	883.5369	33.13	857.5195	37.10	888.5639	64.87
	1626.9414	32.19	871.5659	36.96	887.5639	61.83
	1642.9175	31.93	1642.9175	36.28	1532.8099	61.47
	1627.9478	31.63	1643.9474	34.70	1626.9414	61.25
	752.5599	31.15	869.5500	33.15	1627.9478	59.01
	1643.9474	30.84	752.5599	32.70	752.5599	55.64
	857.5195	29.02	776.5584	31.81	883.5369	55.53
	884.5392	28.81	1644.9251	30.47	1628.9590	53.42
	869.5500	28.23	884.5392	30.08	1533.8367	53.34
	1532.8099	27.20	858.5210	28.18	1642.9175	53.27
	887.5639	27.15	887.5639	27.69	1643.9474	51.60
	776.5584	26.93	746.5143	27.57	872.5693	50.55
	1641.9245	26.18	859.5297	26.23	760.5078	49.13
	1517.8449	25.80	786.5288	25.55	776.5584	48.90
	1533.8367	25.48	1641.9245	24.73	1517.8449	48.54
	1644.9251	25.01	1626.9414	24.70	1644.9251	47.54
	858.5210	23.43	835.5270	23.28	884.5392	46.99
	1628.9590	22.27	860.5320	22.59	716.5190	46.56
	888.5639	21.91	885.5499	22.33	753.5596	45.58

Table 3.3. Segmentation determined ions of interest. *For each biological replicate, the m/z value and t statistic output from spatially shrunken segmentation in Cardinal is shown.*

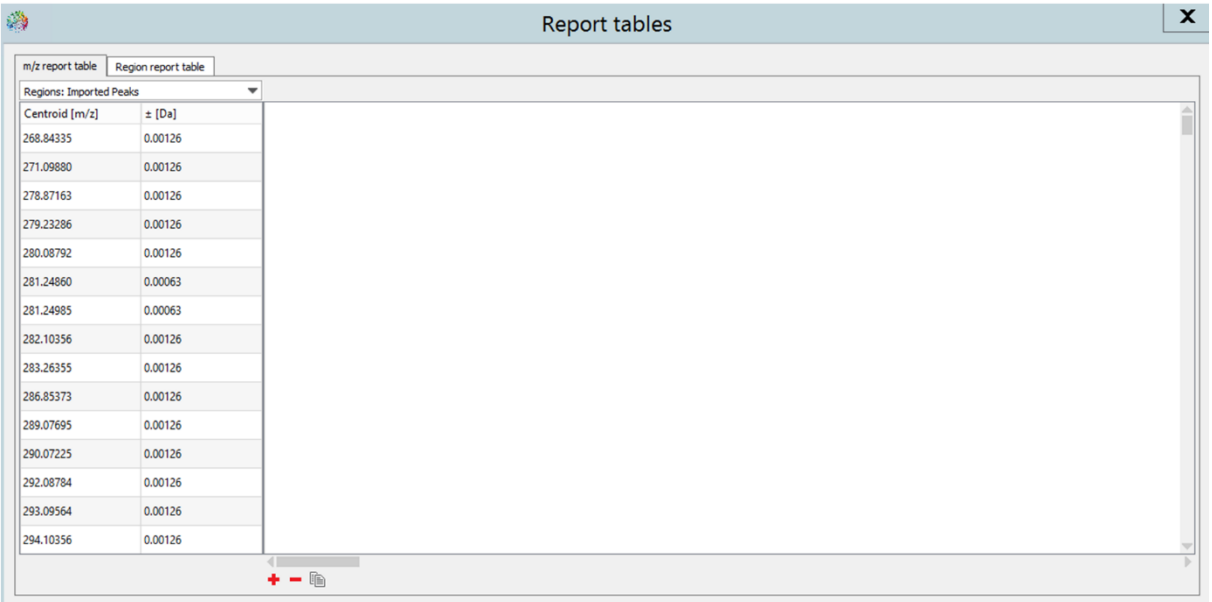

Figure 3.5. An example of a SCiLS report table for exporting peak values. *To export the .imzml equivalent of Bruker data to Rstudio, a report table converted into a .csv is used. This includes centroid m/z values and a ±Da window for each peak.*

For image fusion analysis with IMS data sets, the mass spectrometry data were treated as a data cube in which the x and y coordinates are pixel dimensions, and the z coordinate is m/z. Analogously, the microscopy data map pixel dimensions are x and y, but the z coordinate was the color channels. Image fusion algorithms were then used in two phases – first creating a cross-modality model and then using the model to perform a partial least squares regression correlation to compare image pairs of IMS and Fem data. In the present work, relationships were mined to identify ions of interest that related to a specific color channel, in this case green to correlate IMS with the AID-GFP fluorophore. Further information on this algorithm can be found in previous work.[109] IMS data collection for image fusion processing was performed with 15 µm raster steps in negative ion mode using sectioned (12 µm thickness) spleens of immunized AID-GFP transgenic mice. The mass range was truncated to m/z 500 to 900, and the top 119 most abundant ions were selected for analysis. The white box correlation model was used to identify key ions directly and inversely correlating with the FITC channel in F_{em} microscopy images that were acquired on the same section that was used to acquire IMS data. A full implementation of the image fusion framework is provided as a command-line utility that can be downloaded at http://fusion.vueinnovations.com/. Additional information on preformatting data for image fusion can be found at https://github.com/NHPatterson/aimsMSRC (Table 3.1).

QuPath: region specific annotation and weighted average intensity extraction. To enable statistical analyses, variance was determined for ions of interest discovered through manual interpretation, segmentation, and image fusion. Quantitative Pathology and Bio image analysis (QuPath) software[110] was used to annotate and extract ion intensities from the MALDI imaging datasets. Samples were manually annotated in QuPath, adjusting contrast as needed for GCs to identify the light and dark zones (Figure 3.5-6). Data were then extracted using an R script in

which pixels with a 50% overlap were included in the region of interest and a weighted average (weighted by IMS pixel – annotation ROI overlap) was taken for each such region. To test the null hypothesis – no genuine difference in distribution of the m/z species– these averages and their variances were then compared using ratio T tests (Table 3.4). GC ions were selected based on their significance and then to determine whether these ions were specific to GCs. Once GC co-localizing ions - defined based on results of such statistical testing in comparing GC to all other regions interest - were determined, these m/z features were further probed using serial sections to distinguish the two GC subregions. For these latter analyses, we used only GCs for which both light and dark zones were clearly identified. These pairs were selected using an R script in which Euclidean distance was employed to establish the nearest neighbor within five contiguous pixels (approximately 67 um^2). These weighted averages were then further tested for significance with ratio T tests.

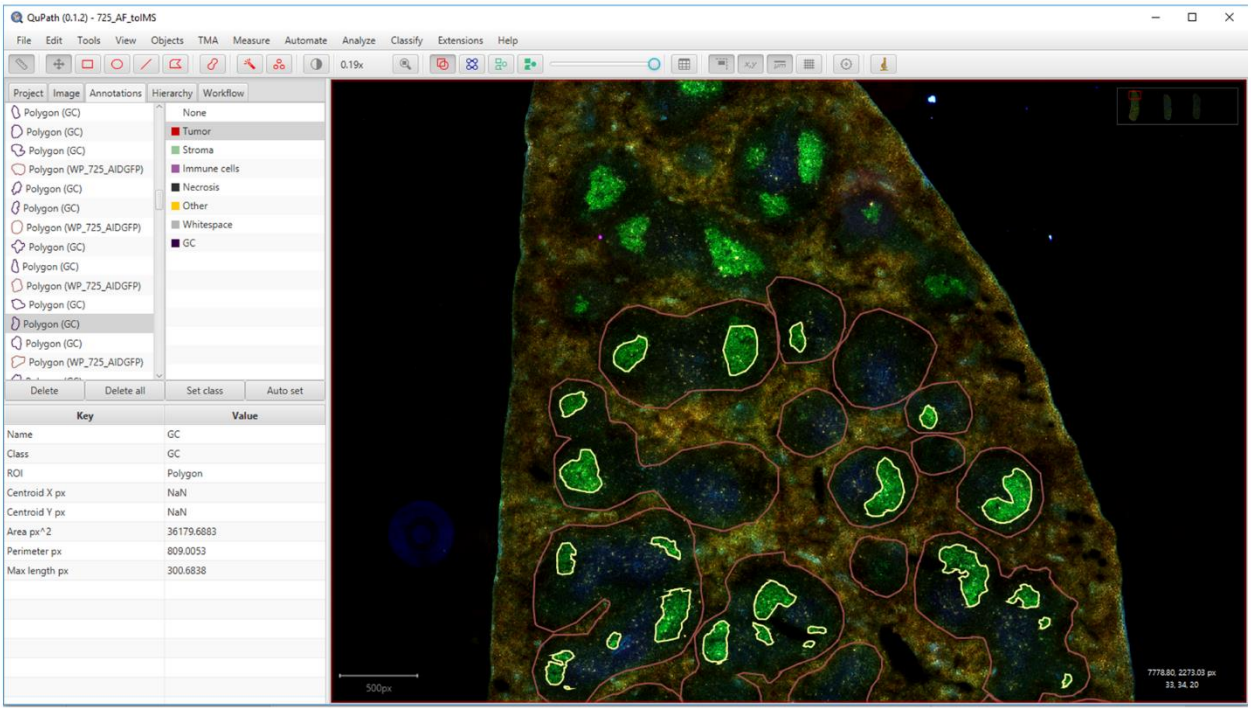

Figure 3.6. An example of the QuPath annotation platform. *In QuPath, annotations of germinal centers and their light and dark zones were made for exporting weighted mean values of ions for these regions.*

Identification of lipid Species

To specify the lipids that corresponded to the GC-enriched ions, provisional identifications were made by comparing accurate masses of the precursor ions and fragment ions to theoretical m/z values in LIPID MAPS (Nature Lipidomics Gateway, http://www.lipidmaps.org/). For further validation, LC-MS/MS of total splenocytes was performed on a Q Exactive HF mass spectrometer from m/z 375-1650 in PRM mode with an isolation window of 2 Da for each ion of interest using eluates from a Vanquish UHPLC (Thermo Scientific, Waltham, MA, USA). MS/MS resolving power was 15,000 at m/z 200, while full scan resolving power was 30,000 at m/z 200. Chromatography was performed on a Waters BEH C8 column (150mm x 2, 1mm x 1, 7µm particle size, Waters, Milford, MA, USA) using solvent A [10 mM ammonium acetate in water/acetonitrile (1:1 v/v)] and solvent B [10 mM ammonium acetate in isopropyl alcohol/acetonitrile (1:1 v/v)], eluting with a gradient as follows: Solvent B was held at 20% B for 1 min followed by a gradient over 8 min to 100% solvent B. Solvent B was held at 100% B for 2 min and then decreased to 20% B in 0.5 minutes followed by an isocratic solution at 2% B for 4.5 minutes. Resultant LC-MS/MS data were analyzed manually using Xcalibur Qual Browser (Thermo Xcalibur 2.2 SP1.48, Thermo Fisher Scientific Inc., Waltham, MA, USA) and Lipid Maps MS tools (Nature Lipidomics Gateway, http://www.lipidmaps.org/tools/ms/).

Complementary analyses were performed using MS/MS based imaging experiments using a 15T Bruker FT-ICR solariX mass spectrometer (Bruker Daltonics, Billerica, MA, USA). The instrument is equipped with a Smartbeam II 2kHz Nd: YAG (wavelength: 355nm) laser and a Paracell ICR cell. Data were collected in negative ion mode from m/z 250-2,000 with 1,000 laser shots per pixel, and a raster step was set to 60-120 µm with a data size of 1 MB per

spectrum. Ions were isolated with a 2-6 Da mass window and fragmented using collision induced dissociation (CID) with a collision energy of 17-27 V.

RESULTS AND DISSCUSSION

Overview

We used multiple microscopy-based imaging modalities (H&E, IF, and F_{em}) registered to IMS measurements to elucidate the lipidomic differences between GC and splenic white pulp or lymphoid follicles (Figure 1). Specifically, the AID-GFP (Activation-Induced Deaminase-Green Fluorescent Protein) transgene provided a cell type and region-specific fluorophore.[50] This tracking allele highlights a micro-anatomical feature that forms within lymphoid follicles after immunization due to a large increase in *Aicda* gene expression in GC B lymphocytes, which diversifies and improves qualities of antibody responses.[50] F_{em} provided a non-destructive means of identifying GC via co-localization with AID-GFP, while AF from endogenous molecules provided histological images of other splenic tissue structures (e.g., red pulp and white pulp surrounding GC). This F_{em}/AF modality also provided a single image type that could be collected from every tissue section prior to other modalities (i.e., H&E-stained microscopy, IF microscopy, and IMS) (Figure 1 b-d), enabling high accuracy image registration (Figure 1e). In H&E stains, the most traditional means of providing biological context to IMS data, red pulp can be differentiated from white pulp, but GCs are less conclusively differentiated, IF microscopy allowed for the identification of GC and their substructures (light zones and dark zones). Because AID expression is similar in LZ and DZ, both H&E and IF after immunostaining were performed on serial sections. As this results in plane-of-section differences from sections used for IMS, advanced registration approaches were needed. By integrating these modalities into a

single multi-planar dataset, we enabled a full integration of imaging modalities to provide a unique combination of molecular coverage, spatial resolution, and biological specificity.

Registration

We first tested whether this method allowed incorporation of F_{em} as an additional modality within each section to enable a high degree of spatially localized biological information. Sections were analyzed for GCs in spleens of mice, immunized or not, and bearing or lacking an AID-GFP transgenic fluorophore. The same tissue sections were then used for IMS, while serial sections were used for IF and H&E. This method was applied to an investigation of the differences between lipids associated with GCs and other regions in spleens using non-destructive F_{em} as a mono-modal registration medium[48] (Figure 1e). Spleens of non-immunized controls were compared to those of immunized mice bearing or lacking the AID-GFP transgene (Figure 1a). IMS was then used to identify m/z features after collection of F_{em} images of the AID-GFP fluorophore.

In addition to identification of GC within the section destined for IMS through F_{em}, we investigated lipid differences in sub-regions of the GC. Accordingly, the workflow incorporated IF staining of adjacent sections with antibodies specific for markers that not only would identify GC by independent criteria (IgDneg GL7+) but also would allow subdivision of the GC into functionally distinct domains termed the dark (DZ, CD35neg) and light (LZ, CD35+) zones. To compare the conventional use of serial sections to intra-section registration, we quantitated the error in overlap between adjacent sections. GC masks annotated for all AID-GFP mouse spleen serial section pairs (n =5) were used to calculate a Dice-Sorenson coefficient (DSC), a statistical means of determining the similarity of two samples that were registered as described by

Patterson et al[48]. The average DSC was 0.81 (±0.3) for the five pairs, indicating that serial sections as registered can be expected to have 81% GC overlap (Figure 3.4, Table 3.2).

m/z	LIPID ID	DB HITS	P VALUE GC VS. NON-GC	P VALUE LZ VS. DZ	PPM ERROR *	MAN. INT.	SEG.	IMAGE FUSION SLOPE
671.4647	PA(18:1_16:1)	6	0.09	0.0007	0.070			222.1
699.4957	PA(18:1_18:1)	6	0.03	0.0002	0.36			277.2
699.4957	PA(18:0_18:2)	7	0.03	0.0002	0.36			277.2
699.4957	PA(20:2_16:0)	7	0.03	0.0002	0.36			277.2
714.5069	PE(18:2 16:0)	4	0.04	0.2	0.053			102.5
716.5224	PE(18:0_16:1)	3	0.1	0.9	0.059			243.8
725.5120	PA(20:3_18:0)	8	0.007	0.02	0.53			63.2
740.5246	PE(18:1_18:2)	4	0.01	0.01	2.9			112.8
742.5389	PE(18:0_18:2)	5	0.04	0.0006	1.0			290.5
746.5130	PE(P-16:0_22:6)	6	0.005	<0.0001	1.5			280.0
748.5273	PE(O-16:0_22:6)	6	0.007	0.2	0.37			236.6
752.5591	PE(O-18:0_20:4)	5	0.01	<0.0001	0.32	X	X	219.0
762.5088	PE(16:0_22:6)	4	0.03	0.2	2.6			167.0
772.5314	PE(P-18:1_22:6)	5	0.03	0.01	5.0			163.3
776.5596	PE(O-18:0_22:6)	5	0.05	<0.0001	0.88	X	X	244.7
786.5303	PS(18:0_18:2)	8	0.02	0.0004	2.9			279.4
812.5460	PS(18:0_20:3)	2	0.03	0.3	3.0			37.1
857.5182	PI(16:0_20:4)	16	0.009	0.002	0.82			400.6
883.5360	PI(18:1_20:4)	6	0.003	0.1	3.3		X	565.8
887.5609	PI(18:0_20:3)	14	0.0006	0.07	3.9		X	252.9

Table 3.4. GC Lipids revealed through all data mining strategies. *From left to right the m/z value, identification of the lipid found via the multimodal workflow validated through MS/MS imaging, matches to the LIPIDMAPS database, p value for a t-test between GC and non-GC regions, p value for a ratio- paired t-test between LZ and DZ, ppm error in identification, manual interpretation discovery, segmentation discovery, or data-driven image fusion discovery.* Note that ppm error was determined from a tune mix doped IMS experiment*

Data Mining. Overall, 1,375 m/z features were detected at a S/N > 3 by IMS, including a variety of lipids with diverse patterns of localization to substructures of spleen that included red and white pulp. In addition to these constitutive features of splenic micro-anatomy, GCs form in the white pulp after lymphocyte activation generates T cell help after immunization. Mice were immunized to increase size and numbers of GCs as observed in all imaging modalities when comparing immunized to non-immunized controls (Figure 3.7). In F_{em} images, a difference in GC-localized GFP expression can be seen between samples with and without AID-GFP (Figure 3.7). AF detected in the DAPI and TRITC channels enhanced the identification of GCs in the FITC channel by distinguishing GCs from other portions of the white pulp highlighted by the AF. The IMS data were first analyzed using manual interpretation (Figure 1f). Two ions of interest were selected by virtue of their association with in-section AID-GFP, m/z 752.5591 and m/z 776.5596 (Figure 3.7a). A ratio-paired T-test applied to the ion intensity was performed to determine significance of correlation and anti-correlation throughout this work. Specifically, GCs were compared to non-GC regions. Because, AID-GFP does not distinguish the GC's sub-regions[27], IF of adjacent sections was employed to identify the LZ and DZ.

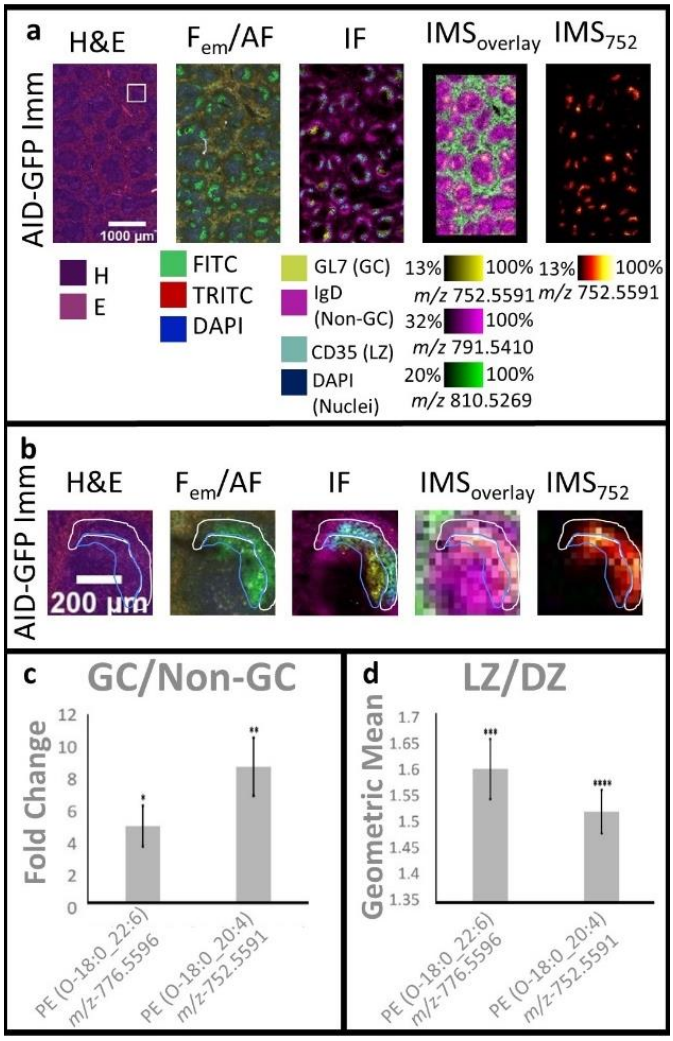

Figure 3.7. High accuracy registration of multimodal data*. a) Representative registered images highlighting the types of detection. Rectangular areas of immunized AID-GFP transgenic (AID-GFP Imm) mouse spleen are shown with each section, from left to right: Hematoxylin and eosin (H&E); fluorescence emission/autofluorescence (Fem /AF); immunofluorescence (IF) after staining with mAb; IMS with three ions [m/z 752.5591, m/z 791.5410, and m/z 810.5269] overlaid for context of white pulp and red pulp; and a single ion image showing m/z 752.5591 (IMS_{752}). Intensity scales from least to greatest total ion intensity and color legends are displayed below each set of images. A 1,000 µm scale bar is depicted in the H&E image. Fem was taken on the same section imaged by IMS. IF and H&E were then taken from serial sections to the IMS section.*

IF was used to identify micro-anatomic portions of lymphoid follicles, which included both indirect and direct staining of GL7, IgD, and CD35. b) Higher magnification images of a single representative GC (designated by a white box in 1a) are shown with the same sample order and modalities. GC LZ and DZ are demarcated by a yellow and blue outline respectively. c) The bar graph shows the ratio of ion intensities in GC to non-GC regions for the m/z features of 776.5596 and 752.5591 [identified by IMS MS/MS in Figure 3.11 as PE (O-18:0 22:6) and PE (O-18:0 20:4), respectively] (p= 0.0409, p=0.0099, n=3). d) The geometric mean of the ratio of LZ/DZ ion intensity of two lipids is 1.6 and 1.5 for PE (O-18:0 20:4) and PE (O-18:0 22:6) (p=0.007, n=65, p=<0.0001, n=65).

Data were further analyzed for significant differences in GC LZs and DZs [111] as identified in F_{em} and IF microscopy images. To obtain ion intensity for statistical analysis, we used QuPath and a custom R program to extract ion intensity values for all GC and non-GC regions identified through F_{em}. Sub-regions of GC, LZ and DZ identified through IF were annotated in QuPath[110] and compared. Pairs of GC LZs and DZs were identified based on shortest Euclidian distance (Figure 3.3).

Ions discovered through manual interpretation, m/z 752.5591 and m/z 776.5596 were mapped to the GC (~8-fold and ~5-fold enrichment; Figure 7b, c), and each of these lipid species was further enriched in the LZ compared to the DZ (~1.6-fold and ~1.5-fold enrichment within the GC; Figure 3.7b, d).

Spatially shrunken centroids segmentation circumvents the potential for cognitive bias introduced through manual interpretation by computationally determining ROIs [108] (Figure 1f). This approach generated a list of four ions that localize to GCs, m/z 752.5591, 776.5596, 883.5360, and 887.5609 (m/z 883.5360 p=0.0025, n=3; m/z 887.5609 p=0.0087, n=3)

[43,108](Table 3.3). Of these, the first two (m/z 752.5591 and 776.5596) matched the ions discovered by manual interpretation, and all localized to GCs, but not all localized to LZ or DZ (m/z 883.5360, p=0.12, n =108 and m/z 887.5609, p=0.070, n=106) (Figure 3.2, Figure 3.8q-r, Table 3.4).

Although segmentation enabled the identification of four ions of interest localizing to GCs (Figure 3.7a; Table 3.4), this approach is well suited only for determining ions that directly correlate to a specific tissue sub-region. Data-driven image fusion connects the spatial and informational content of two imaging modalities by constructing a cross-modality model using highly multivariate linear regression to enable predictive and data mining applications (Figure 3.8, Figure 3.9).[109] In previous work, data-driven image fusion has been used for image enhancement such as spatial sharpening, out-of-sample prediction, and image denoising.[109]

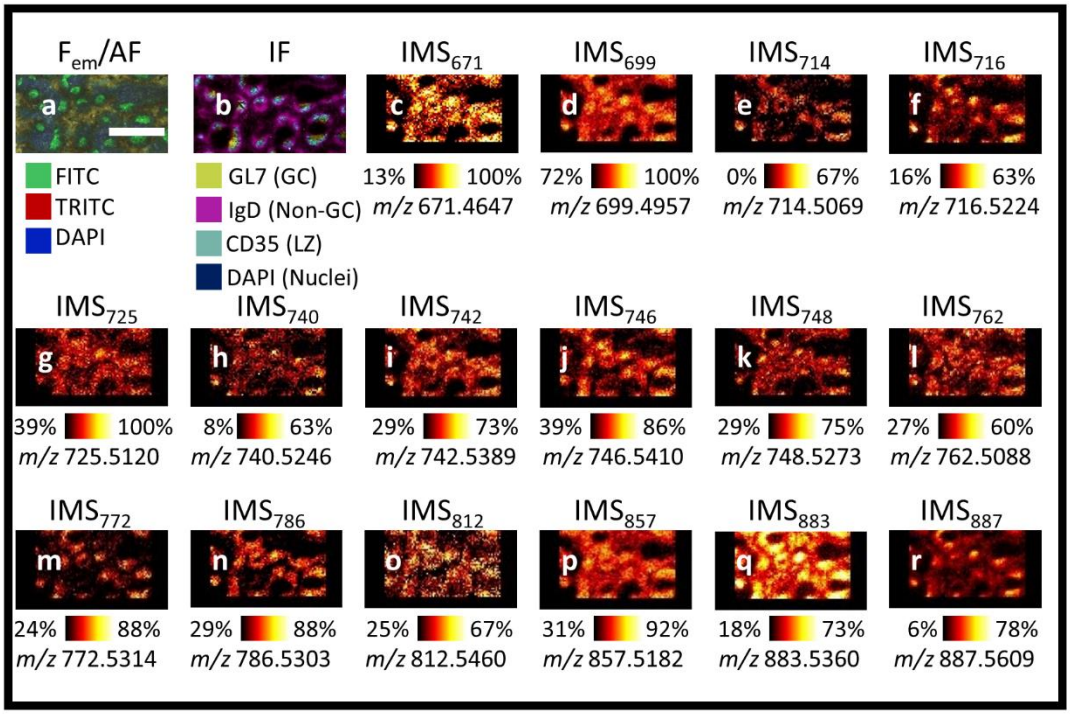

Figure 3.8. Ion images of GC ions discovered through a data-driven image fusion. *a) Magnified regions of Fem/AF and b) IF are shown to identify germinal centers. A scale bar indicating 1,000 µm is shown in the Fem/AF image. Shown in c) through r) magnified ion images of GC related species listed in Table 3.4.*

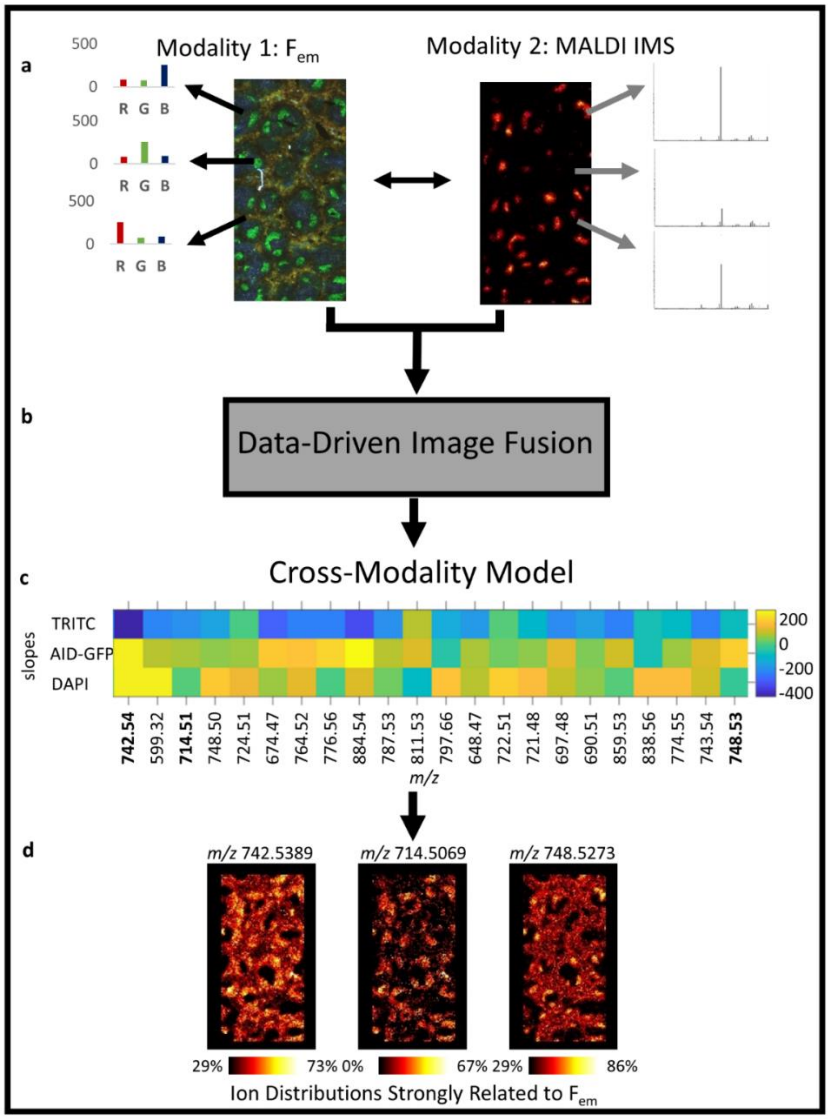

Figure 3.9. Application of an image fusion algorithm substantially increased the yield of GC correlated lipids. *a) Both modalities, F_{em} and IMS are separated into color variables for Fem and m/z variables for IMS data as shown in call-out graphs and mass spectra. b) Data-driven image fusion*[109] *using a multivariate linear regression model was performed. c) A cross modality model between IMS data and the red, green, and blue channels of Fem data. d) This model enables the correlation of IMS ions to the color channels of F_{em}. By mining the data for ions that show a high correlation to the green channel in Fem, ions correlated to GC identified by GFP were extracted.*

In this study, we introduce a new relationship discovery application of data-driven image fusion that does not pursue prediction but rather only executes the first model-building phase of the fusion framework. The second phase, prediction using the built model, is not needed for this discovery application, essentially side-stepping the usual considerations of uncertainty that come with prediction. Instead, we hypothesized that by building a model that ties IMS images to fluorescence emission, the multivariate linear models produced this way could be used directly to empirically uncover new correlative relationships between the two modalities. Building a cross-modal model, and instead of using it for prediction, opening it up to see what relationships it has learned, could potentially enable fluorophore-directed data mining. Accordingly, we tested the use of data-driven image fusion to provide a deeper understanding of all correlative relationships between IMS and fluorescence emission data in germinal centers.

Since we used multivariate linear models, the relationship between a fluorescent channel and an m/z "channel" are encoded by slope values. High relative slope values indicate a strong relationship between the two channels. Although prediction is not a part of this modeling effort, there is always discrepancy between the phenomenon modeled and the model itself. To capture this, we report only ions with acceptable reconstruction scores as described in Van de Plas et al.[109] and acknowledge that, since always some uncertainty remains, the findings should be independently cross-checked by evaluating the genuine ion distributions of the fusion-proposed ion species. The fusion-driven discovery process is simply meant as a rapid and automated means of filtering through a large set of ion species (e.g., in the thousands) and reducing it down to a more digestible panel of potentially correlating ion species (e.g., in the tens) that can be further investigated and validated

From the fusion of a high resolution (15 µm) IMS image and F_{em}, 16 GC-specific ions were revealed, of which four were those highlighted by segmentation-based analyses (Table 3.4). Integration of the image fusion algorithm into the workflow allowed identification of a far greater number of candidates for GC-associated ions along with species that were anti-correlated (e.g. m/z 687.5447 and m/z 788.5442, Figure 3.9-10; Table 3.5).

M/Z	RED CHANNEL	GREEN CHANNEL	BLUE CHANNEL
885.5506	-2910.1	1647.6	6863.1
886.5552	-1413	814.4	3347.6
883.5354	-587.4	565.8	257.8
857.519	-582.6	400.6	351.3
718.5403	-575.3	356.6	422.3
885.5377	-546	345.8	1313.9
884.5386	-345.4	321.7	142
673.482	-467.9	316.7	363.3
742.5399	-445.2	290.5	288.2
746.5143	-394.6	280	218.4
786.529	-507.4	279.4	140.8
699.4981	-457.5	277.2	295.9
810.5302	212.1	273.6	-91.5
887.5686	-579.2	252.9	419.7
647.4662	-406.1	246.1	255.4
776.5604	-237.7	244.7	22.1
861.5505	-357.8	244.6	100.5
716.5246	-457.9	243.8	198.7
748.5301	-69.7	236.6	-12.2
835.5335	-384.3	236.5	243.8
834.5304	-341	222.2	419.1
671.466	-292.4	222.1	86
752.5608	-277.4	219	12.2
747.5174	-398.2	211.3	240.2
887.5556	-350.4	209.4	883.1
858.5234	-323.4	207	199.8
764.5243	-229.8	203	155.8
723.4982	28.7	201.2	334.9
886.5406	-301.3	183.7	726.7
744.5561	-314.8	176.1	462.3
719.5433	-288.2	167.3	219.5

762.509	-362.2	167	319.6
772.529	-139.9	163.3	25.7
697.4823	-214.9	157.9	129.6
747.4978	-286.4	157.6	426.4
674.4851	-230.6	150.8	160.5
811.5335	112.8	149.9	-81.5
743.5426	-238.8	147.7	140.9
888.5696	-320.9	139.4	230.8
788.5245	-149.2	133.4	74.6
859.5346	-240	130.1	24.6
700.5013	-222.8	124.8	123.2
645.4505	-213.7	117.5	45.7
599.3213	-223.4	114.9	286.4
862.5535	-180.6	113.2	47.6
740.5244	-153	112.8	28
749.5317	-39.7	112.1	-1.2
717.5273	-197.6	109.8	59.5
787.5325	-202.5	109	47.9
714.5086	-196.2	102.5	26.4
738.5086	-244.3	98.5	222.2
765.528	-125.4	95.2	83.9
648.4696	-178.2	94.9	116.9
724.5011	17.2	92.4	167.3
774.5457	-79.2	91	193.7
745.5586	-169.9	87.2	239.5
695.467	-149.4	84.1	237.6
790.5405	-409.7	82.7	768.6
869.555	-166.6	82	66.4
748.5012	-153.9	80.5	214.8
672.4697	-116.9	78	35.8
768.5564	-308.5	76.3	336.4
778.5756	-85.7	75.8	56.1
721.4815	-89.2	74.6	197.9
773.533	-92.2	74.4	44.6
690.5085	-167.7	68.4	75.6
770.5707	-158	67.7	274.5
552.2735	-209	63.4	202.6
725.5132	-242.9	63.2	264.1
763.5123	-181.3	63	167.6
750.5453	59.5	62.3	202.2
836.536	-115.2	61.1	65.6
719.4664	-66	57.5	39.5
722.5143	22.7	56.8	229.4
698.4847	-69.2	53.7	33.6
888.5582	-88.3	52.1	178

739.5118	-114.4	51.7	80.5
831.5657	-83.3	44	57.5
581.3104	-67.1	40.4	144.7
812.546	-192.3	37.1	157.7
775.5486	-29.7	33.5	83
696.4697	-54	32.7	78.8
751.5476	32.9	31.6	103.8
791.5426	-230	30.1	429.5
661.4815	-54.7	28.2	36.6
769.5586	-119.7	25.5	133.4
600.3237	-65.1	24.6	88.8
723.5166	12.9	20.9	99.7
722.4852	-20	16.3	58.3
771.5744	-46.8	15.9	91.1
675.4969	-45.8	12.4	69.7
726.5162	-76.7	10.2	90.8
528.2739	-97.8	7.1	208.8
792.5564	-210.4	3.5	459.6
767.5435	-411.3	3.3	937.1
610.2734	-40.4	-1.9	34.3
609.265	-63	-3.6	68.7
749.5132	-116.9	-4.2	312.1
766.5296	-166.7	-6.6	410.9
836.5461	-81.4	-7.4	161.7
750.5162	-32.8	-11.3	113.1
606.2417	-22.6	-11.7	27.9
766.5405	-884.1	-13	2071.8
793.5585	-94.5	-14.1	228.6
798.6572	-49.2	-16.8	80.6
726.5816	-52.5	-22.2	97.8
688.5479	-19.1	-27	129.9
797.6553	-124.4	-29.4	209.2
608.2577	-52.3	-30.7	70.6
616.4718	-32.2	-52.4	233.7
687.5455	-80.7	-57.5	405.3
838.5615	-56.5	-58.1	193.1
795.5742	-56.7	-68.5	338.3
794.5709	-133.2	-78.2	638.4
751.529	-69.1	-78.6	265.7
702.5164	-48.7	-86.8	261.2
789.5486	-66.9	-111.7	330.5
701.5135	-145.9	-151.8	611.8
788.545	-182.4	-202.6	733.6

Table 3.5. Image Fusion Results. *Because image fusion is based on a linear regression model, the relation of ions to a color channel can be drawn from the slope value of the correlation function. Depicted from left to right are the m/z value, the red channel slope value, the green channel slope value, and the blue channel slope value are shown. The higher positive number the greater the correlation and vice versa.*

GC areas annotated in F_{em} images served as a means for identifying GC (p=0.0099, n=3, slope= 219.0 for green channel) and non-GC regions for statistical analysis (p=0.04, n=3, slope= -57.5 for green channel and p=0.04, n=3, slope = -202.6 for green channel respectively) (Figure 3.9-10, Table 3.5). The ion m/z 752.5591 is shown for contrast with non-GC ions m/z 687.5447 and m/z 788.5442 (Figure 3.10). In contrast to manual interpretation and segmentation, ten additional ions revealed through data-driven image fusion were higher in GCs and exhibited a pattern of LZ >DZ (Table 3.4; Figure 3.8-9).

Molecular Identification

Due to the large number of potential isomers at these m/z values, mass accuracy alone was not enough to identify lipid species. For example, the phosphatidylethanolamine ether species PE(O-40:6) and PE(O-38:4) are isomers of the phosphatidylethanolamine plasmalogen species PE(P-40:5) and PE(P-38:3), respectively. Liquid chromatography-tandem mass spectrometry (LC-MS/MS) determined the presence of both ether and plasmalogen species for these ions of interest in total lipid extracts from whole spleen tissue (Figure 3.11a). Thus, a spatial component was needed to confirm the identity of the ions that correlate to F_{em} signals. IMS-MS/MS was performed with sectioned spleens of immunized transgenic AID-GFP mice (Appendix B). The MS/MS-based imaging experiment determined these ions to be ether lipids PE(O-18:0_20:4) (Figure 3.11b-d) and PE(O-18:0_22:6) and not the isomeric plasmalogens

(Figure 3.11e-f). In addition, the co-localization of the specific fragment ions from these ether lipids with F_{em} signals reveals that these species were enriched in splenic GCs (Appendix B).

In addition to plasmalogen and ether species, image fusion enabled the identification of a variety of phosphatidylethanolamine (PE), phosphatidic acid (PA), glycerophosphoserine (PS), and glycerophosphoinositol (PI) lipids that were enriched in GCs, with some observed at higher intensity in GC LZ. Fatty acid tails of 16:0 and 18:0 were most common. We observed many repeats of fatty acid tails 20:3, 20:4, and 22:6. In GC, five out of eight lipids had unsaturated fatty acid tails, whereas in GC LZs, all eight had at least one unsaturated fatty acid tail. Two ions, *m/z* 687.5447, PE-Cer(d36:1) (phosphatidylethanolamine ceramide), and *m/z* 788.5442, PS(18:1_18:0), were identified as anti-correlating with GCs (Figure 3.10). Overall, this unique combination of IMS with biologically driven microscopy modalities, advanced image registration, multimodal data mining, and spatially driven identification provides a pipeline for elucidating molecular drivers of biological processes. As a test of the technology, this process revealed an enrichment of ether and plasmalogen lipid species in GCs, a metabolically stressed environment central to the qualities of antibody responses and humoral memory.

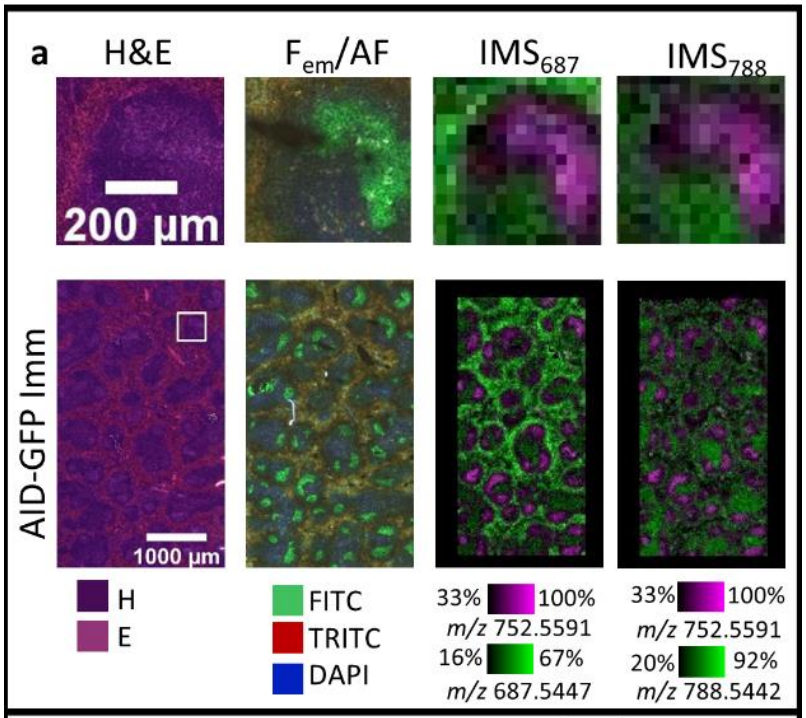

b

m/z	Lipid ID	DB Matches	P value non-GC vs GC	ppm error
687.5447	PE-Cer(d36:1)*	-	0.04	1.7
788.5442	PS(18:1_18:0)	7	0.04	0.72

Figure 3.10. Identification of anti-correlating germinal center (non-GC) ions by image fusion. *a) Shown are representative registered images highlighting the localization of anti-correlating GC ions. From left to right, the following image types are pictured: H&E with scale bar, F_{em}, IF, IMS showing an overlay of non-GC ion m/z 687.5447 and GC ion m/z 752.5591, and IMS showing an overlay of non-GC ion m/z 788.5442. LZ and DZ, as identified by IF, are outlined in yellow and blue respectively. b) From left to right, the m/z value, identification, matches to the LIPIDMAPS database in the IMS MS/MS spectrum, statistical significance, and ppm error in mass identification are listed. These two ions were identified as PE-Cer (d36:1) by accurate mass and PS(18:1 18:0) through IMS MS/MS, respectively. A complete listing of results from image fusion is in Table 3.5; further information is found in Figure 3.8-9).*

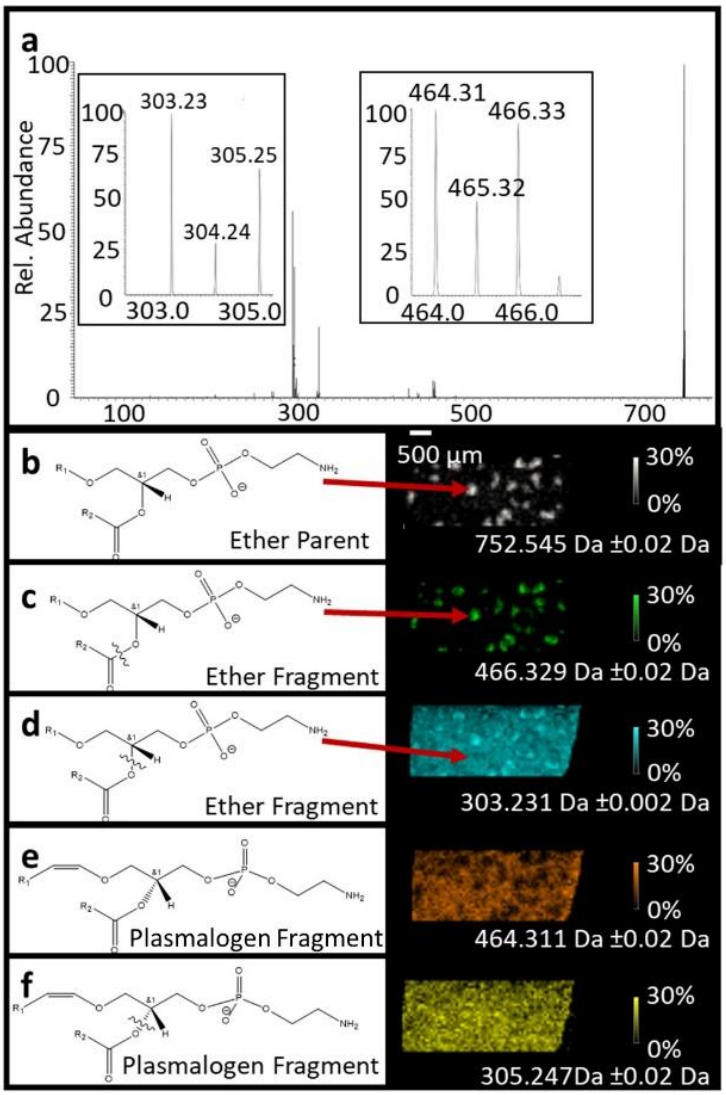

Figure 3.11. Identification of species localizing to germinal centers as ether linked lipids. *a) LC-MS/MS fragmentation spectra of total splenocytes show common fragments for both plasmalogen and ether lipids (enlarged) from a parent mass of m/z 752.545. b) Shown to the left is the chemical structure of the parent ether ion and to the right the corresponding ion image. c,d) The correlating ether fragments are depicted with the chemical structure on the left and ion image on the right. e,f,g,) Similarly, plasmalogen parent ion structure and fragments are shown with chemical structure on the left and corresponding ion images on the right.*

Implications

This multimodal imaging process reported here combines high spatial resolution IMS with a transgenic fluorophore to identify micro-anatomical regions of biological interest. Our approach incorporates high accuracy registration and various data mining tools, including data-driven image fusion, to fully integrate multiple imaging modalities collected from a single tissue section and across adjacent sections, enabling the discovery of molecular drivers of immune response. Unambiguous identification of GCs and the assessment of lipid abundances in light and dark zones was made possible by combining F_{em} of the transgenic tracking allele with traditional microscopy approaches (i.e., stained and IF microscopy). While data-driven image fusion has previously been used for spatial applications in image sharpening and out-of-sample prediction, the evidence presented here indicates that it can also be applied to mine high dimensional data to find correlations between modalities by interpreting the linear models constructed during the fusion process. When compared to conventional approaches, the yield of structure-associated molecules was enhanced four- to five-fold, as 16 GC-associated lipid species were determined.

We identified three key processes in multimodal imaging as (1) registration, (2) data mining, and (3) molecular identification. Due to the small size of a single cells within a tissue, histological depth differences between serial sections are becoming larger challenges as the spatial resolution of IMS increases.[47,112,113] In addition to histological depth differences, accurate data alignment correlating H&E or IF to IMS becomes central as spatial resolution increases and regions of interest approach single cells. Importantly, the technologies presented here should be applicable to fusion of IMS, fluorescence, and spatial transcriptomic or protein data.[114,115]

The unexpected finding that the prevalence of a series of ether lipid species is higher in GCs frames new hypotheses, i.e., that molecular programing of GC lymphocytes is tied to increased ether lipid synthesis and that these species are functionally important in humoral immunity. A higher abundance of ether lipids in the spleen and white blood cells has been reported, but the exact role of these ether lipids remains uninvestigated.[116] Ether lipid synthesis begins in the peroxisome and is completed in the ER.[117] Disruption of this pathway in peroxisome biogenesis in disorders, such as Zellweger spectrum (PBD-ZSD) or by gene-targeting, generates decreased ether lipid levels.[30,117,118] In this light, it was striking that image analysis of IMS uncovered GC PE lipids with the same tail lengths as their ether and plasmalogen counterparts. Most notably, PE(16:0_22:6) localized to GCs as did its ether lipid counterpart PE(O-16:0_22:6) while its plasmalogen derivative, PE(P-16:0_22:6), localized not only to GCs but within them to their LZ (Figure 3.8o-q, Table 3.4-5). This enrichment along a pathway suggests that GCs have enhanced peroxisomal activity, resulting in increased abundance of PE-ether lipids.

The peroxisome also generates reactive oxygen species (ROS).[119] Plasmalogen ether lipids scavenge reactive oxygen species[120]. This capability has not been documented for non-plasmalogen ether lipids, but the structural similarity suggests a connection in synthesis pathways and roles.[121] Starting 3.5 d after immunization, GCs form in the follicles of secondary lymphoid organs and are sites of B-cell proliferation, differentiation, and selection that are central to promoting antibody affinity increases as well as vaccine efficacy and humoral immunity.[27] Substantial AID-mediated mutational[50] and nutrient[27,122] stresses appear to be present in GCs. This micro-anatomic structure consists of LZs and DZs in which the native oxygen levels vary, such that hypoxia is present in an LZ>DZ pattern.[27] While there is strong

evidence of connections between hypoxia and inflammation,[123,124] much remains unknown as to the effect of this hypoxic microenvironment on lipid synthesis within these regions.[11] The role of ether lipids in the adaptive immune microenvironment has not yet been explored, and thus, management of ROS and their levels are crucial for lymphocyte physiology.[125] This point, in conjunction with known metabolic stresses in GC[27,50,126] and influences of hypoxia on ROS generation,[27] suggests that a model in which higher plasmalogen and ether lipid abundance in GC reflects a physiological role in which ether lipid production indicates the need to maintain optimal ROS levels.[119]

CONCLUSION

We demonstrated a multimodal molecular imaging workflow that integrates two key methodological advances documented here: (1) the use of engineered alleles that track gene expression by linking a fluorophore to the normal gene product, and (2) application of data-driven image fusion for data mining. We used this workflow to identify 16 GC-specific ions that led to the formation of a new hypothesis related to ether lipids in GCs.

This approach should be widely applicable to a variety of experiments in a broad range of biological systems. Gene-editing technologies such as CRISPR-Cas9 will further expand an already abundant supply of transgenes that mark specific biological pathways and cell types. Moreover, this new application of image fusion as a means of elucidating ions of interest co-localizing with a specific fluorophore will enable unique applications of data mining, including applications in settings where unambiguous marking of a region of interest by other modalities exists.

CHAPTER IV

MULTIMODAL IMAGING TO ANALYZE THE IMPACT OF AN ETHER SYNTHESIS DEFECT ON LIPID DISTRIBUTION IN SPLEEN

Acknowledgements

This work was supported by NSF DGE-1445197 (M.A.J. and R.M.C.), NIH grants P41 GM103391 (R.M.C.), U45-DK120058 (R.M.C.), R01 AI113292 and R01 HL106812 (M.R.B.). Dr. Sung Hoon Cho and Prof. Mark R. Boothby are gratefully acknowledged for providing the spleen tissues, immunology-based results, and useful discussions. Prof. Clay Semenkovich is gratefully acknowledged for providing the cKO PexRAP mouse line.

Overview

Multimodal imaging allows for the identification of regions with specific biological interest and correlation of these regions to their molecular makeup. In a previous study, we discovered 16 germinal-center-specific ions which led to the hypothesis that molecular programing of GC lymphocytes is tied to increased ether lipid synthesis and that these species are functionally important in humoral immunity. To test this hypothesis, we applied a tamoxifen-induced genetic knockout (KO) of PexRAP, a peroxisomal enzyme that executes a late step in ether lipid synthesis. PexRAP has been used to study the reprograming of lipogenesis in adipose tissue in diet-induced obesity and has been shown to decrease ether lipids, but has not been applied to study an adaptive immune response.[127] To do investigate the effect of a reduction of ether lipids on germinal center function and formation, we targeted our analyses to focus on the 16 germinal-center-specific ions identified by the multimodal approach we developed.

INTRODUCTION

Immunity is the response to pathogens or mutated cells within the body. There are two main types of immunity: innate and adaptive immunity. Germinal centers, the focus of this work, are part of the specified adaptive immune response which consists primarily of B and T lymphocytes and antibodies.[18] B cell proliferation and differentiation occurs within germinal centers of lymphoid organs and are integral to the adaptive immune response. These functions occur in subregions of germinal centers called light and dark zones where native oxygen levels vary.[27] Specifically, germinal center light zones are hypoxic which can produce a variety of downstream effects such as decreases in B cell proliferation that, in turn, cause stricter survival signal thresholds. For instance, the IgG2c isotype, which functions in antimicrobial responses, is decreased in patients with hypoxemic lung disease, which increases their chances for infection.[27,128] However, the connection between hypoxia and the molecular microenvironments has not been fully studied, and identifying the spatial distributions of biomolecules in tissue is crucial for understanding integrated function. Imaging mass spectrometry (IMS) allows simultaneous visualization of thousands of biosynthetic products such as lipids but cannot natively identify specific cell-types or functional states to correlate with molecular localization. Therefore, to identify germinal centers and study their lipid microenvironment, we have developed a multimodal approach consisting of immunofluorescence, MALDI IMS, and histological staining.[84] Through this method, we found 16 germinal-center-specific ions, of which 11 localized specifically to the GC LZ in higher ion intensities.[84] Of these lipids, 5 were phosphatidyl ethanolamine ether or plasmalogen lipids, which led to the hypothesis that molecular programing of GC lymphocytes is tied to increased ether lipid synthesis and that these species are functionally important in humoral immunity.

Ether lipids make up about 20% of all phospholipids in mammals.[117] However, they differ from conventional glycerophospholipids by the ether bond in the *sn-1* position. Plasmalogens are the most common form of ether lipids and are denoted as a subclass due to the *cis* double bond directly adjacent to the *sn-1* ether linkage. (**Figure 4.1**)

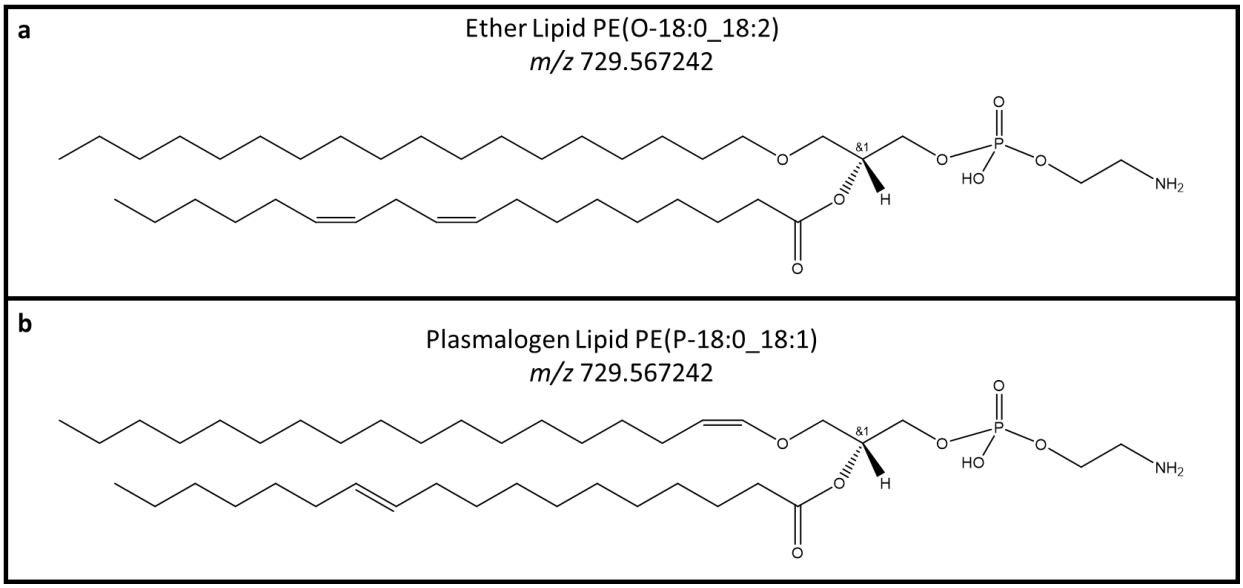

Figure 4.1. Ether and plasmalogen lipid structure. *A figure depicting the structure of the isomeric species a) ether lipid, PE(O-18:0_18:2), and b) the plasmalogen lipid PE(P-18:0_18:1).*

Ether lipid synthesis begins with fatty acids synthesis followed by activation through fatty acyl-CoA synthetase and entrance into the peroxisome. Once inside the peroxisome, a long chain Acyl-CoA acylates DHAP at the sn-1 position. Next, alkylglycerone phosphate synthase catalyzes the formation of an ether bond in the sn-1 position by replacing the acyl chain with an alkyl group. The alkyl-DHAP is reduced to an ether lipid precursor 1-O-alkyl glycerol-3-phosphate, and further adjustments of the head group take place in the ER. In 1974, the protein that reduced alkyl-DHAP in the final step of ether synthesis in the peroxisome was isolated and later renamed PexRAP (peroxisomal reductase activating PPAR gamma). Previous attempts to knock out ether lipid synthesis caused a complete loss of ether lipids, causing poor mortality outcomes, but knockout of this protein in mice led to a 50-80% decrease in ether lipid levels allowing for longer life expectancy. [127]

By decreasing the amount of ether lipids, we seek to determine how germinal center lipids the effect on the germinal center immune response and how lipids are affected. Ether lipids have been shown to have a variety of roles including structural, trafficking, signaling, and differentiation. In addition, ether lipids have been linked to genetic peroxisomal disorders, neurological disorders, cancer, and metabolic disorders. [117]

Beyond ether lipids, lipids in general are integral to understanding adaptive immunity and are targets for treatment of autoimmune diseases. For example, patients with systemic lupus erythematosus show abnormal lipid profiles and a variety of lipid altering drugs have been developed for treatment.[13,129] Lipids have also been linked to antibody responses. For example, anti- lipid IgG have been linked to tuberculosis, autism spectrum disorders, malaria, and a variety of autoimmune disorders. [130–133] Although a connection between lipids and autoimmunity

has been formed, the role of ether lipids in adaptive immunity and specifically in germinal center formation and function has not yet been explored.

In the previous chapter, our finding that some ether lipids showed a higher ion intensity in germinal centers led us to test the hypothesis that molecular programing of GC lymphocytes is tied to increased ether lipid synthesis and that these species are functionally important in humoral immunity. To analyze this hypothesis, we used a tamoxifen-induced genetic knock down (cKO) of PexRAP, the peroxisomal enzyme that executes a late step in the ether lipid synthesis pathway, to reduce the levels of ether lipids. Although this ether lipid cKO had been previously used to study the effect of inhibition of adipose tissue lipogenesis in diet-induced obesity, it had not yet been used to investigate the role of ether lipids in germinal center dynamics.

METHODS

Materials

MALDI matrix 1,5-diaminonapthalene (DAN) was purchased from Sigma-Aldrich Chemical Co. (St. Louis, MO, USA). Sheep red blood cells (SRBC), ammonium formate, carboxymethyl cellulose sodium salt, isopropyl alcohol, mass spectrometry grade water, chloroform, and acetonitrile were purchased from Fisher Scientific (Pittsburg, PA, USA); streptavidin-Alexa647 antibody (Ab) and chemically conjugated monoclonal Ab (GL7-FITC, αIgD-PE and αCD35-biotin) were purchased from BD Biosciences (San Jose, CA).

Tissue Preparation

All mice were housed in ventilated micro-isolators under Specified-Pathogen-Free conditions in a Vanderbilt mouse facility and used in accordance with protocols approved by the Institutional Animal Care & Use Committee. Mouse spleens were obtained from non-perfused mice in a mixture of male and female (M=3, F=2) C57BL/6 control mice aged 6 to 8 weeks. PexRAPf/f ROSA26-ERT2-Cre mice obtained courtesy of Clay Semoncovich[29] were intraperitoneally injected with tamoxifen (1mg/mouse) 3 times every

other day and immunized with SRBC at day five after the last tamoxifen injection. All mice were harvested seven days postimmunization. Each spleen was sectioned into halves for MALDI IMS and flow cytometry. MALDI IMS samples were frozen on dry ice and stored at -80 °C until further analysis.

Matrix Application:

Recrystallized DAN matrix was prepared at a concentration of 10 mg/mL in 90/10 acetonitrile/H_2O and deposited using a matrix sprayer (TM-Sprayer, HTX Technologies, Carrboro, NC, USA). The spray settings for the TM-Sprayer were as follows: solvent flow rate of 0.15 mL/min, nozzle speed of1200 mm/min, nozzle temperature of 85˚C, track spacing of 1.5 mm, 8 passes with 90 rotation on every other pass. Nitrogen was used as a flow gas and was set to 10 PSI.

IMS Analysis

High mass resolution data was acquired with a 15T Bruker MALDI FTICR SolariX mass spectrometer (Bruker Daltonics, Billerica, MA). The instrument is equipped with a Smartbeam II 2kHz Nd:YAG (355nm) laser and a Paracel ICR cell. All data was collected in negative ion mode from *m/z* 200-2000 with a raster step of 50 µm on one half of the sample. The data size was 1 MB per spectrum. Each pixel consisted of 500 laser shots with the small setting of the laser at a frequency of 2000 Hz. The laser power was adjusted to best fit each sample from 50-70%. A resolution of 261,000 was achieved at *m/z* 400. Internal calibration was performed using internal lipids in both positive and negative ion modes. Imaging experiments were performed on four PexRAP cKO and five wildtype samples. After data was obtained, spectra were root mean squared (RMS) normalized and analyzed.

IF and H&E Analysis

IF was performed on one serial section, and H&E staining was performed on a second serial section following a previous protocol.[84] In brief, frozen tissue sections for IF underwent washing, fixation, and blocking buffer washes followed by application of primary antibody [α-

GL7-FITC (1:50), α-IgD-PE (1:200), and α-CD35-biotin (1:200)]. Samples were further washed and incubated with streptavidin-Alexa 647 (1:200) in blocking buffer. Samples were then washed and mounted with Prolong Diamond anti-fade reagent (thermo Fisher, Waltham, MA) and scans were collected using EGFP, DAPI, and DsRed filters at 10x on a Zeiss AxioScan Z_1 slide scanner (Carl Zeiss Microscopy GmbH, Oberkochen, Germany).

Data Processing

Data was analyzed using SCiLS (2017a, version 5.00.9510, Bruker Daltonics, Billerica, MA). Previous work identified 16 germinal-center-specific ions which were the focus of this work. QuPath was used to identify germinal centers and follicles to extract size, number, and area.

RESULTS AND DISCUSSION

Overview

Immunized mice with a cKO of PexRAP were compared to WT mice. Mice were injected with tamoxifen to induce the deletion of PexRAP resulting in the reduction of ether lipids, and mice were immunized to induce an adaptive immune response. To analyze the effects of this cKO, a multimodal imaging approach incorporating MALDI IMS, IF, and H&E was used to enable correlation of biological context. In addition, further immunological approaches were probed with flow cytometry. To confirm the cKO of PexRAP, western blot and real time PCR were used. MALDI IMS was analyzed using ROC analysis, unpaired T-testing, and image comparison to investigate the effect on the 16 germinal center ions previously identified.[84] IF marking splenic follicles, germinal light and dark zones. IF data were analyzed using QuPath to extract the number and areas of these regions. H&E stains were used to further used to analyze basic structure and confirm typical morphology. Herein, we present the initial findings of the effect of a reduction in

ether lipids on germinal center size, number, molecular composition, and specified immune response.

IF analysis

An initial phenotype of reduced size and number of GCs in cKO PexRAP mouse spleen was observed in IF. We identified the germinal center follicles in pink, germinal centers in yellow, and germinal center light zones in blue. The overlaying image allows for whole germinal center identification of as well as light and dark zones and follicles (Figure 2). As shown in Figure 2, GCs are 1.5 times more numerous and 1.6 larger times ($p=0.02$, $p=0.05$) in WT samples compared to cKO PexRAP samples. However, the number of follicles is not significantly different ($p=0.1$), indicating that the ability to activate and adaptive immune response is not follicular in nature. There was approximately one germinal center every 510 ± 170 mm^2 and the average area of a germinal center in cKO PexRAP samples was 17 ± 6.3 mm^2. Conversely in WT tissues, there was approximately one germinal center every 320 ± 47 mm^2 of tissue with an average germinal center area of 28 ± 7.2 mm^2. With a significant decrease in germinal center size and number, these results indicate a disruption of the germinal center response. Not only can this difference be seen numerically, but it can also be seen visually in Figure 2d.

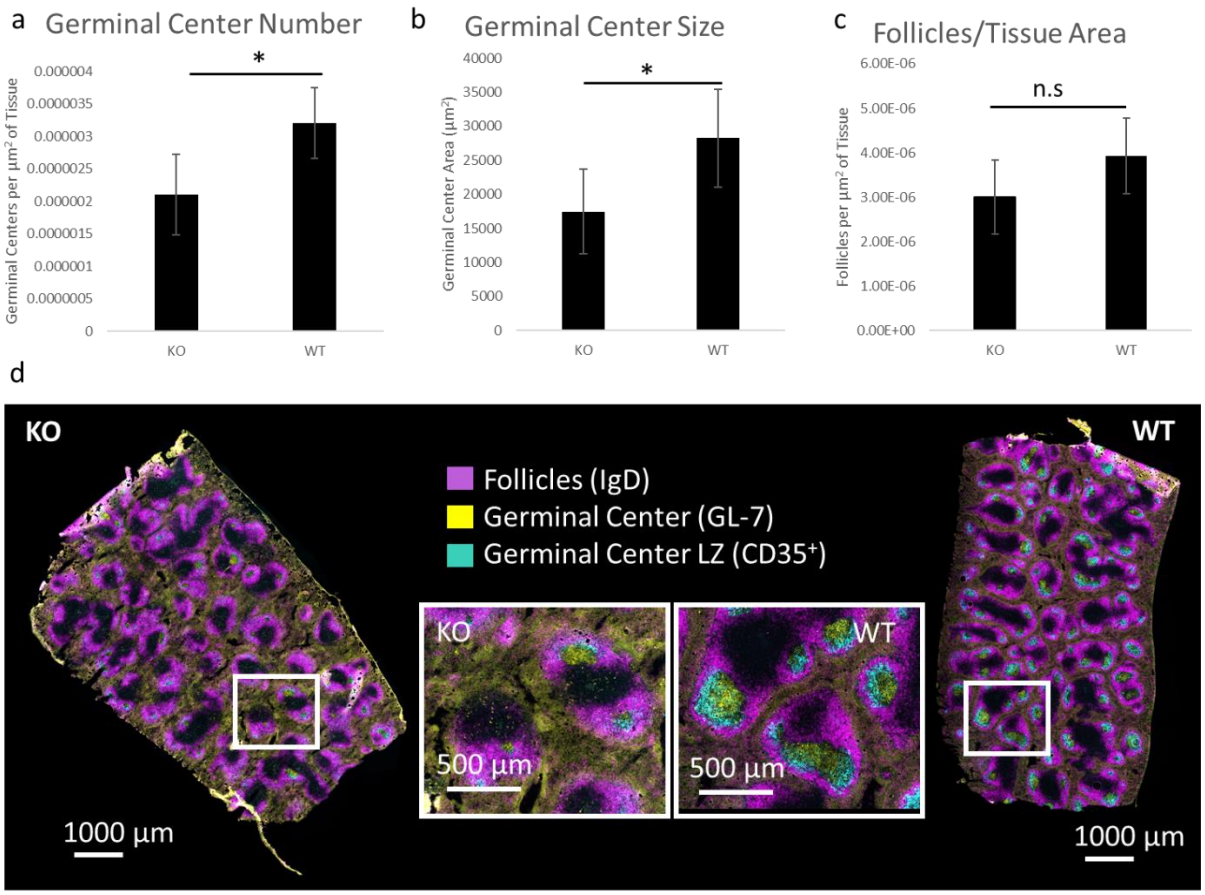

Figure 4.2. Germinal Centers are decreased in size and number. *Bar graphs showing a) decreased germinal center number (p=0.02), b) decreased germinal center size (p=0.05), and c) no significant change in the number of follicles (p=0.1). d) Examples of IF of the whole sample, and a magnified area outlined in white (scale bar 500 µm) of PexRAP cKO (KO) and wild type (WT).*

MALDI IMS Analysis

The disruption of the germinal center response is also reflected in MALDI IMS. Germinal center plasmalogens showed an average 49±1.6% decrease in ion intensity, and ether lipids showed an average 57±10% decrease in ion intensity in splenic cKO PexRAP samples compared to WT.

This indicates that this model is similar to literature in which ether lipids showed a 50-80% decrease in cKO PexRAP samples. All germinal center ether and plasmalogen lipids have a ROC value greater than 0.8 and a p value less than 0.05 indicating a sensitive, specific, and significant change in ion intensity between cKO PexRAP and WT samples. (Table 4.1) In fact, the localization of these ions reflects the size and number reduction shown in IF of cKO PexRAP sample germinal centers (Table 4.1). For example, PE(O-18:0_22:6) had an ROC area under the curve (AUC) of 0.82. WT samples had an average intensity of 90,000±30,000 and cKO PexRAP samples had an average intensity of 34000±11000 ($p=0.004$).

Although only one other germinal center lipid, PE(18:1_18:2), shows a significant change, the ROC value of 0.21 indicates a shift opposite to the shift seen in the ether and plasmalogen lipids (Table 4.1). For example, an average ion intensity of 702022±152055 a.u. was detected for WT samples compared to an average ion intensity of 1222251±367287 a.u. for KO samples ($p=0.02$). When looking at a spatial representation of the data, which is seen in the MALDI IMS ion images, we find that this lipid has a shift in localization. In the WT sample, the lipid localizes to germinal centers, where in the cKO PexRAP sample, the lipid localizes to red pulp regions in addition to germinal center regions (Figure 4.4).

LIPID	ROC AUC VALUE	P VALUE
PA(18:1_16:1)/PA(18:1_18:1)/PA(18:0_18:2)	0.45	0.3
PA(20:2_16:0)	0.42	0.6
PE(18:2 16:0)	0.33	0.09
PE(18:0_16:1)	0.35	0.3
PA(20:3_18:0)	0.49	0.6
PE(18:1_18:2)	0.21	0.02
PE(18:0_18:2)	0.27	0.4
PE(P-16:0_22:6)	**0.83**	**0.001**
PE(O-16:0_22:6)	**0.82**	**0.01**
PE(O-18:0_20:4)	**0.80**	**0.004**
PE(16:0_22:6)	0.49	0.5
PE(P-18:1_22:6)	**0.81**	**0.03**
PE(O-18:0_22:6)	**0.82**	**0.01**
PS(18:0_18:2)	0.56	0.9
PS(18:0_20:3)	0.59	0.9
PI(16:0_20:4)	0.81	0.3
PI(18:1_20:4)	0.37	0.2
PI(18:0_20:3)	0.50	0.4

Table 4.1. GC localizing lipids in WT and PexRAP cKO. *A table showing the lipid identity, ROC AUC value and p value for a t-test comparison of ion intensity between WT and KO samples.*

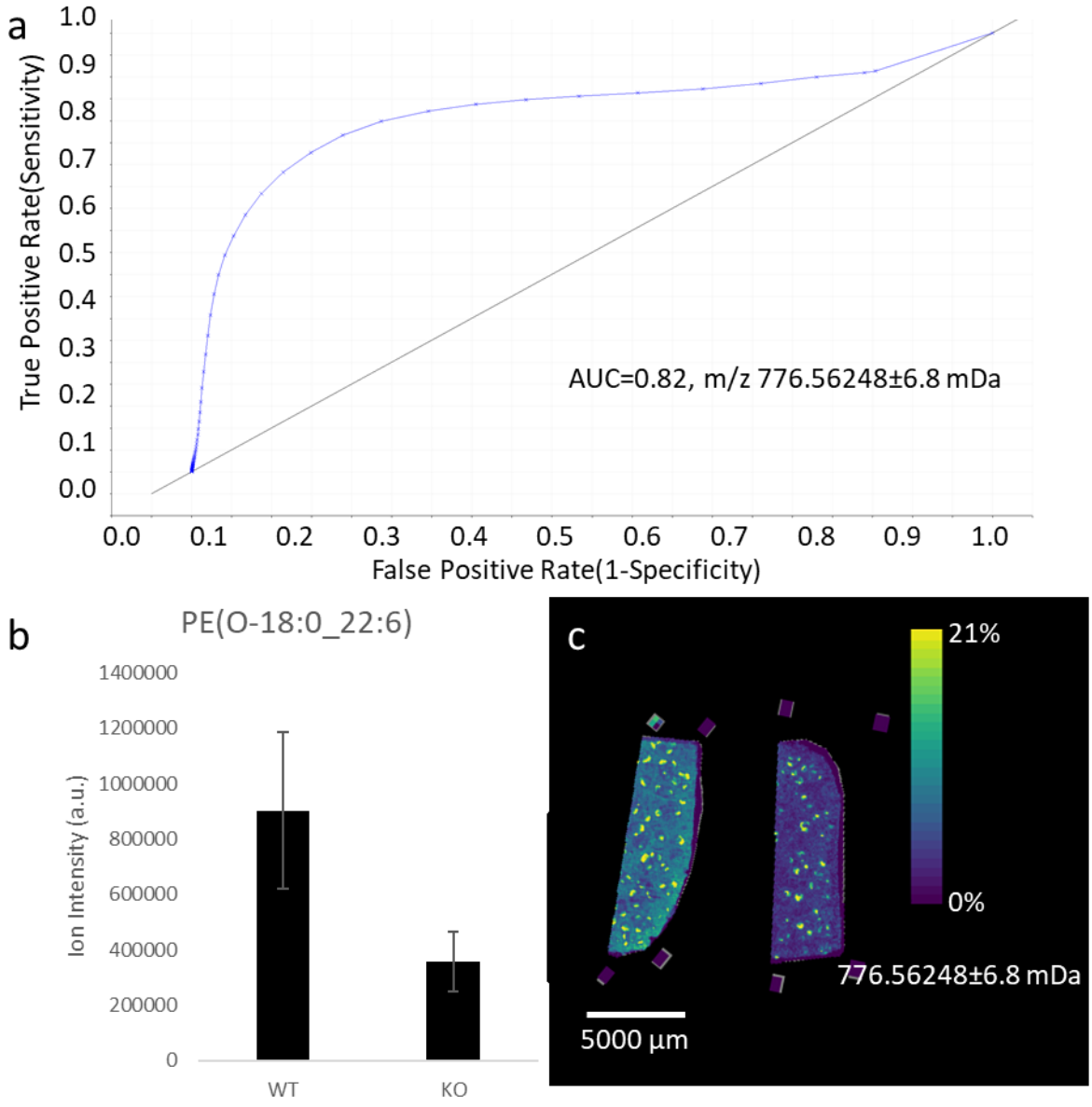

Figure 4.3. WT ether lipids are significantly different than KO ether lipids. *a) An ROC plot of sensitivity on the y axis and 1-specificity on the x axis shows an ROC AUC value of 0.82 for PE(O-18:0_22:6). b) A bar graph showing the average ion intensity (a.u.) for WT tissues(n=5) compared to KO (n=4). c) An ion image depicting the localization of PE(O-18:0_22:6) in WT compared to KO tissues.*

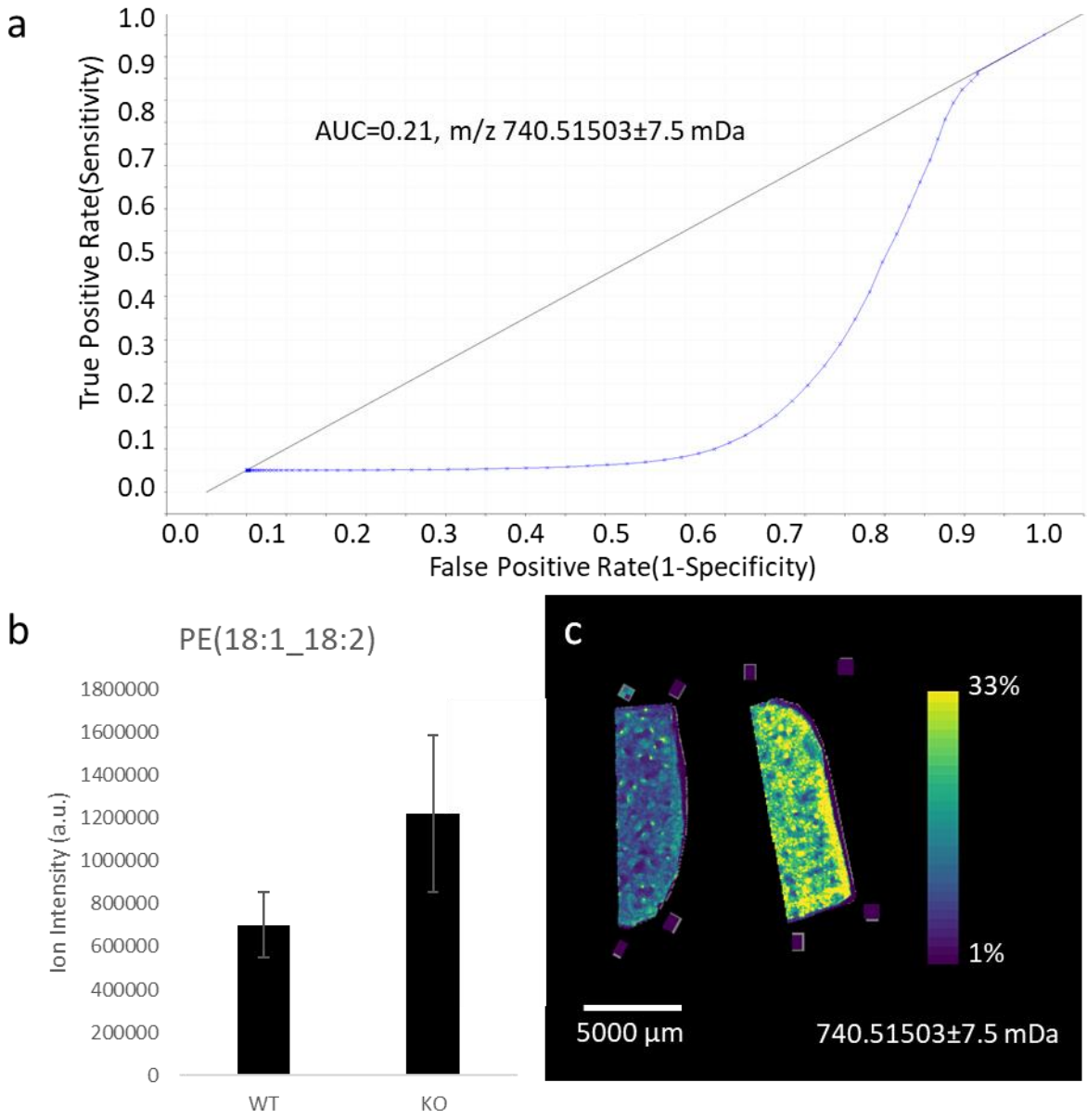

Figure 4.4. WT ether lipids are significantly different than KO ether lipids*. a) An ROC plot of sensitivity on the y axis and 1-specificity on the x axis shows an ROC AUC value of 0.21 for PE(18:1_18:2). b) A bar graph showing the average ion intensity (a.u.) for WT tissues(n=5) compared to KO (n=4) (p=0.02). c) An ion image depicting the localization of PE(18:1_18:2) in WT compared to KO tissues.*

Role of Ether Lipids in Germinal Center Structure and Function

Ether lipid synthesis begins when fatty acids are activated to fatty acyl-CoAs in the peroxisome and involves a key step in which acyl/alkyl DHAP is reduced into the ether lipid precursor 1-*O*-alkyl glycerol-3-phosphate or the diacyl phospholipid precursor lysophosphatidic acid[117]. Within this pathway, ether, plasmalogen, and lysolipids are formed or consumed. PexRAP is peroxisomal reductase responsible for acyl/alkyl-DHAP reduction generating the ether lipid precursor 1-*O*-alkyl glycerol-3-phosphate[117].

By disrupting PexRAP in this manner causes a typical reduction of 50-80% of ether lipids. We found that germinal center size and number were significantly decreased indicating a reduction in the B cell mediated humoral immune response. This change was reflected in the localization of germinal center ether and plasmalogen lipids in MALDI IMS ion images. However, not all germinal center lipids were ether lipids.

Non-ether germinal center lipids showed a different localization than ether lipids in cKO PexRAP samples. It is hypothesized that through the disruption of PexRAP, the precursors to ether lipid synthesis are also decreased and re-introduced into circulation as indicated by the migration of PE(18:0_18:2). This PE could act as the precursor to a lyso PE lipid needed for the formation of both PE(O-18:0_20:4) and PE(O-18:0_22:6). Through the reintroduction of these precursors into circulation, it is hypothesized that this difference in localization is a secondary effect of the inability to utilize these lipids for germinal center ether lipid formation further compounding the phenotype of reduced size and number of germinal centers.

In a collaboration with Prof. Mark Boothby's Lab, we discovered that beyond lipid investigations, immunological function was also affected. A significant decrease in SRBC-specific IgA was observed with an average fold change of four in an in vivo SRBC-immunization model.

This phenotypic change resulting from the disruption of PexRAP is hypothesized to result from one or a combination of two factors: first, PexRAP directly regulates the transcription of genes which play a key role in germinal center response. Second, PexRAP-mediated ether lipid production might differentially regulate the activation of transcription factors, such as PPARg whose activation was known to be regulated by lipid. By the reduction in supply and the recirculation of precursors, the germinal center functions by producing only the most needed antibodies. IgA was differentially regulated in cKO PexRAP samples. The main role of IgA is as a first defense against infection in the gut by inhibiting bacterial and viral adhesion to the intestinal walls[134]. If germinal centers are in distress, it would make sense that they would secrete a first line of defense antibody in higher numbers to provide a generalized immune response.

In vitro however, PexRAP is integral for the survival of B cells, and IgG1-, IgG2c- and IgA-producing plasma cells (4 - 16 fold differences in secreted isotype Ab level between WT and PexRAP cKO B cells). Initial studies investigating a transcriptional phenotypic source show that PexRAP might regulate the expression of Aicda (gene coding AID) and Ialpha (IgA) and Igamma 2c (IgG2c) germline transcripts. The mRNA level of Aicda was reduced ~ 70% in PexRAP cKO compared with WT, and the Ia and Ig2c levels were halved in PexRAP cKO compared with WT. These results indicate that PexRAP regulates the expression of Aicda and affect the level of germline transcripts. There might be mechanistic discrepancy between in vivo and in vitro production of isotype, and also there might be some compensatory mechanism to bypass the defects of PexRAP on some isotype Ab production.

CONCLUSION

In conclusion, the reduction of PexRAP has been shown to cause a decrease in ether and plasmalogen lipids. In this work, PexRAP was used to decrease ether lipids to observe the effect

on lipid localization and immune function. It was found that this reduction resulted in decreased size and number of germinal centers, indicating an immune modulation associated with the reduction of ether lipids. Germinal center ether and plasmalogen lipid localization mirrored this trend. However, not all non-germinal center lipids followed this trend, indicating the specificity of this conditional KO. For example, PE(18:1_18:2) showed a significant difference in ion intensity between cKO PexRAP and WT mice, but when localization was investigated, a shift from germinal center to red pulp localization was observed, indicating a possible shift of this lipid from production of ether lipids in the white pulp to circulation in the red pulp. In addition, antibody class switching was further affected. IgA was significantly decreased in cKO PexRAP samples. This finding indicated that not only were germinal centers structurally affected by this reduction in ether lipids, but they were also functionally affected. Although there are many cell types in germinal centers, our work indicates there may be a tie between B cells and the function of germinal center ether lipids. Although further research into the exact cell type and specific pathway of dysregulation is warranted, this work is the first of our knowledge to make the connection between ether lipids and germinal center structure and function. In addition, this work pioneers the use of cKO PexRAP as a model for ether lipid deficiency in immune studies beyond brown fat studies.

CHAPTER V

CONCLUSIONS AND PERSPECTIVES

The adaptive immune system is essential for immunity, and the germinal center is a key component to this process. This project investigated the lipids involved in the germinal center adaptive immune response by linking their spatial localization to this splenic region. First, the effect of tissue preparation strategies on the lipids detected by MALDI IMS was investigated. Second, a multimodal imaging method for investigating the lipids in mouse spleen was developed and applied to determine germinal-center-specific lipids. Then an ether –lipid-specific knockdown (cKO PexRAP) was used to determine the effect of decreased ether lipids on the lipids involved in germinal center adaptive immune response.

The first goal of this research project was to determine the optimal sample preparation method for multimodal analysis of lipids in spleen. Previous works had focused on the number of features but not the specific lipid types affected by each sample preparation. The average fold change in ion intensity due to fixation, ammonium formate washing and freezing strategies was determined. The effect of each tissue preparation on tissue morphology was also studied.

As expected, FF (fresh frozen) tissues, when compared to formalin fixed tissues, provided broader lipidomic coverage and optimal tissue structure, and ammonium formate washing of FF tissues provided data concerning lipid-specific improvements and losses. Although formalin fixation hindered tissue structure, if formalin fixation must be used, ammonium formate washing is recommended for spatially targeted experiments due to its enhancement of tissue morphology, not

its enhancement of the detection of any lipid class. In negative ion mode, ammonium formate washing provides optimal detection for PE lipids, which are the primary lipid class of interest for germinal center lipids. Similarly, PS lipids show broad coverage in FF ammonium formate washed tissues. Contrarily for lyso, PI, and PG lipids, FF tissue without ammonium formate washing shows the best sensitivity and molecular coverage. Thus, FF ammonium formate washed tissues provided the broadest lipid coverage and increased detection of germinal-center-specific lipids.

In positive ion mode, not only were head group trends present, but so were adduct-specific trends. For PC, PA, PS, SM, and PE lipids, protonated and sodiated species were enhanced by ammonium formate washing but detected in lower ion intensities after fixation. However, the detection of these lipids can be partially recovered by ammonium formate washing of fixed tissues. PG lipids were different from all other headgroups because they are highly soluble and detected in lower ion intensities after ammonium formate washing and fixation, and thus FF unwashed tissues are recommended for PG lipids. Overall, we determined that FF ammonium formate washed tissues provided the widest breadth of coverage with the largest enhancement of germinal center specific lipids, which are primarily PE ether lipids in negative ion mode.

The information obtained from the sample preparation study above was used to study germinal-center-specific lipids in the spleen and determined that FF ammonium formate tissues provided the broadest coverage of our ions of interest. A multimodal method that enabled the use a cell-type-specific fluorophore, AID-GFP, to target these germinal centers was developed. These localizations were further probed using immunofluorescence to identify subregions with varying oxygen levels, the light and dark zones of the germinal center. The next task was to develop an image registration and ion intensity extraction algorithm that allowed us to incorporate and mine MALDI IMS, IF, and H&E modalities. Data-driven image fusion was used to further mine the

MALDI IMS data for germinal-center-specific lipid localizations. Sixteen GC-specific lipids and 11 lipids that were more intensely localized to the hypoxic GC light zones were discovered. Of these lipids, five were ether or plasmalogen lipids. This discovery led to the hypothesis that ether lipids play an important role in germinal center adaptive immune responses.

These 16 GC-specific lipids were further investigated by the systematic reduction of ether lipids using a cKO of PexRAP, an enzyme integral to ether lipid synthesis. It was determined that the reduction of PexRAP had a phenotypic response of reduced geminal center size and number, indicating reduced adaptive immune response capability. GCs were 1.5 times more numerous and 1.6 larger times ($p=0.02$, $p=0.05$) in WT samples than in cKO PexRAP samples. In WT tissues, germinal centers were less dispersed with one germinal center in every 320 ± 47 mm^2 of tissue compared to one germinal center in every 510 ± 170 mm^2 in cKO PexRAP samples. In addition, the average size of germinal centers in WT tissues is 28 ± 7.2 mm^2 while in cKO PexRAP tissues, the average germinal center is 17 ± 6.3 mm^2. However, the number of follicles is not significantly different ($p=0.1$). All these factors indicate that the ability to activate an adaptive immune response is not follicular in nature.

In collaboration with Prof. Mark Boothby's lab, it was found that the production of IgA was significantly reduced in vivo. Molecularly, the localization of germinal center ether and plasmalogen lipids mirrored the phenotype observed in immunofluorescence with decreased size and number of germinal centers as determined by MALDI IMS. However, only one non-ether germinal-center-specific lipid, which was localizing back into circulation with the splenic red pulp, was significantly changed. This indicated the specificity of the PexRAP cKO and showed the potential shift in lipid synthesis pathways to account for the reduction in germinal center ether lipids.

Future Research Directions

While my work has provided the connection between germinal center response and ether lipids, much remains unknown about the adaptive immune response. Two main categories of exploration, biological and analytical technique focused work, remain. For biologically focused work, which cell types are most influenced by ether lipid synthesis deficiencies remains unknown as does how the nutrient microenvironment, such as low oxygen, affects the germinal center response. Future work will be aimed at targeting specific cell types with fluorescent markers and applying the multimodal method I developed to broader biological studies. In this work, the focus remained a simplistic model of adaptive immunity through the injection of SRBC to activate the adaptive immune system. Further biological pathogens need to be tested. For example, a multimodal approach could be used to determine whether the hypoxic light zone of the germinal center could play a different role in a staph infection with anaerobic bacteria.[135] To further study the effect of oxygen levels on the adaptive immune system, hypoxic and normoxic chambers could also be used to analyze the effect of environmental oxygen levels and the lipid programming related to germinal center response.

Secondarily, further analytical techniques can be applied to derive more information from these biological models. One challenge with germinal-center-specific lipids is differentiating the ether and plasmalogen lipid isomers. The application of ion mobility imaging mass spectrometry to differentiate these isomers while imaging could provide a more specified localization of these lipids and perhaps enhance the detection of these lipids through the reduction of ion suppression. Another challenge of this work was the complex cellular matrix of tissue. To better understand the cell types connected to germinal center ether lipids, cell sorting flow cytometry could be applied

prior to ion mobility mass spectrometry. In addition, lipids are not the only class of interest for the study of germinal centers. Low molecular weight metabolites have been shown to be integral to many immune functions. Even though we currently have a method using CASI to analyze many of the glycolysis and glutaminolysis pathway metabolites, IMS of low molecular weight species remains challenging as MS/MS gives non-specific fragmentation. The application of nuclear magnetic resonance for metabolite verification in tandem with MS/MS analysis would provide a more robust identification of low molecular weight metabolites. To further address this challenge, the introduction of ^{13}C glutamine would provide the ability to trace the pathway of glutamine in germinal centers and provide a more accurate identification of low molecular weight metabolites by comparing the theoretical isotopic distributions to detected isotopic distributions. Moreover, because of the challenges associated with using flow cytometry for cell sorting, laser capture microdissection could be used to extract and accumulate germinal center light and dark zones in the spleen. These extracts could then be used for experimentation with non-spatial offline methods such as LC-MS/MS or NMR.

Beyond investigations of germinal centers in the spleen, other lymphatic organs should be studied. For example, it has been reported that draining lymph nodes near cancer tumors reveals a different microenvironment.[136] If cryosectioning were not a limitation, draining lymph nodes of staph-infected areas could provide important information about the adaptive immune response to these staph-related pathogens. Certainly, there is still much to be learned about adaptive immune responses, and much can be accomplished using the combination of traditional immunology experimentation and multimodal imaging, but the use of these other technologies and the application of these methods to more specified pathogens would bring this work to the forefront of scientific discovery. Now that we have a clearer picture of the lipids involved in germinal center

responses, it is likely that the implementation of a multimodal approach with many of these other technologies can provide a clearer understanding of adaptive immunity and help the many people who suffer from adaptive immune disorders.

APPENDIX A

	FF	FORMALIN FIXED	FORMALIN FIXED AMMONIUM FORMATE WASHED
AVERAGE	1115	2285	122
STD DEV	246	307	137

Appendix A Table 2.1. *A table comparing the average and standard deviation for the number of m/z features in negative ion mode after fresh freezing, formalin fixation, and formalin fixation followed by ammonium formate washing (FF vs. formalin fixed p=0.0002, FF vs. formalin fixed ammonium formate washed p=0.6, formalin fixed vs. formalin fixed ammonium formate washed p=0.009).*

	ISOPENTANE	NITROGEN	DRY ICE
AVERAGE	1534	1509	1759
STD DEV	133	177	522

Appendix A Table 2.2. *A table comparing the average and standard deviation for the number of m/z features detected after various freezing strategies in negative ion mode (p=0.4).*

	FF	FF AMMONIUM FORMATE WASHED
AVERAGE	1722	1180
STD DEV	556	310

Appendix A Table 2.3. *A table comparing the average and standard deviation for the number of m/z features in negative ion mode after fresh freezing and fresh freezing followed by ammonium formate washing (p=0.01).*

	ISOPENTANE	NITROGEN	DRY ICE
AVERAGE	1845	1932	2016
STD DEV	287	559	848

Appendix A Table 2.4. *A table comparing the average and standard deviation for the number of m/z features detected in positive ion mode after various freezing strategies in negative ion mode (p=0.9).*

CALC *M/Z*	LIPID NAME	DETECTED *M/Z*	AVG	STD	ROC	P	AVG LOG2 FOLD CHANGE	MASS ERROR (PPM)
536.5043	Cer(d34:1)	536.5039	3.1	3.3	0.63	0.22	-2.56	0.78
646.6138	Cer(d42:2)	646.6134	1.3	0.55	0.62	0.64	-1.64	0.73
616.4706	CerP(d34:1)	616.4703	1.7	0.48	0.76	0.03	-1.84	0.52
644.5019	CerP(d36:1)	644.5015	2	1	0.75	0.42	-1.77	0.70
698.5571	HexCer(d34:1)	698.5556	1.6	0.54	0.68	0.35	-1.81	2.11
782.6510	HexCer(d40:1)	782.6518	1.3	0.85	0.61	0.73	-1.67	-1.02
808.6666	HexCer(d42:2)	808.6679	1.1	0.36	0.73	0.90	-1.54	-1.49
409.2355	LPA(16:0)	409.2357	3.7	2.4	0.82	0.12	-2.86	-0.32
437.2668	LPA(18:0)	437.2670	3.6	2.3	0.84	0.13	-2.82	-0.44
463.2825	LPA(20:1)	463.2825	9	9	0.75	0.12	-5.57	-0.11
457.2355	LPA(20:4)	457.2352	9	7	0.71	0.14	-5.50	0.61
481.2355	LPA(22:6)	481.2355	6	2	0.63	0.04	-4.20	-0.01
633.4859	LPA(32:0)/PA(O-32:0)	633.4854	2	1	0.65	0.43	-1.79	0.85
464.2777	LPC(14:1)	464.2782	5	4	0.67	0.16	-3.32	-1.04
494.3247	LPC(16:0)	494.3246	5	4	0.66	0.20	-3.30	0.10
480.3090	LPE(18:0)	480.3097	3.1	1.7	0.87	0.11	-2.53	-1.34
478.2934	LPE(18:1)	478.2930	3.2	2.3	0.75	0.22	-2.60	0.81
476.2777	LPE(18:2)	476.2779	3	2	0.64	0.10	-2.56	-0.43
508.3403	LPE(20:0)	508.3401	2.4	0.80	0.88	0.06	-2.20	0.39
506.3247	LPE(20:1)	506.3245	3	2	0.75	0.15	-2.25	0.25
504.3090	LPE(20:2)	504.3090	2.2	1.7	0.74	0.29	-2.08	0.07
500.2777	LPE(20:4)	500.2778	1.8	0.9	0.68	0.06	-1.90	-0.13
528.3090	LPE(22:4)	528.3089	2.2	1.7	0.68	0.17	-2.08	0.28
524.2777	LPE(22:6)	524.2782	1.4	0.8	0.68	0.73	-1.68	-0.98
583.3247	LPI(P-18:0)	583.3249	3.1	1.2	0.61	0.09	-2.57	-0.36
480.2726	LPS(P-16:0)	480.2730	2.2	1.4	0.65	0.09	-2.08	-0.85
619.4339	PE(30:0)	619.4339	1.7	0.94	0.73	0.15	-1.86	-0.08
647.4652	PE(32:0)	647.4657	1.2	0.45	0.73	0.67	-1.58	-0.80
645.4495	PE(32:1)	645.4486	1.4	0.89	0.67	0.83	-1.69	1.52

745.4808	PE(40:7)	745.4782	4	4	0.70	0.27		-3.11	3.56
814.5387	PE(42:8)	814.5413	1.7	1.3	0.61	0.31		-1.87	-3.15
923.6166	PE(52:10(OH))	923.6144	1.9	1.3	0.60	0.32		-1.95	2.35
466.3298	PE(O-18:0)/LPE(O-18:0)	466.3300	4.3	3.9	0.64	0.16		-3.16	-0.62
436.2828	PE(P-16:0)/LPE(P-16:0)	436.2829	3.9	3.0	0.77	0.15		-2.97	-0.16
464.3141	PE(P-18:0)/ PE(O-18:1)/LPE(P-18:0)	464.3142	4.0	3.0	0.79	0.12		-3.01	-0.12
492.3454	PE(P-20:0)/LPE(P-20:0)	492.3460	5	4	0.66	0.13		-3.50	-1.15
659.5016	PE(P-34:0)/PE(O-34:1)	659.5019	1.7	0.89	0.69	0.30		-1.86	-0.46
679.4703	PE(P-36:4)	679.4702	2.2	0.49	0.61	0.009		-2.11	0.06
705.4859	PE(P-38:5)	705.4852	1.8	0.26	0.60	0.07		-1.90	0.96
827.5802	PG(40:3)	827.5798	4	2	0.74	0.01		-2.78	0.56

Appendix A Table 2.5. *A table of the theoretical m/z, lipid name, detected m/z, average fold change in intensity, standard deviation fold change of intensity, ROC area under the curve, paired t-test p value, average log_2 fold change, and mass error in ppm for deprotonated ions in negative ion mode with an ROC >0.6 and <0.4 for the comparison of FF tissue vs. FF ammonium formate washed tissue in which ammonium formate washing hinders detection.*

CALC *M/Z*	**LIPID NAME**	**DETECTED *M/Z***	**AVG**	**STD**	**ROC**	**P**	**AVG LOG2 FOLD CHANGE**	**MASS ERROR (PPM)**
752.5958	CerP(d44:3)	752.5963	1.2	0.29	0.60	0.18	0.32	-0.64
810.6823	HexCer(d42:1)	810.6817	2.1	0.75	0.62	0.34	1.05	0.70
599.3196	LPI(18:0)	599.3191	1.2	0.55	0.65	0.53	0.27	0.86
619.2883	LPI(20:4)	619.2873	2	1	0.70	0.10	0.90	1.70
557.3091	LPI(O-16:0)	557.3062	1.3	0.29	0.31	0.22	0.39	5.16
578.3458	LPS(22:1)	578.3458	2.1	0.59	0.28	0.10	1.07	0.05
568.2675	LPS(22:6)	568.2674	4	1	0.24	0.13	1.93	0.19

675.4965	PE(34:0)	675.4962	6	7	0.74	0.22	2.49	0.42
673.4808	PE(34:1)	673.4812	1.1	0.88	0.64	0.20	0.19	-0.57
671.4652	PE(34:2)	671.4650	1.1	0.27	0.64	0.54	0.17	0.35
746.5700	PE(36:0)	746.5662	4	3	0.68	0.21	2.09	5.09
701.5121	PE(36:1)	701.5124	3	2	0.30	0.01	1.79	-0.41
772.5856	PE(38:1)	772.5860	1.3	0.32	0.61	0.08	0.40	-0.46
723.4965	PE(38:4)	723.4965	1.9	0.52	0.31	0.02	0.93	-0.05
749.5121	PE(40:5)	749.5130	4	1	0.32	0.02	1.96	-1.16
806.5336	PE(40:6(OH))	806.5345	2.1	1.8	0.33	0.16	1.06	-1.16
747.4965	PE(40:6)	747.4983	6	2	0.26	0.02	2.55	-2.44
786.5074	PE(40:8)	786.5105	1.3	0.37	0.40	0.16	0.41	-3.95
820.5856	PE(42:5)	820.5875	3.8	0.56	0.60	0.36	1.93	-2.22
818.5700	PE(42:6)	818.5712	1.1	0.42	0.73	0.46	0.10	-1.44
816.5543	PE(42:7)	816.5544	1.2	0.40	0.66	0.67	0.22	-0.13
704.5594	PE(O-34:0)/LPE(34:0)	704.5579	2.2	0.30	0.72	0.19	1.11	2.11
702.5438	PE(P-34:0)	702.5431	1.1	0.28	0.64	0.56	0.12	0.96
700.5281	PE(P-34:1)	700.5283	1.3	0.58	0.61	0.37	0.33	-0.29
730.5751	PE(P-36:0)/PE(O-36:1)	730.5747	1.1	0.38	0.64	0.13	0.10	0.57
707.5016	PE(P-38:4)/PE(O-38:5)	707.5011	1.3	0.48	0.75	0.86	0.34	0.72
802.5751	PE(P-42:6)	802.5761	1.0	0.20	0.68	0.91	0.04	-1.27
704.5230	PE-NMe(32:0)	704.5216	1.1	0.13	0.75	0.59	0.19	1.98
730.5387	PE-NMe(34:1)	730.5386	1.3	0.33	0.62	0.67	0.33	0.07
718.5387	PE-NMe2(32:0)/PE(34:0)	718.5382	1.8	0.78	0.77	0.21	0.87	0.66
782.5336	PI(32:0)	782.5351	2.4	0.05	0.24	0.04	1.25	-1.93
837.5493	PI(34:0)	837.5490	2.6	0.96	0.12	0.02	1.40	0.39
835.5337	PI(34:1)	835.5338	1.2	0.62	0.11	0.01	0.24	-0.12
833.5180	PI(34:2)	833.5190	3	3	0.25	0.01	1.65	-1.14
861.5493	PI(36:2)	861.5517	3	1	0.21	0.02	1.53	-2.78
857.5180	PI(36:4)	857.5183	1.0	0.20	0.22	0.01	0.04	-0.34
885.5493	PI(38:4)	885.5491	6	1	0.22	0.02	2.55	0.20
734.4972	PS(32:0)	734.4976	2.7	0.92	0.27	0.74	1.41	-0.56

762.5285	PS(34:0)	762.5246	1.9	0.31	0.22	0.05	0.91	5.09
760.5129	PS(34:1)	760.5125	4	2	0.16	0.00	1.86	0.53
758.4972	PS(34:2)	758.4965	5	4	0.27	0.01	2.26	0.97
786.5285	PS(36:2)	786.5287	1.4	0.65	0.17	0.02	0.50	-0.21
784.5129	PS(36:3)	784.5139	1.8	0.61	0.14	0.20	0.88	-1.37
782.4972	PS(36:4)	782.4984	4	2	0.29	0.02	2.12	-1.48
812.5442	PS(38:3)	812.5435	2.5	0.95	0.21	0.03	1.33	0.80
810.5285	PS(38:4)	810.5286	4	2	0.16	0.01	1.96	-0.07
806.4972	PS(38:6)	806.4968	2.9	0.74	0.28	0.06	1.53	0.46
838.5598	PS(40:4)	838.5607	3	2	0.20	0.02	1.72	-1.00
836.5442	PS(40:5)	836.5473	3	1	0.10	0.04	1.70	-3.73
834.5285	PS(40:6)	834.5286	3	2	0.09	0.004	1.72	-0.09
864.5755	PS(42:5)	864.5716	4	1	0.35	0.09	1.96	4.51
860.5442	PS(42:7)	860.5422	2.5	0.57	0.36	0.02	1.32	2.29
858.5285	PS(42:8)	858.5239	2.4	0.68	0.23	0.01	1.29	5.38
888.5755	PS(44:7)	888.5725	2.9	0.94	0.25	0.14	1.52	3.36

Appendix A Table 2.6. *A table of the theoretical m/z, lipid name, detected m/z, average fold change in intensity, standard deviation fold change of intensity, ROC area under the curve, paired t-test p value, average log_2 fold change, and mass error in ppm for deprotonated ions in negative ion mode with an ROC >0.6 and <0.4 for the comparison of FF tissue vs. FF ammonium formate washed tissue in which ammonium formate washing improves detection.*

CALC M/Z	LIPID NAME	DETECTED M/Z	AVG	STD	ROC	P	AVG LOG2 FOLD CHANGE
621.30399	LPI(20:3)	621.3031	10	9	0.68	0.07	3.34
457.23552	LPA(20:4)	457.2349	3	2	0.20	0.07	1.77

Appendix A Table 2.7. *A table of the theoretical m/z, lipid name, detected m/z, average fold change in intensity, standard deviation fold change of intensity, ROC area under the curve, paired t-test p value, average log_2 fold change, and mass error in ppm for deprotonated ions in negative ion mode with an ROC >0.6 and <0.4 for the comparison of formalin fixed tissue vs. formalin fixed ammonium formate washed tissue in which ammonium formate washing hinders detection.*

CALC M/Z	LIPID NAME	DETECTED M/Z	AVG	STD	ROC	P	AVG LOG2 FOLD CHANGE	MASS ERROR (PPM)
435.2512	LPA(18:1)	435.2513	1.9	0.64	0.39	0.21	0.90	0.35
437.2668	LPA(18:0)	437.267	3	1	0.30	0.03	1.43	0.37
452.2777	LPE(16:0)	452.2777	9.4	8.8	0.24	0.11	3.23	-0.08
457.2355	LPA(20:4)	457.2349	4	2	0.20	0.04	1.93	-1.26
463.2825	LPA(20:1)	463.2824	7.7	10	0.30	0.31	2.95	-0.23
464.2777	LPC(14:1)	464.2784	6	4	0.27	0.14	2.55	1.43
466.3298	PE(O-18:0)/LPE(O-18:0)	466.3296	1.28	0.07	0.37	0.04	0.36	-0.26
478.2934	LPE(18:1)	478.2928	5	2	0.18	0.07	2.21	-1.12
480.2726	LPS(P-16:0)	480.2736	2.1	0.22	0.34	0.07	1.07	2.02
480.309	LPE(18:0)	480.3091	1.6	0.55	0.31	0.09	0.64	0.13
481.2355	LPA(22:6)	481.2356	8	4	0.15	0.03	2.97	0.21
485.2668	LPA(22:4)	485.2667	4	2	0.35	0.20	2.08	-0.22
492.309	LPC(16:1)	492.3096	8	6	0.21	0.08	3.09	1.16
492.3454	PE(P-20:0)/LPE(P-20:0)	492.3462	2.5	0.63	0.32	0.20	1.33	1.64
494.3247	LPC(16:0)	494.3247	7	3	0.19	0.05	2.73	0.13
500.2777	LPE(20:4)	500.2777	3	1	0.16	0.01	1.55	0.01
504.309	LPE(20:2)	504.3093	4	2	0.28	0.08	1.81	0.46
506.3247	LPE(20:1)	506.3248	2	1	0.27	0.07	1.26	0.16
507.2723	LPG(18:2)	507.2726	4	2	0.20	0.02	1.88	0.52
508.3039	LPS(P-18:0)	508.3045	9	2	0.16	0.01	3.14	1.20
508.3403	LPE(20:0)	508.3403	1.9	0.77	0.26	0.03	0.92	-0.01
509.2879	LPG(18:1)	509.288	6.3	0.27	0.20	0.04	2.65	0.16
514.2934	LPC(18:4)	514.2928	5	3	0.27	0.02	2.27	-1.04
524.2777	LPE(22:6)	524.2783	5	4	0.17	0.01	2.28	1.17
524.2988	LPS(18:0)	524.2988	15	11	0.08	0.03	3.95	-0.05

526.2934	LPE(22:5)	526.2938	5.2	0.78	0.20	0.07	2.37	0.88
528.309	LPE(22:4)	528.3091	4	1	0.23	0.01	2.04	0.19
531.2723	LPG(20:4)	531.272	2.3	1.7	0.40	0.31	1.18	-0.52
536.5043	Cer(d34:1)	536.5041	12	4	0.16	0.00	3.61	-0.35
540.309	LPC(20:5)	540.3094	2.2	0.50	0.39	0.05	1.16	0.62
555.2723	LPG(22:6)	555.2728	4	1	0.29	0.10	1.93	0.85
561.3556	PA(26:1)	561.3553	4	2	0.28	0.05	2.13	-0.58
571.2883	LPI(16:0)	571.2886	13	9	0.21	0.06	3.72	0.36
597.304	LPI(18:1)	597.3034	9	2	0.25	0.08	3.14	-0.94
599.3196	LPI(18:0)	599.3193	4.1	0.83	0.17	0.02	2.05	-0.62
616.4706	CerP(d34:1)	616.4707	3	1	0.21	0.02	1.57	0.09
618.4863	CerP(d34:0)	618.4851	5.3	0.69	0.32	0.03	2.42	-1.81
619.2883	LPI(20:4)	619.2876	3	2	0.29	0.18	1.77	-1.15
619.4339	PA(30:0)	619.4345	5	3	0.21	0.03	2.18	1.00
622.372	PS(24:0)	622.3708	6	5	0.28	0.10	2.66	-1.88
631.4703	PA(O-32:1)/LPA(32:1)/PA(P-32:0)	631.4705	2.3	0.47	0.38	0.09	1.17	0.30
633.4859	LPA(32:0)	633.4854	6	1	0.14	0.01	2.67	-0.87
642.4863	CerP(d36:2)	642.4859	3.5	0.84	0.16	0.01	1.79	-0.58
643.4339	PA(32:2)	643.4341	3.0	1	0.38	0.11	1.60	0.26
644.5019	CerP(d36:1)	644.5022	4.9	0.78	0.16	0.01	2.29	0.40
645.4495	PE(32:1)	645.4491	5	1	0.11	0.00	2.28	-0.67
646.6138	Cer(d42:2)	646.6141	16	6	0.08	0.00	4.02	0.36
647.4652	PA(32:0)	647.4657	5	1	0.08	0.01	2.34	0.72
647.4764	PE-Cer(t32:1)	647.4747	14	4	0.17	0.01	3.82	-2.63
648.4604	PE-NMe(28:0)	648.4598	11	5	0.25	0.02	3.43	-0.94
648.6295	Cer(d42:1)	648.6294	4	2	0.34	0.07	1.97	-0.08
657.4859	PA(O-34:2)/PA(P-34:2)	657.4856	4.9	0.72	0.30	0.02	2.28	-0.44
659.5016	PA(P-34:0)/PA(O-34:1)	659.5043	3	2	0.14	0.07	1.75	4.16
660.5051	HexCer(t30:0)	660.5054	6	4	0.20	0.10	2.65	0.56
669.4495	PA(34:3)	669.4485	5	2	0.32	0.08	2.35	-1.53
671.4652	PA(34:2)	671.4657	4	2	0.11	0.00	2.16	0.70

672.5332	CerP(d38:1)	672.5334	3	1	0.41	0.15	1.55	0.26
673.4808	PA(34:1)	673.4818	4	1	0.10	0.00	1.87	1.50
675.4965	PA(34:0)	675.4974	3.8	0.74	0.11	0.01	1.94	1.28
678.4499	LPC(30:6)	678.4478	8	3	0.21	0.09	3.01	-3.09
681.4859	PA(P-36:3)/PA(O-36:4)	681.4852	6	4	0.28	0.06	2.64	-1.07
685.5172	PA(P-36:1)/PA(O-36:2)	685.5174	10	6	0.24	0.07	3.27	0.25
687.5441	PE-Cer(d36:1)	687.544	3.6	0.75	0.17	0.01	1.85	-0.19
689.5485	PA(O-36:0)	689.5504	4	1	0.33	0.02	2.06	2.79
690.5074	PE(32:0)	690.5079	4	1	0.16	0.00	1.88	0.69
695.4652	PA(36:4)	695.4649	5	2	0.10	0.00	2.20	-0.46
697.4808	PA(36:3)	697.4804	4	1	0.09	0.01	2.06	-0.69
698.5571	HexCer(d34:1)	698.5566	9	3	0.15	0.00	3.17	-0.75
699.4965	PA(36:2)	699.4968	6	1	0.05	0.01	2.65	0.50
699.5077	PE-Cer(t36:3)	699.5072	5	4	0.37	0.18	2.34	-0.71
700.5645	CerP(d40:1)	700.5653	5	1	0.28	0.04	2.24	1.10
701.5121	PA(36:1)	701.5133	7	4	0.05	0.05	2.84	1.59
702.5438	PE(P-34:0)/PE(O-34:1)	702.5431	8	2	0.22	0.02	2.96	-0.94
704.523	PE-NMe(32:0)	704.5227	5	2	0.13	0.01	2.45	-0.47
704.5594	LPE(34:0)	704.5589	3.4	0.54	0.17	0.00	1.75	-0.69
707.5016	PA(P-38:4)/PA(O-38:5)	707.5019	5	2	0.22	0.01	2.45	0.46
709.5172	PA(P-38:3)/PA(O-38:4)	709.5156	3.7	0.60	0.38	0.09	1.90	-2.25
714.5074	PE(34:2)	714.5071	4.9	0.87	0.15	0.04	2.29	-0.46
716.523	PE(34:1)	716.5233	4	2	0.12	0.00	2.04	0.37
718.5387	PE(34:0)	718.5382	3.4	0.52	0.12	0.00	1.77	-0.73
719.4652	PA(38:6)	719.4662	6	3	0.15	0.02	2.56	1.43
721.4808	PA(38:5)	721.4805	4.0	0.26	0.12	0.02	1.99	-0.48
721.502	PG(32:0)	721.5009	3	2	0.39	0.19	1.66	-1.50
723.4965	PA(38:4)	723.4968	6	1	0.04	0.02	2.68	0.38
725.5121	PA(38:3)	725.5126	6	2	0.06	0.02	2.55	0.64
726.5802	CerP(d42:2)	726.581	3.0	0.51	0.20	0.02	1.56	1.15
727.5278	PA(38:2)	727.5271	9	6	0.18	0.05	3.16	-0.97
728.5594	PE(P-36:1)/PE(O-36:2)	728.5604	4	3	0.29	0.12	1.99	1.38

728.5958	CerP(d42:1)	728.5965	3	1	0.35	0.09	1.57	1.01
730.5387	PE-NMe(34:1)	730.5396	4	2	0.21	0.07	2.02	1.23
730.5751	PE(P-36:0)/PE(O-36:1)	730.5747	3.5	0.90	0.15	0.01	1.79	-0.52
734.4972	PS(32:0)	734.4976	4	2	0.35	0.16	1.97	0.47
738.5074	PE(36:4)	738.5082	14	25	0.23	0.15	3.83	1.05
740.523	PE(36:3)	740.5222	3.6	0.78	0.16	0.03	1.84	-1.08
742.5387	PE(36:2)	742.5377	4	2	0.09	0.00	2.15	-1.34
744.5543	PE(36:1)	744.5534	4	1	0.12	0.01	2.01	-1.29
745.4808	PA(40:7)	745.483	4.3	0.81	0.33	0.06	2.11	2.84
746.57	PE(36:0)	746.5676	2.9	0.49	0.19	0.01	1.54	-3.19
747.4965	PA(40:6)	747.4983	8	3	0.04	0.03	2.96	2.36
747.5176	LBPA(34:1)	747.5172	4	1	0.09	0.02	2.13	-0.61
748.5281	PE(P-38:5)/PE(O-38:6)	748.5245	4.0	0.46	0.11	0.02	2.01	-4.85
749.5121	PA(40:5)	749.5132	7	2	0.05	0.02	2.82	1.46
751.5278	PA(40:4)	751.5298	11	4	0.07	0.03	3.52	2.63
752.5594	PE(P-38:3)/PE(O-38:4)	752.5594	2.8	0.88	0.22	0.01	1.49	-0.02
752.5958	CerP(d44:3)	752.5964	4	2	0.27	0.06	2.11	0.81
756.5543	PE-NMe(36:2)	756.5555	5	3	0.21	0.04	2.30	1.49
758.4972	PS(34:2)	758.4967	4	2	0.38	0.10	1.98	-0.70
760.5129	PS(34:1)	760.513	19	4	0.20	0.05	4.26	0.18
762.5074	PE(38:6)	762.5071	3	1	0.22	0.08	1.77	-0.41
762.5285	PS(34:0)	762.5267	3.5	2.4	0.38	0.17	1.79	-2.38
764.523	PE(38:5)	764.5237	2.6	0.57	0.19	0.05	1.40	0.87
766.5387	PE(38:4)	766.5384	3.4	0.94	0.12	0.01	1.76	-0.32
768.5543	PE(38:3)	768.5541	4	2	0.16	0.01	1.83	-0.31
770.57	PE(38:2)	770.5698	4	1	0.11	0.02	2.03	-0.26
771.5176	PG(36:3)	771.5196	6	4	0.29	0.06	2.64	2.58
771.638	PE-Cer(d42:1)	771.6371	3	1	0.26	0.04	1.79	-1.11
772.5856	PE(38:1)	772.5863	3.3	0.9	0.16	0.02	1.74	0.89
773.5333	LBPA(36:2)	773.535	6	2	0.15	0.01	2.57	2.25
774.5438	PE(P-40:6)	774.5444	3	2	0.36	0.29	1.55	0.75
778.5751	PE(P-40:4)/PE(O-40:5)	778.5764	5	6	0.23	0.01	2.24	1.72

780.5907	PE(P-40:3)/PE(O-40:4)	780.5904	3	1	0.37	0.03	1.70	-0.39
782.4972	PS(36:4)	782.4988	6	4	0.32	0.11	2.65	2.05
782.5336	PE(38:4(OH))	782.5349	2.3	0.8	0.39	0.10	1.19	1.64
782.651	HexCer(d40:1)	782.653	7	5	0.24	0.04	2.81	2.50
786.5285	PS(36:2)	786.5295	14	7	0.04	0.03	3.81	1.31
788.523	PE(40:7)	788.5263	7	7	0.27	0.10	2.88	4.16
788.5442	PS(36:1)	788.5459	15	11	0.03	0.06	3.93	2.17
790.5387	PE(40:6)	790.5384	2.7	0.9	0.17	0.02	1.43	-0.37
792.5543	PE(40:5)	792.5548	2.6	0.8	0.18	0.04	1.41	0.58
794.5336	PS(P-38:4)/PS(O-38:5)	794.5345	2.6	0.8	0.27	0.05	1.36	1.16
794.57	PE(40:4)	794.5695	3	1	0.15	0.03	1.75	-0.67
795.5387	LPI(32:0)/PI(O-32:0)	795.5401	3.9	0.8	0.34	0.00	1.97	1.67
796.5856	PE(40:3)	796.5873	4	2	0.27	0.03	2.02	2.06
806.4972	PS(38:6)	806.4985	10	9	0.25	0.10	3.33	1.56
807.5024	PI(32:1)	807.5041	3	2	0.35	0.09	1.74	2.12
808.5129	PS(38:5)	808.5142	6	3	0.30	0.04	2.67	1.64
808.6666	HexCer(d42:2)	808.6677	4	1	0.14	0.02	2.05	1.24
809.518	PI(32:0)	809.5195	8	4	0.26	0.05	2.99	1.82
810.5285	PS(38:4)	810.5294	10	6	0.05	0.05	3.34	1.03
810.6823	HexCer(d42:1)	810.6823	6	3	0.22	0.03	2.51	0.01
812.5442	PS(38:3)	812.546	15	10	0.11	0.04	3.87	2.28
818.57	PE(42:6)	818.5722	4	2	0.26	0.00	1.98	2.69
832.5704	PI-Cer(d38:2)	832.571	5	1	0.10	0.02	2.22	0.80
833.518	PI(34:2)	833.5204	10	4	0.17	0.04	3.32	2.88
834.5285	PS(40:6)	834.5305	13	7	0.02	0.03	3.71	2.32
835.5337	PI(34:1)	835.5352	9	4	0.06	0.05	3.16	1.82
836.5442	PS(40:5)	836.5477	13	5	0.05	0.01	3.75	4.24
837.5493	PI(34:0)	837.551	15	11	0.13	0.05	3.90	1.97
838.5598	PS(40:4)	838.5627	14	8	0.10	0.03	3.79	3.49
857.518	PI(36:4)	857.5187	5	2	0.12	0.03	2.44	0.85
859.5337	PI(36:3)	859.5365	6	3	0.14	0.03	2.56	3.31
860.5442	PS(42:7)	860.5419	7	3	0.20	0.04	2.83	-2.62

861.5493	PI(36:2)	861.5504	6	3	0.12	0.05	2.61	1.22
863.565	PI(36:1)	863.5684	10	7	0.20	0.06	3.38	3.94
864.5755	PS(42:5)	864.5717	4	1	0.31	0.01	1.87	-4.36
869.5544	PI(P-38:4)/PI(O-38:5)	869.5575	6.3	0.6	0.20	0.03	2.66	3.58
871.57	PI(P-38:3)/PI(O-38:4)	871.5728	3	1	0.34	0.09	1.75	3.11
881.518	PI(38:6)	881.5211	6	4	0.23	0.11	2.58	3.54
883.5337	PI(38:5)	883.5349	4	1	0.13	0.04	2.04	1.45
885.5493	PI(38:4)	885.5475	5	1	0.10	0.03	2.40	-2.04
889.5806	PI(38:2)	889.5761	2.9	0.9	0.28	0.12	1.52	-5.05
909.5493	PI(40:6)	909.5503	4	1	0.22	0.05	1.92	1.13
911.565	PI(40:5)	911.5695	3	2	0.22	0.10	1.73	4.94

Appendix A Table 2.8. *A table of the theoretical m/z, lipid name, detected m/z, average fold change in intensity, standard deviation fold change of intensity, ROC area under the curve, paired t-test p value, average log_2 fold change, and mass error in ppm for deprotonated ions in negative ion mode with an ROC >0.6 and <0.4 for the comparison of formalin fixed tissue vs. formalin fixed ammonium formate washed tissue in which ammonium formate washing improves detection.*

CALC M/Z	LIPID NAME	DETECTED M/Z	AVG	STD	ROC	P	AVG LOG2 FOLD CHANGE	MASS ERROR (PPM)
642.4863	CerP(d36:2)	642.4859	2.8	0.58	0.79	0.009	1.46	0.55
715.5754	PE-Cer(d38:1)	715.577	1.5	0.55	0.68	0.08	0.60	-2.25
771.6380	PE-Cer(d42:1)	771.6384	3	2	0.71	0.008	1.62	-0.47
817.5020	PG(40:8)	817.5044	4	2	0.72	0.07	2.12	-2.92
819.5176	PG(40:7)	819.5214	6	2	0.76	0.06	2.59	-4.60

Appendix A Table 2.9. *A table of the theoretical m/z, lipid name, detected m/z, average fold change in intensity, standard deviation fold change of intensity, ROC area under the curve, paired t-test p value, average log_2 fold change, and mass error in ppm for deprotonated ions in negative ion mode with an ROC >0.6 and <0.4 for the comparison of formalin fixed tissue vs. FF tissue in which formalin fixation improves detection.*

CALC M/Z	LIPID NAME	DETECTED M/Z	AVG	STD	ROC	P	AVG LOG2 FOLD CHANGE	MASS ERROR (PPM)
536.5043	Cer(d34:1)	536.5040	14	11	0.99	0.07	3.80	0.48
648.6295	Cer(d42:1)	648.6293	5	1	0.73	0.05	2.24	0.26
646.6138	Cer(d42:2)	646.6135	13	11	0.78	0.17	3.72	0.46
616.4706	CerP(d34:1)	616.4703	6	4	0.84	0.15	2.62	0.47
644.5019	CerP(d36:1)	644.5013	21	30	0.71	0.38	4.36	1.01
700.5645	CerP(d40:1)	700.5647	8	4	0.91	0.07	2.97	-0.33
726.5802	CerP(d42:2)	726.5807	9	6	0.92	0.08	3.25	-0.69
752.5958	CerP(d44:3)	752.5960	11.1	0.39	0.81	0.001	3.47	-0.24
698.5571	HexCer(d34:1)	698.5561	36	42	0.92	0.08	5.17	1.42
782.6510	HexCer(d40:1)	782.6529	5	3	0.75	0.06	2.43	-2.49
810.6823	HexCer(d42:1)	810.6827	3	2	0.67	0.0001	1.69	-0.51
808.6666	HexCer(d42:2)	808.6683	4	3	0.76	0.06	1.83	-2.05
463.2825	LPA(20:1)	463.2828	6	5	0.82	0.03	2.63	-0.72
457.2355	LPA(20:4)	457.2355	2	1	0.76	0.12	1.13	-0.01
481.2355	LPA(22:6)	481.2355	1.8	0.65	0.77	0.09	0.81	0.06
633.4859	LPA(32:0)/PA(O-32:0)	633.4855	11	8	0.98	0.05	3.46	0.64
464.2777	LPC(14:1)	464.2784	4	3	0.87	0.23	1.83	-1.47
494.3247	LPC(16:0)	494.3248	2.0	0.21	0.71	0.01	1.03	-0.29
736.5281	LPC(34:5)	736.5290	30	30	0.92	0.09	4.91	-1.20
452.2777	LPE(16:0)	452.2778	1.4	0.33	0.75	0.26	0.46	-0.16
480.3090	LPE(18:0)	480.3093	6	4	0.78	0.09	2.47	-0.57
478.2934	LPE(18:1)	478.2928	2	1	0.84	0.03	1.21	1.12
476.2777	LPE(18:2)	476.2782	2	2	0.89	0.33	1.18	-0.97
508.3403	LPE(20:0)	508.3402	20	34	0.65	0.42	4.35	0.23
506.3247	LPE(20:1)	506.3246	3	2	0.86	0.06	1.50	0.19
504.3090	LPE(20:2)	504.3094	2.3	0.84	0.85	0.04	1.21	-0.84

500.2777	LPE(20:4	500.2779	1.9	0.59	0.75	0.16	0.92	-0.41
528.3090	LPE(22:4)	528.3091	10	8	0.95	0.03	3.30	-0.23
526.2934	LPE(22:5)	526.2937	26	17	0.98	0.02	4.71	-0.67
524.2777	LPE(22:6)	524.2782	12	7	0.93	0.04	3.58	-0.83
436.2828	LPE(P-16:0)/PE(P-16:0)	436.2829	3	3	0.74	0.29	1.45	-0.18
464.3141	LPE(P-18:0)/ PE(O-18:1)/ PE(P-18:0)	464.3143	3	3	0.88	0.23	1.70	-0.34
492.3454	LPE(P-20:0)/PE(P-20:0)	492.3461	1.8	0.86	0.79	0.20	0.83	-1.36
555.2723	LPG(22:6)	555.2725	6	2	0.81	0.002	2.52	-0.29
571.2883	LPI(16:0)	571.2886	10	8	0.79	0.12	3.35	-0.50
599.3196	LPI(18:0)	599.3190	58	94	0.72	0.41	5.85	1.09
597.3040	LPI(18:1)	597.3034	4	2	0.85	0.03	2.16	1.08
621.3040	LPI(20:3)	621.3021	17	16	0.20	0.07	4.10	3.05
619.2883	LPI(20:4)	619.2876	15	12	0.91	0.04	3.95	1.18
555.2934	LPI(P-16:0)	555.2916	4	3	0.71	0.11	2.15	3.38
583.3247	LPI(P-18:0)	583.3250	4.8	0.20	0.76	0.001	2.26	-0.52
524.2988	LPS(18:0)	524.2987	9	6	0.90	0.04	3.18	0.22
480.2726	LPS(P-16:0)	480.2735	3.2	0.05	0.78	0.01	1.67	-1.77
647.4652	PA(32:0)	647.4656	158	269	0.68	0.42	7.31	-0.69
645.4495	PA(32:1)	645.4488	6	5	0.81	0.22	2.52	1.09
671.4652	PA(34:2)	671.4651	6	2	0.78	0.09	2.48	0.09
701.5121	PA(36:1)	701.5128	3	1	0.79	0.10	1.63	-0.99
699.4965	PA(36:2)	699.4965	101	85	0.92	0.09	6.66	-0.02
697.4808	PA(36:3)	697.4802	11	4	0.93	0.04	3.49	0.89
727.5278	PA(38:2)	727.5269	3	2	0.95	0.23	1.35	1.25
725.5121	PA(38:3)	725.5120	4	2	0.94	0.04	1.87	0.14
723.4965	PA(38:4)	723.4968	245	139	0.92	0.02	7.93	-0.45
721.4808	PA(38:5)	721.4808	11	4	0.91	0.02	3.45	0.02
719.4652	PA(38:6)	719.4654	6	7	0.64	0.26	2.67	-0.25

751.5278	PA(40:4)	751.5296	178	150	0.93	0.07	7.48	-2.39
749.5121	PA(40:5)	749.5134	2.6	0.81	0.88	0.04	1.39	-1.73
747.4965	PA(40:6)	747.4988	4	3	0.77	0.07	2.15	-3.07
745.4808	PA(40:7)	745.4829	2	1	0.65	0.44	0.73	-2.81
689.5485	PA(O-36:0)	689.5507	8	5	0.72	0.11	3.07	-3.22
659.5016	PA(P-34:0)/PA(O-34:1)	659.5017	7	4	0.80	0.13	2.71	-0.25
657.4859	PA(P-34:1)/PA(O-34:2)	657.4854	8	3	0.82	0.04	3.07	0.79
687.5329	PA(P-36:0)/PA(O-36:1)	687.5331	13	11	0.81	0.21	3.65	-0.34
685.5172	PA(P-36:1)/PA(O-36:2)	685.5168	8	7	0.96	0.12	3.04	0.60
681.4859	PA(P-36:3)/PA(O-36:4)	681.4850	44	36	0.92	0.06	5.46	1.32
679.4703	PA(P-36:4)/PA(O-36:5)	679.4702	18	19	0.97	0.10	4.19	0.07
707.5016	PA(P-38:4)/PA(O-38:5)	707.5014	19	13	0.93	0.07	4.27	0.28
705.4859	PA(P-38:5)/PA(O-38:6)	705.4855	10	6	0.95	0.07	3.29	0.66
619.4339	PE(30:0)	619.4341	6	2	0.77	0.03	2.53	-0.35
690.5074	PE(32:0)	690.5076	11	11	0.83	0.17	3.41	-0.32
688.4917	PE(32:1)	688.4919	6	4	0.72	0.14	2.54	-0.29
675.4965	PE(34:0)	675.4964	14	12	0.94	0.10	3.78	0.09
718.5387	PE(34:0)/PE-NMe2(32:0)	718.5382	6	3	0.71	0.09	2.54	0.68
673.4808	PE(34:1)	673.4817	11	5	0.93	0.03	3.48	-1.23
716.5230	PE(34:1)	716.5229	6	3	0.77	0.14	2.56	0.23
714.5074	PE(34:2)	714.5071	61	42	0.92	0.03	5.92	0.46
746.5700	PE(36:0)	746.5675	2	2	0.72	0.29	1.20	3.39
744.5543	PE(36:1)/PE-NMe2(34:1)	744.5536	6	6	0.73	0.23	2.60	1.02
742.5387	PE(36:2)	742.5379	2.4	0.51	0.81	0.01	1.24	1.12

738.5074	PE(36:4)	738.5074	69	117	0.67	0.42	6.11	-0.08
736.4917	PE(36:5)	736.4932	10	5	0.92	0.06	3.34	-1.99
772.5856	PE(38:1)	772.5859	2	1	0.90	0.19	1.04	-0.40
768.5543	PE(38:3)	768.5530	3	2	0.72	0.01	1.42	1.73
770.5700	PE(38:3)/PE-NMe2(36:2)	770.5698	6	5	0.74	0.12	2.61	0.25
766.5387	PE(38:4)	766.5383	358	613	0.71	0.42	8.48	0.54
764.5230	PE(38:5)	764.5230	6	2	0.87	0.02	2.69	0.02
762.5074	PE(38:6)	762.5070	25	16	0.93	0.11	4.66	0.49
796.5856	PE(40:3)	796.5838	2	1	0.82	0.36	1.05	2.31
794.5700	PE(40:4)	794.5700	77	123	0.69	0.39	6.27	0.03
792.5543	PE(40:5)	792.5548	1.9	0.55	0.82	0.02	0.90	-0.54
790.5387	PE(40:6)	790.5386	8	9	0.76	0.29	2.94	0.13
788.5230	PE(40:7)	788.5272	14	13	0.78	0.23	3.84	-5.24
786.5074	PE(40:8)	786.5114	2	1	0.73	0.12	1.22	-5.13
822.6013	PE(42:4)	822.6034	4	2	0.70	0.04	1.85	-2.54
820.5856	PE(42:5)	820.5890	5	3	0.72	0.06	2.20	-4.06
818.5700	PE(42:6)	818.5716	8	9	0.64	0.30	2.99	-1.95
816.5543	PE(42:7)	816.5563	2	2	0.71	0.54	1.18	-2.39
704.5594	PE(O-34:0)/LPE(34:0)	704.5582	6	4	0.89	0.05	2.54	1.70
702.5438	PE(P-34:0)/PE(O-34:1)	702.5433	6	3	0.75	0.10	2.64	0.61
700.5281	PE(P-34:1)/PE(O-34:2)	700.5284	138	113	0.92	0.07	7.11	-0.42
698.5125	PE(P-34:2)/PE(O-34:3)	698.5119	41	29	0.91	0.05	5.36	0.87
730.5751	PE(P-36:0)/PE(O-36:1)	730.5751	2	2	0.85	0.19	1.26	-0.10
728.5594	PE(P-36:1)/PE(O-36:2)	728.5603	221	205	0.92	0.10	7.79	-1.17
726.5438	PE(P-36:2)/PE(O-36:3)	726.5435	172	210	0.94	0.11	7.43	0.38
724.5281	PE(P-36:3)/PE(O-36:4)	724.5259	85	70	0.92	0.07	6.41	3.06
722.5125	PE(P-36:4)/PE(O-36:5)	722.5129	2.7	0.81	0.90	0.12	1.44	-0.57
720.4968	PE(P-36:5)	720.4961	4	2	0.71	0.06	2.05	0.97
752.5594	PE(P-38:3)/PE(O-38:4)	752.5593	4	1	0.90	0.01	1.87	0.21
750.5438	PE(P-38:4)/PE(O-38:5)	750.5430	4	2	0.95	0.05	2.03	1.09

748.5281	PE(P-38:5)/PE(O-38:6)	748.5275	8	6	0.83	0.15	3.00	0.88
746.5125	PE(P-38:6)	746.5121	5	2	0.83	0.06	2.18	0.48
780.5907	PE(P-40:3)/PE(O-40:4)	780.5905	2	1	0.77	0.25	1.06	0.33
778.5751	PE(P-40:4)/PE(O-40:5)	778.5759	3	1	0.87	0.06	1.42	-1.07
776.5594	PE(P-40:5)/PE(O-40:6)	776.5601	7	3	0.76	0.10	2.90	-0.82
774.5438	PE(P-40:6)	774.5440	23	11	0.92	0.03	4.49	-0.30
772.5281	PE(P-40:7)	772.5288	3	1	0.62	0.06	1.72	-0.85
804.5907	PE(P-42:5)/PE(O-42:6)	804.5927	5	2	0.66	0.09	2.29	-2.40
802.5751	PE(P-42:6)	802.5759	6	5	0.67	0.20	2.67	-1.00
673.4921	PE-Cer(t34:2)	673.4909	9	7	0.71	0.19	3.24	1.73
704.5230	PE-NMe(32:0)	704.5225	5	4	0.85	0.10	2.26	0.78
730.5387	PE-NMe(34:1)	730.5392	8	5	0.76	0.09	3.02	-0.64
756.5543	PE-NMe(36:2)	756.5547	3	2	0.89	0.06	1.69	-0.42
721.5020	PG(32:0)	721.5003	1.8	0.94	0.61	0.23	0.85	2.25
749.5333	PG(34:0)	749.5308	15	8	0.78	0.04	3.91	3.27
747.5176	PG(34:1)/LBPA(34:1)	747.5171	5	4	0.71	0.19	2.25	0.74
777.5646	PG(36:0)	777.5624	11	7	0.84	0.12	3.44	2.74
775.5489	PG(36:1)	775.5482	3	2	0.91	0.16	1.43	0.87
773.5333	PG(36:2)	773.5333	2.3	0.4	0.66	0.08	1.19	-0.10
771.5176	PG(36:3)	771.5193	10	8	0.90	0.06	3.32	-2.19
827.5802	PG(40:3)	827.5803	21	11	0.92	0.03	4.41	-0.13
819.5176	PG(40:7)	819.5207	5	3	0.68	0.17	2.31	-3.79
817.5020	PG(40:8)	817.5043	3	2	0.73	0.23	1.44	-2.80
809.5180	PI(32:0)	809.5193	3	2	0.79	0.10	1.78	-1.62
807.5024	PI(32:1)	807.5036	2	2	0.82	0.31	1.18	-1.49
837.5493	PI(34:0)	837.5500	19	3	0.90	0.001	4.28	-0.87
835.5337	PI(34:1)	835.5319	6	4	0.77	0.07	2.67	2.07
833.5180	PI(34:2)	833.5198	1.9	0.69	0.61	0.25	0.94	-2.14
861.5493	PI(36:2)	861.5514	2.0	0.64	0.63	0.16	1.00	-2.45
859.5337	PI(36:3)	859.5330	4	3	0.84	0.06	2.03	0.79
857.5180	PI(36:4)	857.5178	3	2	0.71	0.15	1.50	0.29

885.5493	PI(38:4)	885.5481	428	734	0.72	0.42		8.74	1.33
883.5337	PI(38:5)	883.5350	13	6	0.90	0.02		3.68	-1.53
881.5180	PI(38:6)	881.5225	11	3	0.86	0.03		3.43	-5.08
911.5650	PI(40:5)	911.5682	9	7	0.88	0.08		3.23	-3.60
869.5544	PI(P-38:4)	869.5585	2	1	0.70	0.38		1.15	-4.70
760.5129	PS(34:1)	760.5127	3	2	0.90	0.19		1.38	0.21
788.5442	PS(36:1)	788.5453	18	23	0.70	0.32		4.20	-1.43
786.5285	PS(36:2)	786.5301	5	2	0.71	0.08		2.21	-2.03
782.4972	PS(36:4)	782.4987	3	3	0.64	0.04		1.74	-1.94
812.5442	PS(38:3)	812.5427	5	4	0.75	0.01		2.20	1.75
810.5285	PS(38:4)	810.5289	10	8	0.79	0.18		3.27	-0.48
808.5129	PS(38:5)	808.5152	10	4	0.90	0.001		3.28	-2.87
806.4972	PS(38:6)	806.4984	8	3	0.75	0.04		3.02	-1.50
838.5598	PS(40:4)	838.5619	4	3	0.82	0.03		2.16	-2.51
836.5442	PS(40:5)	836.5475	7	5	0.81	0.08		2.78	-3.98
834.5285	PS(40:6)	834.5292	10.9	0.70	0.82	0.002		3.44	-0.87
832.5129	PS(40:7)	832.5148	9	2	0.87	0.001		3.13	-2.27
860.5442	PS(42:7)	860.5425	1.4	0.25	0.67	0.09		0.53	1.97
888.5755	PS(44:7)	888.5746	1.9	0.39	0.68	0.11		0.96	0.93

Appendix A Table 2.10. *A table of the theoretical m/z, lipid name, detected m/z, average fold change in intensity, standard deviation fold change of intensity, ROC area under the curve, paired t-test p value, average log_2 fold change, and mass error in ppm for deprotonated ions in negative ion mode with an ROC >0.6 and <0.4 for the comparison of formalin fixed tissue vs. FF tissue in which formalin fixation hinders detection.*

CALC M/Z	LIPID NAME	DETECTED M/Z	AVG	STD	ROC	P	AVG LOG2 FOLD CHANGE	MASS ERROR (PPM)
736.52812	LPC(34:5)	736.52960	6	6	0.67	0.27	-2.50	-2.01
452.27772	LPE(16:0)	452.27798	9	5	0.71	0.02	-3.24	-0.58
478.29337	LPE(18:1)	478.29313	4	1	0.75	0.001	-1.83	0.50
476.27772	LPE(18:2)	476.27792	8	7	0.70	0.25	-2.97	-0.43

436.28280	LPE(P-16:0)/PE(P-16:0)	436.28264	8	6	0.80	0.07	-3.07	0.37
557.30908	LPI(O-16:0)	557.30695	9	10	0.67	0.10	-3.12	3.82
555.29343	LPI(P-16:0)	555.29198	12	7	0.80	0.002	-3.57	2.61
583.32473	LPI(P-18:0)	583.32543	7	3	0.61	0.02	-2.71	-1.20
568.26755	LPS(22:6)	568.26782	2	1	0.23	0.05	-1.25	-0.48
480.27263	LPS(P-16:0)	480.27352	12	10	0.71	0.01	-3.60	-1.85
721.48083	PA(38:5)	721.48083	1.2	0.66	0.62	0.90	-0.32	0.00
745.48083	PA(40:7)	745.48380	1.4	0.34	0.61	0.20	-0.48	-3.98
679.47027	PA(P-36:4)/PA(O-36:5)	679.47063	4	3	0.69	0.12	-2.08	-0.53
707.50157	PA(P-38:4)/PA(O-38:5)	707.50155	1.5	0.25	0.71	0.04	-0.55	0.03
705.48592	PA(P-38:5)/PA(O-38:6)	705.48601	4.0	0.38	0.66	0.04	-1.99	-0.13
703.47027	PA(P-38:6)	703.46986	8	1	0.63	0.06	-2.97	0.58
688.49173	PE(32:1)	688.49205	9	8	0.70	0.12	-3.09	-0.46
716.52303	PE(34:1)	716.52348	1.0	0.33	0.72	0.73	-0.02	-0.63
714.50738	PE(34:2)	714.50771	5	2	0.85	0.01	-2.44	-0.46
740.52303	PE(36:3)	740.52241	4	1	0.84	0.004	-1.83	0.84
738.50738	PE(36:4)	738.50863	21	17	0.87	0.01	-4.42	-1.69
768.55433	PE(38:3)	768.55647	1	1	0.75	0.23	-0.43	-2.78
766.53868	PE(38:4)	766.53873	3	1	0.86	0.02	-1.59	-0.06
764.52303	PE(38:5)	764.52427	9	5	0.87	0.02	-3.21	-1.62
762.50738	PE(38:6)	762.50762	23	13	0.87	0.01	-4.55	-0.31
794.56998	PE(40:4)	794.57023	2	1	0.79	0.14	-0.63	-0.31
792.55433	PE(40:5)	792.55510	3	2	0.84	0.07	-1.66	-0.97
790.53868	PE(40:6)	790.53896	6	2	0.86	0.02	-2.60	-0.35
822.60128	PE(42:4)	822.60368	4	3	0.64	0.20	-1.95	-2.92
820.58563	PE(42:5)	820.58936	3	1	0.72	0.05	-1.48	-4.54
818.56998	PE(42:6)	818.57196	1.6	0.38	0.77	0.04	-0.71	-2.42

816.55433	PE(42:7)	816.55626	4	3	0.80	0.05	-2.06	-2.36
464.31410	PE(P-18:0)/PE(O-18:1)	464.31441	12	7	0.85	0.03	-3.61	-0.66
702.54377	PE(P-34:0)/PE(O-34:1)	702.54402	4	1	0.80	0.01	-2.00	-0.36
700.52812	PE(P-34:1)/PE(O-34:2)	700.52928	4	2	0.90	0.003	-1.97	-1.66
698.51247	PE(P-34:2)/PE(O-34:3)	698.51244	20	10	0.84	0.02	-4.31	0.04
728.55942	PE(P-36:1)/PE(O-36:2)	728.56108	3	1	0.70	0.004	-1.46	-2.28
726.54377	PE(P-36:2)/PE(O-36:3)	726.54426	11	10	0.83	0.07	-3.40	-0.68
722.51247	PE(P-36:4)/PA(O-36:5)	722.51359	271	198	0.90	0.01	-8.08	-1.55
720.49682	PE(P-36:5)	720.49625	17	10	0.81	0.04	-4.08	0.79
752.55942	PE(P-38:3)/PE(O-38:4)	752.55935	3	2	0.83	0.05	-1.64	0.09
750.54377	PE(P-38:4)/PE(O-38:5)	750.54371	213	139	0.90	0.01	-7.73	0.08
748.52812	PE(P-38:5)/PE(O-38:6)	748.52808	35	21	0.89	0.09	-5.12	0.05
746.51247	PE(P-38:6)	746.51195	332	253	0.90	0.02	-8.38	0.69
778.57507	PE(P-40:4)/PE(O-40:5)	778.57645	4	2	0.86	0.09	-1.85	-1.78
776.55942	PE(P-40:5)/PE(O-40:6)	776.56130	20	10	0.88	0.04	-4.33	-2.43
774.54377	PE(P-40:6)	774.54393	100	83	0.89	0.03	-6.64	-0.21
772.52812	PE(P-40:7)	772.52961	60	42	0.90	0.03	-5.92	-1.93
804.59072	PE(P-42:5)/PE(O-42:6)	804.59312	6	4	0.72	0.08	-2.68	-2.99
802.57507	PE(P-42:6)	802.57785	7	5	0.81	0.07	-2.90	-3.47
749.53326	PG(34:0)	749.53200	95	64	0.90	0.03	-6.57	1.69
747.51761	PG(34:1)	747.51760	2	1	0.77	0.05	-1.01	0.02
777.56456	PG(36:0)	777.56305	14	2	0.88	0.10	-3.76	1.95

775.54891	PG(36:1)	775.54883	56	41	0.89	0.04	-5.80	0.11
773.53326	PG(36:2)/LBPA(36:2)	773.53491	2	1	0.78	0.06	-1.01	-2.13
827.58021	PG(40:3)	827.58174	5	4	0.72	0.11	-2.44	-1.85
819.51761	PG(40:7)	819.52113	2	1	0.65	0.16	-0.84	-4.29
817.50196	PG(40:8)	817.50398	3	1	0.67	0.09	-1.64	-2.47
891.60450	PI(38:1)	891.60600	2	1	0.67	0.12	-1.17	-1.68
782.49721	PS(36:4)	782.49941	4	3	0.29	0.20	-2.05	-2.81
808.51286	PS(38:5)	808.51510	1.1	0.40	0.62	0.91	-0.14	-2.77
806.49721	PS(38:6)	806.49850	1.2	0.36	0.26	0.76	-0.25	-1.60
838.55981	PS(40:4)	838.56271	3	1	0.13	0.04	-1.48	-3.46
836.54416	PS(40:5)	836.54235	1	1	0.62	0.32	-0.52	2.16
832.51286	PS(40:7)	832.51442	2	1	0.68	0.04	-1.11	-1.87
880.57038	PS(42:5(OH))	880.57317	1	1	0.66	0.26	-0.46	-3.17
856.51286	PS(42:9)	856.51391	2	1	0.71	0.24	-1.25	-1.22

Appendix A Table 2.11. *A table of the theoretical m/z, lipid name, detected m/z, average fold change in intensity, standard deviation fold change of intensity, ROC area under the curve, paired t-test p value, average log_2 fold change, and mass error in ppm for deprotonated ions in negative ion mode with an ROC >0.6 and <0.4 for the comparison of FF vs. formalin fixed ammonium formate washed tissue in which formalin fixation in combination with ammonium formate washing hinders detection.*

CALC M/Z	LIPID NAME	DETECTED M/Z	AVG	STD	ROC	P	AVG LOG2 FOLD CHANGE	MASS ERROR (PPM)
724.5645	CerP(d42:3)	724.5637	2	1	0.38	0.01	-1.25	-1.16
660.5051	HexCer(t30:0)	660.5061	2	1	0.38	0.16	-1.06	1.58
701.5121	PA(36:1)	701.5131	3.0	0.62	0.28	0.05	-1.60	1.32
727.5278	PA(38:2)	727.5275	3	1	0.34	0.03	-1.38	-0.35
723.4965	PA(38:4)	723.4970	2	1	0.37	0.02	-1.29	0.77
719.4652	PA(38:6)	719.4662	1.1	0.37	0.60	0.38	-0.11	1.43
749.5121	PA(40:5)	749.5138	2.2	0.84	0.27	0.02	-1.16	2.17
747.4965	PA(40:6)	747.4994	4	2	0.26	0.01	-1.85	3.85
782.5336	PE(38:4(OH))	782.5351	3	2	0.22	0.13	-1.77	1.97
762.5074	PE(38:6)	762.5076	1.2	0.46	0.87	0.50	-0.26	0.31
809.5180	PI(32:0)	809.5192	3	1	0.27	0.11	-1.33	1.51

837.5493	PI(34:0)	837.5504	1.7	0.68	0.07	0.08	-0.78	1.24
833.5180	PI(34:2)	833.5201	2.4	0.49	0.20	0.04	-1.26	2.47
861.5493	PI(36:2)	861.5524	4	1	0.18	0.02	-1.91	3.59
857.5180	PI(36:4)	857.5198	2.1	0.48	0.22	0.04	-1.10	2.14
887.5650	PI(38:3)	887.5602	1.8	0.40	0.27	0.11	-0.84	5.35
885.5493	PI(38:4)	885.5490	3	1	0.22	0.03	-1.33	-0.38
832.5704	PI-Cer(d38:2)	832.5727	2.1	0.79	0.32	0.02	-1.08	2.78
858.5860	PI-Cer(d40:3)	858.5843	3	2	0.36	0.01	-1.73	-2.07
734.4972	PS(32:0)	734.4979	4	2	0.25	0.16	-1.97	0.96
760.5129	PS(34:1)	760.5140	1.9	0.39	0.09	0.06	-0.92	1.46
758.4972	PS(34:2)	758.4968	4	2	0.25	0.11	-2.05	-0.49
786.5285	PS(36:2)	786.5298	1.9	0.88	0.13	0.10	-0.92	1.69
856.5704	PS(40:3(OH))	856.5725	2.1	0.93	0.38	0.01	-1.10	2.53
838.5598	PS(40:4)	838.5627	1.4	0.50	0.13	0.05	-0.47	3.46
864.5755	PS(42:5)	864.5717	5	1	0.34	0.01	-2.31	-4.35
862.5598	PS(42:6)	862.5558	5	3	0.18	0.01	-2.46	-4.63
860.5442	PS(42:7)	860.5427	3	2	0.31	0.05	-1.65	-1.74
858.5285	PS(42:8)	858.5251	3	2	0.20	0.03	-1.67	-3.97

Appendix A Table 2.12. *A table of the theoretical m/z, lipid name, detected m/z, average fold change in intensity, standard deviation fold change of intensity, ROC area under the curve, paired t-test p value, average log_2 fold change, and mass error in ppm for deprotonated ions in negative ion mode with an ROC >0.6 and <0.4 for the comparison of FF vs. formalin fixed ammonium formate washed tissue in which formalin fixation in combination with ammonium formate washing improves detection.*

	[M-H]$^-$
IMPROVES DETECTION	2
HINDERS DETECTION	68

Appendix A Table 2.13. PE Lipids: FF vs. Formalin Fixed*. A table showing the number of PE lipids divided into adducts that were improved or hindered in detection after formalin fixation when compared to FF tissues in negative ion mode.*

	[M-H]$^-$
IMPROVES DETECTION	0
HINDERS DETECTION	52

Appendix A Table 2.14. PE Lipids: Formalin Fixed vs. Formalin Fixed Ammonium Formate Washing*. A table showing the number of PE lipids divided into adducts that were improved or hindered in detection after formalin fixation and ammonium formate washing when compared to formalin fixed tissues in negative ion mode.*

	[M-H]$^-$
IMPROVES DETECTION	2
HINDERS DETECTION	38

Appendix A Table 2.15. PE Lipids: FF vs. Formalin Fixed Ammonium Formate Washing. *A table showing the number of PE lipids divided into adducts that were improved or hindered in detection after formalin fixation and ammonium formate washing when compared to FF tissues in negative ion mode.*

	[M-H]$^-$

IMPROVES DETECTION	23
HINDERS DETECTION	22

Appendix A Table 2.16. PE Lipids: FF vs. FF Ammonium Formate Washing. *A table showing the number of PE lipids divided into adducts that were improved or hindered in detection after FF ammonium formate washing when compared to FF tissues in negative ion mode.*

	$[M-H]^-$
IMPROVES DETECTION	3
HINDERS DETECTION	13

Appendix A Table 2.17. Cer Lipids: FF vs. Formalin Fixed. *A table showing the number of Cer lipids divided into adducts that were improved or hindered in detection after formalin fixation when compared to FF tissues in negative ion mode.*

	$[M-H]^-$
IMPROVES DETECTION	2
HINDERS DETECTION	7

Appendix A Table 2.18. Cer Lipids: FF vs. FF Ammonium Formate Washing. *A table showing the number of Cer lipids divided into adducts that were improved or hindered in detection after FF ammonium formate washing when compared to FF tissues in negative ion mode.*

	$[M-H]^-$

IMPROVES DETECTION	21
HINDERS DETECTION	0

Appendix A Table 2.19. Cer Lipids: Formalin Fixed vs. Formalin Fixed Ammonium Formate Washing*. A table showing the number of Cer lipids divided into adducts that were improved or hindered in detection after formalin fixation and ammonium formate washing when compared to formalin fixed tissues in negative ion mode.*

	$[M-H]^-$
IMPROVES DETECTION	4
HINDERS DETECTION	0

Appendix A Table 2.20. Cer Lipids: FF vs. Formalin Fixed Ammonium Formate Washing*. A table showing the number of Cer lipids divided into adducts that were improved or hindered in detection after formalin fixation and ammonium formate washing when compared to FF tissues in negative ion mode.*

	$[M-H]^-$
IMPROVES DETECTION	10
HINDERS DETECTION	1

Appendix A Table 2.21. PI Lipids: FF vs. FF Ammonium Formate Washing*. A table showing the number of PI lipids divided into adducts that were improved or hindered in detection after FF ammonium formate washing when compared to FF tissues in negative ion mode.*

	$[M-H]^-$
IMPROVES DETECTION	23

HINDERS DETECTION	1

Appendix A Table 2.22. PI Lipids: Formalin Fixed vs. Formalin Fixed Ammonium Formate Washing*. A table showing the number of PI lipids divided into adducts that were improved or hindered in detection after formalin fixation and ammonium formate washing when compared to formalin fixed tissues in negative ion mode.*

	$[M-H]^-$
IMPROVES DETECTION	0
HINDERS DETECTION	22

Appendix A Table 2.23. PI Lipids: FF vs. Formalin Fixed*. A table showing the number of PI lipids divided into adducts that were improved or hindered in detection after formalin fixation when compared to FF tissues in negative ion mode.*

	$[M-H]^-$
IMPROVES DETECTION	10
HINDERS DETECTION	3

Appendix A Table 2.24. PI Lipids: FF vs. Formalin Fixed Ammonium Formate Washing*. A table showing the number of PI lipids divided into adducts that were improved or hindered in detection after formalin fixation and ammonium formate washing when compared to FF tissues in negative ion mode.*

	$[M-H]^-$
IMPROVES DETECTION	0
HINDERS DETECTION	18

Appendix A Table 2.25. PS Lipids: FF vs. Formalin Fixed*. A table showing the number of PS lipids divided into adducts that were improved or hindered in detection after formalin fixation when compared to FF tissues in negative ion mode.*

	$[M-H]^-$
IMPROVES DETECTION	21
HINDERS DETECTION	0

Appendix A Table 2.26. PS Lipids: Formalin Fixed vs. Formalin Fixed Ammonium Formate Washing*. A table showing the number of PS lipids divided into adducts that were improved or hindered in detection after formalin fixation and ammonium formate washing when compared to formalin fixed tissues in negative ion mode.*

	$[M-H]^-$
IMPROVES DETECTION	19
HINDERS DETECTION	1

Appendix A Table 2.27. PS Lipids: FF vs. FF Ammonium Formate Washing*. A table showing the number of PS lipids divided into adducts that were improved or hindered in detection after FF ammonium formate washing when compared to FF tissues in negative ion mode.*

	$[M-H]^-$
IMPROVES DETECTION	11
HINDERS DETECTION	11

Appendix A Table 2.28. PS Lipids: FF vs. Formalin Fixed Ammonium Formate Washing*. A table showing the number of PS lipids divided into adducts that were improved or hindered in detection after formalin fixation and ammonium formate washing when compared to FF tissues in negative ion mode.*

	$[M-H]^-$
IMPROVES DETECTION	6
HINDERS DETECTION	20

Appendix A Table 2.29. Lyso Lipids: FF vs. FF Ammonium Formate Washing*. A table showing the number of Lyso lipids that were improved or hindered in detection after FF ammonium formate washing when compared to FF tissues in negative ion mode.*

	$[M-H]^-$
IMPROVES DETECTION	2
HINDERS DETECTION	38

Appendix A Table 2.30. Lyso Lipids: Formalin Fixed vs. Formalin Fixed Ammonium Formate Washing*. A table showing the number of Lyso lipids divided into adducts that were improved or hindered in detection after formalin fixation and ammonium formate washing when compared to formalin fixed tissues in negative ion mode.*

	$[M-H]^-$
IMPROVES DETECTION	0
HINDERS DETECTION	32

Appendix A Table 2.31. Lyso Lipids: FF vs. Formalin Fixed*. A table showing the number of Lyso lipids divided into adducts that were improved or hindered in detection after formalin fixation when compared to FF tissues in negative ion mode.*

	[M-H]$^-$
IMPROVES DETECTION	0
HINDERS DETECTION	11

Appendix A Table 2.32. Lyso Lipids: FF vs. Formalin Fixed Ammonium Formate Washing*. A table showing the number of Lyso lipids divided into adducts that were improved or hindered in detection after formalin fixation and ammonium formate washing when compared to FF tissues in negative ion mode.*

	FF	FORMALIN FIXED	FORMALIN FIXED AMMONIUM FORMATE WASHED
AVERAGE	1741	2684	1836
STD DEV	273	1028	682

Appendix A Table 2.33. *A table comparing the average and standard deviation for the number of m/z features in positive ion mode after fresh freezing, formalin fixation, and formalin fixation followed by ammonium formate washing (FF vs. formalin fixed p=0.09, FF vs. formalin fixed ammonium formate washed p=0.8, formalin fixed vs. formalin fixed ammonium formate washed p=0.05).*

	FF	FF AMMONIUM FORMATE WASHED
AVERAGE	1902	1592
STD DEV	312	335

Appendix A Table 2.34. *A table comparing the average and standard deviation for the number of m/z features in positive ion mode after fresh freezing and fresh freezing followed by ammonium formate washing (p=0.002).*

CALC M/Z	LIPID NAME	DETECTED M/Z	AVG	STD	ROC	P	AVG LOG2 FOLD CHANGE	MASS ERROR (PPM)
746.6064	CerP(t42:1)/PC(O-34:1)/ PC(P-34:0)	746.6063	1.2	0.22	0.39	0.08	0.27	0.05
925.5207	CL(36:4)/PIP(O-36:4)/ PIP(P-36:3)	925.5222	13	1	0.71	0.004	14.56	-1.59
775.5278	PA(42:7)	775.5282	7	5	0.73	0.11	14.03	-0.55
732.5543	PC(32:1)/PE-NMe(34:1)	732.5543	1.4	0.52	0.35	0.35	0.48	0.07
748.5856	PE(36:0)	748.5861	1.1	0.54	0.37	0.92	0.12	-0.60
744.5543	PE(36:2)	744.5555	1.2	0.84	0.40	0.54	0.20	-1.54
742.5387	PE(36:3)	742.5352	29	24	0.92	0.01	5.68	4.76
852.6482	PE(44:4)	852.645	9	4	0.79	0.02	14.39	3.79
745.5020	PG(34:3)	745.4987	17	12	0.80	0.04	15.64	4.44
801.5646	PG(38:3)	801.5607	9	7	0.74	0.09	14.45	4.79
797.5333	PG(38:5)	797.5292	71	45	0.96	0.03	17.56	5.11
825.5646	PG(40:5)	825.5609	17	12	0.88	0.04	15.61	4.41
823.5489	PG(40:6)	823.5454	11	7	0.79	0.07	14.73	4.25
849.5646	PG(42:7)	849.5611	17	12	0.87	0.04	15.65	4.06

847.5489	PG(42:8)	847.5458	6	4	0.74	0.07	13.88	3.63
845.5333	PG(42:9)	845.5301	7	4	0.72	0.10	13.64	3.80
759.5540	PG(O-36:3)/PG(P-36:2)	759.5506	7	4	0.71	0.05	14.11	4.49
785.5696	PG(O-38:4)/PG(P-38:3)	785.5656	16	10	0.82	0.03	15.56	5.17
792.5179	PS(P-38:6)	792.5199	3	2	0.65	0.04	2.06	-2.49
796.5245	SHexCer(t34:1)	796.5246	102	104	0.99	0.02	18.06	-0.17
824.5558	SHexCer(t36:1)	824.5565	91	85	0.97	0.08	7.55	-0.84

Appendix A Table 2.35. *A table of the theoretical m/z, lipid name, detected m/z, average fold change in intensity, standard deviation fold change of intensity, ROC area under the curve, paired t-test p value, average log_2 fold change, and mass error in ppm for the protonated ions with an ROC >0.6 and <0.4 for the comparison of FF tissue vs. FF ammonium formate washed tissue in which ammonium formate washing hinders detection.*

CALC M/Z	LIPID NAME	DETECTED M/Z	AVG	STD	ROC	P	AVG LOG2 FOLD CHANGE	MASS ERROR (PPM)
692.5594	CerP(t38:0)/LPC(30:0)	692.5614	2.3	0.80	0.37	0.02	-1.18	-2.89
701.5598	SM(d34:2)	701.5613	2.4	0.72	0.35	0.03	-1.28	-2.18
704.5230	PC(30:1)	704.5241	1.7	0.81	0.35	0.15	-0.79	-1.57
706.4659	PS(30:1)/LPE(34:0)	706.4672	1.6	0.53	0.37	0.20	-0.71	-1.85
718.5387	PE(34:1)	718.5392	2.1	0.76	0.35	0.06	-1.10	-0.73
721.4808	PA(38:6)	721.4792	2.3	0.96	0.29	0.15	-1.19	2.24
723.4965	PA(38:5)	723.4953	2.6	0.74	0.30	0.11	-1.35	1.70
728.5230	PC(32:3)	728.5214	3	2	0.31	0.12	-1.49	2.28
730.5387	PC(32:2)	730.5389	1.3	0.55	0.37	0.30	-0.38	-0.30
732.5907	PE(O-36:1)/PE(P-36:0)	732.591	1.8	0.50	0.35	0.05	-0.87	-0.41
742.5751	PC(O-34:3)/PC(P-34:2)	742.5736	1.4	0.42	0.33	0.10	-0.51	2.04
744.5907	CerP(t42:2)/ PC(O-34:2)/PC(P-34:1)	744.5909	1.1	0.29	0.35	0.60	-0.13	-0.18

754.5387	PC(34:4)	754.5394	3	1	0.39	0.02	-1.67	-0.98
756.5543	PC(34:3)	756.551	1.6	0.88	0.40	0.30	-0.70	4.38
758.5700	PC(34:2)/PE-NMe(36:2)	758.5688	1.1	0.13	0.37	0.16	-0.15	1.57
760.5856	PC(34:1)	760.5846	1.2	0.14	0.36	0.08	-0.23	1.42
760.6220	PE(O-38:1)/PE(P-38:0)	760.6207	1.4	0.29	0.29	0.33	-0.44	1.73
768.5543	PE(38:4)	768.5556	2	1	0.32	0.07	-0.87	-1.61
768.5907	PC(O-36:4)/PC(P-36:3)	768.5904	1.5	0.34	0.32	0.02	-0.55	0.48
770.6064	PC(O-36:3)/PC(P-36:2)	770.6069	1.5	0.32	0.28	0.03	-0.61	-0.69
774.5649	PS(O-36:2)/PS(P-36:1)	774.5642	1.8	0.48	0.27	0.02	-0.81	0.86
780.5473	LacCer(d28:0)	780.5501	1.7	0.78	0.37	0.04	-0.74	-3.56
784.5856	PC(36:3)	784.584	1.1	0.20	0.27	0.32	-0.20	2.08
785.6537	SM(d40:2)	785.6535	2.0	0.35	0.31	0.01	-1.00	0.24
786.6013	PC(36:2)	786.5999	1.1	0.38	0.24	0.47	-0.20	1.81
788.6169	PC(36:1)	788.6159	1.3	0.22	0.31	0.03	-0.34	1.28
804.5543	PC(38:7)	804.551	1.7	0.43	0.32	0.005	-0.80	4.10
811.6693	SM(d42:3)	811.6693	1.2	0.38	0.39	0.25	-0.29	-0.01
813.6850	SM(d42:2)	813.6837	1.3	0.33	0.38	0.11	-0.37	1.53
830.5700	PC(40:8)	830.5686	2	1	0.29	0.01	-1.19	1.62
832.5856	PC(40:7)	832.5878	3	2	0.34	0.03	-1.44	-2.57
838.6326	PC(40:4)	838.6342	1.0	0.16	0.33	0.70	-0.02	-1.93

Appendix A Table 2.36. *A table of the theoretical m/z, lipid name, detected m/z, average fold change in intensity, standard deviation fold change of intensity, ROC area under the curve, paired t-test p value, average log_2 fold change, and mass error in ppm for the protonated ions with an ROC >0.6 and <0.4 for the comparison of FF tissue vs. FF ammonium formate washed tissue in which ammonium formate washing improves detection.*

CALC M/Z	LIPID NAME	DETECTED M/Z	AVG	STD	ROC	P	AVG LOG2 FOLD CHANGE	MASS ERROR (PPM)

756.5543	PC(34:3)	756.5506	1.3	0.52	0.75	0.29		-0.33	-4.93

Appendix A Table 2.37. *A table of the theoretical m/z, lipid name, detected m/z, average fold change in intensity, standard deviation fold change of intensity, ROC area under the curve, paired t-test p value, average log_2 fold change, and mass error in ppm for the protonated ions with an ROC >0.6 and <0.4 for the comparison of formalin fixed tissue vs. formalin fixed ammonium formate washed tissue in which ammonium formate washing hinders detection.*

None

Appendix A Table 2.38. *A table of the theoretical m/z, lipid name, detected m/z, average fold change in intensity, standard deviation fold change of intensity, ROC area under the curve, paired t-test p value, average log_2 fold change, and mass error in ppm for the protonated ions with an ROC >0.6 and <0.4 for the comparison of formalin fixed tissue vs. formalin fixed ammonium formate washed tissue in which ammonium formate washing improves detection.*

CALC M/Z	LIPID NAME	DETECTED M/Z	AVG	STD	ROC	P	AVG LOG2 FOLD CHANGE	MASS ERROR (PPM)
925.5207	CL(36:4)/PIP(O-36:4)/ PIP(P-36:3)	925.5222	19	4	0.72	0.02	-4.22	-1.58
806.5630	LacCer(d30:1)	806.5613	1.9	0.46	0.70	0.10	-0.96	2.03
806.5630	LacCer(d30:1)	806.5613	2	0.46	0.70	0.10	-0.96	2.03
775.5278	PA(42:7)	775.528	10	3	0.72	0.04	-3.29	-0.29
786.6013	PC(36:2)	786.5997	0.9	0.35	0.64	0.83	0.11	2.05
784.5856	PC(36:3)	784.5841	1.6	0.98	0.71	0.06	-0.68	1.99
782.5700	PC(36:4)	782.5685	1.4	0.58	0.76	0.13	-0.47	1.84
780.5543	PC(36:5)	780.5528	1.1	0.04	0.62	0.16	-0.10	1.97
780.5543	PC(36:5)	780.5528	1	0.04	0.62	0.16	-0.10	1.97
810.6013	PC(38:4)	810.5996	1.2	0.51	0.74	0.14	-0.32	2.05
808.5856	PC(38:5)	808.5838	1.6	0.73	0.75	0.11	-0.69	2.29

806.5700	PC(38:6)	806.5686	1.9	0.66	0.80	0.06	-0.91	1.78
838.6326	PC(40:4)	838.6335	2.2	0.78	0.61	0.05	-1.11	-1.05
836.6169	PC(40:5)	836.6173	1.7	0.67	0.65	0.11	-0.79	-0.46
834.6013	PC(40:6)	834.6012	1.7	0.77	0.69	0.09	-0.79	0.11
832.5856	PC(40:7)	832.5851	2	1	0.69	0.11	-1.32	0.66
830.5700	PC(40:8)	830.5684	3.3	0.91	0.69	0.12	-1.73	1.87
768.5907	PC(O-36:4)/PC(P-36:3)	768.59	1.1	0.51	0.68	0.30	-0.18	0.88
766.5751	PC(O-36:5)/PC(P-36:4)	766.5748	6.2	0.86	0.76	0.02	-2.63	0.36
796.6220	PC(O-38:4)/PC(P-38:3)	796.6212	1.3	0.34	0.63	0.07	-0.37	1.01
794.6064	PC(O-38:5)/PC(P-38:4)	794.6054	1.6	0.75	0.69	0.09	-0.70	1.18
792.5907	PC(O-38:6)/PC(P-38:5)	792.59	1.6	0.62	0.68	0.09	-0.64	0.96
820.6220	PC(O-40:6)/PC(P-40:5)	820.6225	2.9	0.69	0.68	0.04	-1.53	-0.58
818.6064	PC(P-40:6)	818.6066	2.2	0.80	0.68	0.06	-1.12	-0.31
744.5543	PE(36:2)	744.5549	2.3	0.95	0.67	0.11	-1.19	-0.71
772.5856	PE(38:2)/PE-NMe2(36:2)	772.5864	1.3	0.26	0.65	0.07	-0.35	-0.99
768.5543	PE(38:4)	768.5556	5.9	0.97	0.74	0.04	-2.56	-1.69
796.5856	PE(40:4)	796.5853	2.1	0.24	0.69	0.003	-1.06	0.37
852.6482	PE(44:4)	852.6456	12	2	0.75	0.01	-3.54	3.15
801.5646	PG(38:3)	801.5607	13	1	0.73	0.01	-3.65	4.78
799.5489	PG(38:4)	799.5446	90	81	0.84	0.08	-6.49	5.41
827.5802	PG(40:4)	827.5759	10	4	0.66	0.05	-3.26	5.22
825.5646	PG(40:5)	825.5614	17	16	0.78	0.10	-4.11	3.89
823.5489	PG(40:6)	823.5455	16	5	0.76	0.04	-4.02	4.19
849.5646	PG(42:7)	849.5606	15	13	0.77	0.07	-3.92	4.62
847.5489	PG(42:8)	847.5464	8	1	0.73	0.01	-3.01	2.93
845.5333	PG(42:9)	845.5304	8	2	0.72	0.03	-2.91	3.42
759.5540	PG(O-36:3)/PG(P-36:2)	759.5501	9	2	0.68	0.01	-3.15	5.08
782.5547	PI-Cer(d34:0)	782.5565	1.7	0.44	0.70	0.06	-0.79	-2.24
798.5496	PI-Cer(t34:0)	798.5476	8	1	0.61	0.07	-3.04	2.51
792.5179	PS(P-38:6)	792.5197	10	5	0.63	0.02	-3.30	-2.16

796.5245	SHexCer(t34:1)	796.5237	273	238	0.84	0.07		-8.09	0.99
824.5558	SHexCer(t36:1)	824.5563	95	86	0.80	0.08		-6.57	-0.60

Appendix A Table 2.39. *A table of the theoretical m/z, lipid name, detected m/z, average fold change in intensity, standard deviation fold change of intensity, ROC area under the curve, paired t-test p value, average log_2 fold change, and mass error in ppm for the protonated ions with an ROC >0.6 and <0.4 for the comparison of FF tissue vs. formalin fixed ammonium formate washed tissue in which formalin fixation in combination with ammonium formate washing hinders detection.*

CALC M/Z	LIPID NAME	DETECTED M/Z	AVG	STD	ROC	P	AVG LOG2 FOLD CHANGE	MASS ERROR (PPM)
678.4346	PS(28:1)	678.4367	4	3	0.40	0.09	1.97	-3.14
690.4710	LPS(30:2)/PS(P-30:1)	690.4728	5	4	0.35	0.08	2.30	-2.57
703.5390	PE-Cer(t36:2)	703.5408	5	2	0.35	0.02	2.24	-2.46
705.5911	SM(d34:0)	705.5918	1.2	0.32	0.40	0.12	0.22	-1.02
706.4659	PS(30:1)	706.4671	5	4	0.37	0.13	2.30	-1.62
706.5387	PC(30:0)/PE-NMe(32:0)	706.5394	1.1	0.46	0.34	0.25	0.07	-1.06
706.5751	LPE(34:0)/PE(O-34:0)	706.5757	4	1	0.40	0.08	1.83	-0.91
720.5543	PE(34:0)/PE-NMe2(32:0)	720.5547	1.0	0.43	0.31	0.25	0.05	-0.51
720.5907	CerP(t40:0)/LPC(32:0)/PC(O-32:0)	720.5912	1.0	0.51	0.39	0.33	0.03	-0.71
772.5492	PS(O-36:3)/PS(P-36:2)	772.5495	7	4	0.35	0.06	2.82	-0.26
774.5649	PS(O-36:2)/PS(P-36:1)	774.5632	29	18	0.24	0.08	4.87	2.17
776.5805	PS(O-36:1)/PS(P-36:0)	776.5804	7	6	0.30	0.09	2.89	0.18

790.5598	PS(36:1)	790.5593	11	7	0.30	0.10	3.47	0.65
798.5649	PS(O-38:4)/PS(P-38:3)	798.5656	11	7	0.26	0.05	3.48	-0.82
800.5805	PS(O-38:3)/PS(P-38:2)	800.5798	9	7	0.29	0.05	3.24	0.93
814.5598	PS(38:3)	814.5609	7	4	0.34	0.10	2.87	-1.27
760.5856	PC(34:1)	760.5842	1.27	0.23	0.61	0.15	0.34	1.86
758.5700	PC(34:2)/PE-NMe(36:2)	758.5685	2	1	0.72	0.74	0.71	1.90

Appendix A Table 2.40. *A table of the theoretical m/z, lipid name, detected m/z, average fold change in intensity, standard deviation fold change of intensity, ROC area under the curve, paired t-test p value, average log_2 fold change, and mass error in ppm for the protonated ions with an ROC >0.6 and <0.4 for the comparison of FF tissue vs. formalin fixed ammonium formate washed tissue in which formalin fixation in combination with ammonium formate washing improves detection.*

CALC M/Z	LIPID NAME	DETECTED M/Z	AVG	STD	ROC	P	AVG LOG2 FOLD CHANGE	MASS ERROR (PPM)
720.5907	CerP(t40:0)/LPC(32:0) / PC(O-32:0)	720.5909	7	5	0.88	0.08	-0.20	-0.24
748.6220	CerP(t42:0)/LPC(34:0) / PC(O-34:0)	748.6218	12	9	0.77	0.08	-0.01	0.32
746.6064	CerP(t42:1)/PC(O-34:1)/ PC(P-34:0)	746.606	10	6	0.89	0.07	-0.52	0.45
925.5207	CL(36:4)/PIP(O-36:4)/ PIP(P-36:3)	925.5219	19	3	0.71	0.08	-1.32	-1.30
775.5278	PA(42:7)	775.5281	10	3	0.71	0.09	-1.32	-0.38
706.5387	PC(30:0)/PE-NMe(32:0)	706.5394	7	7	0.86	0.09	-0.31	-0.96

732.5543	PC(32:1)/PE-NMe(34:1)	732.5539	6	3	0.87	0.12	-0.29	0.56
762.6013	PC(34:0)/PE-NMe(36:0)	762.5995	9	7	0.88	0.09	-0.13	2.39
760.5856	PC(34:1)	760.5842	9	6	0.88	0.10	-0.35	1.86
758.5700	PC(34:2)/PE-NMe(36:2)	758.5686	8	5	0.89	0.09	-0.66	1.82
788.6169	PC(36:1)	788.6159	9	7	0.89	0.08	-0.03	1.30
786.6013	PC(36:2)	786.5994	9	6	0.89	0.08	-0.29	2.41
784.5856	PC(36:3)	784.5843	10	8	0.88	0.08	-0.83	1.75
782.5700	PC(36:4)	782.568	6	4	0.87	0.08	-0.60	2.60
810.6013	PC(38:4)	810.599	9	6	0.86	0.07	-1.04	2.86
808.5856	PC(38:5)	808.5841	10	7	0.85	0.09	-0.69	1.96
806.5700	PC(38:6)	806.5683	12	10	0.84	0.08	-1.04	2.09
838.6326	PC(40:4)	838.6325	12	4	0.70	0.10	-0.44	0.15
836.6169	PC(40:5)	836.616	18	17	0.79	0.08	-1.69	1.07
834.6013	PC(40:6)	834.6006	13	10	0.82	0.07	-2.12	0.77
768.5907	PC(O-36:4)/PC(P-36:3)	768.5899	9	6	0.85	0.08	-0.39	1.06
796.6220	PC(O-38:5)/PC(P-38:4)	796.6206	15	12	0.87	0.08	-0.80	1.84
718.5387	PE(34:1)	718.5386	11	6	0.65	0.14	-1.22	0.10
852.6482	PE(44:4)	852.6453	12	1	0.74	0.07	-1.32	3.47

732.5907	PE(O-36:1)/PE(P-36:0)	732.5902	9	3	0.64	0.11	-1.25	0.65
801.5646	PG(38:3)	801.5606	13	1	0.73	0.07	-1.32	4.92
827.5802	PG(40:4)	827.5758	10	3	0.66	0.10	-1.32	5.34
825.5646	PG(40:5)	825.5606	22	12	0.78	0.07	-2.32	4.86
823.5489	PG(40:6)	823.5453	16	4	0.76	0.09	-2.32	4.35
849.5646	PG(42:7)	849.5609	19	11	0.78	0.08	-2.32	4.26
847.5489	PG(42:8)	847.5461	8	1	0.72	0.08	-2.31	3.38
845.5333	PG(42:9)	845.5303	8	2	0.72	0.08	-1.32	3.46
759.5540	PG(O-36:3)/PG(P-36:2)	759.5501	9	1	0.68	0.08	-1.32	5.20
810.5860	PI-Cer(d36:0)	810.5861	11	3	0.62	0.09	-1.27	-0.05
796.5245	SHexCer(t34:1)	796.5237	344	176	0.79	0.06	-8.73	0.99
824.5558	SHexCer(t36:1)	824.5556	122	63	0.78	0.06	-2.32	0.19

Appendix A Table 2.41. *A table of the theoretical m/z, lipid name, detected m/z, average fold change in intensity, standard deviation fold change of intensity, ROC area under the curve, paired t-test p value, average log_2 fold change, and mass error in ppm for the protonated ions with an ROC >0.6 and <0.4 for the comparison of FF tissue vs. formalin fixed tissue in which formalin fixation hinders detection.*

None

Appendix A Table 2.42. *A table of the theoretical m/z, lipid name, detected m/z, average fold change in intensity, standard deviation fold change of intensity, ROC area under the curve, paired t-test p value, average log_2 fold change, and mass error in ppm for the protonated ions with an ROC >0.6 and <0.4 for the comparison of FF tissue vs. formalin fixed tissue in which formalin fixation improves detection.*

CALC M/Z	LIPID NAME	DETECTED M/Z	AVG	STD	ROC	P	AVG LOG2 FOLD CHANGE	MASS ERROR (PPM)
771.51521	LBPA(34:1)/PG(34:1)	771.5129	8	4	0.88	0.008	-2.93	3.02
797.53086	LBPA(36:2)/PG(36:2)	797.5282	20	5	0.96	0.001	-4.29	3.31
759.55159	LPG(34:0)/PG(O-34:0)	759.5507	2.0	0.19	0.71	0.01	-0.99	1.14
775.52538	PA(40:4)	775.5282	2.2	0.72	0.73	0.3	-1.11	-3.57
782.56758	PC(34:1)	782.5674	1.0	0.28	0.41	0.8	-0.04	0.25
742.53628	PE(34:0)/PE-NMe2(32:0)	742.5341	18	7	0.92	0.001	-4.14	2.90
852.64583	PE(42:1)	852.6453	2.3	0.88	0.79	0.06	-1.23	0.62
772.52571	PE(O-38:6)/PE(P-38:5)	772.5240	51	26	1.00	0.002	-5.66	2.27
800.55701	PE(O-40:6)/PE(P-40:5)	800.5555	11	5	0.90	0.01	-3.46	1.89
744.49441	PE(P-36:5)	744.4945	15	3	0.93	<<0.001	-3.95	-0.10
770.51006	PE(P-38:6)	770.5095	23	7	0.96	0.002	-4.49	0.76
798.54136	PE(P-40:6)	798.5398	70	12	1.00	0.001	-6.13	1.97
796.52571	PE(P-40:7)	796.5244	61	18	0.99	<<0.001	-5.94	1.63
826.57266	PE(P-42:6)	826.5731	3	1	0.82	0.03	-1.68	-0.54
745.49956	PG(32:0)	745.4982	4	2	0.80	0.028	-2.07	1.78
773.53086	PG(34:0)	773.5284	55	8	0.99	0.001	-5.77	3.20
801.56216	PG(36:0)	801.5606	2.5	0.87	0.74	0.1	-1.32	1.93
799.54651	PG(36:1)	799.5444	24	9	0.98	0.002	-4.61	2.70
827.57781	PG(38:1)	827.5761	1.8	0.54	0.64	0.3	-0.85	2.08
825.56216	PG(38:2)	825.5608	4	2	0.88	0.02	-2.03	1.69

823.54651	PG(38:3)	823.5455	2.7	0.99	0.79	0.09	-1.45	1.27
821.53086	PG(38:4)	821.5273	22	11	0.95	0.008	-4.43	4.34
849.56216	PG(40:4)	849.5616	5	2	0.87	0.01	-2.38	0.61
847.54651	PG(40:5)	847.5461	1.8	0.19	0.74	0.02	-0.82	0.47
845.53086	PG(40:6)	845.5306	1.6	0.48	0.72	0.18	-0.65	0.28
785.56724	PG(O-36:1)/PG(P-36:0)	785.5653	4.8	0.38	0.82	<<0.001	-2.25	2.44
792.51554	PS(O-36:4)/PS(P-36:3)	792.5197	2.7	1.4	0.65	0.1	-1.43	-5.21
820.52207	SHexCer(t34:0)	820.5247	38	22	0.99	0.01	-5.23	-3.23
846.53772	SHexCer(t36:1)	846.5416	7	3	0.90	0.007	-2.77	-4.63

Appendix A Table 2.43. *A table of the theoretical m/z, lipid name, detected m/z, average fold change in intensity, standard deviation fold change of intensity, ROC area under the curve, paired t-test p value, average log_2 fold change, and mass error in ppm for the sodiated ions with an ROC >0.6 and <0.4 for the comparison of FF tissue vs. FF ammonium formate washed tissue in which ammonium formate washing hinders detection.*

CALC M/Z	LIPID NAME	DETECTED M/Z	AVG	STD	ROC	P	AVG LOG2 FOLD CHANGE	MASS ERROR (PPM)
742.5727	CerP(t40:0)/LPC(32:0) / PC(O-32:0)	742.57301	1.5	0.46	0.34	0.13	0.57	0.47
770.604	CerP(t42:0)/LPC(34:0) / PC(O-34:0)	770.60662	2	1	0.29	0.01	0.96	3.45
768.5883	CerP(t42:1)/PC(O-34:1)/ PC(P-34:0)	768.59046	1.5	0.34	0.16	0.02	0.55	2.79
766.5727	CerP(t42:2)/PC(O-34:2)/ PC(P-34:1)	766.57448	2	1	0.39	0.05	1.08	2.37
794.604	CerP(t44:2)/PC(O-36:2)/	794.60589	1.2	0.22	0.18	0.19	0.22	2.43

	PC(P-36:1)							
723.4941	PA(36:2)	723.49538	2.6	0.74	0.26	0.11	1.35	1.80
721.4784	PA(36:3)	721.47907	2	1	0.16	0.15	1.19	0.89
756.5519	PC(32:0)	756.55089	1.6	0.88	0.60	0.30	0.70	-1.37
754.5363	PC(32:1)/PE-NMe(34:1)	754.53699	2.4	0.65	0.11	0.01	1.27	0.95
784.5832	PC(34:0)/PE-NMe(36:0)	784.5838	1.1	0.20	0.17	0.32	0.20	0.73
780.5519	PC(34:2)/PE-NMe(36:2)	780.5504	1.7	0.78	0.24	0.04	0.74	-1.96
804.5519	PC(36:4)	804.55117	1.7	0.43	0.13	0.005	0.80	-0.94
832.5832	PC(38:4)	832.58395	3	1	0.29	0.01	1.41	0.87
830.5676	PC(38:5)	830.56796	2	1	0.35	0.02	1.04	0.46
792.5883	PC(O-36:3)/PC(P-36:2)	792.5896	1.4	0.89	0.35	0.39	0.54	1.63
820.6196	PC(O-38:3)/PC(P-38:2)	820.62317	2	1	0.66	0.77	0.73	4.34
798.5625	PS(O-36:1)/PS(P-36:0)	798.56535	70	12	0.06	0.001	6.13	3.58
802.5115	SHexCer(d34:1)	802.51389	2.4	0.64	0.21	0.09	1.29	2.97
725.5573	SM(d34:1)	725.55701	1.1	0.28	0.25	0.37	0.17	-0.46
753.5886	SM(d36:1)	753.58806	2	1	0.15	0.23	1.05	-0.78
811.6669	SM(d40:0)	811.66892	1.2	0.38	0.21	0.25	0.29	2.49

Appendix A Table 2.44. *A table of the theoretical m/z, lipid name, detected m/z, average fold change in intensity, standard deviation fold change of intensity, ROC area under the curve, paired t-test p value, average log_2 fold change, and mass error in ppm for the sodiated ions with an ROC >0.6 and <0.4 for the comparison of FF tissue vs. FF ammonium formate washed tissue in which ammonium formate washing improves detection.*

CALC M/Z	LIPID NAME	DETECTED M/Z	AVG	STD	ROC	P	AVG LOG2 FOLD CHANGE	MASS ERROR (PPM)
651.44780	PE-Cer(d32:3)	651.4466	2.2	1.2	0.24	0.03	-1.14	-1.82

679.47910	PE-Cer(d34:3)	679.4762	3	1.6	0.25	0.01		-1.63	-4.26
802.51151	SHexCer(d34:1)	802.5128	4	4	0.30	0.18		-1.98	1.59

Appendix A Table 2.45. *A table of the theoretical m/z, lipid name, detected m/z, average fold change in intensity, standard deviation fold change of intensity, ROC area under the curve, paired t-test p value, average log_2 fold change, and mass error in ppm for the sodiated ions with an ROC >0.6 and <0.4 for the comparison of FF tissue vs. formalin fixed ammonium formate washed tissue in which the combination of formalin fixation and ammonium formate washing improves detection.*

CALC M/Z	LIPID NAME	DETECTED M/Z	AVG	STD	ROC	P	AVG LOG2 FOLD CHANGE	MASS ERROR (PPM)
768.5883	CerP(t42:1)/PC(O-34:1)/ PC(P-34:0)	768.5898	1.4	0.75	0.68	0.38	0.45	-1.99
766.5727	CerP(t42:2)/PC(O-34:2)/ PC(P-34:1)	766.5735	7	0.52	0.76	<<0.001	2.89	-1.05
796.6196	CerP(t44:1)/PC(O-36:1)/ PC(P-36:0)	796.6206	1.5	1.0	0.63	0.25	0.58	-1.28
794.6040	CerP(t44:2)/PC(O-36:2)/ PC(P-36:1)	794.6049	1.7	0.85	0.69	0.19	0.76	-1.19
771.5152	LBPA(34:1)/PG(34:1)	771.5127	8	5	0.80	0.03	2.91	3.21
797.5309	LBPA(36:2)/PG(36:2)	797.5284	17	6	0.80	<<0.001	4.10	3.07
759.5516	LPG(34:0)/PG(O-34:0)	759.5506	1.8	0.27	0.68	0.03	0.87	1.35
775.5254	PA(40:4)	775.5277	1.9	0.28	0.72	0.03	0.90	-2.99

784.5832	PC(34:0)/PE-NMe(36:0)	784.5839	1.5	0.52	0.71	0.10	0.60	-0.83
782.5676	PC(34:1)	782.5679	1.6	0.51	0.76	0.04	0.63	-0.37
780.5519	PC(34:2)/PE-NMe(36:2)	780.5507	1.2	0.50	0.65	0.39	0.28	1.53
810.5989	PC(36:1)	810.5986	2.0	0.39	0.74	0.003	0.97	0.38
808.5832	PC(36:2)	808.5833	1.9	0.48	0.75	0.02	0.91	-0.04
806.5676	PC(36:3)	806.5679	2.5	0.70	0.80	0.01	1.30	-0.45
838.6302	PC(38:1)	838.6326	2.0	0.3	0.61	0.09	1.03	-2.91
836.6145	PC(38:2)	836.6162	2.6	0.77	0.65	0.002	1.37	-2.02
834.5989	PC(38:3)	834.6007	2.9	0.55	0.69	<<0.001	1.55	-2.16
830.5676	PC(38:5)	830.5684	3	1	0.69	0.13	1.51	-0.99
792.5883	PC(O-36:3)/PC(P-36:2)	792.5895	1.7	1.2	0.68	0.29	0.76	-1.46
820.6196	PC(O-38:3)/PC(P-38:2)	820.6215	3.0	0.29	0.68	0.07	1.61	-2.31
818.6040	PC(O-38:4)/PC(P-38:3)	818.6056	3.6	0.97	0.68	0.00	1.83	-2.05
742.5363	PE(34:0)/PE-NMe2(32:0)	742.5337	15	11	0.79	0.04	3.88	3.44
768.5519	PE(36:1)/PE-NMe2(34:1)	768.5548	3.0	0.87	0.74	0.06	1.57	-3.73
796.5832	PE(38:1)	796.5852	2.9	0.59	0.69	0.02	1.54	-2.41
852.6458	PE(42:1)	852.6454	2.6	0.88	0.75	0.09	1.36	0.49
772.5257	PE(O-38:6)/PE(P-38:5)	772.5238	169	58	0.85	<<0.001	7.40	2.49
800.5570	PE(O-40:6)/PE(P-40:5)	800.5558	12	8	0.80	0.06	3.56	1.49
744.4944	PE(P-36:5)	744.4938	19	10	0.80	0.01	4.22	0.86
770.5101	PE(P-38:6)	770.509	26	10	0.81	0.002	4.69	1.40
798.5414	PE(P-40:6)	798.5401	99	42	0.87	0.002	6.63	1.54
796.5257	PE(P-40:7)	796.5233	81	28	0.84	0.001	6.33	2.99
826.5727	PE(P-42:6)	826.5732	4	1	0.77	0.04	2.13	-0.68

745.4996	PG(32:0)	745.4972	8	4	0.78	0.08	3.04	3.19
773.5309	PG(34:0)	773.5278	73	23	0.85	<<0.001	6.19	3.98
801.5622	PG(36:0)	801.5608	2.7	0.74	0.73	0.06	1.41	1.76
799.5465	PG(36:1)	799.5438	24	10	0.84	0.004	4.58	3.44
827.5778	PG(38:1)	827.5758	1.9	0.71	0.66	0.17	0.90	2.41
825.5622	PG(38:2)	825.5608	5	2	0.78	0.006	2.30	1.71
823.5465	PG(38:3)	823.5453	3.0	0.81	0.76	0.05	1.57	1.50
821.5309	PG(38:4)	821.5275	26	10	0.80	0.001	4.70	4.05
849.5622	PG(40:4)	849.5609	5	1	0.77	0.001	2.21	1.50
847.5465	PG(40:5)	847.5459	1.6	0.21	0.73	0.05	0.70	0.72
845.5309	PG(40:6)	845.5304	1.5	0.37	0.72	0.08	0.57	0.58
785.5672	PG(O-36:1)/PG(P-36:0)	785.5651	5	1	0.77	0.04	2.30	2.79
792.5155	PS(O-36:4)/PS(P-36:3)	792.5192	3	1.7	0.63	0.54	1.40	-4.67
846.5377	SHexCer(t36:1)	846.541	8	3	0.79	0.001	2.97	-3.91

Appendix A Table 2.46. *A table of the theoretical m/z, lipid name, detected m/z, average fold change in intensity, standard deviation fold change of intensity, ROC area under the curve, paired t-test p value, average log_2 fold change, and mass error in ppm for the sodiated ions with an ROC >0.6 and <0.4 for the comparison of FF tissue vs. formalin fixed ammonium formate washed tissue in which the combination of formalin fixation and ammonium formate washing hinders detection.*

CALC M/Z	LIPID NAME	DETECTED M/Z	AVG	STD	ROC	P	AVG LOG2 FOLD CHANGE	MASS ERROR (PPM)
772.5468	LPS(34:0)/PS(O-34:0)	772.5493	1.3	0.25	0.38	0.12	-0.41	-3.13
756.5519	PC(32:0)	756.5503	2	1	0.75	0.002	-1.02	2.10
834.5989	PC(38:3)	834.6006	2.3	2.2	0.32	0.31	-1.23	-2.04
800.5781	PS(O-36:0)	800.5803	2.0	0.65	0.33	0.06	-1.01	-2.71
798.5625	PS(O-36:1)/PS(P-36:0)	798.5653	2.0	0.36	0.30	0.03	-0.99	-3.53

651.4478	PE-Cer(d32:3)	651.4468	1.3	0.81	0.38	0.28	-0.40	1.48
782.5676	PC(34:1)	782.5678	1.1	0.22	0.36	0.58	-0.08	-0.26

Appendix A Table 2.47. *A table of the theoretical m/z, lipid name, detected m/z, average fold change in intensity, standard deviation fold change of intensity, ROC area under the curve, paired t-test p value, average log_2 fold change, and mass error in ppm for the sodiated ions with an ROC >0.6 and <0.4 for the comparison of formalin fixed tissue vs. formalin fixed ammonium formate washed tissue in which ammonium formate washing hinders detection.*

CALC M/Z	LIPID NAME	DETECTED M/Z	AVG	STD	ROC	P	AVG LOG2 FOLD CHANGE	MASS ERROR (PPM)
679.4791	PE-Cer(d34:3)	679.4761	2	1	0.36	0.91	0.77	4.44
768.5883	CerP(t42:1)/ PC(O-34:1)/ PC(P-34:0)	768.5898	3	2	0.28	0.19	1.36	-1.98
770.6040	CerP(t42:0)/ LPC(34:0)/ PC(O-34:0)	770.6069	3	2	0.29	0.08	1.76	-3.75
784.5832	PC(34:0)/PE-NMe(36:0)	784.5841	1.6	0.84	0.34	0.39	0.65	-1.13
792.5883	PC(O-36:3)/PC(P-36:2)	792.5892	4	3	0.29	0.19	1.92	-1.11
794.6040	CerP(t44:2)/ PC(O-36:2)/ PC(P-36:1)	794.6052	1	1	0.33	0.80	0.57	-1.60
796.5832	PE(38:1)	796.5853	3	1	0.30	0.12	1.41	-2.55
796.6196	CerP(t44:1)/ PC(O-36:1)/ PC(P-36:0)	796.6211	4	3	0.29	0.11	2.05	-1.88
802.5115	SHexCer(d34:1)	802.513	1.1	0.25	0.35	0.43	0.12	-1.89

806.5676	PC(36:3)	806.5679	1.1	0.66	0.36	0.83		0.17	-0.41
808.5832	PC(36:2)	808.5833	1.0	0.61	0.37	0.60		0.05	-0.10
812.6145	PC(36:0)	812.6128	1.1	0.77	0.30	0.98		0.19	2.10
818.6040	PC(O-38:4)/PC(P-38:3)	818.6055	2	1	0.35	0.18		1.20	-1.89
836.6145	PC(38:2)	836.616	1.0	0.58	0.31	0.46		-0.01	-1.76

Appendix A Table 2.48. *A table of the theoretical m/z, lipid name, detected m/z, average fold change in intensity, standard deviation fold change of intensity, ROC area under the curve, paired t-test p value, average log_2 fold change, and mass error in ppm for the sodiated ions with an ROC >0.6 and <0.4 for the comparison of formalin fixed tissue vs. formalin fixed ammonium formate washed tissue in which ammonium formate washing improves detection.*

CALC M/Z	LIPID NAME	DETECTED M/Z	AVG	STD	ROC	P	AVG LOG2 FOLD CHANGE	MASS ERROR (PPM)
768.5883	CerP(t42:1)/ PC(O-34:1)/ PC(P-34:0)	768.5898	1.4	0.75	0.68	0.38	0.45	-1.99
766.5727	CerP(t42:2)/ PC(O-34:2)/ PC(P-34:1)	766.5735	7	0.52	0.76	<<0.001	2.89	-1.05
796.6196	CerP(t44:1)/PC(O-36:1)/ PC(P-36:0)	796.6206	1.5	1.0	0.63	0.25	0.58	-1.28
794.6040	CerP(t44:2)/PC(O-36:2)/ PC(P-36:1)	794.6049	1.7	0.85	0.69	0.19	0.76	-1.19
771.5152	LBPA(34:1)/PG(34:1)	771.5127	8	5	0.80	0.03	2.91	3.21
797.5309	LBPA(36:2)/PG(36:2)	797.5284	17	6	0.80	<<0.001	4.10	3.07

759.5516	LPG(34:0)/PG(O-34:0)	759.5506	1.8	0.27	0.68	0.03	0.87	1.35
775.5254	PA(40:4)	775.5277	1.9	0.28	0.72	0.03	0.90	-2.99
784.5832	PC(34:0)/PE-NMe(36:0)	784.5839	1.5	0.52	0.71	0.10	0.60	-0.83
782.5676	PC(34:1)	782.5679	1.6	0.51	0.76	0.04	0.63	-0.37
780.5519	PC(34:2)/PE-NMe(36:2)	780.5507	1.2	0.50	0.65	0.39	0.28	1.53
810.5989	PC(36:1)	810.5986	2.0	0.39	0.74	0.003	0.97	0.38
808.5832	PC(36:2)	808.5833	1.9	0.48	0.75	0.02	0.91	-0.04
806.5676	PC(36:3)	806.5679	2.5	0.70	0.80	0.01	1.30	-0.45
838.6302	PC(38:1)	838.6326	2.0	0.3	0.61	0.09	1.03	-2.91
836.6145	PC(38:2)	836.6162	2.6	0.77	0.65	0.002	1.37	-2.02
834.5989	PC(38:3)	834.6007	2.9	0.55	0.69	<<0.001	1.55	-2.16
830.5676	PC(38:5)	830.5684	3	1	0.69	0.13	1.51	-0.99
792.5883	PC(O-36:3)/PC(P-36:2)	792.5895	1.7	1.2	0.68	0.29	0.76	-1.46
820.6196	PC(O-38:3)/PC(P-38:2)	820.6215	3.0	0.29	0.68	0.07	1.61	-2.31
818.6040	PC(O-38:4)/PC(P-38:3)	818.6056	3.6	0.97	0.68	0.00	1.83	-2.05
742.5363	PE(34:0)/PE-NMe2(32:0)	742.5337	15	11	0.79	0.04	3.88	3.44
768.5519	PE(36:1)/PE-NMe2(34:1)	768.5548	3.0	0.87	0.74	0.06	1.57	-3.73
796.5832	PE(38:1)	796.5852	2.9	0.59	0.69	0.02	1.54	-2.41
852.6458	PE(42:1)	852.6454	2.6	0.88	0.75	0.09	1.36	0.49
772.5257	PE(O-38:6)/PE(P-38:5)	772.5238	169	58	0.85	<<0.001	7.40	2.49
800.5570	PE(O-40:6)/PE(P-40:5)	800.5558	12	8	0.80	0.06	3.56	1.49
744.4944	PE(P-36:5)	744.4938	19	10	0.80	0.01	4.22	0.86
770.5101	PE(P-38:6)	770.509	26	10	0.81	0.002	4.69	1.40
798.5414	PE(P-40:6)	798.5401	99	42	0.87	0.002	6.63	1.54

796.5257	PE(P-40:7)	796.5233	81	28	0.84	0.001	6.33	2.99
826.5727	PE(P-42:6)	826.5732	4	1	0.77	0.04	2.13	-0.68
745.4996	PG(32:0)	745.4972	8	4	0.78	0.08	3.04	3.19
773.5309	PG(34:0)	773.5278	73	23	0.85	<<0.001	6.19	3.98
801.5622	PG(36:0)	801.5608	2.7	0.74	0.73	0.06	1.41	1.76
799.5465	PG(36:1)	799.5438	24	10	0.84	0.004	4.58	3.44
827.5778	PG(38:1)	827.5758	1.9	0.71	0.66	0.17	0.90	2.41
825.5622	PG(38:2)	825.5608	5	2	0.78	0.006	2.30	1.71
823.5465	PG(38:3)	823.5453	3.0	0.81	0.76	0.05	1.57	1.50
821.5309	PG(38:4)	821.5275	26	10	0.80	0.001	4.70	4.05
849.5622	PG(40:4)	849.5609	5	1	0.77	0.001	2.21	1.50
847.5465	PG(40:5)	847.5459	1.6	0.21	0.73	0.05	0.70	0.72
845.5309	PG(40:6)	845.5304	1.5	0.37	0.72	0.08	0.57	0.58
785.5672	PG(O-36:1)/PG(P-36:0)	785.5651	5	1	0.77	0.04	2.30	2.79
792.5155	PS(O-36:4)/PS(P-36:3)	792.5192	3	1.7	0.63	0.54	1.40	-4.67
846.5377	SHexCer(t36:1)	846.541	8	3	0.79	0.001	2.97	-3.91

Appendix A Table 2.49. *A table of the theoretical m/z, lipid name, detected m/z, average fold change in intensity, standard deviation fold change of intensity, ROC area under the curve, paired t-test p value, average log_2 fold change, and mass error in ppm for the sodiated ions with an ROC >0.6 and <0.4 for the comparison of FF tissue vs. formalin fixed tissue in which formalin fixation hinders detection. No lipids showed improved detection after fixation in the sodiated adduct.*

CALC M/Z	LIPID NAME	DETECTED M/Z	AVG	STD	ROC	P	AVG LOG2 FOLD CHANGE	MASS ERROR (PPM)
597.2806	LPI(O-16:0)	597.2817	1.6	0.98	0.69	0.33	0.21	-1.81
602.3224	PC(20:1)	602.3202	7	9	0.66	0.34	0.82	3.71
682.4578	CerP(d36:2)	682.4600	21	15	0.76	0.08	1.33	-3.27

711.4367	PA(34:2)	711.4377	9	3	0.61	0.20		0.96	-1.37
713.4524	PA(34:1)	713.4527	54	40	0.92	0.04		1.74	-0.48
734.4527	LPE(34:5)/PE(P-34:4)	734.4508	1.6	0.52	0.69	0.05		0.20	2.59
737.4524	PA(36:3)	737.4521	23	11	0.80	0.04		1.37	0.41
739.4680	PA(36:2)	739.4681	31	23	0.85	0.04		1.49	-0.17
741.5313	SM(d34:1)	741.5308	179	103	0.98	0.02		2.25	0.67
743.5469	SM(d34:0)	743.5463	6	4	0.62	0.10		0.79	0.83
744.4946	PC(30:0)	744.4946	58	30	0.93	0.01		1.77	0.02
758.5102	PE(34:0)/PE-NMe2(32:0)	758.5107	17	10	0.85	0.02		1.23	-0.59
758.5466	CerP(t40:0)/ LPC(32:0)/ PC(O-32:0)	758.5476	20	9	0.88	0.01		1.31	-1.25
761.4524	PA(38:5)	761.4528	13	6	0.74	0.11		1.12	-0.61
765.4837	PA(38:3)	765.4848	6	1	0.60	0.19		0.76	-1.48
769.5626	SM(d36:1)	769.5612	4	3	0.74	0.09		0.61	1.81
770.5102	PC(32:1)/PE-NMe(34:1)	770.5097	51	17	0.96	0.04		1.71	0.71
772.5259	PC(32:0)	772.5246	38	28	1.00	0.05		1.58	1.59
775.5255	LPG(34:0)/PG(O-34:0)	775.5278	7	5	0.73	0.11		0.84	-2.98
776.4997	LPC(34:5)/PC(P-34:4)	776.4984	1.1	0.38	0.66	0.98		0.03	1.65

782.5102	PE(36:2)	782.5107	4	2	0.62	0.11	0.65	-0.66
782.5466	CerP(t42:2)/ PC(O-34:2)/ PC(P-34:1)	782.5480	4	3	0.61	0.18	0.63	-1.81
784.5259	PE(36:1)/PE-NMe2(34:1)	784.5270	6	4	0.67	0.17	0.77	-1.38
784.5623	CerP(t42:1)/ PC(O-34:1)/PC(O-34:1)	784.5624	30	21	0.91	0.04	1.48	-0.14
786.4840	PE(P-38:6)	786.4841	4	3	0.64	0.19	0.58	-0.14
789.4837	PA(40:5)	789.4836	6	3	0.62	0.12	0.80	0.05
790.5153	PE(O-38:5)/PE(P-38:4)	790.5130	1.0	0.25	0.77	0.97	0.00	2.92
792.5310	PE(O-38:4)/PE(P-38:3)	792.5288	1.6	0.74	0.60	0.36	0.19	2.73
794.5102	PC(34:3)	794.5106	5	4	0.64	0.21	0.67	-0.51
796.5259	PC(34:2)/PE-NMe(36:2)	796.5242	102	104	0.99	0.02	2.01	2.13
798.5415	PC(34:1)	798.5410	47	60	0.71	0.15	1.68	0.70
800.5572	PC(34:0)/PE-NMe(36:0)	800.5560	45	34	0.90	0.04	1.65	1.43
806.5102	PE(38:4)	806.5097	11	13	0.61	0.16	1.06	0.69
806.5466	PC(O-36:4)/PC(P-36:3)	806.5464	12	8	0.79	0.05	1.09	0.31
816.5310	PE(O-40:6)/PE(P-40:5)	816.5295	1.0	0.71	0.62	0.56	0.01	1.80
818.5466	PE(O-40:5)/PE(P-40:4)	818.5449	1.2	0.53	0.75	0.89	0.08	2.09
820.5259	PC(36:4)	820.5250	165	149	0.99	0.07	2.22	1.01

822.5415	PC(36:3)	822.5408	45	39	0.93	0.07		1.65	0.84
824.5572	PC(36:2)	824.5563	91	85	0.97	0.08		1.96	1.06
826.5728	PC(36:1)	826.5734	15	10	0.82	0.08		1.17	-0.71
830.5102	PE(40:6)	830.5098	7	6	0.67	0.13		0.87	0.46
832.5623	PC(O-38:5)/PC(P-38:4)	832.5636	10	6	0.78	0.08		0.98	-1.56
844.5259	PC(38:6)	844.5275	15	11	0.85	0.09		1.18	-1.94
846.5415	PC(38:5)	846.5418	27	23	0.90	0.07		1.42	-0.37
848.5572	PC(38:4)	848.5582	43	29	0.96	0.03		1.63	-1.19
849.6252	SM(d42:3)	849.6261	10	5	0.77	0.06		0.99	-1.10
851.6408	SM(d42:2)	851.6409	35	26	0.92	0.04		1.54	-0.02
872.5572	PC(40:6)	872.5590	5	2	0.63	0.11		0.73	-2.13
925.5208	Glc-GP(38:4)/PI(38:4)	925.5223	10	5	0.71	0.06		1.00	-1.55

Appendix A Table 2.50. *A table of the theoretical m/z, lipid name, detected m/z, average fold change in intensity, standard deviation fold change of intensity, ROC area under the curve, paired t-test p value, average log_2 fold change, and mass error in ppm for the potassiated ions with an ROC >0.6 and <0.4 for the comparison of FF tissue vs. FF ammonium formate washed tissue in which ammonium formate washing hinders detection.*

CALC M/Z	LIPID NAME	DETECTED M/Z	AVG	STD	ROC	P	AVG LOG2 FOLD CHANGE	MASS ERROR (PPM)
706.46603	HexCer(d32:3)	706.4672	2.7	0.84	0.37	0.23	0.43	-1.66

745.47858	LPG(32:1)/PG(O-32:1)/ PG(P-32:0)	745.4800	4	2	0.40	0.22	-2.17	-1.96
757.55135	PA(O-38:0)	757.5553	4	2	0.28	0.03	-1.47	-5.21
762.48400	PE(O-36:5)/PE(P-36:4)	762.4812	1.5	0.78	0.71	0.37	-0.24	3.62
797.59388	SM(d38:1)	797.5910	5.7	0.79	0.35	0.03	-1.69	3.59
802.51530	PC(P-36:5)	802.5142	4	1	0.36	0.09	-2.47	1.35
810.58614	HexCer(t38:1)	810.5859	5	2	0.34	0.07	-1.28	0.26

Appendix A Table 2.51. *A table of the theoretical m/z, lipid name, detected m/z, average fold change in intensity, standard deviation fold change of intensity, ROC area under the curve, paired t-test p value, average log_2 fold change, and mass error in ppm for the potassiated ions with an ROC >0.6 and <0.4 for the comparison of FF tissue vs. FF ammonium formate washed tissue in which ammonium formate washing improves detection.*

CALC M/Z	LIPID NAME	DETECTED M/Z	AVG	STD	ROC	P	AVG LOG2 FOLD CHANGE	MASS ERROR (PPM)
639.2912	LPI(18:0)	639.2914	1.1	0.19	0.36	0.50	-0.08	-0.30
757.5514	PA(O-38:0)	757.5544	1.5	0.29	0.68	0.05	-0.54	-4.00

Appendix A Table 2.52. *A table of the theoretical m/z, lipid name, detected m/z, average fold change in intensity, standard deviation fold change of intensity, ROC area under the curve, paired t-test p value, average log_2 fold change, and mass error in ppm for the potassiated ions with an ROC >0.6 and <0.4 for the comparison of formalin fixed tissue vs. formalin fixed ammonium formate washed tissue in which ammonium formate washing hinders detection.*

CALC M/Z	LIPID NAME	DETECTED M/Z	AVG	STD	ROC	P	AVG LOG2 FOLD CHANGE	MASS ERROR (PPM)
706.466026	HexCer(d32:3)	706.4671	3	4	0.36	0.34	1.74	-1.53
782.554842	HexCer(t36:1)	782.5563	1.4	0.36	0.37	0.12	0.47	-1.91

734.4527	LPE(34:5)/PE(P-34:4)	734.4519	1.4	0.75	0.35	0.26		0.52	1.13
597.28061	LPI(O-16:0)	597.2817	1.5	0.56	0.37	0.29		0.59	-1.84
783.567001	PA(O-40:1)/PA(P-40:0)	783.5654	2	1	0.34	0.05		1.11	2.04
809.58265	PA(O-42:2)/PA(P-42:1)	809.5868	3	2	0.31	0.12		1.40	-5.14
602.322415	PC(20:1)	602.3201	3	2	0.39	0.45		1.45	3.88
802.5153	PC(P-36:5)	802.514	1.3	0.25	0.35	0.12		0.34	1.62
762.484	PE(O-36:5)/PE(P-36:4)	762.4812	2	1	0.35	0.26		0.89	3.63
792.53095	PE(O-38:4)/PE(P-38:3)	792.5293	2.0	0.65	0.41	0.12		0.97	2.06
816.53095	PE(O-40:6)/PE(P-40:5)	816.5285	2.2	0.73	0.25	0.11		1.16	3.05
760.46835	PE(P-36:5)	760.4675	1.4	0.32	0.30	0.24		0.49	1.10
788.49965	PE(P-38:5)/PE(O-38:6)	788.4996	1.4	0.21	0.36	0.25		0.45	0.01
814.5153	PE(P-40:6)	814.5141	2.1	0.54	0.28	0.12		1.07	1.53

Appendix A Table 2.53. *A table of the theoretical m/z, lipid name, detected m/z, average fold change in intensity, standard deviation fold change of intensity, ROC area under the curve, paired t-test p value, average log_2 fold change, and mass error in ppm for the potassiated ions with an ROC >0.6 and <0.4 for the comparison of formalin fixed tissue vs. formalin fixed ammonium formate washed tissue in which ammonium formate washing improves detection.*

CALC M/Z	LIPID NAME	DETECTED M/Z	AVG	STD	ROC	P	AVG LOG2 FOLD CHANGE	MASS ERROR (PPM)
758.5466	CerP(t40:0)/LPC(32:0) / PC(O-32:0)	758.5448	5	4	0.70	0.14	-2.35	2.39

784.5623	CerP(t42:1)/PC(O-34:1) /PC(P-34:0)	784.5622	6	2	0.79	0.01	-2.55	0.11
925.5208	Glc-GP(38:4)/PI(38:4)	925.5223	3.8	0.76	0.72	0.09	-1.94	-1.61
782.5548	HexCer(t36:1)	782.5566	2.63	0.93	0.70	0.11	-1.39	-2.18
775.5255	LPG(34:0)/PG(O-34:0)	775.5278	1.9	0.23	0.72	0.09	-0.90	-2.93
713.4524	PA(34:1)	713.4527	13	7	0.81	0.07	-3.68	-0.51
739.468	PA(36:2)	739.4676	12	4	0.80	0.11	-3.55	0.52
737.4524	PA(36:3)	737.4519	6	1	0.77	0.08	-2.67	0.58
761.4524	PA(38:5)	761.4527	3	1	0.71	0.17	-1.46	-0.46
785.5827	PA(O-40:0)	785.581	2.1	0.50	0.67	0.08	-1.08	2.10
783.567	PA(O-40:1)/PA(P-40:0)	783.5651	1.4	0.69	0.68	0.19	-0.49	2.49
744.4946	PC(30:0)/PE-NMe(32:0)	744.494	19	9	0.80	0.01	-4.22	0.72
772.5259	PC(32:0)	772.5245	169	52	0.85	<<0.001	-7.40	1.79
770.5102	PC(32:1)/PE-NMe(34:1)	770.5098	26	9	0.81	0.002	-4.69	0.59
800.5572	PC(34:0)/PE-NMe(36:0)	800.5558	12	7	0.80	0.07	-3.56	1.72
798.5415	PC(34:1)	798.5401	99	38	0.87	0.002	-6.63	1.78
796.5259	PC(34:2)/PE-NMe(36:2)	796.5239	81	25	0.84	0.001	-6.33	2.44
794.5102	PC(34:3)	794.5104	1.2	0.14	0.63	0.35	-0.21	-0.18
826.5728	PC(36:1)	826.573	4.4	0.99	0.77	0.09	-2.13	-0.24
824.5572	PC(36:2)	824.556	37	12	0.80	0.003	-5.20	1.45
822.5415	PC(36:3)	822.5406	15	6	0.80	0.01	-3.87	1.10
820.5259	PC(36:4)	820.5246	60	19	0.82	0.001	-5.91	1.51
848.5572	PC(38:4)	848.558	24	16	0.78	0.05	-4.59	-0.99
846.5415	PC(38:5)	846.5418	8	2	0.79	0.002	-2.97	-0.34
844.5259	PC(38:6)	844.5272	3	1	0.80	0.06	-1.63	-1.62
872.5572	PC(40:6)	872.559	1.9	0.47	0.66	0.13	-0.94	-2.10

806.5466	PC(O-36:4)/PC(P-36:3)	806.5465	4	1	0.76	0.11	-2.03	0.15
832.5623	PC(O-38:5)/PC(P-38:4)	832.5633	2.8	0.73	0.75	0.11	-1.47	-1.24
758.5102	PE(34:0)/PE-NMe2(32:0)	758.5101	5	1	0.78	0.09	-2.38	0.11
806.5102	PE(38:4)	806.5097	5	4	0.74	0.20	-2.38	0.59
830.5102	PE(40:6)	830.5101	2.4	0.62	0.70	0.11	-1.26	0.10
790.5153	PE(O-38:5)/PE(P-38:4)	790.5123	2	1	0.63	0.003	-1.29	3.85
818.5466	PE(O-40:5)/PE(P-40:4)	818.5446	3	1	0.63	0.12	-1.61	2.42
786.484	PE(P-38:6)	786.4837	1.7	0.38	0.67	0.13	-0.80	0.36
849.6252	SM(d42:3)	849.6261	2.4	0.75	0.74	0.13	-1.27	-1.03

Appendix A Table 2.54. *A table of the theoretical m/z, lipid name, detected m/z, average fold change in intensity, standard deviation fold change of intensity, ROC area under the curve, paired t-test p value, average log_2 fold change, and mass error in ppm for the potassiated ions with an ROC >0.6 and <0.4 for the comparison of FF tissue vs. formalin fixed ammonium formate washed tissue in which the combination of formalin fixation and ammonium formate washing hinders detection.*

CALC M/Z	LIPID NAME	DETECTED M/Z	AVG	STD	ROC	P	AVG LOG2 FOLD CHANGE	MASS ERROR (PPM)
706.466	HexCer(d32:3)	706.467	3	4	0.37	0.24	1.67	-1.36
760.4684	PE(P-36:5)	760.4669	1.2	0.39	0.37	0.32	0.23	1.96
778.5153	LPC(34:4)/PC(O-34:4)/PC(P-34:3)	778.514	2	2	0.31	0.36	1.26	1.66
790.5599	HexCer(d38:3)	790.5589	4	2	0.30	0.03	1.89	1.32
802.5153	PC(P-36:5)	802.5134	2	1	0.30	0.19	0.83	2.39

Appendix A Table 2.55. *A table of the theoretical m/z, lipid name, detected m/z, average fold change in intensity, standard deviation fold change of intensity, ROC area under the curve, paired t-test p value, average log_2 fold change, and mass error in ppm for the potassiated ions with an ROC >0.6 and <0.4 for the comparison of FF tissue vs. formalin fixed ammonium formate washed tissue in which the combination of formalin fixation and ammonium formate washing improves detection.*

CALC M/Z	LIPID NAME	DETECTED M/Z	AVG	STD	ROC	P	AVG LOG2 FOLD CHANGE	MASS ERROR (PPM)
682.457785	CerP(d36:2)	682.4592	5	2	0.28	0.09	-2.31	2.12
758.5466	CerP(t40:0)/LPC(32:0)/PC(O-32:0)	758.5471	5	4	0.21	0.12	-2.39	0.66
784.56225	CerP(t42:1)	784.5627	7	2	0.18	0.02	-2.78	0.52
925.520841	Glc-GP(38:4)/PI(38:4)	925.5222	3.8	0.94	0.28	0.09	-1.94	1.47
810.586142	HexCer(t38:1)	810.5859	2.0	0.49	0.38	0.11	-1.02	-0.27
776.49965	LPC(34:5)/PC(P-34:4)	776.4975	4	2	0.33	0.37	-2.00	-2.73
734.4527	LPE(34:5)/PE(P-34:4)	734.4511	2.0	0.75	0.35	0.11	-0.98	-2.21
775.525531	LPG(34:0)/PG(O-34:0)	775.5275	1.9	0.28	0.28	0.09	-0.90	2.54
713.452366	PA(34:1)	713.4525	17	3	0.19	0.08	-4.05	0.23
711.436715	PA(34:2)	711.4373	1.5	0.59	0.41	0.34	-0.57	0.82
739.468016	PA(36:2)	739.4676	12	5	0.20	0.11	-3.55	-0.51
737.452366	PA(36:3)	737.4522	6	1	0.23	0.08	-2.67	-0.28
761.452366	PA(38:5)	761.4527	3	1	0.29	0.17	-1.46	0.44
785.58265	PA(O-40:0)	785.5806	4.6	0.42	0.24	0.07	-2.21	2.58

783.567001	PA(O-40:1)/PA(P-40:0)	783.5651	4	4	0.28	0.12	-2.14	-2.38
744.494565	PC(30:0)/PE-NMe(32:0)	744.4937	22	9	0.16	0.04	-4.44	-1.16
772.525865	PC(32:0)	772.5244	224	36	0.08	0.02	-7.81	-1.96
770.510215	PC(32:1)/PE-NMe(34:1)	770.5089	30	7	0.14	0.02	-4.89	-1.69
800.557164	PC(34:0)/PE-NMe(36:0)	800.5558	15	4	0.19	0.08	-3.93	-1.70
798.541515	PC(34:1)	798.5397	115	27	0.09	0.02	-6.85	-2.25
796.525865	PC(34:2)/PE-NMe(36:2)	796.5238	92	13	0.10	0.02	-6.53	-2.66
794.510215	PC(34:3)	794.5101	1.2	0.20	0.37	0.35	-0.21	-0.16
826.572815	PC(36:1)	826.5727	4	1	0.23	0.09	-2.13	-0.11
824.557164	PC(36:2)	824.556	38	15	0.12	0.03	-5.26	-1.41
822.541515	PC(36:3)	822.5403	17	6	0.15	0.03	-4.06	-1.51
848.557164	PC(38:4)	848.5577	22	20	0.13	0.13	-4.46	0.68
846.541515	PC(38:5)	846.5412	8	3	0.17	0.03	-3.06	-0.38
844.525865	PC(38:6)	844.5271	3	1	0.20	0.06	-1.63	1.43
872.557164	PC(40:6)	872.5591	1.9	0.57	0.34	0.13	-0.94	2.18
806.5466	PC(O-36:4)/PC(P-36:3)	806.5462	6	4	0.26	0.07	-2.49	0.46
804.53095	PC(O-36:5)/PC(P-36:4)	804.5282	2	1	0.35	0.45	-0.71	3.47
832.56225	PC(O-38:5)/PC(P-38:4)	832.5635	3	0.89	0.25	0.11	-1.47	1.50

830.5466	PC(O-38:6)/PC(P-38:5)	830.5442	2	1	0.36	0.71	-1.02	2.88
758.510215	PE(34:0)/PE-NMe2(32:0)	758.5103	5	2	0.21	0.09	-2.38	0.07
806.510215	PE(38:4)	806.509	6	4	0.07	0.06	-2.49	1.56
830.510215	PE(40:6)	830.5102	2.4	0.76	0.30	0.11	-1.26	-0.04
762.484	PE(O-36:5)/PE(P-36:4)	762.4808	3	2	0.33	0.03	-1.52	-4.22
792.53095	PE(O-38:4)/PE(P-38:3)	792.5283	2	2	0.33	0.57	-1.28	3.41
790.5153	PE(O-38:5)/PE(P-38:4)	790.5124	1.4	0.83	0.39	0.40	-0.51	-3.69
788.49965	PE(O-38:6)/PE(P-38:5)	788.4987	2	2	0.38	0.87	-1.15	1.26
818.5466	PE(O-40:5)/PE(P-40:4)	818.5443	2	2	0.40	0.96	-0.63	2.79
816.53095	PE(O-40:6)/PE(P-40:5)	816.5281	6	3	0.27	0.08	-2.52	-3.55
786.484	PE(P-38:6)	786.4839	1.7	0.46	0.31	0.13	-0.80	0.11
820.525865	PE(P-40:4)	820.5238	65	20	0.10	0.03	-6.03	-2.48
814.5153	PE(P-40:6)	814.5137	3	2	0.72	0.59	-1.59	1.98
743.546934	SM(d34:0)	743.546	3	1	0.31	0.12	-1.61	-1.28
741.531284	SM(d34:1)	741.5309	65	26	0.13	0.04	-6.02	-0.46
769.562584	SM(d36:1)	769.5617	5.2	0.11	0.23	0.07	-2.38	-1.11
851.640834	SM(d42:2)	851.6405	8	4	0.18	0.05	-3.00	-0.44
849.625184	SM(d42:3)	849.6257	2.4	0.91	0.26	0.13	-1.27	0.58

Appendix A Table 2.56. *A table of the theoretical m/z, lipid name, detected m/z, average fold change in intensity, standard deviation fold change of intensity, ROC area under the curve, paired t-test p value, average log_2 fold change, and mass error in ppm for the potassiated ions with an ROC >0.6 and <0.4 for the comparison of FF tissue vs. formalin fixed tissue in which formalin fixation hinders detection.*

CALC M/Z	LIPID NAME	DETECTED M/Z	AVG	STD	ROC	P	AVG LOG2 FOLD CHANGE	MASS ERROR (PPM)
778.5153	LPC(34:4)/ PC(O-34:4)/ PC(P-34:3)	778.5143	4	3	0.65	0.08	4.32	1.28
757.5514	PA(O-38:0)	757.5541	1.4	0.55	0.67	0.13	1.11	-3.64

Appendix A Table 2.57. *A table of the theoretical m/z, lipid name, detected m/z, average fold change in intensity, standard deviation fold change of intensity, ROC area under the curve, paired t-test p value, average log_2 fold change, and mass error in ppm for the potassiated ions with an ROC >0.6 and <0.4 for the comparison of FF tissue vs. formalin fixed tissue in which formalin fixation improves detection.*

	PROTONATED	SODIATED	POTASSIATED
IMPROVES DETECTION	0	11	2
HINDERS DETECTION	1	3	0

Appendix A Table 2.58. PC Lipids: Formalin Fixed vs. Formalin Fixed Ammonium Formate Washing*. A table showing the number of PC lipids divided into adducts that were improved or hindered in detection after formalin fixed ammonium formate washing when compared to formalin fixed tissues in positive ion mode.*

	PROTONATED	SODIATED	POTASSIATED
IMPROVES DETECTION	0	0	1
HINDERS DETECTION	20	12	19

Appendix A Table 2.59. PC Lipids: FF vs. Formalin Fixed*. A table showing the number of PC lipids divided into adducts that were improved or hindered in detection after formalin fixation when compared to FF tissues in positive ion mode.*

	PROTONATED	SODIATED	POTASSIATED
IMPROVES DETECTION	17	14	1
HINDERS DETECTION	2	1	21

Appendix A Table 2.60. PC Lipids: FF vs. FF Ammonium Formate Washing*. A table showing the number of PC lipids divided into adducts that were improved or hindered in detection after FF ammonium formate washing when compared to FF tissues in positive ion mode.*

	PROTONATED	SODIATED	POTASSIATED
IMPROVES DETECTION	3	0	2
HINDERS DETECTION	20	17	19

Appendix A Table 2.61. PC Lipids: FF vs. Formalin Fixed Ammonium Formate Washed*. A table showing the number of PC lipids divided into adducts that were improved or hindered in detection after formalin fixation and ammonium formate washing when compared to FF tissues in positive ion mode.*

	PROTONATED	SODIATED	POTASSIATED
IMPROVES DETECTION	5	3	1
HINDERS DETECTION	5	9	13

Appendix A Table 2.62. PE Lipids: FF vs. FF Ammonium Formate Washing*. A table showing the number of PE lipids divided into adducts that were improved or hindered in detection after FF ammonium formate washing when compared to FF tissues in positive ion mode.*

	PROTONATED	SODIATED	POTASSIATED
IMPROVES DETECTION	0	3	7
HINDERS DETECTION	0	1	0

Appendix A Table 2.63. PE Lipids: Formalin Fixed vs. Formalin Fixed Ammonium Formate Washing*. A table showing the number of PE lipids divided into adducts that were improved or hindered in detection after formalin fixed ammonium formate washing when compared to formalin fixed tissues in positive ion mode.*

	PROTONATED	SODIATED	POTASSIATED
IMPROVES DETECTION	0	0	0
HINDERS DETECTION	7	11	17

Appendix A Table 2.64. PE Lipids: FF vs. Formalin Fixed*. A table showing the number of PE lipids divided into adducts that were improved or hindered in detection after formalin fixation when compared to FF tissues in positive ion mode.*

	PROTONATED	SODIATED	POTASSIATED
IMPROVES DETECTION	3	6	2
HINDERS DETECTION	3	2	4

Appendix A Table 2.65. Cer Lipids: FF vs. FF Ammonium Formate Washing*. A table showing the number of Cer lipids divided into adducts that were improved or hindered in detection after FF ammonium formate washing when compared to FF tissues in positive ion mode.*

	PROTONATED	SODIATED	POTASSIATED
IMPROVES DETECTION	0	5	2
HINDERS DETECTION	0	1	0

Appendix A Table 2.66. Cer Lipids: Formalin Fixed vs. Formalin Fixed Ammonium Formate Washing*. A table showing the number of Cer lipids divided into adducts that were improved or hindered in detection after formalin fixed ammonium formate washing when compared to formalin fixed tissues in positive ion mode.*

	PROTONATED	SODIATED	POTASSIATED
IMPROVES DETECTION	3	2	1

HINDERS DETECTION	5	13	10

Appendix A Table 2.67. PE Lipids: FF vs. Formalin Fixed Ammonium Formate Washed*. A table showing the number of PE lipids divided into adducts that were improved or hindered in detection after formalin fixation and ammonium formate washing when compared to FF tissues in positive ion mode.*

	PROTONATED	**SODIATED**	**POTASSIATED**
IMPROVES DETECTION	0	0	0
HINDERS DETECTION	6	4	4

Appendix A Table 2.68. Cer Lipids: FF vs. Formalin Fixed*. A table showing the number of Cer lipids divided into adducts that were improved or hindered in detection after formalin fixation when compared to FF tissues in positive ion mode.*

	PROTONATED	**SODIATED**	**POTASSIATED**
IMPROVES DETECTION	2	3	2
HINDERS DETECTION	6	5	3

Appendix A Table 2.69. Cer Lipids: FF vs. Formalin Fixed Ammonium Formate Washed*. A table showing the number of Cer lipids divided into adducts that were improved or hindered in detection after formalin fixation and ammonium formate washing when compared to FF tissues in positive ion mode.*

	PROTONATED	**SODIATED**	**POTASSIATED**
IMPROVES DETECTION	3	2	1
HINDERS DETECTION	4	3	7

Appendix A Table 2.70. PA Lipids: FF vs. FF Ammonium Formate Washing*. A table showing the number of PA lipids divided into adducts that were improved or hindered in detection after FF ammonium formate washing when compared to FF tissues in positive ion mode.*

	PROTONATED	SODIATED	POTASSIATED
IMPROVES DETECTION	0	0	2
HINDERS DETECTION	0	0	1

Appendix A Table 2.71. PA Lipids: Formalin Fixed vs. Formalin Fixed Ammonium Formate Washing*. A table showing the number of PA lipids divided into adducts that were improved or hindered in detection after formalin fixed ammonium formate washing when compared to formalin fixed tissues in positive ion mode.*

	PROTONATED	SODIATED	POTASSIATED
IMPROVES DETECTION	0	0	1
HINDERS DETECTION	1	3	7

Appendix A Table 2.72*.* ***PA Lipids: FF vs. Formalin Fixed****. A table showing the number of PA lipids divided into adducts that were improved or hindered in detection after formalin fixation when compared to FF tissues in positive ion mode.*

	PROTONATED	SODIATED	POTASSIATED
IMPROVES DETECTION	0	0	0
HINDERS DETECTION	1	3	6

Appendix A Table 2.73. PA Lipids: FF vs. Formalin Fixed Ammonium Formate Washed*. A table showing the number of PA lipids divided into adducts that were improved or hindered in detection after formalin fixation and ammonium formate washing when compared to FF tissues in positive ion mode.*

	PROTONATED	SODIATED	POTASSIATED
IMPROVES DETECTION	4	3	1
HINDERS DETECTION	0	0	5

Appendix A Table 2.74. SM Lipids: FF vs. FF Ammonium Formate Washing*. A table showing the number of SM lipids divided into adducts that were improved or hindered in detection after FF ammonium formate washing when compared to FF tissues in positive ion mode.*

	PROTONATED	SODIATED	POTASSIATED
IMPROVES DETECTION	0	0	0
HINDERS DETECTION	0	0	0

Appendix A Table 2.75. SM Lipids: Formalin Fixed vs. Formalin Fixed Ammonium Formate Washing*. A table showing the number of SM lipids divided into adducts that were improved or hindered in detection after formalin fixed ammonium formate washing when compared to formalin fixed tissues in positive ion mode.*

	PROTONATED	SODIATED	POTASSIATED
IMPROVES DETECTION	0	0	0
HINDERS DETECTION	0	0	5

Appendix A Table 2.76. SM Lipids: FF vs. Formalin Fixed*. A table showing the number of SM lipids divided into adducts that were improved or hindered in detection after formalin fixation when compared to FF tissues in positive ion mode.*

	PROTONATED	SODIATED	POTASSIATED
IMPROVES DETECTION	1	0	0
HINDERS DETECTION	0	0	1

Appendix A Table 2.77. SM Lipids: FF vs. Formalin Fixed Ammonium Formate Washed*. A table showing the number of SM lipids divided into adducts that were improved or hindered in detection after formalin fixation and ammonium formate washing when compared to FF tissues in positive ion mode.*

	PROTONATED	SODIATED	POTASSIATED
IMPROVES DETECTION	3	1	0
HINDERS DETECTION	1	1	0

Appendix A Table 2.78. PS Lipids: FF vs. FF Ammonium Formate Washing*. A table showing the number of PS lipids divided into adducts that were improved or hindered in detection after FF ammonium formate washing when compared to FF tissues in positive ion mode.*

	PROTONATED	SODIATED	POTASSIATED
IMPROVES DETECTION	0	0	0
HINDERS DETECTION	0	3	0

Appendix A Table 2.79. PS Lipids: Formalin Fixed vs. Formalin Fixed Ammonium Formate Washing*. A table showing the number of PS lipids divided into adducts that were improved or hindered in detection after formalin fixed ammonium formate washing when compared to formalin fixed tissues in positive ion mode.*

	PROTONATED	SODIATED	POTASSIATED

IMPROVES DETECTION	0	0	0
HINDERS DETECTION	0	0	0

Appendix A Table 2.80. PS Lipids: FF vs. Formalin Fixed*. A table showing the number of PS lipids divided into adducts that were improved or hindered in detection after formalin fixation when compared to FF tissues in positive ion mode.*

	PROTONATED	**SODIATED**	**POTASSIATED**
IMPROVES DETECTION	10	0	0
HINDERS DETECTION	1	1	0

Appendix A Table 2.81. PS Lipids: FF vs. Formalin Fixed Ammonium Formate Washed*. A table showing the number of PS lipids divided into adducts that were improved or hindered in detection after formalin fixation and ammonium formate washing when compared to FF tissues in positive ion mode.*

	PROTONATED	**SODIATED**	**POTASSIATED**
IMPROVES DETECTION	0	0	0
HINDERS DETECTION	0	0	0

Appendix A Table 2.82. PG Lipids: Formalin Fixed vs. Formalin Fixed Ammonium Formate Washing*. A table showing the number of PG lipids divided into adducts that were improved or hindered in detection after formalin fixed ammonium formate washing when compared to formalin fixed tissues in positive ion mode.*

	PROTONATED	**SODIATED**	**POTASSIATED**
IMPROVES DETECTION	0	0	0

HINDERS DETECTION	8	15	1

Appendix A Table 2.83. PG Lipids: FF vs. Formalin Fixed*. A table showing the number of PG lipids divided into adducts that were improved or hindered in detection after formalin fixation when compared to FF tissues in positive ion mode.*

	PROTONATED	**SODIATED**	**POTASSIATED**
IMPROVES DETECTION	0	0	1
HINDERS DETECTION	10	15	1

Appendix A Table 2.84. PG Lipids: FF vs. FF Ammonium Formate Washing*. A table showing the number of PG lipids divided into adducts that were improved or hindered in detection after FF ammonium formate washing when compared to FF tissues in positive ion mode.*

	PROTONATED	**SODIATED**	**POTASSIATED**
IMPROVES DETECTION	0	0	0
HINDERS DETECTION	9	15	1

Appendix A Table 2.85. PG Lipids: FF vs. Formalin Fixed Ammonium Formate Washed*. A table showing the number of PG lipids divided into adducts that were improved or hindered in detection after formalin fixation and ammonium formate washing when compared to FF tissues in positive ion mode.*

Appendix B: Imaging MS/MS Validation of GC correlating and anticorrelating ions. *Selected ion images of each lipid are shown in Table 3.1 and Figure 3.3. Fragmentation data for PE(O-18:0_22:6) and PE-(O-18:0_20:4) can be found in Figure 3.4. Lipids were identified using the lipid maps MS/MS spectrum prediction and MS/MS data search tool.*

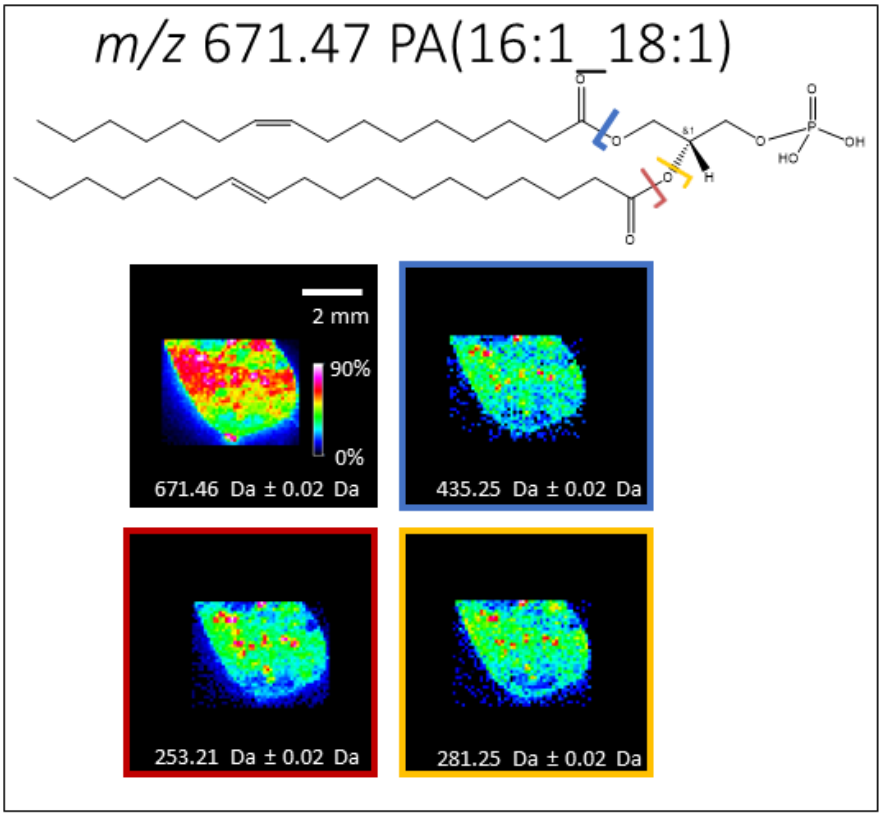

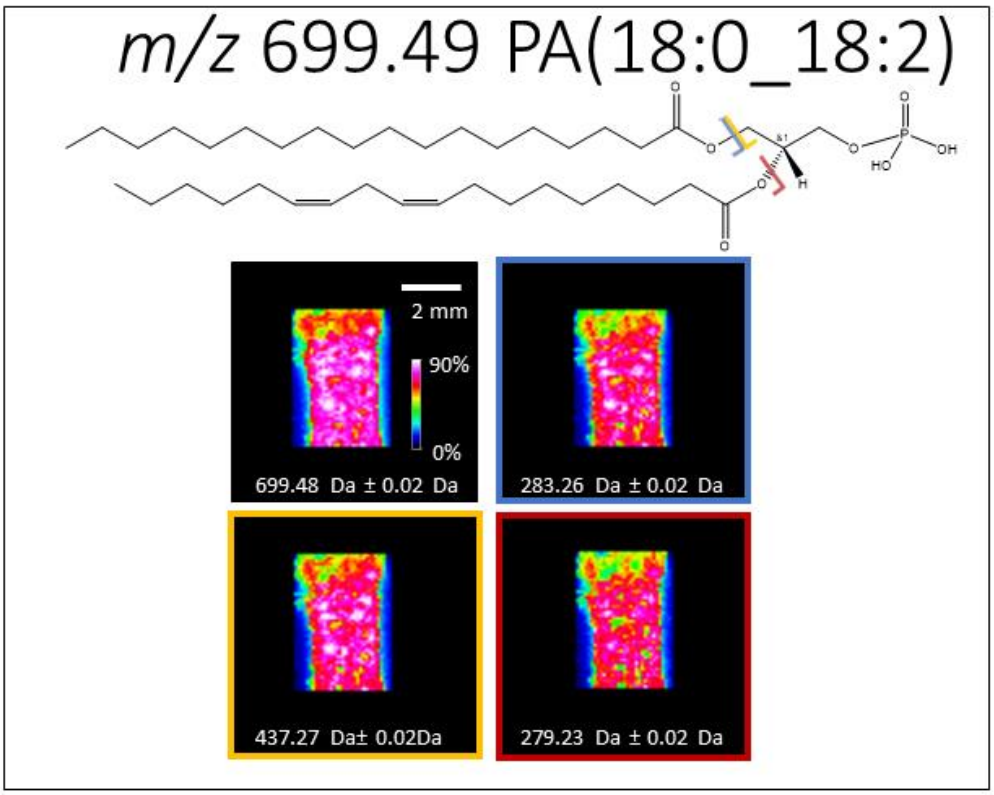
m/z 699.49 PA(18:0_18:2)
2 mm
90%
0%
699.48 Da ± 0.02 Da
283.26 Da ± 0.02 Da
437.27 Da± 0.02Da
279.23 Da ± 0.02 Da

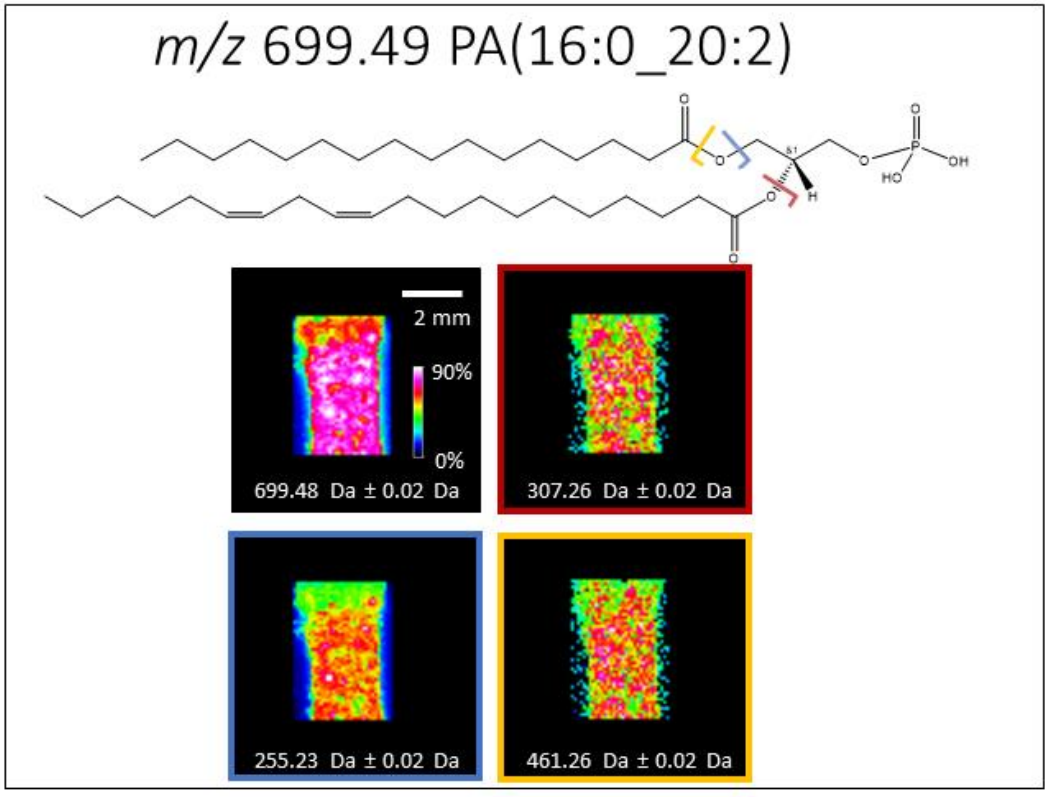
m/z 699.49 PA(16:0_20:2)
2 mm
90%
0%
699.48 Da ± 0.02 Da
307.26 Da ± 0.02 Da
255.23 Da ± 0.02 Da
461.26 Da ± 0.02 Da

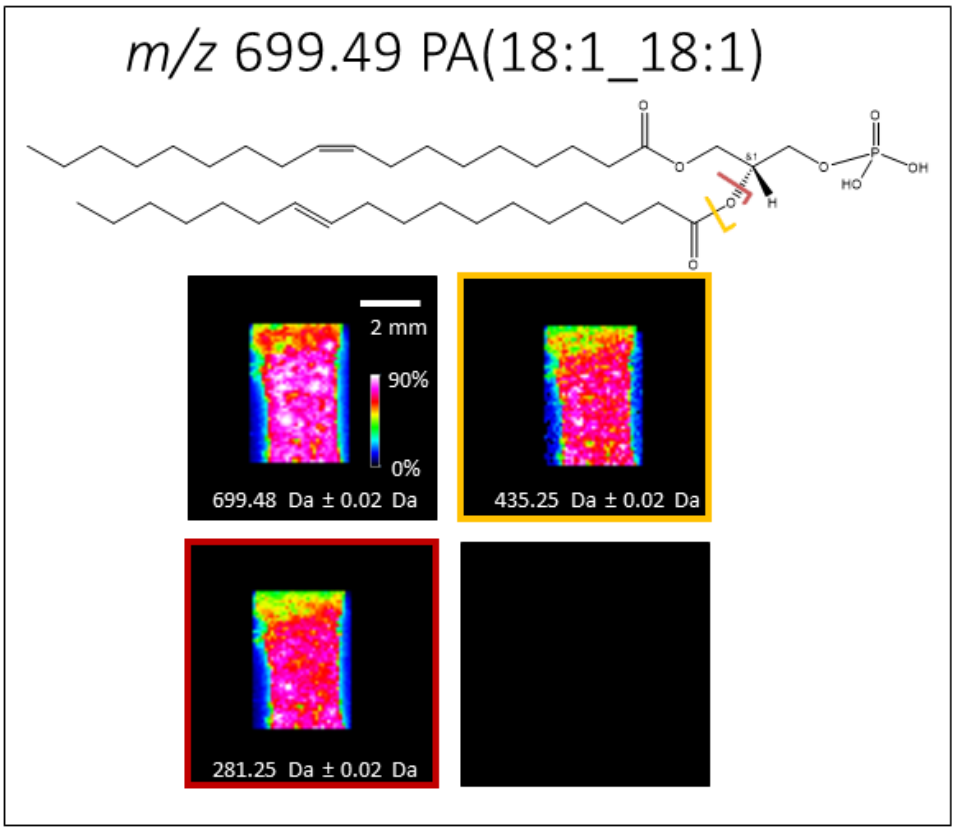
m/z 699.49 PA(18:1_18:1)
2 mm
90%
0%
699.48 Da ± 0.02 Da
435.25 Da ± 0.02 Da
281.25 Da ± 0.02 Da

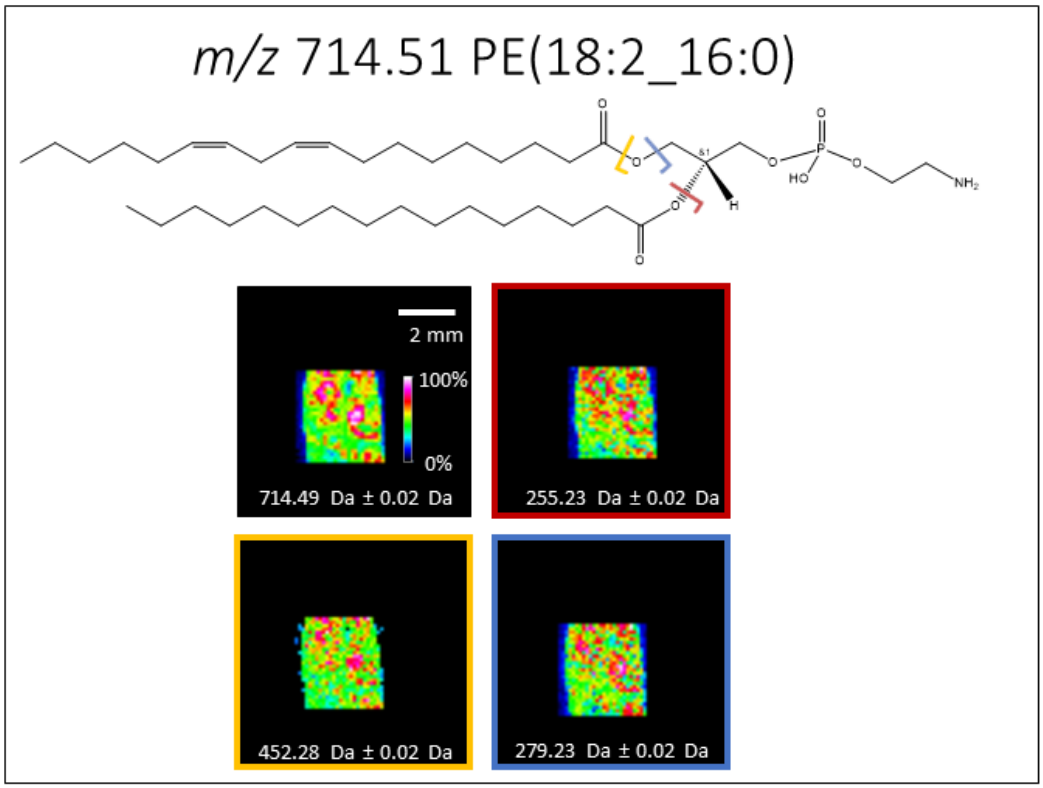
m/z 714.51 PE(18:2_16:0)
2 mm
100%
0%
714.49 Da ± 0.02 Da
255.23 Da ± 0.02 Da
452.28 Da ± 0.02 Da
279.23 Da ± 0.02 Da

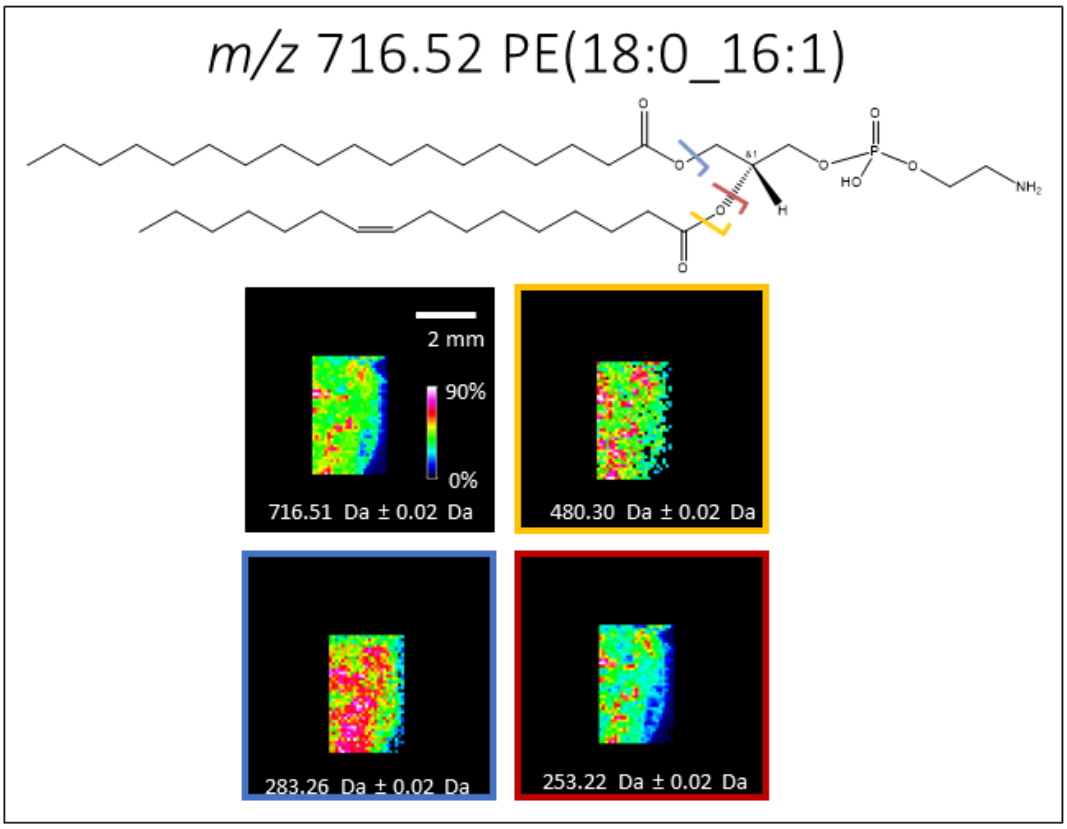
m/z 716.52 PE(18:0_16:1)
2 mm
90%
0%
716.51 Da ± 0.02 Da
480.30 Da ± 0.02 Da
283.26 Da ± 0.02 Da
253.22 Da ± 0.02 Da

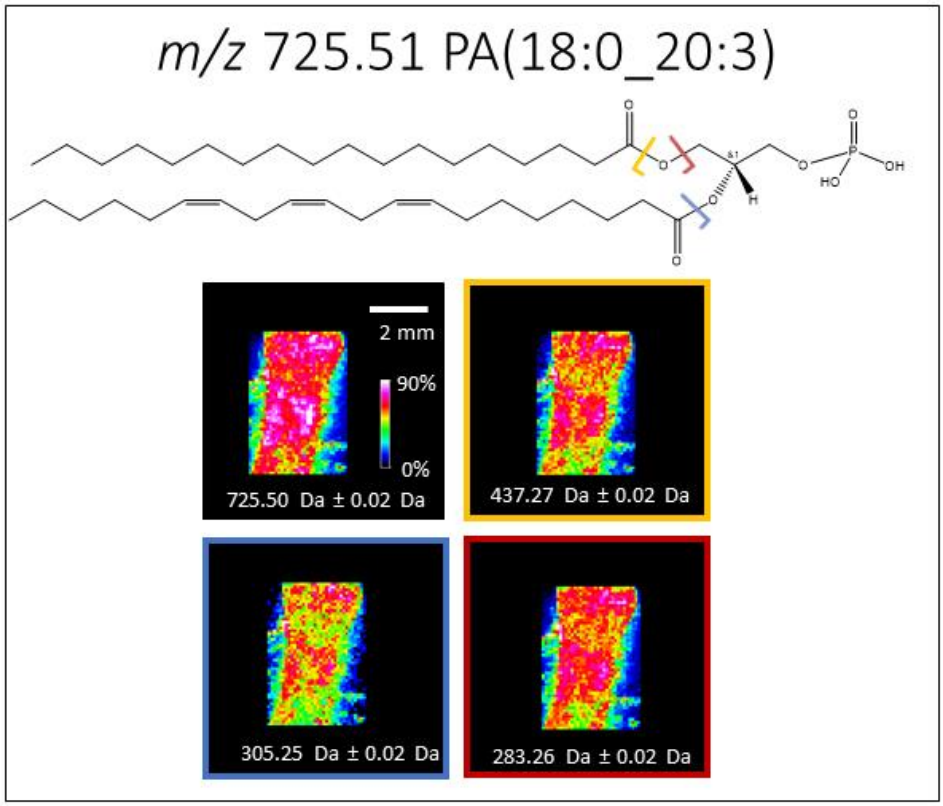
m/z 725.51 PA(18:0_20:3)
2 mm
90%
0%
725.50 Da ± 0.02 Da
437.27 Da ± 0.02 Da
305.25 Da ± 0.02 Da
283.26 Da ± 0.02 Da

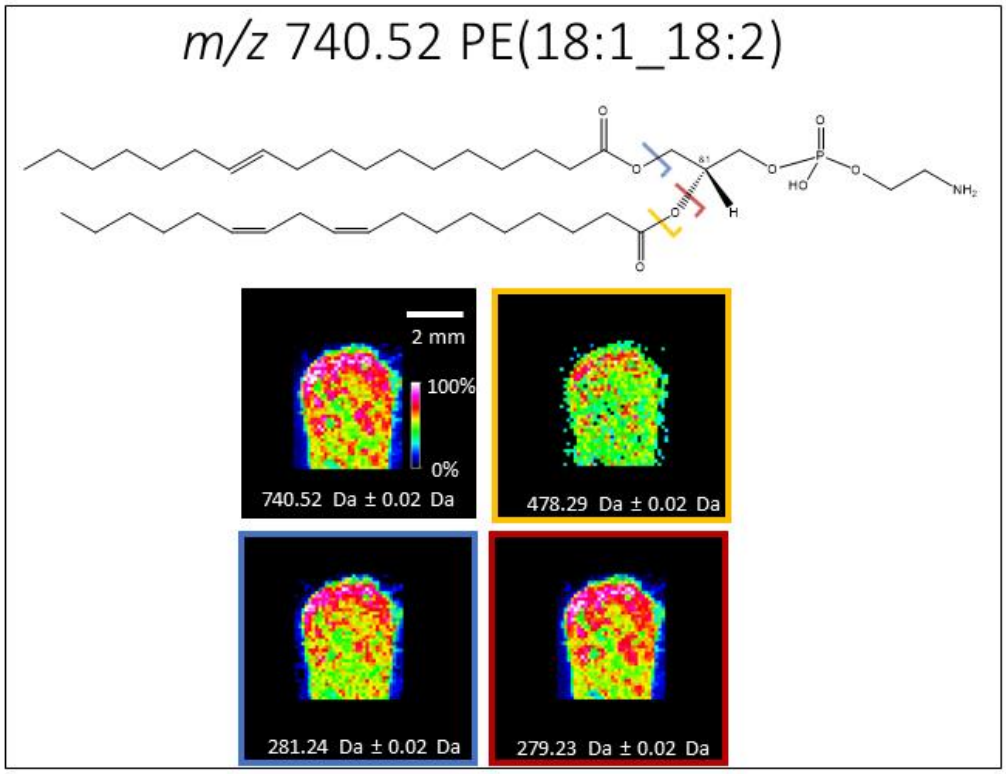
m/z 740.52 PE(18:1_18:2)
2 mm
100%
0%
740.52 Da ± 0.02 Da
478.29 Da ± 0.02 Da
281.24 Da ± 0.02 Da
279.23 Da ± 0.02 Da

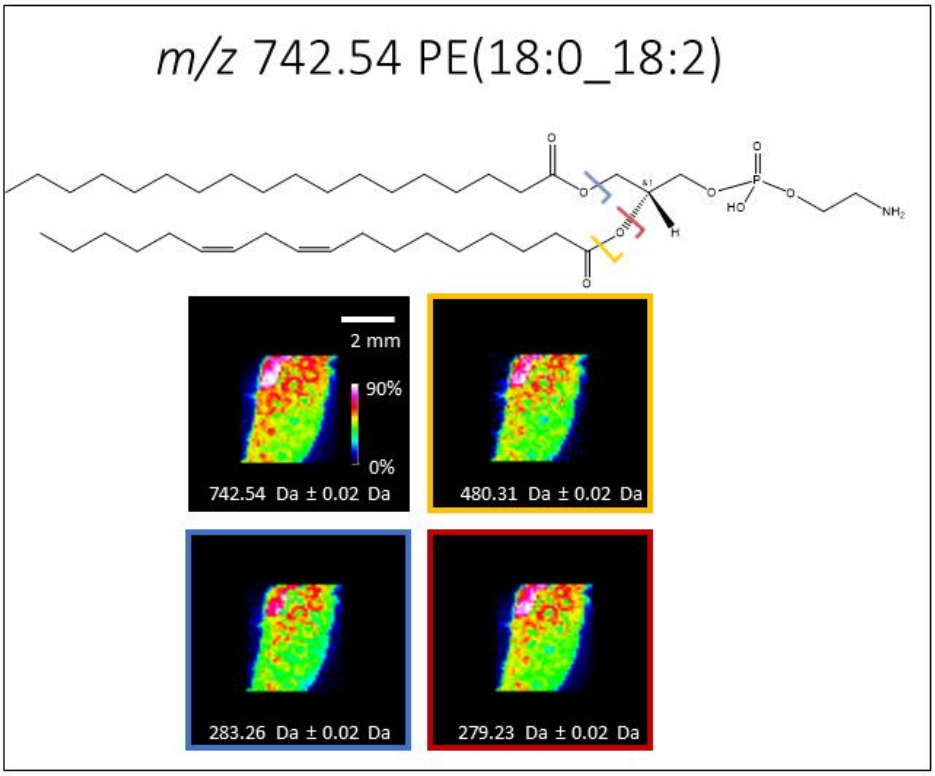
m/z 742.54 PE(18:0_18:2)
2 mm
90%
0%
742.54 Da ± 0.02 Da
480.31 Da ± 0.02 Da
283.26 Da ± 0.02 Da
279.23 Da ± 0.02 Da

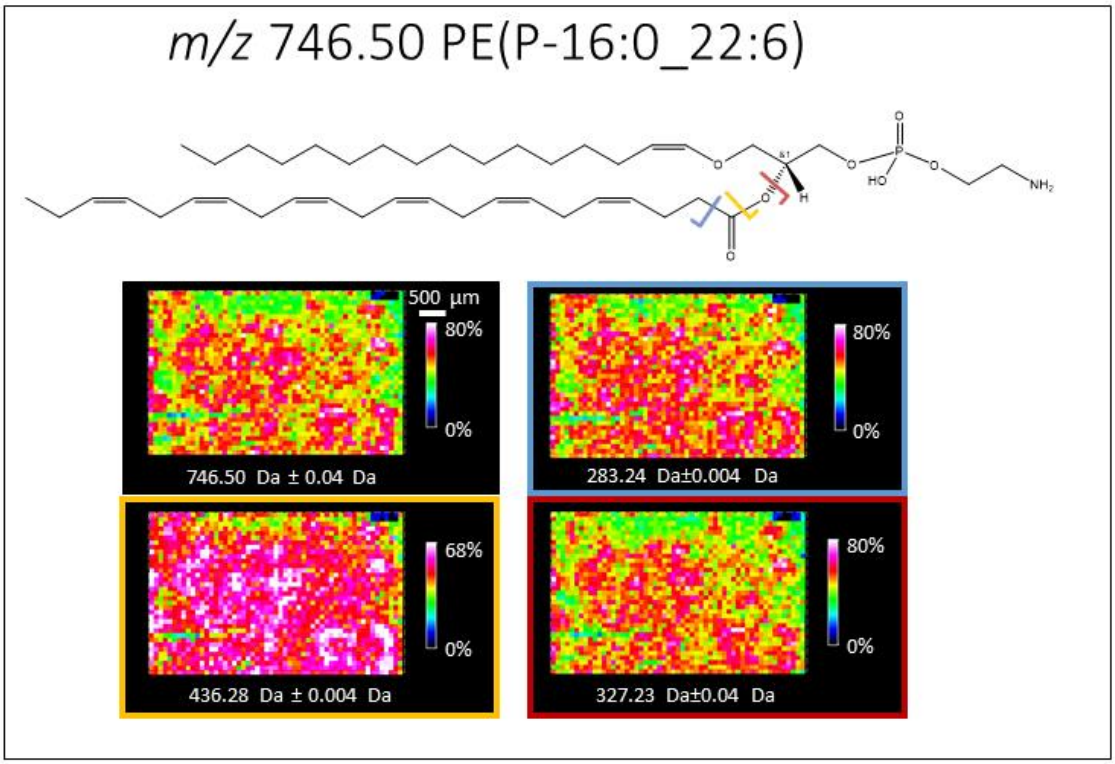
m/z 746.50 PE(P-16:0_22:6)
500 µm
80%
0%
746.50 Da ± 0.04 Da
80%
0%
283.24 Da±0.004 Da
68%
0%
436.28 Da ± 0.004 Da
80%
0%
327.23 Da±0.04 Da

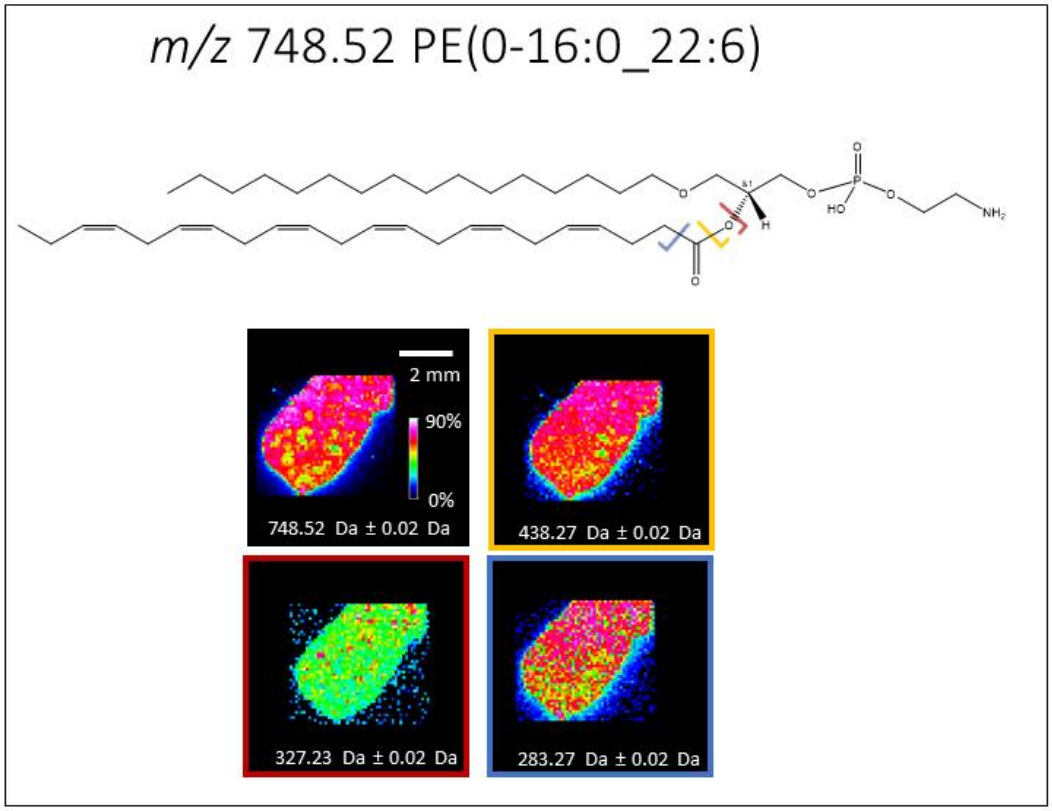
m/z 748.52 PE(0-16:0_22:6)
2 mm
90%
0%
748.52 Da ± 0.02 Da
438.27 Da ± 0.02 Da
327.23 Da ± 0.02 Da
283.27 Da ± 0.02 Da

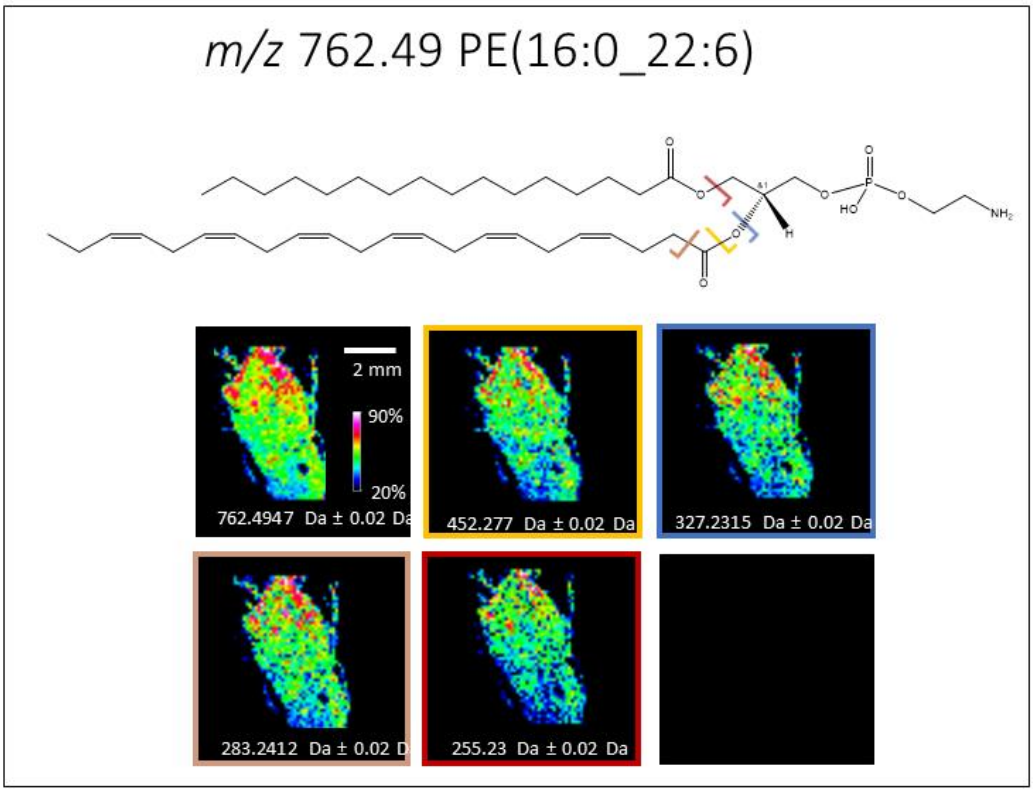
m/z 762.49 PE(16:0_22:6)
2 mm
90%
20%
762.4947 Da ± 0.02 Da
452.277 Da ± 0.02 Da
327.2315 Da ± 0.02 Da
283.2412 Da ± 0.02 D
255.23 Da ± 0.02 Da

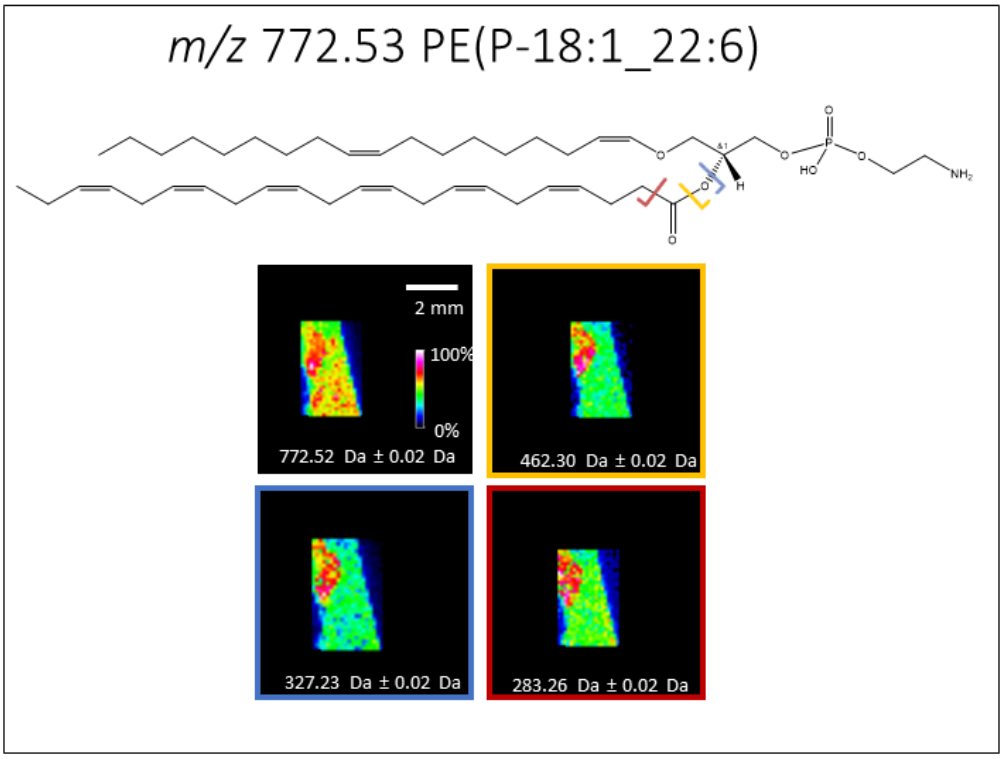
m/z 772.53 PE(P-18:1_22:6)
2 mm
100%
0%
772.52 Da ± 0.02 Da
462.30 Da ± 0.02 Da
327.23 Da ± 0.02 Da
283.26 Da ± 0.02 Da

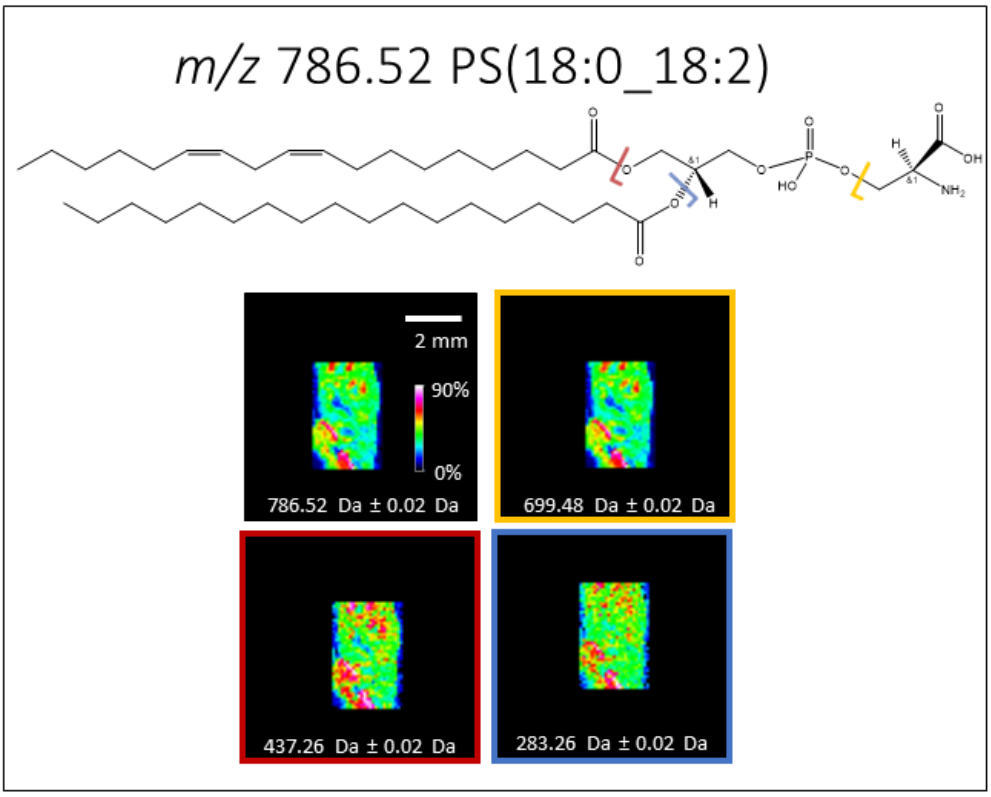
m/z 786.52 PS(18:0_18:2)
2 mm
90%
0%
786.52 Da ± 0.02 Da
699.48 Da ± 0.02 Da
437.26 Da ± 0.02 Da
283.26 Da ± 0.02 Da

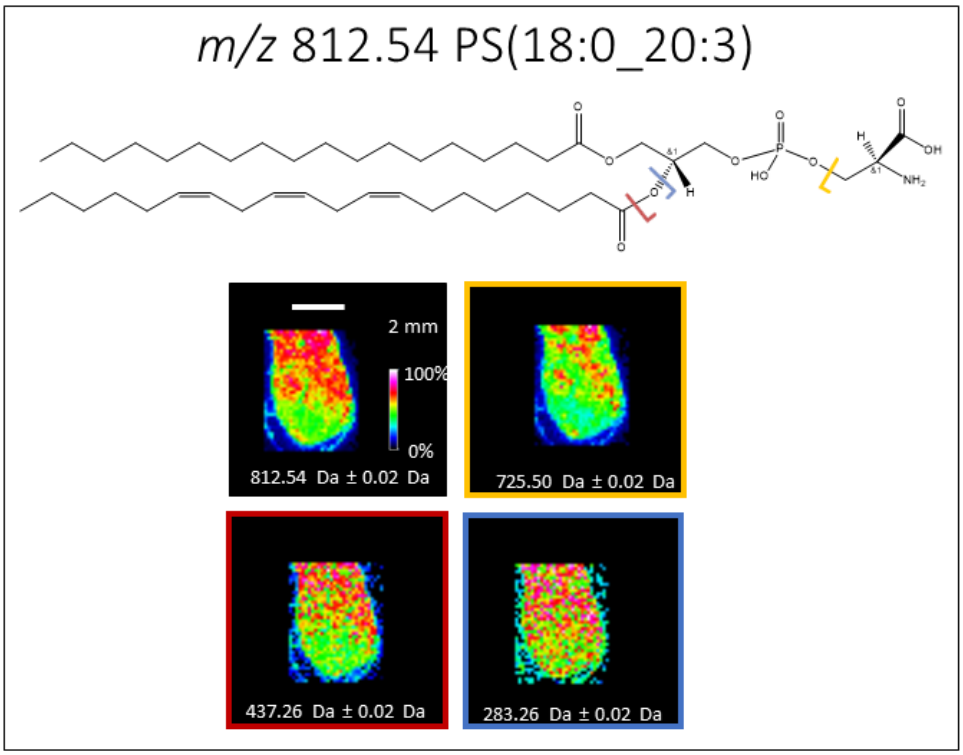
m/z 812.54 PS(18:0_20:3)
2 mm
100%
0%
812.54 Da ± 0.02 Da
725.50 Da ± 0.02 Da
437.26 Da ± 0.02 Da
283.26 Da ± 0.02 Da

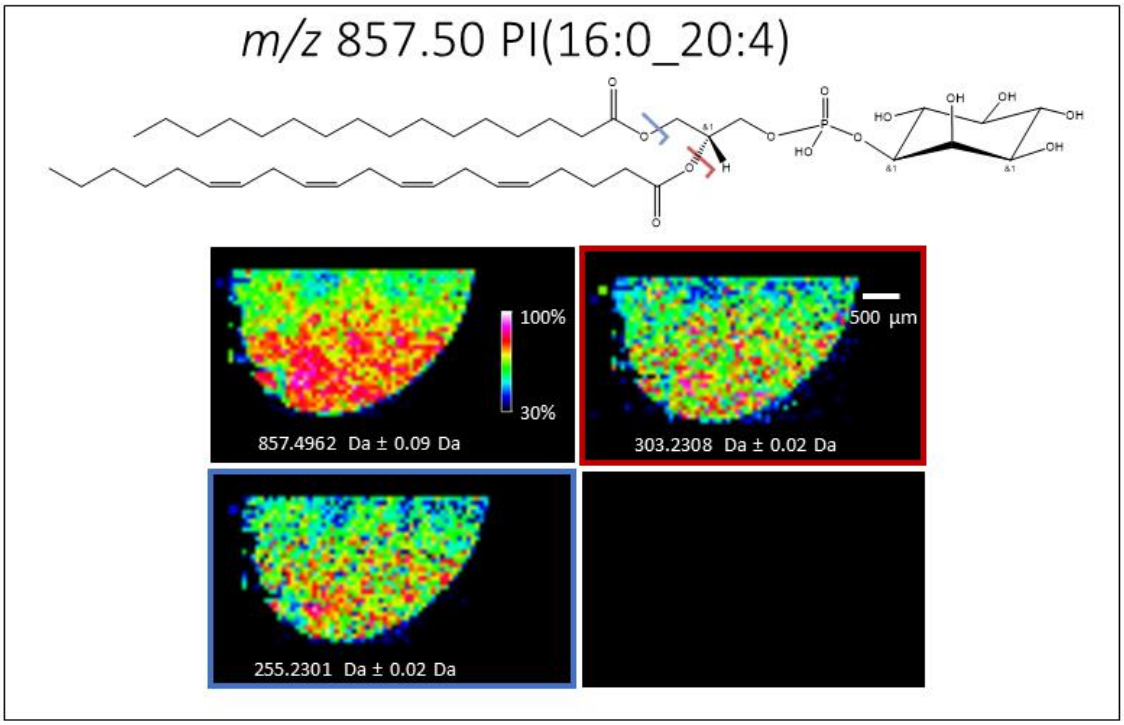
m/z 857.50 PI(16:0_20:4)
100%
30%
857.4962 Da ± 0.09 Da
500 µm
303.2308 Da ± 0.02 Da
255.2301 Da ± 0.02 Da

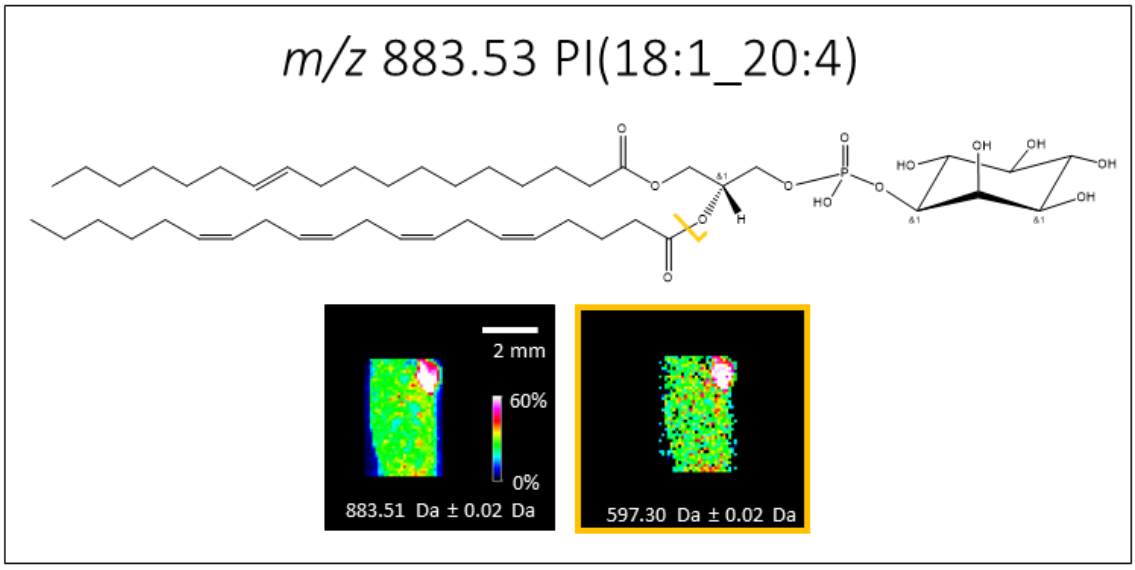
m/z 883.53 PI(18:1_20:4)
2 mm
60%
0%
883.51 Da ± 0.02 Da
597.30 Da ± 0.02 Da

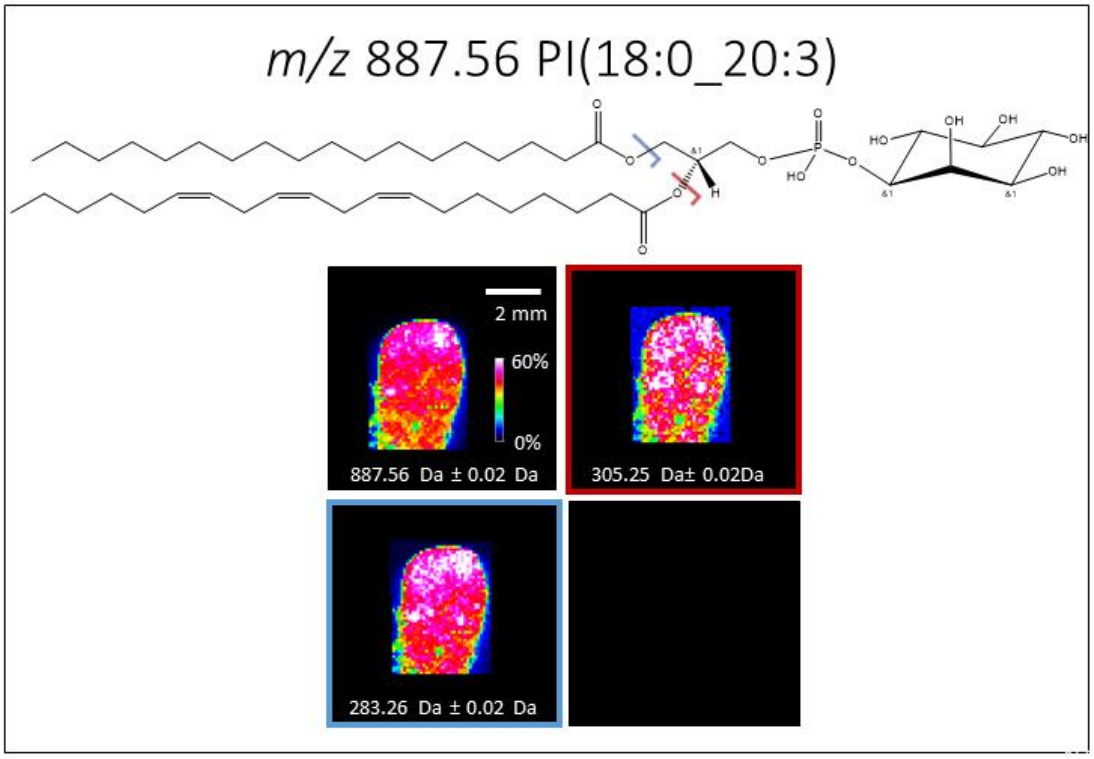
m/z 887.56 PI(18:0_20:3)
2 mm
60%
0%
887.56 Da ± 0.02 Da
305.25 Da± 0.02Da
283.26 Da ± 0.02 Da

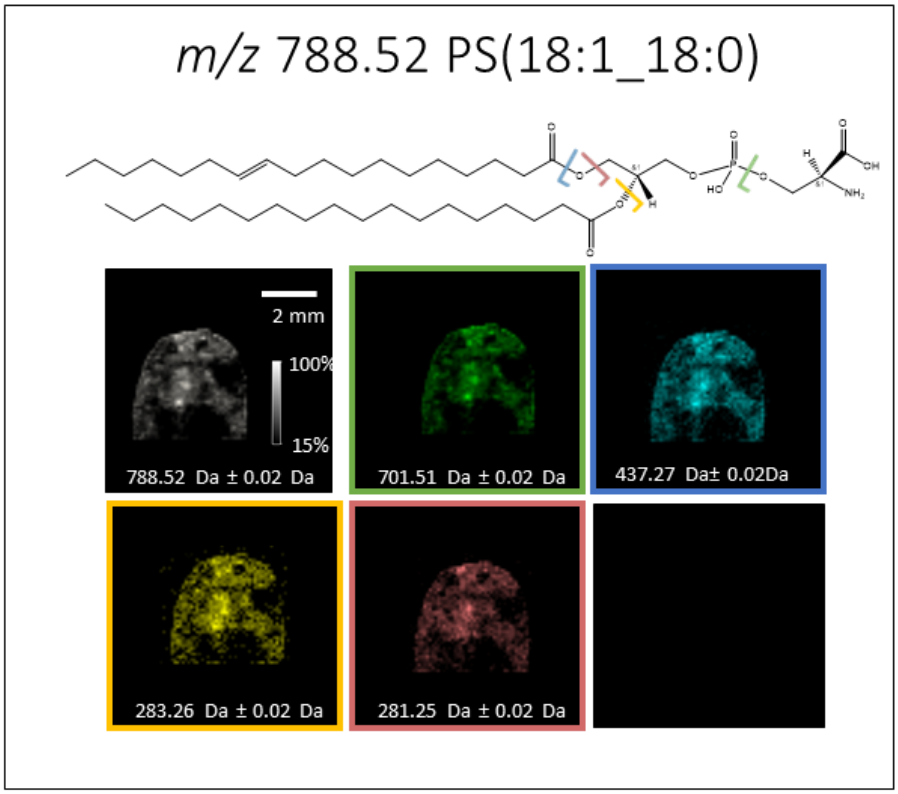
m/z 788.52 PS(18:1_18:0)
2 mm
100%
15%
788.52 Da ± 0.02 Da
701.51 Da ± 0.02 Da
437.27 Da± 0.02Da
283.26 Da ± 0.02 Da
281.25 Da ± 0.02 Da

Appendix B 3.2. The localization of germinal center specific ether lipid PE(O-18:0_20:4) with RMS normalization and with normalization to a non-biological internal standard, 23:2 Diyne PE [DC(8,9)PE] showing the same distribution*. This internal standard was dissolved in chloroform to make a 1 mg/mL solution and added to 1,5 DAN. This matrix mixture was sprayed using a robotic spotter. These distributions demonstrate the lack of ionization efficiency differences in germinal center light and dark zones.*

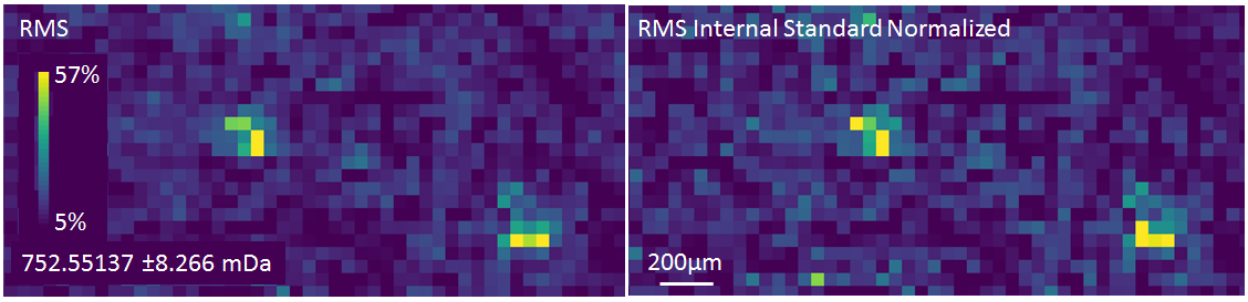

REFERENCES

1. Fischer, A. *et al.* Severe combined immunodeficiency. A model disease for molecular immunology and therapy. *Immunol. Rev.* **203**, 98–109 (2005).

2. Cunningham-Rundles, C. & Bodian, C. Common variable immunodeficiency: Clinical and immunological features of 248 patients. *Clin. Immunol.* **92**, 34–48 (1999).

3. Winkelstein, J. A. *et al.* X-Linked Agammaglobulinemia. *Medicine (Baltimore).* **85**, 193–202 (2006).

4. Hammad, H. & Lambrecht, B. N. Dendritic cells and epithelial cells: Linking innate and adaptive immunity in asthma. *Nature Reviews Immunology* **8**, 193–204 (2008).

5. Recent Advances in Ophthalmology - 13 - HV Nema, Nitin Nema - Google Books. Available at: https://books.google.com/books?hl=en&lr=&id=XrlEDwAAQBAJ&oi=fnd&pg=PA71&dq=eczema,+adaptive+immunity+review&ots=sW599rH6RQ&sig=BEUmPlkGMjKpZojc2SzUuo6OAdk#v=onepage&q=eczema%2C adaptive immunity review&f=false. (Accessed: 18th February 2020)

6. Abreo, A. M., Gardner, K. G. & Hemler, J. A. Overview and Understanding of Allergic Reactions and Allergic Disease. in *Allergy and Sleep* 59–64 (Springer International Publishing, 2019). doi:10.1007/978-3-030-14738-9_5

7. Niaid. *Progress in Autoimmune Diseases Research*.

8. Fairweather, D. L. & Rose, N. R. Women and autoimmune diseases. in *Emerging Infectious Diseases* **10**, 2005–2011 (Centers for Disease Control and Prevention (CDC), 2004).

9. Walsh, S. J. & Rau, L. M. Autoimmune diseases: A leading cause of death among young and middle-aged women in the United States. *Am. J. Public Health* **90**, 1463–1466 (2000).

10. Lindbladh, I., Andersson Svärd, A. & Lernmark, Å. Autoimmune (Type 1) Diabetes. in *The Autoimmune Diseases* 769–787 (Elsevier, 2020). doi:10.1016/b978-0-12-812102-3.00041-5

11. Quiñonez-Flores, C. M., González-Chávez, S. A. & Pacheco-Tena, C. Hypoxia and its implications in rheumatoid arthritis. *J Biomed Sci* **23**, (2016).

12. Marston, B., Palanichamy, A. & Anolik, J. H. B cells in the pathogenesis and treatment of rheumatoid arthritis. *Current Opinion in Rheumatology* **22**, 307–315 (2010).

13. Lipsky, P. E. Systemic lupus erythematosus: An autoimmune disease of B cell hyperactivity. *Nat. Immunol.* **2**, 764–766 (2001).

14. Somers, E., Thomas, S., Smeeth, L. & Hall, A. The Cost Burden of Autoimmune Disease: The Latest Front in the War on Healthcare Spending. *Am J Epidemiol* **169**, 749–755 (2009).

15. DeFranco, A. L. Germinal centers and autoimmune disease in humans and mice. *Immunol. Cell Biol.* **94**, 918–924 (2016).

16. DeFranco, A. L. The germinal center antibody response in health and disease. *F1000Res* **5**, (2016).

17. Weissert, R. Adaptive immunity is the key to the understanding of autoimmune and paraneoplastic inflammatory central nervous system disorders. *Frontiers in Immunology* **8**, (2017).

18. The innate and adaptive immune systems. (2016).

19. Berg, J. M., Tymoczko, J. L. & Stryer, L. *Biochemistry* . (W. H. Freeman and Company, 2012).

20. Murphy, K. (Kenneth M. ., Travers, P., Walport, M. & Janeway, C. *Janeway's immunobiology.* (Garland Science, 2008).

21. Akira, S., Uematsu, S. & Takeuchi, O. Pathogen recognition and innate immunity. *Cell* **124**, 783–801 (2006).

22. Charles A Janeway, J., Travers, P., Walport, M. & Shlomchik, M. J. Principles of innate and adaptive immunity. (2001).

23. Cueni, L. N. & Detmar, M. The lymphatic system in health and disease. *Lymphatic Research and Biology* **6**, 109–122 (2008).

24. Boothby, M. & Rickert, R. C. Metabolic Regulation of the Immune Humoral Response. *Immunity* **46**, 743–755 (2017).

25. Cesta, M. F. Normal Structure, Function, and Histology of the Spleen. *Toxicol. Pathol.* **34**, 455–465 (2006).

26. De Silva, N. S. & Klein, U. Dynamics of B cells in germinal centres. *Nat. Rev. Immunol.* **15**, 137–148 (2015).

27. Cho, S. H. *et al.* Germinal centre hypoxia and regulation of antibody qualities by a hypoxia response system. *Nature* **537**, 234–238 (2016).

28. Duffney, P. F. *et al.* Key roles for lipid mediators in the adaptive immune response. *Journal of Clinical Investigation* **128**, 2724–2731 (2018).

29. Lodhi, I. J. *et al.* Inhibiting adipose tissue lipogenesis reprograms thermogenesis and PPARγ activation to decrease diet-induced obesity. *Cell Metab.* **16**, 189–201 (2012).

30. Lodhi, I. J. *et al.* Peroxisomal lipid synthesis regulates inflammation by sustaining neutrophil membrane phospholipid composition and viability. *Cell Metab.* **21**, 51–64 (2015).

31. Lindgren, G., Ols, S., Thompson, E. A. & Loré, K. Comparative analysis of the germinal center response by flow cytometry and immunohistology. *J. Immunol. Methods* **472**, 16–24 (2019).

32. Jacobsen, J. T. & Victora, G. D. Microanatomical labeling of germinal center structures for flow cytometry using photoactivation. in *Methods in Molecular Biology* **1623**, 51–58 (Humana Press Inc., 2017).

33. Fenn, J. B., Mann, M., Meng, C. K., Wong, S. F. & Whitehouse, C. M. Electrospray ionization for mass spectrometry of large biomolecules. *Science* **246**, 64–71 (1989).

34. Karas, M. & Hillenkamp, F. Laser Desorption Ionization of Proteins with Molecular Masses Exceeding 10 000 Daltons. *Analytical Chemistry* **60**, 2299–2301 (1988).

35. Marshall, A. G., Hendrickson, C. L. & Jackson, G. S. Fourier Transform Ion Cyclotron Resonance Mass Spectrometry: A Primer. *Mass Spectrom. Rev.* **17**, 1–35 (1998).

36. Marshall, A. G. *et al.* Fourier transform ion cyclotron resonance mass spectrometry: A primer. *Mass Spectrom. Rev.* **17**, 1–35 (2017).

37. Takáts, Z., Wiseman, J. M., Gologan, B. & Cooks, R. G. Mass spectrometry sampling under ambient conditions with desorption electrospray ionization. *Science (80-.).* **306**, 471–473 (2004).

38. Wittmaack, K. Pre-equilibrium variation of the secondary ion yield. *Int. J. Mass Spectrom. Ion Phys.* **17**, 39–50 (1975).

39. Liebl, H. Ion microprobe mass analyzer. *J. Appl. Phys.* **38**, 5277–5283 (1967).

40. Zemski Berry, K. A. *et al.* MALDI Imaging of Lipid Biochemistry in Tissues by Mass Spectrometry. *Chem. Rev.* **111**, 6491–6512 (2011).

41. Zavalin, A., Yang, J., Hayden, K., Vestal, M. & Caprioli, R. M. Tissue protein imaging at 1 μm laser spot diameter for high spatial resolution and high imaging speed using transmission geometry MALDI TOF MS. *Anal Bioanal Chem* **407**, 2337–2342 (2015).

42. Zavalin, A. *et al.* Direct imaging of single cells and tissue at sub-cellular spatial resolution using transmission geometry MALDI MS. *Journal of Mass Spectrometry* **47**, 1473–1481 (2012).

43. Bemis, K. D. *et al.* Cardinal: An R package for statistical analysis of mass spectrometry-based imaging experiments. *Bioinformatics* **31**, 2418–2420 (2015).

44. Alexandrov, T. MALDI imaging mass spectrometry: statistical data analysis and current computational challenges. *BMC Bioinformatics* **13 Suppl 1**, S11 (2012).

45. Palmer, A. *et al.* FDR-controlled metabolite annotation for high-resolution imaging mass spectrometry. *Nat. Methods* **14**, 57–60 (2017).

46. *SCiLS Lab 2D: Comparative Analysis for Uncovering Discriminative M/z-markers*.

47. Patterson, N. H. *et al.* Next Generation Histology-Directed Imaging Mass Spectrometry Driven by Autofluorescence Microscopy. *Anal. Chem.* **90**, 12404–12413 (2018).

48. Patterson, N. H., Tuck, M., Van de Plas, R. & Caprioli, R. M. Advanced Registration and Analysis of MALDI Imaging Mass Spectrometry Measurements through Autofluorescence Microscopy. *Anal. Chem.* **90**, 12395–12403 (2018).

49. Cornett, D. S. *et al.* A novel histology-directed strategy for MALDI-MS tissue profiling that improves throughput and cellular specificity in human breast cancer. *Mol. Cell. Proteomics* **5**, 1975–83 (2006).

50. Crouch, E. E. *et al.* Regulation of AID expression in the immune response. *J. Exp. Med.* **204**, 1145–56 (2007).

51. Caprioli, R. M., Farmer, T. B. & Gile, J. Molecular imaging of biological samples: localization of peptides and proteins using MALDI-TOF MS. *Anal. Chem.* **69**, 4751–60 (1997).

52. Scott, A. J. *et al.* Host-based lipid inflammation drives pathogenesis in Francisella infection. *Proc. Natl. Acad. Sci. U. S. A.* **114**, 12596–12601 (2017).

53. Wenk, M. R. The emerging field of lipidomics. *Nat Rev Drug Discov* **4**, 594–610 (2005).

54. E, G. de S. R., I, M., MT, G., I, F. & R, R.-P. Imaging mass spectrometry (IMS) of cortical lipids from preclinical to severe stages of Alzheimer's disease ☆. *Biochim. Biophys. Acta - Biomembr.* **1859**, 1604–1614 (2017).

55. Jiang, L. *et al.* MALDI-Mass Spectrometric Imaging Revealing Hypoxia-Driven Lipids and Proteins in a Breast Tumor Model. (2015). doi:10.1021/ac504503x

56. Thomas, A. *et al.* Mass spectrometry for the evaluation of cardiovascular diseases based on proteomics and lipidomics. *Thromb Haemost* **106**, 20–33 (2011).

57. Kaya, I. *et al.* Histology-Compatible MALDI Mass Spectrometry Based Imaging of Neuronal Lipids for Subsequent Immunofluorescent Staining. *Anal. Chem.* **89**, 4685–4694 (2017).

58. Willems, S. M. *et al.* Imaging mass spectrometry of myxoid sarcomas identifies proteins and lipids specific to tumour type and grade, and reveals biochemical intratumour heterogeneity. *J Pathol* **222**, 400–409 (2010).

59. Jones, E. E. *et al.* MALDI imaging mass spectrometry profiling of proteins and lipids in clear cell renal cell carcinoma. *Proteomics* **14**, 924–935 (2014).

60. Roux, A. *et al.* Mass spectrometry imaging of rat brain lipid profile changes over time following traumatic brain injury - ScienceDirect. *J. Neurosci. Methods* **272**, 19–32 (2017).

61. Tanaka, H. *et al.* Distribution of phospholipid molecular species in autogenous access grafts for hemodialysis analyzed using imaging mass spectrometry. *Anal Bioanal Chem* **400**, 1873–1880 (2011).

62. Pietrowska, M., Gawin, M., Polanska, J. & Widlak, P. Tissue fixed with formalin and processed without paraffin embedding is suitable for imaging of both peptides and lipids by MALDI-IMS. *Proteomics* **16**, 1670–1677 (2016).

63. Kiernan, J. A. Formaldehyde, formalin paraformaldehyde and glutaraldehyde: What they are and what they do. *Micros. Today* **1**, 8–12 (2000).

64. Cleary, T. J., Morales, A. R., Nadji, M., Nassiri, M. & Vincek, V. Antimicrobial activity of UMFix tissue fixative. *J. Clin. Pathol.* **58**, 22–25 (2005).

65. Chen, N. H., Djoko, K. Y., Veyrier, F. J. & McEwan, A. G. Formaldehyde stress responses in bacterial pathogens. *Frontiers in Microbiology* **7**, (2016).

66. Otali, D. *et al.* Combined effects of formalin fixation and tissue processing on immunorecognition. *Biotech. Histochem.* **84**, 223–247 (2009).

67. Heslinga, F. J. M. & Deirkauf, F. A. the Action of Formaldehyde Solutions on Human Brain Lipids. *J. Histochem. Cytochem.* **10**, 704–709 (1962).

68. Knoblaugh, S., Randolph-Habecker, J. & Rath, S. *Comparative Anatomy and Histology*. (Academic Press, 2011).

69. Smith, C. FFPE or Frozen? Working with Human Clinical Samples. *Life Sci. Artic.* (2017).

70. Neumann, E. K., Comi, T. J., Rubakhin, S. S. & Sweedler, J. V. Lipid Heterogeneity between Astrocytes and Neurons Revealed by Single-Cell MALDI-MS Combined with Immunocytochemical Classification. *Angew. Chemie* **131**, 5971–5975 (2019).

71. Buck, A. *et al.* High-resolution MALDI-FT-ICR MS imaging for the analysis of metabolites from formalin-fixed, paraffin-embedded clinical tissue samples. *J Pathol* **237**, 123–132 (2015).

72. TPSR & V. T. P. S. R. Sucrose Infiltration.

73. Palmer, A. D. *et al.* Sucrose cryo-protection facilitates imaging of whole eye sections by MALDI mass spectrometry. *J Mass Spectrom* **47**, 237–241 (2012).

74. Hopkins, J. B., Badeau, R., Warkentin, M. & Thorne, R. E. Effect of Common Cryoprotectants on Critical Warming Rates and Ice Formation in Aqueous Solutions. *Cryobiology* **65**, 169–178 (2012).

75. Deutskens, F. *et al.* High spatial resolution imaging mass spectrometry and classical histology on a single tissue section. *J. Mass Spectrom.* **46**, 568–571 (2017).

76. Shimma, S. *et al.* MALDI-based imaging mass spectrometry revealed abnormal distribution of phospholipids in colon cancer liver metastasis. *J. Chromatogr. B* **855**, 98–103 (2007).

77. Yalcin, E. B. & de la Monte, S. M. Review of Matrix-Assisted Laser Desorption Ionization-Imaging Mass Spectrometry for Lipid Biochemical Histopathology. in *J Histochem Cytochem* **63**, 762–771 (2015).

78. Berry, K. A. Z. *et al.* MALDI Imaging of Lipid Biochemistry in Tissues by Mass Spectrometry. (2011). doi:10.1021/cr200280p

79. Wakeman, C. A. *et al.* The innate immune protein calprotectin promotes Pseudomonas aeruginosa and Staphylococcus aureus interaction. *Nat Commun* **7**, 11951 (2016).

80. Eriksson, C., Masaki, N., Yao, I., Hayasaka, T. & Setou, M. MALDI Imaging Mass Spectrometry-A Mini Review of Methods and Recent Developments. *Mass Spectrom. (Tokyo, Japan)* **2**, S0022 (2013).

81. Angel, P. M., Spraggins, J. M., Baldwin, H. S. & Caprioli, R. Enhanced sensitivity for high spatial resolution lipid analysis by negative ion mode matrix assisted laser desorption ionization imaging mass spectrometry. *Anal. Chem.* **84**, 1557–1564 (2012).

82. *Freezing tissues for histology: Embedding protocol for Frozen Samples*.

83. Brand, R. D. s. A. B. T. & R&D Systems. Protocol for Making a 4% Formaldehyde Solution in PBS: R&D Systems. Available at: https://www.rndsystems.com/resources/protocols/protocol-making-4-formaldehyde-solution-pbs. (Accessed: 5th February 2019)

84. Jones, M. A. *et al.* Discovering new lipidomic features using cell type specific fluorophore expression to provide spatial and biological specificity in a multimodal workflow with MALDI Imaging Mass Spectrometry. *Anal. Chem.* (2020). doi:10.1021/acs.analchem.0c00446

85. Thomas, A., Charbonneau, J. L., Fournaise, E. & Chaurand, P. Sublimation of new matrix candidates for high spatial resolution imaging mass spectrometry of lipids: Enhanced information in both positive and negative polarities after 1,5-diaminonapthalene deposition. *Anal. Chem.* **84**, 2048–2054 (2012).

86. Perry, W. J. *et al.* Uncovering matrix effects on lipid analyses in MALDI imaging mass spectrometry experiments. *J. Mass Spectrom.* **55**, e4491 (2020).

87. Kubo, A., Kajimura, M. & Suematsu, M. Matrix-Assisted Laser Desorption/Ionization (MALDI) Imaging Mass Spectrometry (IMS): A Challenge for Reliable Quantitative Analyses. *Mass Spectrom.* **1**, A0004–A0004 (2012).

88. Fahy, E., Sud, M., Cotter, D. & Subramaniam, S. LIPID MAPS online tools for lipid research. *Nucleic Acids Res.* **35**, W606 (2007).

89. Fahy, E., Cotter, D., Sud, M. & Subramaniam, S. Lipid classification, structures and tools. *Biochim. Biophys. Acta - Mol. Cell Biol. Lipids* **1811**, 637–647 (2011).

90. Sud, M. *et al.* LMSD: LIPID MAPS structure database. *Nucleic Acids Res.* **35**, (2007).

91. Fahy, E. *et al.* Update of the LIPID MAPS comprehensive classification system for lipids. *Journal of Lipid Research* **50**, S9 (2009).

92. Metsalu, T. & Vilo, J. ClustVis: a web tool for visualizing clustering of multivariate data using Principal Component Analysis and heatmap. *Web Serv. issue Publ. online* **43**, (2015).

93. Lotz, J. M. *et al.* Integration of 3D multimodal imaging data of a head and neck cancer and advanced feature recognition. *Biochim. Biophys. Acta - Proteins Proteomics* **1865**, 946–956 (2017).

94. Feider, C. L. *et al.* Molecular Imaging of Endometriosis Tissues using Desorption Electrospray Ionization Mass Spectrometry. *Sci. Rep.* **9**, (2019).

95. Eberlin, L. S. *et al.* Desorption electrospray ionization then MALDI mass spectrometry imaging of lipid and protein distributions in single tissue sections. *Anal. Chem.* **83**, 8366–8371 (2011).

96. Zavalin, A., Yang, J., Haase, A., Holle, A. & Caprioli, R. Implementation of a Gaussian beam laser and aspheric optics for high spatial resolution MALDI imaging MS. *J. Am. Soc. Mass Spectrom.* **25**, 1079–82 (2014).

97. Norris, J. L. & Caprioli, R. M. Analysis of Tissue Specimens by Matrix-Assisted Laser Desorption/ Ionization Imaging Mass Spectrometry in Biological and Clinical Research. *Chem. Rev.* **113**, 2309–2342 (2013).

98. Heeren, R. M. A. *et al.* Multimodal molecular imaging: Insight into the complexity of biological surfaces through speed, resolution and identification. *Microsc. Microanal.* **21**, 2235–2236 (2015).

99. Oliveira, F. P. M., Manuel, J., Tavares, R. S. & Tavares, J. M. R. S. Medical image registration: a review. *Comput. Methods Biomech. Biomed. Engin.* **17**, 73–93 (2014).

100. Whitehead, S. N. *et al.* Imaging Mass Spectrometry Detection of Gangliosides Species in the Mouse Brain following Transient Focal Cerebral Ischemia and Long-Term Recovery. *PLoS One* **6**, e20808 (2011).

101. Amstalden Van Hove, E. R. *et al.* Integrated Systems and Technologies Multimodal Mass Spectrometric Imaging of Small Molecules Reveals Distinct Spatio-Molecular Signatures in Differentially Metastatic Breast Tumor Models. *Cancer Res.* **70**, 9012–9021 (2010).

102. Abdelmoula, W. M. *et al.* Automatic 3D Nonlinear Registration of Mass Spectrometry Imaging and Magnetic Resonance Imaging Data. *Anal. Chem.* **91**, 6206–6216 (2019).

103. Hanselmann, M. *et al.* Concise Representation of Mass Spectrometry Images by Probabilistic Latent Semantic Analysis. *Anal. Chem.* **80**, 9649–9658 (2008).

104. Chughtai, K., Jiang, L., Greenwood, T. R., Glunde, K. & Heeren, R. M. A. Mass spectrometry images acylcarnitines, phosphatidylcholines, and sphingomyelin in MDA-MB-231 breast tumor models. *J. Lipid Res.* **54**, 333–44 (2013).

105. Oetjen, J. *et al.* MRI-compatible pipeline for three-dimensional MALDI imaging mass spectrometry using PAXgene fixation. *J. Proteomics* **90**, 52–60 (2013).

106. Verbeeck, N. *et al.* Automated Anatomical Interpretation of Ion Distributions in Tissue: Linking Imaging Mass Spectrometry to Curated Atlases. *Anal. Chem.* **86**, 8974–8982 (2014).

107. Holzlechner, M., Bonta, M., Lohninger, H., Limbeck, A. & Marchetti-Deschmann, M. Multisensor Imaging-From Sample Preparation to Integrated Multimodal Interpretation of LA-ICPMS and MALDI MS Imaging Data. *Anal. Chem.* **90**, 8831–8837 (2018).

108. Bemis, K. D. *et al.* Probabilistic Segmentation of Mass Spectrometry (MS) Images Helps Select Important Ions and Characterize Confidence in the Resulting Segments. *Mol. Cell. Proteomics* **15**, 1761–72 (2016).

109. Van de Plas, R., Yang, J., Spraggins, J. & Caprioli, R. M. Image fusion of mass spectrometry and

microscopy: a multimodality paradigm for molecular tissue mapping. *Nat Methods* **12**, 366–372 (2015).

110. Bankhead, P. *et al.* QuPath: Open source software for digital pathology image analysis. *Sci. Rep.* **7**, 16878 (2017).

111. Prism Ratio Paired T-test. *Ratio Paired T-test* (2019). Available at: www.graphpad.com.

112. Schober, Y., Guenther, S., Spengler, B. & Römpp, A. Single Cell Matrix-Assisted Laser Desorption/Ionization Mass Spectrometry Imaging. *Anal. Chem.* **84**, 6293–6297 (2012).

113. Kompauer, M., Heiles, S. & Spengler, B. Atmospheric pressure MALDI mass spectrometry imaging of tissues and cells at 1.4-μm lateral resolution. *Nat. Methods* **14**, 90–96 (2017).

114. Perkel, J. M. Starfish enterprise: finding RNA patterns in single cells. *Nature* **572**, 549–551 (2019).

115. Vickovic, S. *et al.* High-definition spatial transcriptomics for in situ tissue profiling. *Nat. Methods* **16**, 987–990 (2019).

116. Braverman, N. E. & Moser, A. B. Functions of plasmalogen lipids in health and disease. *Biochim. Biophys. Acta - Mol. Basis Dis.* **1822**, 1442–1452 (2012).

117. Dean, J. M. & Lodhi, I. J. Structural and functional roles of ether lipids. *Protein Cell* **9**, 196–206 (2018).

118. Braverman, N. E. *et al.* Peroxisome biogenesis disorders in the Zellweger spectrum: An overview of current diagnosis, clinical manifestations, and treatment guidelines. *Mol. Genet. Metab.* **117**, 313–21 (2016).

119. Sandalio, L. M., Rodríguez-Serrano, M., Romero-Puertas, M. C. & del Río, L. A. Role of Peroxisomes as a Source of Reactive Oxygen Species (ROS) Signaling Molecules. *Subcell Biochem* **69**, 231–255 (2013).

120. Farooqui, A. A. & Horrocks, L. A. Book Review: Plasmalogens: Workhorse Lipids of Membranes in Normal and Injured Neurons and Glia. *Neurosci.* **7**, 232–245 (2001).

121. Zoeller, R. A., Morand, O. H. & Raetz, C. R. A possible role for plasmalogens in protecting animal cells against photosensitized killing. *J. Biol. Chem.* **263**, 11590–6 (1988).

122. Raybuck, A. L. *et al.* B Cell-Intrinsic mTORC1 Promotes Germinal Center-Defining Transcription Factor Gene Expression, Somatic Hypermutation, and Memory B Cell Generation in Humoral Immunity. *J. Immunol.* **200**, 2627–2639 (2018).

123. Colgan, S. P. & Taylor, C. T. Hypoxia: an alarm signal during intestinal inflammation. *Nat Rev Gastroenterol Hepatol* **7**, 281–287 (2010).

124. Konisti, S., Kiriakidis, S. & Paleolog, E. M. Hypoxia--a key regulator of angiogenesis and inflammation in rheumatoid arthritis. *Nat Rev Rheumatol* **8**, 153–162 (2012).

125. Chen, X., Song, M., Zhang, B. & Zhang, Y. Reactive Oxygen Species Regulate T Cell Immune Response in the Tumor Microenvironment. *Oxid Med Cell Longev* **2016**, (2016).

126. Jellusova, J. *et al.* Gsk3 is a metabolic checkpoint regulator in B cells. *Nat. Immunol.* **18**, 303–312 (2017).

127. Lodhi, I. J. *et al.* Inhibiting adipose tissue lipogenesis reprograms thermogenesis and PPARγ

activation to decrease diet-induced obesity. *Cell Metab.* **16**, 189–201 (2012).

128. O'Keeffe, S. *et al.* Immunoglobulin G subclasses and spirometry in patients with chronic obstructive pulmonary disease. *Eur. Respir. J.* **4**, 932–6 (1991).

129. Ali Abdalla, M., Mostafa El Desouky, S. & Sayed Ahmed, A. Clinical significance of lipid profile in systemic lupus erythematosus patients: Relation to disease activity and therapeutic potential of drugs. *Egypt. Rheumatol.* **39**, 93–98 (2017).

130. Suurmond, J. & Diamond, B. Autoantibodies in systemic autoimmune diseases: Specificity and pathogenicity. *J. Clin. Invest.* **125**, 2194–2202 (2015).

131. de los Angeles García, M. *et al.* Evaluation of specific humoral immune response and cross reactivity against Mycobacterium tuberculosis antigens induced in mice immunized with liposomes composed of total lipids extracted from Mycobacterium smegmatis. *BMC Immunol.* **14 Suppl 1**, S11 (2013).

132. Careaga, M., Hansen, R. L., Hertz-Piccotto, I., Van de Water, J. & Ashwood, P. Increased anti-phospholipid antibodies in autism spectrum disorders. *Mediators Inflamm.* **2013**, 935608 (2013).

133. Wong-Baeza, C. *et al.* Anti-Lipid IgG Antibodies Are Produced via Germinal Centers in a Murine Model Resembling Human Lupus. *Front. Immunol.* **7**, 396 (2016).

134. Mantis, N. J., Rol, N. & Corthésy, B. Secretory IgA's complex roles in immunity and mucosal homeostasis in the gut. *Mucosal Immunology* **4**, 603–611 (2011).

135. Rowlinson, M. C. *et al.* Isolation of a strictly anaerobic strain of Staphylococcus epidermidis. *J. Clin. Microbiol.* **44**, 857–860 (2006).

136. Chandrasekaran, S. & King, M. R. Microenvironment of tumor-draining lymph nodes: Opportunities for liposome-based targeted therapy. *International Journal of Molecular Sciences* **15**, 20209–20239 (2014).